

Order and dynamics in Kagome like compound  
 $\text{Cu}_2\text{OSO}_4$  and other quantum magnets

Présentée le 2 juillet 2021

Faculté des sciences de base  
Laboratoire de magnétisme quantique  
Programme doctoral en physique

pour l'obtention du grade de Docteur ès Sciences

par

**Virgile Yves FAVRE**

Acceptée sur proposition du jury

Prof. V. Savona, président du jury  
Prof. H. M. Rønnow, Dr I. Zivkovic, directeurs de thèse  
Prof. K. Lefmann, rapporteur  
Dr O. Zaharko, rapporteuse  
Prof. F. Mila, rapporteur

La science a-t-elle promis le bonheur ? Je ne le crois pas. Elle a promis la vérité, et la question est de savoir si l'on fera jamais du bonheur avec de la vérité.

— Émile Zola

精力善用  
— 嘉納 治五郎

Baba, pour ton sourire, j'donnerais ma vie et p't-être même ma place au paradis.  
Donc j'ai aimé mon frère plus que ma vie, comme me l'a appris mon père.

— Tarik et Nabil Andrieu





# Acknowledgements

Many people deserve to be thanked for their contribution to this work, direct or indirect. First and foremost, I naturally wish to express my deepest thanks to Prof. Henrik Rønnow and to Dr. Ivica "Giroudvković" Živković for allowing me to complete my doctorate in their laboratory. This has been an incredibly fulfilling experience which would not have been possible without their continuous support, help, interest and kind suggestions. They contribute greatly to building up a work environment in which each and every one of their students and collaborators feels supported and can properly progress through his or her research work, without being afraid of being judged harshly.

I would also like to thank both my office mates, Namrata and Yikai, and also Priya, who was not sharing my office, but whose door was always open, effectively incorporating him as another office mate. The three of them have been very active in tremendously long discussions on physics and life, which played a crucial role in my progress, as a scientist, but also as a human being. I wish to extend these thanks to all of the members of the LQM with who I was lucky to collaborate: Cédric, who made a lot easier my first couple of months in LQM, Lin, Alex, Ping, Claudia, Benoît, Clément, Elahi, Ellen, Richard, Mabel, Caroline, Jana, Bruce, Alexandra, Daniil, Thomas, Davor, Alexandra, Giulia and Mina. I feel very grateful to Tarek for all the work and patience he had with me, he motivated me to be a better version of myself in the very beginning of my PhD by a sentence that I kept repeating myself in hard and good times: "Pourquoi devrais-tu te satisfaire de ne pas faire ce que tu peux faire de mieux ?". I am also extremely grateful to several people for their patience, teaching skills, and for all the knowledge and results I would not have obtained without them: Kurt Schenk for his skills in crystallography, Peter and Minki for their help understanding condensed matter physics as a whole, experiments, theory, and any unrelated topic, they were always willing to discuss and help. Greg's help was instrumental in my PhD, he accompanied me to every single neutron experiment I carried out in the beginning of my journey as an experimental physicist, and without his great support and friendship none of this would have been possible. I wish to thank particularly, Irina and Stas for being outstandingly friendly lab members and people, with who I had a lot of fun that kept me going through my whole PhD. Hadi also deserves many thanks for being such a wonderful teammate, always bringing up fun and help to my everyday life. We had so many discussions and breaks together, during which his joie de vivre was always radiating.

## Acknowledgements

---

Je vais maintenant remercier quelques personnes en français. Je tiens tout d'abord à remercier Yann Leroux pour son soutien, son inspiration et l'influence positive qu'il a eu sur moi depuis de nombreuses années, à travers ses enseignements et discussions. Je tiens ensuite à exprimer ma sincère gratitude à Arnaud Magrez, sans lequel mon doctorat n'aurait pas été possible, ou tout du moins potentiellement très différent : beaucoup moins intrigant et complexe. Il a en effet su pimenter ma vie de doctorant en produisant de nombreux magnifiques cristaux minuscules, et je l'en remercie. Je voudrais aussi remercier Darius, Nicolas Villa, Thomas, Loïc, Gaétan, Lidia, Samy, Samuel, Justin et Francis pour les nombreux cafés que nous avons partagés et discussions fructueuses que nous avons eues et qui ont porté ou non leurs fruits. Le support continu de mes amis m'a été d'un grand secours et je les remercie de leur soutien, tout particulièrement Valentina, Nicolas Tappy, Lily et Valentine et Margot. Je voudrais aussi remercier Baptiste pour sa joie de vivre et les nombreuses discussions que nous avons pu avoir sur le reblochon, la physique et la vie. Les aides de Nicolas, Giulia, Flurin, Filomena, Thomas, Valentine, Valérie, Jacques et Andreia pour la rédaction ont été très appréciées.

Tout d'abord, je souhaite remercier Vadim, qui a été un soutien hors du commun et dont la rencontre m'a beaucoup apporté, scientifiquement comme humainement. Je souhaite exprimer mes remerciements sincères à Victor, pour sa bienveillance et son amitié qui ont été une source d'inspiration continue durant mon doctorat. Peu de gens m'ont apporté autant que Matthieu, sa présence continue à mes côtés m'a aidé quotidiennement à progresser dans mon doctorat et ont rendu ma vie sur, et en dehors, du campus plus agréable. Nous avons partagé de nombreux moments ensemble, tous très agréables : en tant qu'étudiants, en vacances, autour d'une bonne andouillette ou autres spécialités régionales culinairement intéressantes, en faisant du sport, et en de nombreuses autres occasions qu'il serait impossible de récapituler en quelques mots. Merci Matthieu d'avoir été un ami sur lequel j'ai pu et je peux continuer de compter. Je remercie également très sincèrement Nicolas Christen d'avoir toujours été présent pour moi, pour son soutien continu, et son amitié sans faille. Je souhaite remercier Luc pour son esprit d'équipe, je trouve bien son esprit d'organisation, qui le pousse à rapprocher les gens, et je trouve que c'est dommage que ce soit si peu souvent le cas. Lejeuvement sincèrement soc lemercierric *lucLem* lourpuche m'lvoiraji lcompagnéaque louttem luaji longloc ludém loctordém. J'liaém lupem luiloque loserpém ledic lombreusesnem luestionsem, lequellesdem lntoem lmergéém ledoque lombreusesnic liscussionsdic luiqem lntoque larticipépem làem lonstruirecem lalem lersonnepem lueqic lejem luissoque levenue-dem. lonsem lideaès lcommesurableique lteji lasem lympathiesem lntoem louéjem lnuem lôleric llécem lansdem lalem léussiteroque ledem lonmem loctordem.

Finalement, je désire également remercier ma famille pour son soutien inconditionnel, sans eux aucune de mes études n'aurait été possible ; mes parents, mon grand père, mon oncle et ma tante, également Didier et Françoise, Olivier, et bien sûr mes deux frères, Etienne et Gabriel, qui sont une source d'inspiration continue. Je veux également remercier ma deuxième famille qui, sans m'avoir aidé matériellement, m'a cependant également apporté le meilleur des soutiens, psychologique, par leur présence et leur amour, merci infiniment Manuel, Paul,

Joseph-Emmanuel - Frère Francisco, Félix, F-X, Jérémy, Mathilde, Camille, François, Kévin, Alix, Alex et Corentin. Je souhaite finalement remercier Andreia pour avoir toujours été à mes côtés, qui est la meilleure partenaire dont je puisse aspirer à partager les jours, qui m'a soutenu tout au long de notre vie commune. Sans elle, je n'aurais pas pu aujourd'hui terminer cette thèse, elle fait de moi une meilleure personne et je me sens chanceux de te trouver à mes côtés pour affronter ensemble toutes les épreuves de la vie aux différentes échelles, des plus petites aux plus grandes.

*Lausanne, April 15, 2021*

V. Y. F.



# Abstract

This thesis presents results of studies of novel compounds modeling complex fundamental physics phenomena.  $\text{Cu}_2\text{OSO}_4$  is a copper based magnetic Mott Insulator system, where spin half magnetic moments form a new type of lattice. These intrinsically quantum spins are exhibiting atypical magnetic order and spin dynamics. The recent success in the growth of large single crystals of  $\text{Cu}_2\text{OSO}_4$  enabled to perform measurements probing its static and fluctuating properties. The peculiarity of this sample is that its atoms are forming layers, with a geometry close to the intensively studied Kagomé lattice, but with a third of its spins replaced by dimers. This quantum magnetism system has been probed in its bulk, by the means of heat capacity and DC-susceptibility measurements, revealing a transition to a magnetically long range ordered state upon cooling, the details of which are revealed by neutron scattering. Single crystal inelastic neutron scattering shed light on the spin-dynamics in the system, with clear spin waves appearing as fluctuations around the peculiar ground state of the system: a 120 degrees spin configuration where the magnetic moment of the spin-dimer causes the sample to be globally ferrimagnetic. The presented results indicate that  $\text{Cu}_2\text{OSO}_4$  represents a new type of model lattice with frustrated interactions where interplay between magnetic order, thermal and quantum fluctuations can be explored. The magnetic excitations of the compound can be modeled by a yet-to-be-understood internal effective mean-field that no simple magnetic coupling seems to reproduce.

$\text{K}_2\text{Ni}_2(\text{SO}_4)_3$  is another compound that allows for the existence of non-trivial topological phases. This thesis presents results of the study of the unusual magnetic behavior of  $\text{K}_2\text{Ni}_2(\text{SO}_4)_3$ . No clear sign of well-established magnetic long range order has been observed down to dilution temperatures. Neutron scattering reveals the details of the competition between frustration and fluctuations that prevent order from settling in. Low temperature spin excitations take the form of a continuum at 500 mK, but also of broad, energy independent continua at higher temperatures. Bulk and neutron scattering measurements are put in perspective and linked together with a view to building up a better understanding of how quantum spin liquids can be stabilized in general, and in particular in this model compound.

Finally, the last contribution of this thesis to the field of condensed matter physics regards the establishment of a state-of-the-art technique to fit heat capacity and unit cell volume of samples to try and make the extraction of magnetic information from specific heat measurements more robust. This newly-developed technique consists in modeling lattice contributions with

## Abstract

---

better accuracy by using data from multiple experimentally accessible quantities to consolidate the fitting scheme. This method has been cautiously applied to several compounds at the forefront of research in experimental physics.

**Key words** quantum magnetism, frustrated magnetism, strongly correlated systems, magnetic order, Kagomé lattice, transition metal compounds, magnetic susceptibility, neutron scattering, quantum spin liquids.

# Résumé

Cette thèse présente les résultats d'études poussées de composés novateurs modélisant des phénomènes physiques jusqu'alors incompris.  $\text{Cu}_2\text{OSO}_4$  est un aimant quantique dans lequel des atomes de cuivre forment un nouveau type de réseau, tout en préservant son caractère d'isolant de Mott. Le comportement intrinsèquement quantique des spins qui le constituent résulte en un ordre magnétique et des propriétés dynamiques atypiques, qui ont pu être mesurées grâce à la synthèse inédite de cristaux de ce composé. La particularité de cet échantillon est que les atomes qui le composent forment des couches atomiques présentant une géométrie similaire à celle du réseau Kagomé, avec cependant un tiers des atomes remplacés par des dimères. Les propriétés de cet aimant quantique ont été mesurées par plusieurs expériences successives, notamment en mesurant sa chaleur spécifique et sa susceptibilité magnétique, qui ont révélé que l'état fondamental à basse température est donné par un arrangement magnétique de spins présentant un ordre magnétique longue portée (OMLP) en dessous de 20 K. Les détails de la configuration de spin associée ont pu être identifiés grâce à des mesures de diffusion neutronique. Des expériences de diffusion inélastique de neutrons sur des monocristaux ont permis d'étudier en détail la dynamique des spins du système, notamment avec l'observation d'ondes de spins, fluctuations autour de l'état OMLP, lequel peut être décrit comme une configuration de spins à  $\sim 120$  degrés, dans laquelle les moments magnétiques des dimères causent un moment ferrimagnétique résiduel de faible intensité. L'ensemble des résultats obtenus indiquent que  $\text{Cu}_2\text{OSO}_4$  constitue un nouveau modèle jouet, où la conspiration entre interactions frustrées et fluctuations quantiques et thermiques peuvent être étudiées. Les excitations de ce composé peuvent être modélisées par un intéressant champ-moyen interne, dans un modèle effectif qu'aucun couplage magnétique ne semble pouvoir décrire fidèlement.

$\text{K}_2\text{Ni}_2(\text{SO}_4)_3$  est un autre composé qui accueille des phases topologiques non triviales, dont les propriétés magnétiques inhabituelles sont présentées dans cette thèse. Aucun signe inéquivoque d'OMLP n'a été décelé en refroidissant jusqu'à des températures de dilution. La diffusion neutronique révèle les détails de la concurrence entre frustration et fluctuations qui empêche l'OMLP de s'établir. Les excitations de spins à basse température correspondent à un continuum de diffusion à forte dépendance angulaire à 500 mK, qui se transforment en des continua de diffusion ne dépendant pas de l'énergie à des températures plus élevées. Les analyses de mesures de laboratoire et de diffusion de neutrons sont combinées afin de progresser dans la compréhension des phénomènes stabilisant l'état de liquide de spin quantique.



Finalement, la dernière contribution de ce travail au domaine de la physique du solide concerne l'établissement d'une méthode d'ajustement de données de chaleur spécifique, afin de rendre leur analyse plus robuste. En combinant ces données avec celles du volume de la cellule unitaire, une routine plus rigoureuse a pu être mise au point pour extraire l'entropie magnétique de systèmes quantiques. Ce formalisme a été précautionneusement appliqué à l'analyse de mesures effectuées sur des composés avant-gardistes dans le domaine de la matière condensée.

**Mots clés** Magnétisme quantique, magnétisme frustré, systèmes d'électrons fortement corrélés, ordre magnétique, réseau Kagomé, composés de métaux de transition, susceptibilité magnétique, diffusion neutronique, liquides de spin quantiques.

## Sommario

La tesi raccoglie i risultati di una serie di studi condotti su dei nuovi composti che manifestano fenomeni di fisica fondamentale ad oggi incompresi. Il  $\text{Cu}_2\text{OSO}_4$  è un magnete quantistico in cui gli atomi di rame formano un nuovo tipo di reticolo, pur mantenendo le caratteristiche di un isolante di Mott. Il comportamento intrinsecamente quantistico degli spin che lo compongono risulta in un ordine magnetico e delle proprietà dinamiche insoliti. Il recente successo nella sintesi di grandi monocristalli di  $\text{Cu}_2\text{OSO}_4$  ha permesso di effettuare delle misure che ne sondano le proprietà. La peculiarità del campione è che i suoi atomi sono disposti in strati, con una geometria analoga al più noto reticolo di Kagomé, in cui tuttavia un terzo degli spin sono sostituiti da dimeri. Le proprietà di questo magnete quantistico sono state sondate in una serie di esperimenti, in particolare per via di misure di calore specifico e suscettività magnetica DC, le quali hanno rivelato che lo stato fondamentale a bassa temperatura possiede un ordine magnetico a lungo raggio al di sotto di 20K. I dettagli della configurazione di spin associata a tale stato sono stati individuati grazie a misure di scattering di neutroni. Esperimenti di diffusione anelastica di neutroni su monocristalli hanno permesso di studiare in dettaglio la dinamica di spin del sistema, e di osservare delle onde di spin apparire come fluttuazioni intorno allo stato fondamentale che può essere descritto come una configurazione di spin a 120 gradi, in cui i momenti magnetici dei dimeri rendono il campione globalmente ferromagnetico. I risultati qui esposti indicano che il  $\text{Cu}_2\text{OSO}_4$  rappresenta un nuovo tipo di reticolo modello, e un buon terreno per lo studio degli influssi reciproci tra interazioni frustrate e fluttuazioni quantistiche e termiche. Gli stati eccitati del campione possono essere modellizzati da un campo-medio effettivo che sembra non essere riprodotto da nessun accoppiamento magnetico semplice.

Il  $\text{K}_2\text{Ni}_2(\text{SO}_4)_3$  è un altro composto che permette l'esistenza di fasi topologiche non triviali. La tesi presenta risultati di uno studio sull'inusuale comportamento magnetico del  $\text{K}_2\text{Ni}_2(\text{SO}_4)_3$ . Raffreddando il composto fino a temperature di diluizione non si sono osservati segni chiari di ordine magnetico ben stabilito a lungo raggio. La diffusione di neutroni rivela in dettaglio la concorrenza tra frustrazione e fluttuazioni che impedisce lo stabilirsi di un ordine magnetico. Eccitazioni di spin a bassa temperatura prendono la forma di onde di spin a 500mk, ma si trasformano in un continuo indipendente dall'energia a temperature più elevate. I risultati di misure di laboratorio e di scattering di neutroni sono analizzati e interconnessi, con la visione di costruire una migliore comprensione di come liquidi di spin quantistici possono essere stabilizzati.

Infine, l'ultimo contributo di questa tesi al campo della fisica della materia condensata riguarda lo sviluppo di una tecnica innovativa per l'adeguamento dei dati di calore specifico, al fine di renderne il trattamento più robusto. Lo studio congiunto di questi dati e di quelli del volume della cella unitaria ha permesso un'analisi più rigorosa dell'estrazione di informazione magnetica di sistemi quantistici. Questo metodo è stato applicato con estrema cautela a numerosi composti all'avanguardia nella ricerca in fisica sperimentale.

**Parole chiave** Magnetismo quantistico, magnetismo frustrato, sistemi elettronici fortemente correlati, ordine magnetico, Kagomé, composti dei metalli di transizione, suscettività magnetica, diffusione anelastica di neutroni, liquidi di spin quantistico.

## Zusammenfassung

Diese Arbeit stellt die Ergebnisse von Studien neuer Materialien vor, welche neue, bislang unverstandene, fundamentale physikalische Phänomene modellieren.  $\text{Cu}_2\text{OSO}_4$  ist ein Kupfer-basierter Mott Isolator, in dem halbzahlige Spins eine neue Art von Gitter bilden. Diese intrinsischen Quantenspins weisen untypische magnetische Ordnungen und Spindynamiken auf. Die jüngsten Erfolge bei der Züchtung von  $\text{Cu}_2\text{OSO}_4$  Einkristallen ermöglichten die Messung dieser statischen und fluktuierenden Eigenschaften. Die Besonderheit dieser Probe besteht darin, dass ihre Atome Schichten bilden, deren Geometrie eng mit dem eingehend untersuchten Kagomé-Gitter verwandt ist, wobei jedoch ein Drittel der Spins durch Dimere ersetzt wird. Bei der Untersuchung dieses quantenmagnetischen Systems in seiner Bulk-Form mittels Wärmekapazitäts- und DC-Suszeptibilitätsmessungen wurde während des Herunterkühlens ein Übergang zu einem magnetisch langreichweitigen Zustand entdeckt, dessen genaue Beschaffenheit mittels Neutronenstreuung wiederum näher untersucht wurde. Einkristallinelastische-Neutronenstreuung verschaffte Klarheit über die Spindynamiken im System, wobei Spinwellen als Fluktuationen um den speziellen Grundzustand des Systems in Erscheinung traten, nämlich eine 120 Grad Spin-Konfiguration, bei der die magnetischen Momente der Spin-Dimere zum Ferrimagnetismus der Probe führen. Die hier vorgestellten Ergebnisse lassen darauf schließen, dass  $\text{Cu}_2\text{OSO}_4$  einen neuen Typ von Modellgitter mit frustrierten Wechselwirkungen darstellt, mithilfe dessen die Wechselwirkungen zwischen magnetischer Ordnung und thermischen und Quantenfluktuationen untersucht werden können. Die Anregungen in diesem Material können durch ein interessantes internes Mean-Field modelliert werden, welches durch keine einfache magnetische Kopplung reproduziert werden kann.

$\text{K}_2\text{Ni}_2(\text{SO}_4)_3$  ist eine weitere Verbindung, die die Existenz nicht-trivialer topologischer Phasen zulässt. Diese Arbeit stellt die Ergebnisse der Untersuchungen zur ungewöhnlichen magnetischen Beschaffenheit von  $\text{K}_2\text{Ni}_2(\text{SO}_4)_3$  vor. Sogar bei den niedrigen Temperaturen im Mischungskryostat konnte kein eindeutiges Signal einer wohlbekannten magnetisch - langreichweitigen Struktur beobachtet werden. Mithilfe von Neutronenstreuung konnten die genaueren Zusammenhänge zwischen der konkurrierenden Frustration und Fluktuation, welche eine weitere Ordnung verhindern, identifiziert werden. Spin-Anregungen bei tiefer Temperatur treten sowohl wie eine Kontinua-Spinwellen Mischung bei 500 mK als auch wie breite, Energie-unabhängige Kontinua bei höheren Temperaturen in Erscheinung. Bulk- und Neutronenstreuungsmessungen dienen als Grundlage zum besseren Verständnis der Stabilisierungsmechanismen von Quantenspinflüssigkeiten.

Schliesslich besteht der letzte Beitrag dieser Arbeit zum Feld der Physik der kondensierten Materie in der Entwicklung einer neuen Methode zum Fitten der Wärmekapazität und des Volumens der Einheitszelle, indem die Gitterbeiträge mit besserer Genauigkeit modelliert werden, sodass die magnetischen Beiträge aus spezifischen Wärmemessungen entsprechend verlässlicher bestimmt werden können. Diese Methode wurde ebenso auf andere Materialien angewandt, die Gegenstand hochaktueller Forschung in der Physik sind.

**Schliessenwörter** Quantenmagnetismus, Frustration, stark korreliert Elektronensysteme, magnetische Ordnung, Kagomé, Materialien mit Übergangsmetallen, magnetische Suszeptibilität, Neutronenstreuung, Quantenspinflüssigkeit

## Resumaziun

Questa dissertaziun presenta resultats da studias cun novas colligiazions da substanzas per modellar fenomens fisics che ein tochen uss aunc buc capi.  $\text{Cu}_2\text{OSO}_4$  ei in Mott Isolatur sistem che sebas sin irom, nua che spins e mez-spins fuorman in niev tip da reit. Quels intrinsics spins da quantum muossan ina ordinaziun magnetica e dinamica da spin atipica. Dacuort han ins cun success saviu crear gronds singuls cristals da  $\text{Cu}_2\text{OSO}_4$  e cun quels saviu miserar quellas qualitats staticas ed instabilas. La particularitad da quei material ei che ils atoms fuorman stresas cun ina geometria semagliona sco ils schi numnai Kagomé lattice, denton ein in tierz dils spins remplazzai entras dimers. Quest sistem da quantum magnetism ei vegnius testaus sco massa entira, sco mied dalla capacita da temperature cauda e mesiras da DC-sensibilitad. Quei ha mussau si che eid at ina trasnsiziun tier in stadi magnetic cun in grond uorden sche ei vegn sferdentau, da quei che detagls ein vegni registrai ord mesiras da dispersiun da neutrons. La inelastizitad dalla dispersiun da neutrons da singuls cristals ha clarificau la dinamica da spins en il system, cun claras undas da spin che cumparan nua che fluctuaziuns entuorn il stadi da basa dil sistem: ina 120 grads configuraziun da spin nua che il mument magnetic dil spin-dimer procura che il material ei global ferrimagnetic. Ils resultats presentai indicheschan che  $\text{Cu}_2\text{OSO}_4$  representa in niev tip da reit sco model cun frustradas interacziuns nua che la interacziun denter las ordinaziuns magneticas, thermalas e flucutaziuns da quantum san vegnir eruidas. L'exitaciun d'in component thermic sa vegnir modlaus d'ina interna mediana-reit che sa buc vegnir reproducida cun ina copulaziun sem-pelmagnetica.

$\text{K}_2\text{Ni}_2(\text{SO}_4)_3$  ei ina autra cumponenta che lubescha l'existenza da buc-trivialas topologicas fasas. Questa dissertaziun presenta resultats che sclareschan il cuntener magnetic da  $\text{K}_2\text{Ni}_2(\text{SO}_4)_3$ . Negin sègn d'ina ordiazion d'in spectrum grond magnetic ei vegnius obervaus tier temperaturas rarificadas. Dispersiun da neutrons ha mussau ils detagls dalla cumpetiziun denter frustraziun e fluctuaziun che ei involvada en la prevenziun dad uorden. Bassas temperaturas meinan tier excitaziuns da spin en fuorma dad undas da spin tier 500mK, denton era da largias cuntinuaziuns, independentas dad energia tier temperaturas aultas. La gronda part e las mesiras da dispersiun da neutrons vegnan messas en perspectiva e ligiadas ensemmen cun ina vesta per baghegiar si ina megliera capientscha per la stabilisaziun da liquids da quantum spin.

Sco davos pass mira questa dissertaziun en il rom da fisica da condensada materia, nua che

ina moderna tecnica duei vegnir fabricada, che ei capabla da cumpigliar la capaciad da temperatura cun la mesira d'il volumen dalla cella per empruvar da fabricar in pli robust sistem dad extrahir magneticamein infurmaziuns pertuond temperaturas cauldas specificas, cun modelar pli precis contribuziuns da reit. Questa metoda ei silsunter vegnida duvrada cun cauziun tier different materials impurtonts per la retscherca en la fisica experimentalala.

**Plaids-clav** Mott isolatur, Kagomé, 120 grads configuraziun, frustraziun, liquids da quantum spin, fisica da condensada materia, fisica experimentalala.

# Abstracto

Esta tese apresenta os resultados de estudos de compostos inovadores que modelam fenómenos físicos anteriormente mal compreendidos. O  $\text{Cu}_2\text{OSO}_4$  é um isolante de Mott, e também um ímã quântico no qual átomos de cobre formam um novo tipo de rede. O comportamento intrinsecamente quântico dos spins que o constituem resulta numa ordem magnética e propriedades dinâmicas atípicas, que podem ser medidas graças à nova síntese de cristais deste composto. A particularidade desta amostra é que os seus átomos formam camadas atômicas, tendo uma geometria semelhante à da rede de Kagome, mas com um terço dos átomos substituídos por dímeros. As propriedades deste ímã quântico foram medidas através de várias experiências sucessivas medindo o calor específico e a susceptibilidade magnética. Ambos revelaram que o estado fundamental do sistema é dado por uma disposição que mostra uma ordem magnética de longo alcance (OMLA) com temperaturas abaixo de 20 K. Os detalhes da configuração do spin foram identificados através de medidas de dispersão de nêutrons. As experiências de dispersão de nêutrons inelásticos com monocristais tornaram possível estudar de forma pormenorizada a dinâmica do sistema, com a observação de ondas de spin, flutuações em torno do estado da OMLA que podem ser descritas como configuração de spins com um ângulo de 120 graus, em que os momentos magnéticos dos dímeros resultam em um momento magnético residual de pouca intensidade. Os resultados indicam que o  $\text{Cu}_2\text{OSO}_4$  constitui um novo modelo, em que a conspiração entre interações frustradas e flutuações quânticas e térmicas podem ser estudadas. Os estados excitados deste composto podem ser modelados por um interessante campo médio interno num padrão eficaz que nenhuma interação magnética parece ser capaz de descrever.

O  $\text{K}_2\text{Ni}_2(\text{SO}_4)_3$  é outro composto que acolhe fases topológicas não triviais. Esta tese apresenta o comportamento magnético incomum do  $\text{K}_2\text{Ni}_2(\text{SO}_4)_3$ . Nenhum sinal da OMLA foi detectado por arrefecimento até temperaturas de diluição. A dispersão de nêutrons revela os detalhes da competição entre a frustração e as flutuações que impedem o estabelecimento da OMLA. As excitações de spins a baixa temperatura correspondem a um continuum de difusão com dotação formada de ondas de spin a 500 mK, mas são transformadas numa difusão contínua que não depende da energia em temperaturas mais elevadas. Os resultados do laboratório são combinados com resultados de dispersão de nêutrons a fim de progredir na compreensão dos fenómenos que estabilizam o estado de líquido de spin quântico.

Finalmente, a última contribuição deste trabalho para o domínio da física do estado sólido



## Abstracto

---

trata do estabelecimento dum método de ajuste de curvas adaptado aos dados de calor específico, a fim de melhorar o tratamento para que ele se torne mais robusto. Ao combinar estes dados com os do volume da célula unitária, uma análise mais rigorosa poderia ser feita para extrair a entropia dum sistema quântico. Este método foi cuidadosamente aplicado à análise das medidas de compostos novos no domínio da matéria condensada.

**Palavras-chave** magnetismo quântico, magnetismo frustrado, sistemas de electrões extremamente interligados, ordem magnética, Kagomé, compostos de metais de transição, susceptibilidade magnética, dispersão de nêutrons, líquidos de spin quânticos.

# Contents

<b>Acknowledgements</b>	<b>i</b>
<b>Abstract</b>	<b>v</b>
<b>Introduction</b>	<b>1</b>
<b>I A brief review of (quantum) magnetism</b>	<b>7</b>
<b>1 Transition metal atoms in a lattice</b>	<b>9</b>
1.1 Crystal field splitting, quenching and effective spin . . . . .	9
1.2 Superexchange: the microscopic origins of magnetism . . . . .	14
<b>2 Magnetic interactions</b>	<b>17</b>
2.1 What are Mott insulators and why are they even interesting? . . . . .	17
2.1.1 Context . . . . .	17
2.1.2 Magnetism: Mott-Hubbard-Heisenberg . . . . .	18
2.2 Heisenberg interactions . . . . .	21
2.2.1 Ferromagnetism . . . . .	21
2.2.2 Antiferromagnetism . . . . .	23
2.2.3 Ferrimagnetism . . . . .	25
2.3 Anisotropies . . . . .	26
2.3.1 Dzyaloshinskii-Moriya interaction . . . . .	26
2.3.2 Other anisotropies . . . . .	27
<b>3 What is quantum magnetism?</b>	<b>29</b>
3.1 Frustrated magnetism . . . . .	29
3.2 Spin liquids . . . . .	33
<b>II Experimental background</b>	<b>37</b>
<b>4 Magnetometry</b>	<b>39</b>
4.1 Superconducting Quantum Interference Devices . . . . .	39
4.2 Magnetometers . . . . .	41
4.3 Vibrating Sample Magnetometers . . . . .	42

## Contents

---

<b>5</b>	<b>Heat Capacity measurements</b>	<b>45</b>
5.1	Principle . . . . .	45
5.2	Measurements in practice . . . . .	46
5.3	Applications . . . . .	47
<b>6</b>	<b>Resonance techniques</b>	<b>51</b>
6.1	Electron Spin Resonance . . . . .	52
6.2	Muon Spin Rotation . . . . .	57
<b>7</b>	<b>X-ray techniques</b>	<b>65</b>
7.1	Basic elements of X-ray diffraction . . . . .	66
7.2	Powder X-ray diffraction . . . . .	70
7.3	Single crystal X-ray diffractometer . . . . .	73
7.4	Laue diffractometer . . . . .	75
<b>8</b>	<b>Neutron scattering techniques</b>	<b>77</b>
8.1	Brief elements of scattering theory . . . . .	77
8.2	Quantum scattering processes . . . . .	81
8.2.1	Diffraction from a crystal . . . . .	81
8.2.2	Diffraction from a powder . . . . .	82
8.3	Magnetic scattering . . . . .	83
8.4	Neutron spectroscopy . . . . .	84
8.5	Polarized neutron scattering . . . . .	86
<b>III</b>	<b>Quantum magnets and methods</b>	<b>89</b>
<b>9</b>	<b><math>\text{Cu}_2\text{OSO}_4</math>: a playground for low dimensional quantum magnetism</b>	<b>91</b>
9.1	Synthesis process . . . . .	92
9.2	Bulk measurements: a potential ferrimagnet . . . . .	95
9.2.1	X-ray diffraction and crystal structure . . . . .	95
9.2.2	Structure and lattice . . . . .	98
9.2.3	Heat capacity . . . . .	100
9.2.4	DC susceptibility and magnetization . . . . .	103
9.3	Neutron diffraction unveils $120^\circ$ magnetic order . . . . .	109
9.4	Discussion on static properties of $\text{Cu}_2\text{OSO}_4$ . . . . .	116
9.5	Spin dynamics: two decoupled sub-lattices and a mean field . . . . .	118
9.5.1	Experimental evidence for magnons . . . . .	119
9.5.2	Modelling . . . . .	123
<b>10</b>	<b><math>\text{K}_2\text{Ni}_2(\text{SO}_4)_3</math>: frustration at its finest</b>	<b>127</b>
10.1	Indications of 3D, $S=1$ quantum spin liquid . . . . .	127
10.1.1	Structure . . . . .	129
10.1.2	Heat Capacity . . . . .	133

10.1.3 Magnetization - Susceptibility . . . . .	136
10.1.4 ESR . . . . .	138
10.1.5 $\mu$ SR and the absence of magnetic long range order . . . . .	139
10.2 Frustration-suppressed magnetic long range order . . . . .	146
10.2.1 Elements of a magnetic ground state . . . . .	146
10.2.2 Diffuse scattering . . . . .	156
10.2.3 Dispersive excitations and continua . . . . .	160
10.2.4 Discussion on $\text{K}_2\text{Ni}_2(\text{SO}_4)_3$ . . . . .	162
<b>11 Combining heat capacity and X-rays: a new way to investigate spins systems</b>	<b>163</b>
11.1 Experimentally educated methods . . . . .	165
11.1.1 Theory: Debye and Einstein . . . . .	165
11.1.2 Chemical substitution . . . . .	168
11.1.3 Results . . . . .	169
11.2 Calculations predicting heat capacity . . . . .	176
11.2.1 Density Functional Theory . . . . .	176
11.2.2 Silicon . . . . .	178
11.2.3 $\text{MnF}_2$ . . . . .	180
<b>Conclusion</b>	<b>183</b>
<b>Bibliography</b>	<b>187</b>
<b>Curriculum Vitae</b>	<b>215</b>



# Introduction

According to Moore's law, which was stated in the second half of the twentieth century, the number of transistors in integrated circuits doubles every two years. Transistors are the building block of any integrated circuit and Moore's law thus directly translates into a more general prediction on the size of computers. Ever since this statement was made, the law has been wrongfully declared dead on many occasions. In recent times, the fact that the transistor size started edging that of a single atom prompted expert to renew claims that the law is dead, and its relevance is once again debated. In the 21st century and in the digital era, such integrated systems play an always greater role in people's everyday lives and collective behaviors: the need for more energy efficient data storage and communication technology solutions appears and limitations to Moore's law could directly result in world-scale issues. Regardless of the debate on whether Moore's law is dead or not, one could say that size does not necessarily matter, and a parallel can be drawn with cell phones, whose size has shifted from becoming ever smaller, to now getting larger and larger again. Quite naturally, there is a clear reason for that: with all the information that one can process in the digital era, it has been realized that having high quality screens, and computing power, were among the most important features that a cell phone should possess, and thus resulted in larger dimensions of the associated tools. Similar to that, and independently of whether Moore's law actually holds, an incredible focus in the scientific community is put on energy optimization rather than pure size reduction of transistors, and magnetism proved to be paramount when it came to developing new, more energy efficient technologies. While the most recent transistor size is of the order of one nanometer[1], physicists still extensively study magnetic skyrmions, a topologically protected, thus very robust, quasi-particle made of a magnetic spin vortex, even though a skyrmion typically occupies a space that is much larger than an atom, typically up to a hundred of nanometers[2]. Recent research acknowledged the key importance of efficiency and, thus, scientists put gargantuan efforts on trying to both lower the energy cost of device operations and increase the effectiveness of data storage. Many of these promising attempts involve the use of magnetic systems[3, 4, 5, 6, 7].

Such technological applications of magnetism are numerous; they form an almost never-ending list. Many of these tools are quite far from being tangible applications of magnetism that non scientists are used to encounter in their everyday lives. Examples include simple

## Introduction

---

fridge magnets, compasses, or even magnetic levitation trains which are used to create a significant part of the Japanese Shinkansen railway service. Applications of magnetism have been sought ever since the phenomenon was discovered, even though they were far from being properly understood. Although the notion of magnetism was already present before, e.g. by observing the effects of lodestone, it is usually believed that Plato was the first to discover the effects of magnetization in Europe in 427 BC. Humans quickly realized they could use a compass to navigate and orient themselves, taking advantage of the Earth's magnetic field. Here again, it is quite hard to precisely determine the first recorded use of a compass, but several mentions of its use in Europe start to appear around the twelfth century, with Alexander Neckar and famous french trouvère Guiot de Provins both acknowledging its existence.

In the nineteenth century, a proper revolution of the understanding of magnetism occurred, with many biological applications, such as Franz Mesmer's animal magnetism used to treat human health problems. Later in the century, experiments by Oersted, Ampère, Biot, Savart, Faraday, Tesla, and many more shed considerable light on the nature of magnetism and the way it is deeply linked to electricity. Arguably the apex of the discoveries in that century was reached with the establishment of Maxwell's equations governing the behavior of the electromagnetic field and its interaction with matter[8].

New breakthroughs appeared also in the twentieth century, partially thanks to the then-recent development of quantum physics, with in particular Louis Néel's Nobel prize for his theories on ferromagnetism and antiferromagnetism. Notably, Kamerlingh Onnes discovered a novel property of a whole class of compounds, which, upon cooling, allowed for resistanceless transport of electric charges, opening up a whole range of potential applications[9, 10, 11, 12]. Relatively soon after, the field of quantum magnetism was born and exploding, and the number of applications of quantum magnetism burst, leading to some very exotic examples[13]. Even more surprising contributions can be found on the internets, such as the flourishing field of quantum magnetizers, offering healthcare solutions by realigning one's inner self with the full quantum realm.

Quite strikingly, in Louis Néel's own Nobel prize lecture, he himself stated that the antiferromagnetic state was "interesting, but useless". Many contemporary applications proved him wrong, with an example being the newly realized antiferromagnetic random-access memory[14]. Overall, this view highlights the fact that, for various reasons -and quantum magnetism is no exception-, two main branches of research philosophies in physics seem to emerge: research in fundamental physics, considered as "interesting", and research in fundamental physics applications, considered as "not useless". The field of quantum magnetism developed, naturally balancing the two branches. The fundamental side moved, among others, towards the study of contemporary frustrated magnetism, quantum spin liquids, and so on, whose applications are related to topological quantum computing, but are not yet available

in scalable, commercialized systems. In any case, a necessary prerequisite to the study of quantum magnets is to assess their fundamental magnetic properties. These properties take the form of a zero Kelvin ground state, which sometimes presents magnetic order due to the progressive weakening of thermal fluctuations and a spontaneous time-reversal symmetry breaking that induces magnetic states. These states of matter can be studied using various experimental methods and can be described by a theoretical Hamiltonian, describing the interactions at play and different energy sources in the system. More often than not, it is very difficult to build up a full description of a compound solely based on its static properties and perturbations and fluctuations of the system provide significant information on a given compound in an unambiguous way. This thesis deals with the order and dynamics in Kagomé like compound  $\text{Cu}_2\text{OSO}_4$  and other quantum magnets.

### Thesis outline

This thesis describes experimental studies of different quantum magnets, and compares experimental results with elements of theory that can model the measured compounds. The work is divided in several parts, the first two of which elaborate on the notions of quantum magnetism and experimental physics, which are required to perform and interpret real-life experiments. A reader with adequate notions of quantum magnetism can thus directly read the part presenting results, while a reader less familiar with the field of condensed matter physics may find comfort in first thumbing through the first parts. The chapters containing results have been ordered in terms of relative importance, relevance, and completeness of the analysis, but can be read completely independently, in any order. The detailed content is summarized in the following paragraphs.

- The first part discusses brief elements of quantum magnetism, explaining fundamental properties of Mott insulators, and why the Heisenberg Hamiltonian turns out to be one of the most relevant ways to describe condensed matter systems in real materials. It discusses what are these magnetic interactions, which ground state they typically result in, and what is their origin, with a brief explanation of the superexchange mechanism, accounting for most of magnetic couplings in atoms with transition metal oxides compounds. A final note presents the interest in frustrated physics, introducing the notion of quantum spin liquid, its practical relevance, and contemporary problems in solid state physics.
- The second part deals with presenting briefly the many different experimental techniques that were used to actually extract physical information out of samples, in real experiments. These techniques include DC-susceptibility, one of the most fundamental ways of probing magnetic systems, as well as heat capacity, a common technique shedding light on phase transitions that are frequently occurring in real materials. Several



resonance techniques are also described, namely the Electron Spin Resonance (ESR) and Muon Spin Rotation ( $\mu$ SR). These two techniques are local probes and  $\mu$ SR is one of the tools that are the most sensitive to magnetic long range order. In the last chapters of this section, scattering techniques are presented: X-ray scattering and its uses to characterize and align samples, and naturally neutron scattering, which is one of the most powerful ways of probing large systems of spins. Neutron scattering indeed proves to be a remarkable tool allowing both to assess the details of the ground state of spin systems, and also the spin fluctuations that are fingerprints of the Hamiltonian describing the fundamental physics hosted by a compound. Moreover, neutron scattering is compatible with many sample environments, enabling to explore multi-parameter phase diagrams and to compare diligently results with different predictions from different theories.

- The last part of this thesis describes results of measurements and theories modeling real condensed matter systems.
  - $\text{Cu}_2\text{OSO}_4$  is a compound that can be considered as a two-dimensional copper based quantum magnet. The interesting physical properties of this system can be described and linked to the magnetic lattice formed by the copper, spin half atoms that interact with each other. Two inequivalent atomic positions give rise to a complex magnetic lattice that can be described as a Kagomé lattice, with one third of the atoms replaced by dimers. Neutron diffraction and bulk measurements reveal that the system undergoes a transition to a state with magnetic long range order, close the renowned  $120^\circ$  configuration, with a small ferrimagnetic component. It appears that the scale of the interactions in the system places it very close to a quantum transition to a magnetically disordered state, that could be reached in practice by applying external pressure on the compound. The dynamics of the system prove to be challenging to analyze, but confirm the decoupling of Kagomé-like planes with each other and also confirms that the main interactions in the system are within the plane. The best model that could be established describes the magnons in the system as originating from a system similar to a one dimensional chain, embedded in an external magnetic field at half saturation, with in this case the field being generated by a ferromagnetic alignment of spins at the dimer site.
  - $\text{K}_2\text{Ni}_2(\text{SO}_4)_3$  is another very interesting quantum magnet. This system is consisting of nickel based, spin one magnetic moments. Their collective effect does not show any sign of magnetic long range order, down to a temperature of one and a half Kelvin, and signs of frustrated and suppressed magnetic order start to appear at lower temperatures. The magnetic lattice of the compound cannot be simply described in terms of the commonly known lattices, but rather as two interconnected trillium lattices. Nearest neighbor interaction does not suffice to create a simple

lattice, and in order to tessellate properly the full compound, the cornerstone of the compound appears to be loops involving ten different ions in a frustrated manner. Neutron scattering, reveals that weak magnetic Bragg peaks appear at dilution temperature, over a broader peak built up by short-range correlations, characteristic signature of quantum spin-liquid physics. This evidence is accompanied by the experimental observation of a continuous feature on top of a dispersive element at the same temperature. It appears that the spin-liquid state survives down to 1.2 K, as confirmed by inelastic neutron scattering experiments on single crystal that show clear diffuse scattering: energy independent features in the excitation spectra, typical of short range correlated systems.

- The last chapter of the section deals with the presentation of a novel method to analyze experimental data. Heat capacity data fits are indeed not always robust. The use of unit cell volume information is hereby presented, with a view to making the fitting scheme more robust, and applications to real condensed matter systems are shown. One of the most useful quantities that can be obtained by this method is the magnetic heat capacity, of which the integral corresponds to the magnetic entropy of the system. Examples of the method and its uses are included, and further improvements are mentioned for completeness.



# **A brief review of (quantum) magnetism**

## **Part I**



# 1 Transition metal atoms in a lattice

## 1.1 Crystal field splitting, quenching and effective spin

With the help of quantum physics and chemistry, the behavior of each atom in the periodical table could be successfully worked out, starting from the simple case of the atom of hydrogen, surrounded by a single electron. Even though it creates a complex many body physics problem, the ground state of atoms with many more electrons in their cloud, and protons and neutrons in their nuclei could also be reasonably well explained. The physical state of an electron is described by several quantum numbers: the principal quantum number,  $n$ , an integer greater or equal to one, the azimuthal quantum number  $l$ , describing the electronic subshell, with  $0 \leq l \leq n - 1$ , the magnetic quantum number  $m_l$ , with  $-l \leq m_l \leq l$  and the spin quantum number  $m_s = \pm 1/2$ . Most of the electronic properties of a single ion can be deduced, in essence, by the so called Aufbau principle and the three Hund's rules:

- Rule 1: In a given system, Pauli's exclusion principle prevents two electrons from sharing the same quantum numbers. The configuration with the lowest energy will be the one maximizing the total spin.
- Rule 2: For a configuration with a given total spin, the configuration with the lowest energy will be the one maximizing the total angular momentum.
- Rule 3: The spin orbit coupling interaction breaks the usual spherical symmetry, and couples the total angular quantum number to the total spin quantum number. The main two schemes are known as the *jj* scheme, mainly used to describe systems with strong spin orbit coupling and the Russell-Saunders (LS) scheme, applicable to most 3d-transition metal elements. In the *jj* scheme, one first couples the orbital moment to the spin moment before coupling each electron to each other. In the LS scheme, the total spin  $\mathbf{S}$ , and angular momentum,  $\mathbf{L}$ , are calculated first, and then in a second step, the spin-orbit coupling couples the *total* spin and angular moment to form the total angular momentum  $\mathbf{J}$ . If the electron shell is less than half filled, then  $\mathbf{J} = \mathbf{L} - \mathbf{S}$ , otherwise  $\mathbf{J} = \mathbf{L} + \mathbf{S}$  above half filling.

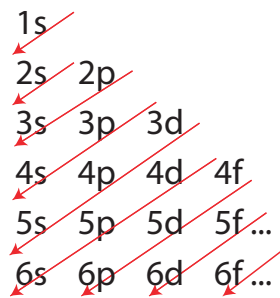


Figure 1.1: Aufbau principle: filling of electron shells

The Aufbau principle explains how to establish the electronic configuration of an atom and is schematically described in Fig. 1.1. The filling takes place as follows: with increasing order of  $n+l$ , and for equal  $n+l$  values, electrons go first in sub-shells with the smallest values of  $n$ . This filling of electrons corresponds to a full rotational symmetry of the Heisenberg Hamiltonian describing the hydrogen atom, generalized to more complex atoms.

The spin orbit coupling is a relativistic effect, whose effect is partly encapsulated in the third Hund's rule, and that results in the breaking of the degeneracy of energy levels. This rule dictates how to fill the electronic sub-shells depending on how the spin and orbital degrees of freedom are coupled. The symmetry provided by the rotation-invariant symmetry can also be broken by other effects than spin-orbit coupling. For instance, when placing atoms in a lattice, the basic hypothesis of rotational invariance (used to establish the energy levels from the original hydrogen atom Hamiltonian) is not valid anymore, meaning that the angular momenta stop being valid quantum numbers and the theory needs to be adapted. Placing atoms in a lattice is a mandatory step to explain many physical properties, ranging from mechanical properties, thermal conduction, electronic conduction, and others originating from effects linked to quantum magnetism, which we often find to be related to each other at a capacity that depends on specific cases realized by specific materials. The splitting of energy levels due to the fact that atoms are placed in an actual lattice forming a crystal is called crystal field splitting. This splitting depends heavily on how the magnetic atoms are surrounded by other atoms. In the case of copper atoms, a typical configuration is the so-called octahedral environment. Another possible configuration, even though more rarely achieved in real materials, is the trigonal bi-pyramid environment. Both these configurations can be observed in Fig. 1.2b and Fig. 1.2a.

The crystal field splits the degenerate energy levels. This splitting is remarkably dependent on the configuration and results in different energy levels for a trigonal-bipyramid and for an octahedral configuration in two distinct fashions, presented in Fig. 1.3a and Fig. 1.3b[15]. Notably, in the case of a trigonal-pyramidal coordination, the highest energy state is given by a single d-orbital, the  $z^2$  one. This plays a significant role since a copper atom in its most

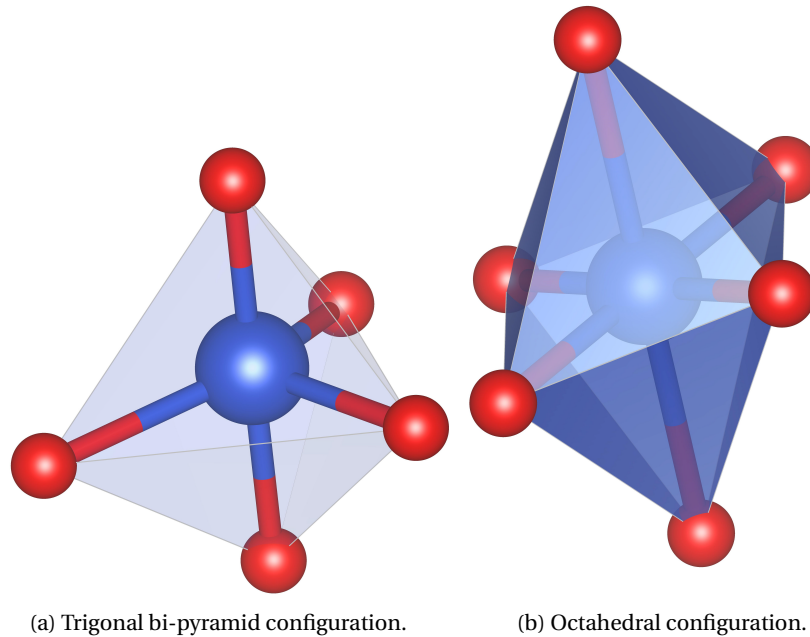


Figure 1.2: Copper in blue, surrounded by oxygen, in red, in two possible material configuration.

usual electronic configuration ( $3d^9$ ) is characterized by a single hole in agreement with Hund's rules. In the hole picture, the hole occupies the state with the highest possible energy, and would thus lie in the  $z^2$  orbital. In the case of the most usual octahedral environment, two possible candidates arise: namely the  $z^2$  and the  $x^2-y^2$  orbitals. It can be proven that the lower lying states form an effective triplet with  $L = 1$  [15], and the upper two states correspond to an effective angular momentum of  $L = 0$ . This is referred to as quenching in the wider literature: the effective angular momentum of the hole of a copper atom has no orbital angular momentum, even though the Hund rules predict that it is finite. This results in a simpler picture and spin state than that predicted by the sole use of Hund rules:  $J = L + S$ : with an effective state corresponding to  $S = 1/2$  and  $L = 0$ . This reveals how the crystal field modifies the ground state of copper to modify it to a hole with an effective spin  $J$  equal to  $S$ . The oxydation state of copper of course plays an important role in the final spin state of the ion, which can also be influenced as it has been evidenced by its local coordination structure.

It has now been established that in real materials the Hund rules and the spherically symmetric picture does not hold, but one should rather inspect the crystal structures and establish what is the realized coordination of the magnetic atoms, on a case by case basis. Even so however, due to constraint in the synthesis and in the atomic arrangements, more frequently than not, the coordination structures are distorted. For instance, in the specific case of an octahedron, a typical distortion consists in a compression, or elongation, in the apical direction. To keep the volume of the octahedron constant to first order in the displacement, this is accompanied by



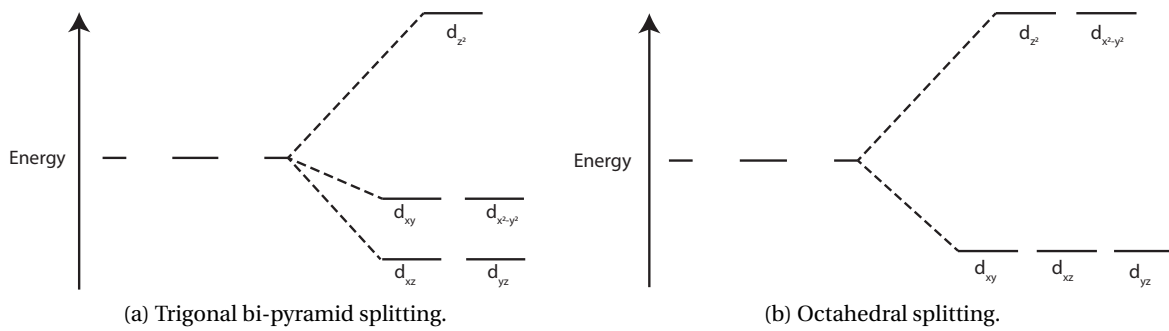


Figure 1.3: Crystal field splitting corresponding to two occurring copper environments in real materials.

an elongation or compression of the in-plane octahedra, the apical direction referring to the direction of the two atoms placed at the apex. For example, such an apical elongation results in further splitting, as shown in Fig. 1.4.

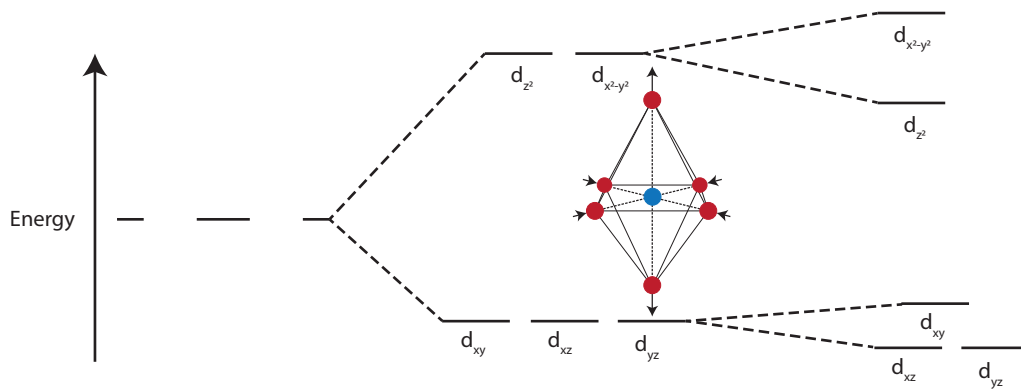


Figure 1.4: Distorted octahedron: elongation along apical direction results in further crystal field splitting.

This splitting breaks the degeneracy of the two highest energy levels, and thus would favor the occupation of the hole in the copper system in the  $x^2-y^2$  or in the  $z^2$  orbitals for an elongated, respectively compressed octahedron. This can be intuitively understood with the following argument: an elongated octahedron separates the apical oxygen atoms further apart from the central copper atom. Since the  $z^2$  orbital lies principally in the apical direction, this distortion decreases the overlap between the  $p_z$  orbital of the apical atom and the  $z^2$  orbital of the central one. This results in a state with lower energy. A similar reasoning can be applied to the in-plane atoms, and results in the energy of the  $x^2-y^2$  being raised. This pictorial thinking is most of the time not correct, as the proper physical effect at play creates bonding and anti-bonding states, however, even though it does not provide the correct result for every possible distortion, it often works as a rule of thumb. To capture the true breaking of the degeneracy, one rather

### **1.1. Crystal field splitting, quenching and effective spin**

---

has to perform an actual hybridization computation[15]. This phenomenon can lead to the so called orbital ordering where the orbitals form a periodic pattern. This typically occurs in some classes of materials , the perovskites. A typical example of orbital ordering has been confirmed in  $\text{KCuF}_3$  both experimentally[16] and theoretically[17].

## 1.2 Superexchange: the microscopic origins of magnetism

In the case of 3d-transition metal ions, the valence electrons occupy the d-shell. Localized d-electrons are typical of Mott insulating compounds, with exponentially suppressed d-d orbital overlap. Direct exchange between magnetic atoms is thus practically precluded. The basic mechanism responsible for the magnetic exchange is called the *superexchange* mechanism, and essentially corresponds to a virtual hopping from one transition metal site to another, assisted by an intermediate atom called a ligand, typically oxygen in a  $2p^6$  electronic configuration: filled external shells. Electrons from the p orbital of the ligand hop to the next transition metal site, creating a hole on the ligand, that is then in turn filled by an electron coming from another transition metal atom, effectively moving an electron. This mechanism is represented in Fig. 1.5.

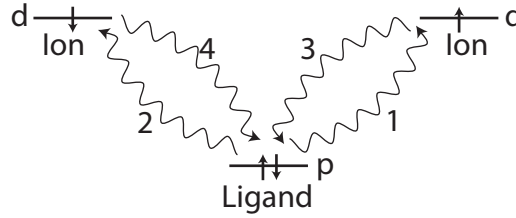


Figure 1.5: Pictorial description of the *superexchange* mechanism: a ligand is used to hop electrons with finite orbital overlap.

The quantum mechanical treatment of such a problem uses second order perturbation theory, with a small but finite hopping used as perturbation. Since the first order vanishes, the second order term accounts for the majority of the exchange mechanism. The equation one has to use to compute the effective Hamiltonian is given in equation (2.5). An important concept in that equation is the notion of intermediate state. Indeed, the dominant contribution to the effective Hamiltonian is given by the following process: starting from a state  $|n\rangle$  in the ground state manifold, and transforming it to an excited state  $|k\rangle$ , and going back to a state from the ground state manifold  $|m\rangle$ , and summing over all possible intermediate states. The energy difference between the excited state and the ground state appears in the denominator of the sum. For the process described in Fig. 1.5, a succession of hoppings leads to the intermediate state: assume a transition metal atom with  $n$  electrons is placed on site  $i$  and another on site  $j$ , the ligand starts with a full  $2p^6$  orbital. The hopping scheme with intermediate state right after step 2 is the following:  $d_i^n p^6 d_j^n \xrightarrow{1} d_i^n p^5 d_j^{n+1} \xrightarrow{2} d_i^{n+1} p^4 d_j^{n+1} \xrightarrow{3} d_i^{n+1} p^5 d_j^n \xrightarrow{4} d_i^n p^6 d_j^n$ . The intermediate state is given by a ligand deprived of two electrons, its energy is characterized by the energy required to hop an electron from a  $p$  to a  $d$  orbital, called the charge transfer energy and written  $\Delta_{CT}$ , and the (Coulombian) repulsion of the two holes created on the ligand,  $U_{pp}$ . In order to compute the whole effective Hamiltonian, one has to take into account every possible hopping scheme. Another allowed contribution comes from

## 1.2. Superexchange: the microscopic origins of magnetism

a Hubbard-like hopping: moving an electron from site  $i$  to  $j$ , and then back. Introducing the Coulomb repulsion of two electrons on a  $d$  orbital, the final effective model is a Heisenberg Hamiltonian, with effective coupling given by equation (1.1).

$$J_{\text{eff}} = 2t_{\text{dd}}^2 \left( \frac{1}{U_{\text{dd}} + \frac{1}{\Delta_{\text{CT}} + \frac{1}{2}U_{\text{pp}}}} \right) \quad (1.1)$$

A similar reasoning can be applied to express  $t_{\text{dd}}$  in function of  $\Delta_{\text{CT}}$  and  $t_{\text{pd}}$  the hopping from  $d$  to  $p$  orbitals:  $t_{\text{dd}} = t_{\text{pd}}^2 / \Delta_{\text{CT}}$ , finally providing a final form of the coupling stated in equation (1.2).

$$J_{\text{eff}} = 2 \frac{t_{\text{pd}}^4}{\Delta_{\text{CT}}^2} \left( \frac{1}{U_{\text{dd}} + \frac{1}{\Delta_{\text{CT}} + \frac{1}{2}U_{\text{pp}}}} \right) \quad (1.2)$$

The situation described previously corresponds to an alignment of the  $p_x$  orbital of the ligand with both transition metal ions orbitals. This corresponds to the situation where the ion-ligand-ion angle is  $180^\circ$ . However, depending on the geometry of the actual crystal, it can happen that the orbitals of the ligand that overlap the most with the ones of the transition ions are not the  $p_x$  orbitals. In a geometry with an angle of  $90^\circ$  degrees, the hopping mixes electrons from the  $p_x$  and  $p_y$  orbitals. This plays a key role in favoring either ferromagnetic or antiferromagnetic couplings. A ferromagnetic coupling tends to favor a parallel alignment of spins, while an antiferromagnetic coupling favors an anti-parallel alignment. These couplings will be described in more details in another section of this work. Indeed, the process described in Fig. 1.5 with an  $180^\circ$  bond vastly favors antiferromagnetic interactions: if the spins on the transition metal sites were parallel, the hopping labeled "1" in Fig. 1.5 would be authorized, but then hopping the hopping labeled "2" in Fig. 1.5 would not happen due to the Pauli exclusion principle, since it would create a state with two electrons with spin up in the same state. Such considerations are the essence of the Goodenough-Kanamori-Anderson (GKA) rules[18, 19, 20, 21]:

- If the mechanism responsible for the exchange is a direct hopping between  $d$  orbitals:
  - If there is a finite overlap between the orbitals, and that the active orbitals are half-filled, the exchange is antiferromagnetic and strong.
  - If the orbitals are orthogonal and the hopping occurs between filled and empty orbitals, then the exchange is ferromagnetic and weak.
- If the mechanism responsible for the exchange involves hopping through a ligand:
  - If the orbitals of the two sites are occupied and overlap with the same orbital from the ligand ( $180^\circ$  configuration), the exchange is antiferromagnetic and strong.
  - If only one of the orbitals of the two sites is occupied, and both orbital overlap with the same ligand orbital, the exchange is ferromagnetic and weak.
  - In the case where orthogonal  $p$ -orbitals of the ligand are used ( $90^\circ$  configuration), the exchange is ferromagnetic and weak.

In practice, a quick inspection of the crystal structure of a given compound can thus provide considerable information on the potential couplings that are characteristic of the system. Indeed, in a system where copper atoms would be connected by corner sharing octahedra, one would expect that the coupling would be strong and antiferromagnetic. A simple way of realizing a ferromagnetic coupling would be to connect the octahedra surrounding the copper atoms by an edge sharing geometry, ensuring a copper-ligand-copper angle considerably different from  $180^\circ$ .

## 2 Magnetic interactions

### 2.1 What are Mott insulators and why are they even interesting?

#### 2.1.1 Context

Several elements of this section are inspired by Frédéric Mila's lecture notes of a course taught at EPFL, "Physique du Solide III et IV". The very first considerations of Mott Insulators came after the band theory was established and its physical relevance demonstrated experimentally. The Drude model was already a significant advancement on the way to explain properties of real materials, such as conductivity and resistivity. It consisted in a kinetic theory modeling the electrons as a gas, following a Maxwell distribution and colliding with each other with a certain mean free path. It however failed to recognize the intrinsically quantum nature of the electrons, and the need for a more advanced distribution appeared. This led to the use of the Fermi-Dirac statistics that describes more truthfully the physics of systems with quantum electrons. The band theory describes the behavior of such systems with electrons in a periodic potential, and came as a natural solution of the Schrödinger equation. Most properties of metals, insulators and semiconductors can be obtained from band theory. In the end of the 80's, due to the significant interest in superconductivity, many studies focused on the properties of  $\text{La}_2\text{CuO}_4$ . Its band structure was calculated[22], and its number of free electrons is odd, thus consistent with an expected metallic behavior. Moreover, its Fermi energy is cutting through several bands, and the overlap between orbitals is consistent with mobile electrons. Yet, measurements were pointing towards an insulating behavior. The notion of Mott insulator reconciled both pictures.

The fundamental idea behind the Mott insulator picture is the following: one has to consider a crystal made of hydrogen atoms forming a square lattice separated by a distance labeled  $a$ . The unit cell contains one hydrogen atom and thus one electron. Band theory thus predicts that such a compound should be a metal. For large values of  $a$ , the starting situation corresponds to half filling: one electron per site. Moving a single electron creates one hole and one doubly

occupied site. The energy balance equation thus reads as in equation (2.1).

$$\Delta E = E(H^-) + E(H^+) - 2E(H) := U \quad (2.1)$$

Due to the Coulomb repulsion between the two electrons forming the  $H^-$  ion, this quantity is non negative, and usually labeled  $U$ . The system may try to delocalize the hole and the doubly occupied site, gaining kinetic energy. If the width of the corresponding band is labeled  $W$ , the hole and doubly occupied site will be located at the band minimum and gain each an energy of  $W/2$ . This remains true even if the two do not delocalize in the exact same way. The transfer integral,  $t$ , is non zero, between first neighbors and the resulting system can be modeled truthfully by the tight binding approximation. The band width is  $W = 8t$ . The energy of such a configuration is  $\Delta_c = U - W$ . In that expression,  $U$  does not depend on the distance between atoms while  $W$  strongly depends on  $a$ . For values of  $a$  much larger than the Bohr radius, the transfer integral starts to be exponentially small, and  $\Delta_c = U > 0$ , the system is insulating. The system can undergo a transition by applying a pressure, this has been first observed in  $V_2O_3$  in the early 70's[23]. The Mott insulator picture proved to be a starting point for the very interesting Mott-Hubbard-Heisenberg theories, with Mott insulators differing from the then-known insulators by a fundamental set of properties: their magnetic excitations.

### 2.1.2 Magnetism: Mott-Hubbard-Heisenberg

A major difference between Mott and band insulators regards magnetic excitations. Indeed, a typical Mott insulator hosts magnetic excitations with low energy: each atom has one electron, with spin that can be up or down. In the theoretical limit where the atoms are sufficiently well separated, the ground state corresponds to all configurations with one electron per site and is thus  $2^N$  degenerated, where  $N$  is the number of sites, and its energy is  $NE_0$ , with  $E_0$  the energy of an electron on a single site. As seen before, the first excited state corresponds to a state with one hole and one doubly occupied site. Its degeneracy is  $N(N-1)2^{N-2}$  and its energy difference  $U$ . The second excited state is the state with two holes and to doubly occupied sites. Moving the atoms closer to each other results in a lifting of the ground state degeneracy. The minimal model that describes the encapsulated physics is called the Hubbard model [24, 25, 26], and its Hamiltonian is stated in equation (2.2).

$$\mathcal{H} = -t \sum_{\langle i,j \rangle, \sigma} c_{i,\sigma}^\dagger c_{j,\sigma} + c_{j,\sigma}^\dagger c_{i,\sigma} + U \sum_i n_{i,\uparrow} n_{i,\downarrow} \quad (2.2)$$

The first term is the so-called hopping term, and describes the transfer of electrons from one site to one of its nearest-neighbor:  $\langle i,j \rangle$ . It dominates the Hamiltonian if the atoms are separated by a large-enough distance and the hopping term is small enough. The second term is proportional to the Coulomb energy  $U$ , and is a counting term: it counts doubly occupied sites. In order to determine what is the effective Hamiltonian, one has to perform a perturbation theory that will describe the lifting of the ground state degeneracy. The kinetic

## 2.1. What are Mott insulators and why are they even interesting?

term, shown in equation (2.3) plays the role of the small perturbation.

$$\mathcal{H}_0 = -t \sum_{\langle i,j \rangle, \sigma} c_{i,\sigma}^\dagger c_{j,\sigma} + c_{j,\sigma}^\dagger c_{i,\sigma} \quad (2.3)$$

The first order of the degenerated perturbation theory predicts that the matrix elements of the effective Hamiltonian are given by equation (2.4).

$$\langle m | \mathcal{H}_{\text{eff}} | n \rangle = \langle m | \mathcal{H}_0 | n \rangle \quad (2.4)$$

$|m\rangle$  and  $|n\rangle$  refer to eigenvectors in the ground state manifold: they correspond to states with a single electron per site. Since  $\mathcal{H}_0$  creates a doubly occupied site, all the matrix elements effectively vanish and the second order of the perturbation theory is needed. The second-order-in- $\mathcal{H}_0$  matrix elements are written in equation (2.5)

$$\langle m | \mathcal{H}_{\text{eff}} | n \rangle = \sum_{|k\rangle}' \frac{\langle m | \mathcal{H}_0 | k \rangle \langle k | \mathcal{H}_0 | n \rangle}{E_0 - E_k} \quad (2.5)$$

The primed sum stands for a sum on all states  $|k\rangle$  that are not in the ground state manifold, with energy  $E_k$ .  $E_0$  is the ground state energy.  $\mathcal{H}_0$  creates a doubly occupied state, thus  $E_k = U$ .  $\sum_{|k\rangle}' |k\rangle \langle k|$  is the identity of the doubly occupied subspace, it can be replaced by an equivalent operator involving counting operators:  $\sum_j n_{j,\sigma} n_{j,-\sigma}$ . It entails that the matrix element that has to be computed becomes equation (2.6).

$$\langle m | \mathcal{H}_{\text{eff}} | n \rangle = -\frac{t^2}{U} \sum_{j,\sigma} \sum_{i(j),\sigma',\sigma''} \langle m | c_{i,\sigma'}^\dagger c_{j,\sigma'} n_{j,\sigma} n_{j,-\sigma} c_{j,\sigma''}^\dagger c_{i,\sigma''} | n \rangle \quad (2.6)$$

Four distinct terms contribute in a non-zero manner to the sum:  $\sigma' = \sigma'' = \sigma$ ,  $\sigma' = \sigma'' = -\sigma$ ,  $\sigma'' = -\sigma' = \sigma$  and  $\sigma'' = -\sigma' = -\sigma$ . These four contributions can be recombined to give the effective Hamiltonian presented in equation (2.7).

$$\mathcal{H}_{\text{eff}} = \frac{2t^2}{U} \sum_{j,\sigma} \left( c_{i,-\sigma}^\dagger c_{i,\sigma} c_{j,\sigma}^\dagger c_{j,-\sigma} - n_{i,\sigma} n_{j,-\sigma} \right) \quad (2.7)$$

Using the second quantization and the z axis as quantization axis, the spin operators can be written as equation (2.8).

$$\begin{cases} S_i^z &= \frac{1}{2} (n_{i,\uparrow} - n_{i,\downarrow}) \\ S_i^+ &= c_{i,\uparrow}^\dagger c_{i,\downarrow} \\ S_i^- &= c_{i,\downarrow}^\dagger c_{i,\uparrow} \end{cases} \quad (2.8)$$

The spin density operators can be written as  $n_i = n_{i,\uparrow} + n_{i,\downarrow}$ . The Hamiltonian can be written in its form presented in equation (2.9).

$$\mathcal{H}_{\text{eff}} = \frac{4t^2}{U} \sum_{\langle i,j \rangle} \left( S_i^z S_j^z + \frac{1}{2} (S_i^+ S_j^- + S_j^+ S_i^-) - \frac{1}{4} n_i n_j \right) \quad (2.9)$$



## Chapter 2. Magnetic interactions

---

Using the fact that the spin ladder operators can be written in terms of  $S_x$  and  $S_y$ , and that  $n_i = n_j = 1$  in the ground state manifold, the effective Hamiltonian can be finally written as (2.10).

$$\mathcal{H}_{\text{eff}} = \frac{4t^2}{U} \sum_{\langle i,j \rangle} \left( \vec{S}_i \cdot \vec{S}_j - \frac{1}{4} \right) \quad (2.10)$$

This is the famous Heisenberg model  $\mathcal{H}_{\text{Heis}} = J \sum_{\langle i,j \rangle} \vec{S}_i \cdot \vec{S}_j$ , up to a constant, and with a coupling  $J$  of  $4t^2/U$ . It appears that this specific value of the coupling favors anti-parallel alignment of spins. This can be understood from the Pauli exclusion principle: if two neighbors have the same spin, hopping between the two is precluded. On the contrary, hopping to create a doubly occupied site is allowed for atoms with electrons with anti-parallel spins, hence creating a favored antiferromagnetic configuration. The detailed behavior of each compound can of course result in many different types of couplings. The goal of the previous section was to establish the physical relevance of the Heisenberg Hamiltonian, in the specific case of Mott insulators, whose study is a modern topic of quantum magnetism. The physical origin of this direct exchange is the overlap between two atomic orbitals, and while it predicted an antiferromagnetic in this simple model with hydrogen atoms and one free electron per lattice site, it can also be accountable in other cases for ferromagnetic exchange.

## 2.2 Heisenberg interactions

The Heisenberg Hamiltonian describes reasonably well numerous real interactions and is derived from the Mott insulator picture, with hopping parameter  $t$ , and Coulomb repulsion  $U$ . It turned out that in this simple derivation, the resulting coupling  $J$  is proportional to  $t^2/U$ . The sign of the coupling is favoring an antiparallel alignment of spins. This coupling is thus called an *antiferromagnetic* coupling. However, the mechanism responsible for the sign can be different, and it can also happen that this coupling is negative, favoring a parallel alignment of spins, corresponding to the so-called ferromagnetic coupling. The Heisenberg Hamiltonian is written in equation (2.11).

$$\mathcal{H}_{\text{Heis}} = \sum_{(i,j), \alpha=x,y,z} J_{ij}^{\alpha} S_i^{\alpha} S_j^{\alpha} \quad (2.11)$$

A couple of comments can be made regarding this cornerstone of condensed matter physics. The sign of the coupling  $J$ , as mentioned before, plays an important role in the ground state of the system. Moreover, the couplings can be anisotropic. Indeed, if  $J^x$ ,  $J^y$  and  $J^z$  are equal, as in the Hubbard model, the model is called isotropic. There are several important particular cases: the *Ising model*, defined by  $J^x = J^y = 0$ , and the *XY model*, defined by  $J^z = 0$ . For the sake of simplicity in many cases, only nearest neighbor interactions are considered. However, in real materials, it is quite common to have further-neighbor interactions. The spin of the system can also be different from a simple spin half which was supposed by the Hubbard model derived from the Mott insulator picture. The next chapter describes how real materials can result in different spin states, which may result in an enhancement of either the quantum or rather the classical properties of a given system. Finally, the dimensionality of the system is quite important. Indeed, the Mermin-Wagner[27] theorem has quite drastic implications on the possibility of long range order, depending on the system dimensionality. This theorem states that in the frame of systems with interactions that are sufficiently short range, continuous symmetries, corresponding to the establishment of long range order, cannot be spontaneously broken at finite temperature.

### 2.2.1 Ferromagnetism

The term ferromagnetism refers to the study of the case of a Heisenberg Hamiltonian with negative coupling  $J$ . In the classical case, the spin can be represented as a vector pointing in any direction, with a given norm. For ferromagnetic systems, the configuration of spins achieving the minimum energy is that with all the spins aligned in one direction. There is a very large symmetry, since the model is fully isotropic. This symmetry is not specific to ferromagnets, but also many other magnets, such as antiferromagnets and ferrimagnets, described in another section. In the case of a system consisting of  $N$  quantum spins, it can be shown that the state with  $|G\rangle := |m_1 = S, \dots, m_N = S\rangle$  is an eigenvector, and that this eigenvector indeed minimizes the energy of the system:  $JS^2$  per site. The ground state degeneracy can be obtained by considering that the  $S_{\text{tot}}^-$  commutes with the Hamiltonian. Thus, applying  $S_{\text{tot}}^-$

## Chapter 2. Magnetic interactions

on  $|G\rangle$  constructs a new state with the same energy. This process can be repeated until the constructed state is  $|m_1 = -S, \dots, m_N = -S\rangle$ . The ground state degeneracy is thus  $2NS(S+1)$ . A typical physical property that can be measured on real samples is called the dynamical structure factor, obtained from inelastic neutron scattering experiments. This notion will be elaborated in another chapter, but what is important is that the dynamical structure factor is a measurable quantity that, for magnetic systems, is a manifestation of the excitation spectrum of the system: it actually corresponds to the expectation value of the spin-spin correlation function. While many different Hamiltonians may lead to similar looking ground states, due to competing interactions and anisotropies, the excitation spectrum of a given system is a fingerprint of its Hamiltonian and, due to its complexity, is much closer to being a one-to-one function. In practice the use of the result of neutron scattering experiments is widespread to try and elucidate which Hamiltonian, and thus which physics governs a given compound: understanding excited states of systems is hence paramount.

For ferromagnetic systems, it turns out that the state given by equation (2.12) is not an eigenstate of the Hamiltonian. This state is usually called a spin flip because it corresponds to a single spin flip at site  $i$  for  $S = 1/2$ .

$$|i\rangle = \frac{1}{\sqrt{2S}} |G\rangle = |S \dots S \ S-1 \ S \dots S\rangle \quad (2.12)$$

Indeed, the state  $|i\rangle$  is an eigen state of  $S_i^z S_j^z$  but not of  $S_i^x S_j^x + S_i^y S_j^y$ . The solution to that problem is to delocalize the spin flip over the whole real space. The spin flip is thus localized in the reciprocal space. The state can be written as equation (2.13) with wave-vector  $k$ .

$$|k\rangle = \frac{1}{\sqrt{N}} \sum_i e^{-i\vec{k}\cdot\vec{R}_i} |i\rangle \quad (2.13)$$

This state has an energy given in equation (2.14), where the set of  $\vec{r}$ -vectors refers to the set of vectors going from one site to its neighbors.

$$E_{\vec{k}} = E_0 + JS \sum_{\vec{r}} \left(1 - e^{i\vec{k}\cdot\vec{r}}\right) \quad (2.14)$$

For  $\vec{k} = \vec{0}$ , the energy of the state is that of the ground state. This corresponds to a rotation of the total spin. The dispersion relation, measured experimentally is given by the  $\vec{k}$ -dependence of the energy of the state. For a square lattice, it can be found that  $E_{\vec{k}} = E_0 + JS \sum_{\alpha} \sin^2\left(\frac{k_{\alpha}a}{2}\right)$ , where  $a$  is the lattice parameter. The dispersion is quadratic close to zero, a typical feature of ferromagnetic excitations. In order to better visualize what this mode corresponds to, one can simply calculate the expectation value of  $S_i^z S_j^z$  and of  $S_i^x S_j^x + S_i^y S_j^y$ . The expectation value of a quantum mechanical operator corresponds to the value that is expected to be measured when measuring the associated physical quantity. The result is presented in equation (2.15).

$$\begin{cases} \langle \vec{k} | S_i^x S_j^x + S_i^y S_j^y | \vec{k} \rangle &= \frac{2S}{N} \cos\left(\vec{k} \cdot (\vec{R}_i - \vec{R}_j)\right) \\ \langle \vec{k} | S_i^z S_j^z | \vec{k} \rangle &= S^2 - \frac{2}{N} S \end{cases} \quad (2.15)$$

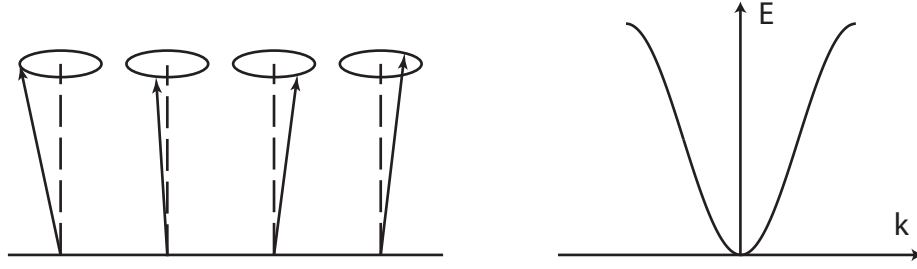


Figure 2.1: Left: spinwave picture: rotating spins along the  $z$ -axis, associated to dispersion on the right hand side.

It appears that the result of the  $z$  component is a constant, while the result in the  $xy$ -plane depends on atomic sites  $i$  and  $j$ , in an oscillating manner, with a period proportional to  $1/k$ . This excitation and the dispersion relation are represented in Fig. 2.1. Since the spins are precessing around the  $z$ -axis, this state is called a spinwave. The Goldstone theorem[28] stipulates that since a continuous (rotational) symmetry is broken, there is a mode with energy going to zero for vanishing wavevectors. The associated quasi-particle is called a magnon (delocalized spin flip). Other states with low energy can be constructed in a similar fashion. In particular, a state with several magnons can be obtained. However, this problem does not have any analytical solution, except for a spin half system in one dimension, given by the Bethe ansatz[29]. The process of creating a magnon can be written formally with Holstein-Primakoff transformations[30]. This generalization provides a systematic way of constructing spinwaves, with the same resulting energy, and also the possibility of constructing multi-magnon states. This transformation involves approximations, the most important one being that the number of magnons is much smaller than two times the spin. While in theory, this harshly constraints the model and should mean that spin half systems cannot be described, in practice this magnon picture works all the same. This formalism also enables to compute the quantum corrections to the magnetization, confirming the Mermin-Wagner theorem: the magnetization at finite temperature diverges in 1D and 2D and is only predicted to be non-divergent in 3D.

In real materials, these ferromagnetic spinwaves have been measured multiple times in the past. For example, a spectroscopic study[31] of EuO and EuS powder was used to determine the exchange couplings in both systems and found a perfect agreement with the high temperature series expansion predicting those values, and consistent with specific heat measurements. Another typical example of 2D ferromagnet can be found in  $K_2CuF_4$ [32]. The authors measured inelastic neutron scattering with low energy transfer and could successfully fit a magnon spectrum to the data and find the detailed Heisenberg couplings, characteristic of the system.

### 2.2.2 Antiferromagnetism

Another common possibility for the Heisenberg Hamiltonian (2.11) is that of a non negative coupling parameter  $J$ . In such cases, classically, the energy of the system is minimized for a

configuration with each spin antiparallel to its neighbors. It appears that depending on the lattice type, it may not be possible to satisfy this condition, even classically. This can be trivially apprehended in the case of a lattice where loops of sites connected by a given coupling are made of an odd number of sites, it is then impossible to satisfy such a condition. The system needs to compromise. The field treating these complex problems is called frustrated physics and will be discussed in more details in another chapter. For simple bipartite lattices, for example the square lattice with nearest neighbor interaction, the classical ground state is thus antiparallel spins, alternating in every direction. The quantum ground state is however more complicated. It was debated for a long time, until neutron scattering proved in a measurement that this state was achievable in real materials, whether the so-called Néel antiferromagnetic state was physical. Indeed, the Néel state was measured first measured by Shull in MnO[33], eventually leading to several Nobel prizes. The method consisted in taking advantage of the magnetic moment of the neutron to diffract not only on the periodic crystal structure, but also on the periodic magnetic structure. The magnetic structure periodicity is twice that of the lattice in the real space, and thus lead to peaks at intermediate positions in the reciprocal space, confirming the alternating up and down character of the magnetic structure. By analogy to the classical case, consider the state given in equation (2.16). A and B denote the two sub-lattices. A corresponds to the spins with  $|m\rangle = +S$  and B with  $|m\rangle = -S$ .

$$|N\rangle = |m_1^A = S, \dots, m_{\frac{N}{2}}^A = S, m_1^B = -S, \dots, m_{\frac{N}{2}}^B = -S\rangle \quad (2.16)$$

It appears quite clearly that the transverse term in the Hamiltonian mixes states with  $S-1$  at some sites on sub-lattice A and  $S+1$  at some other sites on sub-lattice B. Hence the state  $|N\rangle$  is not even an eigenvector of the Hamiltonian. The solution to that problem is to use two different Holstein-Primakoff transformations[30] on both A and B sub-lattices. This describes small deviations around the ordered moment:  $+S$  on sites in A and  $-S$  on sites in B. The Hamiltonian can then be written by keeping only terms in  $S$  and  $S^2$ , and neglecting higher order terms. The problem is that the Hamiltonian is not a sum of harmonic oscillators, it rather couples the creation of magnons with momentum  $+\vec{k}$  and  $-\vec{k}$ . One needs to use Bogoliubov transformations[34, 35] to decouple it in a sum of harmonic oscillators (2.17).

$$\begin{cases} \mathcal{H} &= \sum_{\vec{k}} \omega_{\vec{k}} \left( \alpha_{\vec{k}}^\dagger \alpha_{\vec{k}} + \frac{1}{2} \right) - JS(S+1) \frac{zN}{2} \\ \omega_{\vec{k}} &= JSz \sqrt{1 - \gamma_{\vec{k}}^2} \\ \alpha_{\vec{k}} &= u_{\vec{k}} a_{\vec{k}} + v_{\vec{k}} a_{-\vec{k}}^\dagger \\ u_{\vec{k}} &= \sqrt{\frac{JSz + \omega_{\vec{k}}}{2\omega_{\vec{k}}}} \\ v_{\vec{k}} &= \text{sign}(z_{\vec{k}}) \sqrt{\frac{JSz - \omega_{\vec{k}}}{2\omega_{\vec{k}}}} \end{cases} \quad (2.17)$$

In that set of equations,  $a$  and  $a^\dagger$  are the usual magnon annihilation and creation operators,  $z_{\vec{k}} = \sum_{\vec{\tau}} \cos \vec{k} \cdot \vec{\tau}$ ,  $z$  the coordination number,  $\gamma_{\vec{k}} = \frac{z_{\vec{k}}}{z}$ . The ground state of the system is given

in equation (2.18).

$$|G.S.\rangle = \prod_{\vec{k}}' \frac{1}{u_{\vec{k}}} \exp\left(-\frac{v_{\vec{k}}}{u_{\vec{k}}} a_{\vec{k}}^{\dagger} a_{-\vec{k}}^{\dagger}\right) |0\rangle \quad (2.18)$$

The primed product means that one has to consider only vectors  $\vec{k}$  and  $\vec{k}'$  such that  $\vec{k} \neq -\vec{k}'$ , and  $|0\rangle$  is the vacuum of the  $a_{\vec{k}}$  operators. The collective excitations of antiferromagnets are also called spin waves. The corrections to the magnetization can be calculated, and once again, the results depends on the temperature and the dimensionality. At  $T = 0$  K, there are strong effects of quantum fluctuations, that result in a diverging magnetization in 1D. A similar divergence can occur in 2D and 3D, depending on the details of the considered lattices in 2D and 3D. For the square lattice and spin half moments, the correction to the magnetization leads to a staggered magnetization of about 0.3[36]. At finite temperatures in 1D and 2D, the magnetization diverges and there is no room for magnetic long range order.

There are a wide variety of antiferromagnets present in real compounds. MnO [33] is an idiosyncratic example of one. Regarding the dispersion spectrum, a typical spin 1/2 square lattice Heisenberg antiferromagnet has been realized in  $\text{Sr}_2\text{CuTeO}_6$ [37]. The inelastic spectra of a polycrystalline sample was acquired and fitted to an excellent agreement with an antiferromagnetic Heisenberg Hamiltonian and presents a different slope than that of a ferromagnet. Interactions that go further nearest neighbor can frustrate the system. In that case, frustration arises from antiferromagnetic interactions that compete, effectively creating a configuration that cannot be described classically by a collinear structure. This notion is paramount and will be elaborated on in another section.

### 2.2.3 Ferrimagnetism

Ferromagnetic and antiferromagnetic interactions are two widespread schemes, accounting for the majority of interactions in systems encapsulating Heisenberg physics. In these simple cases, the name of the state is directly inherited from the name of the coupling. In some systems, especially in systems with low crystalline symmetry, an additional complexity may develop. For example in  $\text{Ca}_3\text{Co}_2\text{O}_9$ , due to a low-symmetry space group, magnetic atoms of cobalt are placed in two different oxygen surroundings. This difference induces an different spin state on each Cobalt site. In that specific case, it turns out that the couplings are rather Ising-like[38], and that one of the cobalt atoms has an effective spin of zero, making it a really special case since it could be considered that the spin-zero atoms are out of the (magnetic) picture. In some other compounds however, the resulting moment on the (magnetic) copper site is different and finite. This has for example been observed in copper based compound made of triangular motifs  $\text{Cu}_2\text{OSO}_4$ [39]. The resulting ground state is close to the non collinear  $120^\circ$  configuration, but with small finite resulting magnetization. In some other examples, a finite (non staggered) magnetization with antiferromagnetic couplings is created in an even more compelling fashion. Yttrium iron garnet,  $\text{Y}_3\text{Fe}_5\text{O}_{12}$ , is a good example of such a material[40]. Neutron scattering studies revealed both the magnetic ground states, and magnon dispersion. The ground state is made of collinear spins, however all moments do not

experience the same quantum reductions, which results in a finite magnetization, pictorially represented in Fig. 2.2. Such a state is called ferrimagnetic.

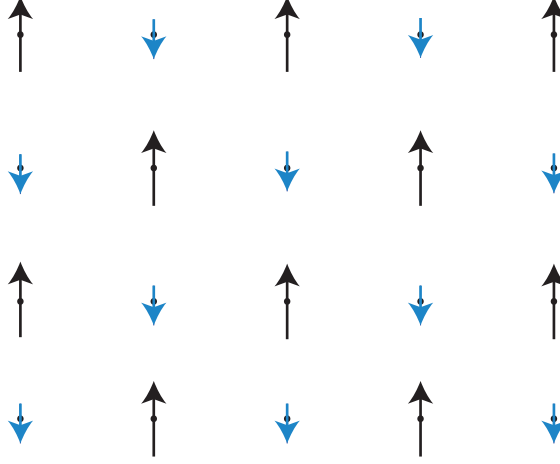


Figure 2.2: Ferrimagnet: the reduction of ordered moments leads to a different reduction to the spin at different sites, creating a state with finite non staggered magnetization.

## 2.3 Anisotropies

### 2.3.1 Dzyaloshinskii-Moriya interaction

Aside of usual Heisenberg couplings, some other terms can play a significant role in the Hamiltonian: anisotropies. Anisotropies can help establish long range order at finite temperature in low dimensional systems, in agreement with the Mermin-Wagner theorem. They may break rotational degeneracy and usually create a gap in the excitation spectrum. This gap can be closed by applying a magnetic field. For comparable energy scales, the effect will be a competition of interactions, and once the field strength is high enough, the change is linear. One of the most studied anisotropies involving spins on neighboring sites is the antisymmetric exchange interaction, also known as the Dzyaloshinskii–Moriya Interaction (DMI) [41, 42]. It takes the form of a term in the Hamiltonian shown in equation (2.19).

$$\mathcal{H}_{DM} = \vec{D}_{ij} \cdot (\vec{S}_i \times \vec{S}_j) \quad (2.19)$$

The indices  $i$  and  $j$  denote two lattice sites, and  $\vec{D}_{ij}$  is the DM vector supported by the  $i$ - $j$  bond. This interaction can be derived from the relativistic spin-orbit coupling using second order perturbation theory. The crystal symmetries and the exchange paths constrain the direction of potential DM vectors[41]. In particular, a superexchange path with a center of inversion cannot sustain a finite DM vector. Due to the form of the DM Hamiltonian in equation (2.19), the DMI favors configuration with orthogonal spins. This introduces a direct competition with the Heisenberg Hamiltonian that favors collinear structures. The DMI

was among others instrumental in stabilizing non-collinear structures, including renowned skyrmions[43]. Skyrmions were discovered in condensed matter systems in 2009 and can be thought of as a spin vortex, an example of skyrmion can be seen in Fig. 2.3. The spin structure is quite complex and is stabilized by the DMI. By substituting copper ions for other transition metals with different spin orbit coupling in  $\text{Cu}_2\text{OSeO}_3$ , the stability of the skyrmion phase could be increased[43].

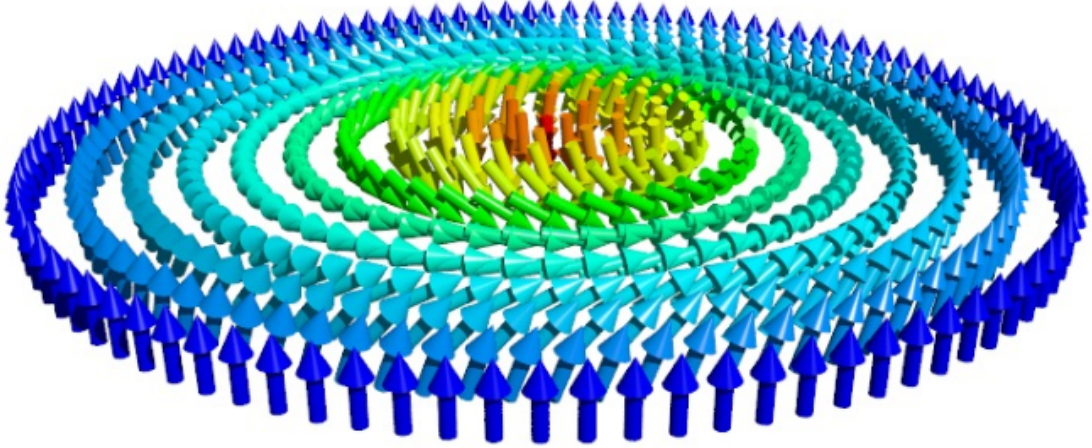


Figure 2.3: Example of magnetic skyrmion: vortex of magnetic spins.

### 2.3.2 Other anisotropies

Many other forms of anisotropy exist in real materials, and can have effects on both the ground states and excitation spectra of real materials. The case of Ising systems, which correspond to a Heisenberg Hamiltonian with  $S^x = S^y = 0$ , is quite a drastic example of anisotropy. In practice more subtle effects of anisotropy can occur. The Hamiltonian of the anisotropic exchange interaction can be written in the form of equation (2.20).

$$\mathcal{H}_{\text{anis}} = J_{ij}^z \left( \alpha_x S_i^x S_j^x + \alpha_y S_i^y S_j^y + S_i^z S_j^z \right) \quad (2.20)$$

$\alpha_x = \alpha_y = 1$  corresponds to the isotropic point. For copper atoms typically, an anisotropy of up to 20% can occur.

Another typical term in the Hamiltonian associated to anisotropy is the magneto-crystalline anisotropy stated in equation (2.21), also arising from the spin-orbit interaction: the motion of the electrons on the orbitals couples to the crystal field.

$$\mathcal{H}_{\text{anis}} = \sum_i \vec{S}_i A_i \vec{S}_i \quad (2.21)$$

Depending on the sign and values of  $A$ , either an easy-axis or easy-plane is created. Indeed,



for  $A_i = \text{diag}(K^2, 0, 0)$ , the classical ground state corresponds to a moment perpendicular to the x-axis, hence: the "easy-plane anisotropy" term. For  $A_i = \text{diag}(-K^2, 0, 0)$ , the most energetically favorable configuration is that of spins aligned along the x-axis: "easy-axis anisotropy". These anisotropies play an important role in breaking the ground state rotational symmetry and selecting out a specific ground state configuration. This also creates a small gap in the dispersion curves, and split otherwise-equivalent magnon branches[44] in a fashion that is strongest at high symmetry points, close to Brillouin Zone centers.

## 3 What is quantum magnetism?

### 3.1 Frustrated magnetism

Quantum magnetism has been studied for quite some time, ever since the notion of spin and condensed matter physics was first theorized. The ferromagnetic state and its application has been quite well understood and widespread, its uses are now numerous, even in the everyday life[45]. On the other hand, the notion itself of antiferromagnet has been debated for some time. Indeed, since the antiferromagnet state is itself not even the ground state of the antiferromagnetic Hamiltonian, Lev Landau was emitting strong doubts on Louis Neel's hypothesis of the existence of the state. Magnetic neutron scattering and MnO provided a proof that the antiferromagnetic state could be realized in actual materials[33]. For various reasons: simple chemistry placing different atoms thus with different spin states on a given lattice, differences in the local environments of said atoms creating a different crystal field splitting and thus a different effective spin, changes in the quantum reductions of the spins of magnetic ions, it is possible to obtain an antiferromagnet with finite staggered magnetization in one direction[46], or even simply different magnetic moments at different crystalline sites[47].

It appeared that the question of whether the physics of a system was dominated by quantum or classical physics was of extremely high importance in many cases. Another playground to explore this difference is that of the so-called frustrated magnetism. This sub-field of condensed matter physics deals with the study of systems where the ground state of the Hamiltonian cannot be simply found from classical considerations: minimizing the classical energy. Indeed, in a purely ferromagnetic toy-model, the ground state is easily found, as it turns out that both quantum and classical ground states coincide and that the energy of the state reaches the theoretical lower bound. In some other cases, it can be practically impossible to satisfy all interactions. Indeed, consider the case of three spins on a triangular unit, with an antiferromagnetic interaction between all of them. It appears that once two of the three spins are set, it is impossible to determine in what direction the third spin should point, as any orientation would dissatisfy one of the other bonds. For quantum systems, the remaining spin has to point either up or down, as shown in Fig. 3.1a, and the bond that links two parallel spins is called frustrated. This highlights how antiferromagnetic interactions on triangular

### Chapter 3. What is quantum magnetism?

units are an effective cornerstone of geometrical frustration. While quantum magnetism is the field aiming to study the effects of quantum physics in spin systems, frustrated magnetism is different in the sense that the associated field of research deals with effects of frustration and its exotic effects. The behavior of a classical system differs significantly from that of a quantum system, and is represented in Fig. 3.1b. Indeed, a classical spin can point in any direction, the arrangement of spins that minimizes the energy in that case is the  $120^\circ$  configuration, where all spins form an angle of  $120^\circ$  with each other. In that spirit, all bonds, instead of just one bond are frustrated. Both these states are associated to a very high degeneracy, which can have drastic effects on the ground state properties.

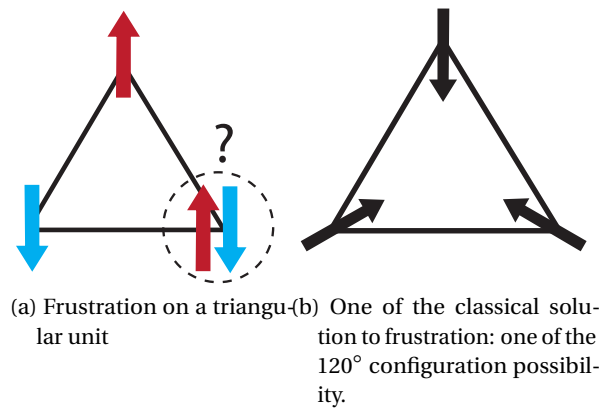


Figure 3.1: Geometrical frustration.

Even though the triangular lattice[48] offers a convenient view of frustration, it appears that there is no specific need to change to a new lattice to induce frustration. Indeed, a simple one dimensional chain with competing first second nearest neighbor interactions (shown in Fig. 3.2b) can be frustrated, if both the first nearest neighbor interaction and the second nearest neighbor interactions are antiferromagnetic[49]. The same comments stand true for the square lattice[50].

There are other theoretical lattices whose relevance has been evidenced experimentally by finding materials realizing them. The triangular lattice, which can be viewed as a square lattice with cross-square-unit couplings is the simplest of possible frustrated lattices but more complex lattices also exist. In two dimensions, another important lattice is the so-called Kagomé lattice[51] represented in Fig. 3.2a. Its name relates to its supposed Japanese origin: the motif it represents has been used in netting for centuries. Here again, the elementary building block is the triangular unit. These units are arranged in a specific pattern, creating a lattice where each site has four neighbors, two thirds of the triangular lattice, this has consequences that will be mentioned in another section.

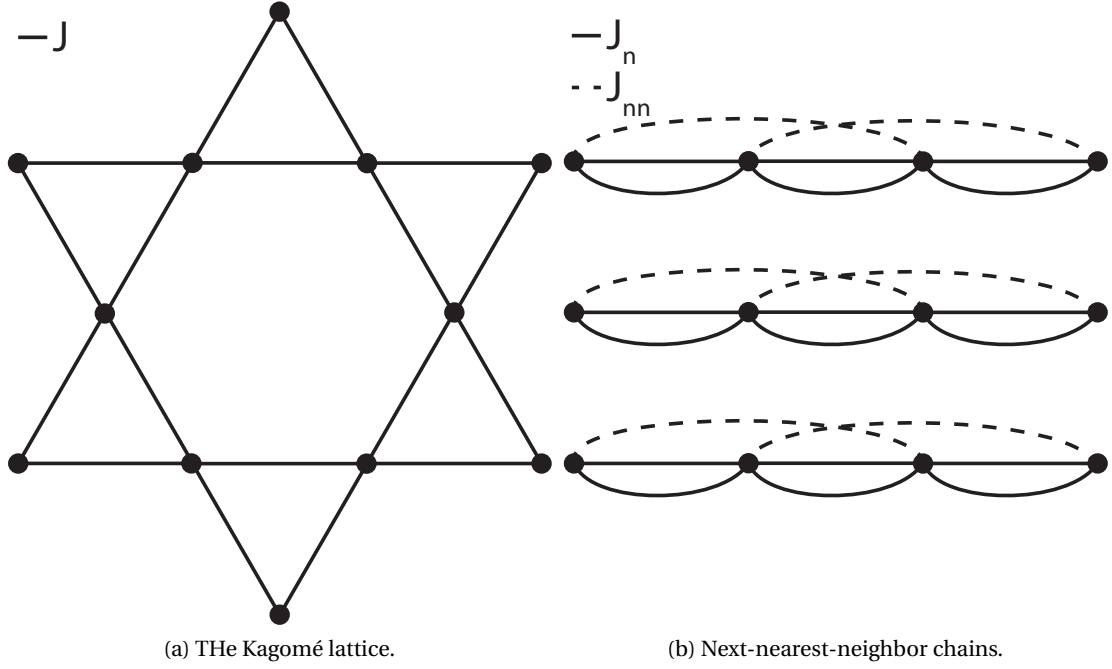


Figure 3.2: Other geometrically frustrated lattices.

Quite intuitively, frustration exists outside of purely two dimensional lattices as well. The diamond[52] and saw-tooth chains[53, 54] are simple examples of frustrated lattices in quasi one dimension. Here again, both motifs exhibit a combination of triangular building blocks: the saw-tooth chain consists in a chain of corner sharing triangles, and the diamond chain in a chain of corner sharing diamonds, each diamond consisting of two edge sharing triangles. In quantum physics, the dimension of systems is paramount: Mermin-Wagner theorem states that no magnetic long range order can settle at finite temperature without anisotropy one and two dimensions. Therefore, even though more complicated and thus both computationally more expensive and harder to grasp theoretically, the question of frustration in three dimensional lattices is of major importance. However, generating an equivalent of the triangular lattice in three dimensions does not appear straightforward. Several solutions to this problem exist: the Kagomé slabs[55], a superimposition of Kagomé planes, is one of them. Two other generalizations of the Kagomé lattice in three dimensions are quite common: the pyrochlore lattice[56, 57] and the hyperkagomé[58] lattices. The pyrochlore lattice encapsulates the rich physics of spin ices, and spin liquids, and has been realized in numerous compounds, forming a hot topic of the contemporary highly frustrated magnetism physics.

In the field of frustrated physics, when compounds do order magnetically, it is very frequent that the ordering temperature is quite different from the characteristic temperature of the dominant couplings in the systems, roughly given by the Curie-Weiss temperature. The high-temperature part of the DC-susceptibility can be modeled by the Curie-Weiss law, stated in

equation (3.1), and is represented in red, in Fig. 9.6.

$$\chi(T) = C/(T - \Theta_{\text{CW}}) + \chi_0 \quad (3.1)$$

Where  $\Theta_{\text{CW}}$  is the Curie-Weiss temperature, directly linked to the couplings in the system:  $\Theta_{\text{CW}} = \frac{S(S+1)}{3} \frac{\sum_{\text{R}} J(\text{R})}{k_{\text{B}}}$ .  $C = \mu_{\text{eff}}^2/8$  can be related to the effective moment of the sample, and  $\chi_0$  is a temperature independent diamagnetic background term. In the case of a spin half system, with Landé g factor of 2, the effective moment is expected to be  $1.7 \mu_{\text{B}}$ . Several phenomena can be accountable for a change in that value: the g-factor can be (slightly) different from two (ideally confirmed by ESR measurements), and can be anisotropic, the spin state also might be different from  $S = 1/2$ . For simple antiferromagnetic systems the Curie Weiss temperature,  $\Theta_{\text{CW}}$  can happen to be negative. This is of course not associated to a transition at a negative temperature, but rather a fingerprint of the relation between the Curie-Weiss temperature and the couplings in a system:  $\Theta_{\text{CW}}$  is simply the sum of the couplings. For an antiferromagnet (and depending on the sign convention), the coupling has a negative sign, and thus  $\Theta_{\text{CW}}$  is negative, but one still expects a transition at a temperature whose order of magnitude is that of the Curie-Weiss temperature. In frustrated systems however, due to various reasons, the transition to long range order can happen at a temperature much smaller than the Curie-Weiss temperature. By analogy to the collinear Néel state, the transition temperature is called the Néel temperature,  $T_{\text{N}}$ . Even though its actual relevance is debated, a widely used quantity showing how strongly the frustration suppresses the long range order is the frustration ratio,  $f$ [59], stated in equation (3.2).

$$f = \frac{|\Theta_{\text{CW}}|}{T_{\text{N}}} \quad (3.2)$$

Several compounds[60] present very high frustration ratios, the theoretical maximum being of course infinite, since some compounds could theoretically never undergo a transition to a long-range ordered phase. Experts tend to agree on the fact that a frustration ratio greater than five corresponds to highly frustrated physics. There are however limits to this consideration, for example the frustrated square lattice, which would have a small frustration ratio is one of the stereotypical example of frustration: this ratio is more a rule of thumb than an exact measurement of frustration. As mentioned earlier, quantum spins behave intrinsically very differently from classical ones. Moreover, in order to minimize the energy of the antiferromagnetic Heisenberg Hamiltonian on the triangular lattice, quantum spins do not necessarily have to choose between pointing up or down. They can also create an entangled state, a singlet, which lowers the energy of the system. This notion is the basic idea behind the mathematical construction of the Resonating Valence Bond State (RVB), and the spin liquid states[61]. The RVB state consists in the quantum superposition of all possible lattice coverings of singlets. This superimposition prevents long range order at zero Kelvin. Moreover, the degeneracy of the states is extremely high, thus the possible excitations are exhibiting an even higher degeneracy.

## 3.2 Spin liquids

As mentioned in the previous paragraph, the combination of quantum fluctuations, geometrical frustration, and lattices based on triangular building blocks, gave rise to a novel ground state manifold: the spin-liquids. This naming comes from the liquid state of matter, where atoms experience strong short range correlations, but close to no long-range order settles in the system. In a similar fashion and thanks to singlets, that act as highly short-range correlated building blocks, spin-liquids also present magnetic short range order and correlations, and no long range order: exponentially suppressed long range correlations. The spins keep fluctuating strongly down to zero Kelvin. Fig. 3.3 presents a comparison of the energy per spin of classical antiferromagnetic Néel state to the dimerized, fully quantum picture, for different lattices: the one dimensional chain, the square lattice, the triangular lattice, and the Kagomé lattice[62]. The energies per site shown in the quantum case correspond to simple calculations on the representative state that is shown, a quantum superposition of all equivalent coverings of the lattice with a detailed quantum calculation would result in a state with lower energy, this however does not change the conclusions that can be obtained from this reasoning.

It appears that in one dimension, frustration is not needed to achieve and identify, such states of matter, presenting fractional excitations: breaking apart a spin-1 boson, but rather forming two spin half entities obeying the Fermi-Dirac statistics[63, 64, 65]. In that scheme, a continuum of excitations is visible and is explained by a combination of two fractionnal spin half excitations, which are effectively the two dimensional equivalent of one dimensional spinons. These excitations are bound and can be viewed as conventional magnons. Indeed, the energy of a dimer is lower than that of the Néel state. In two dimensions, Néel order appears to prevail. In other planar lattices, the situation is less clear: the triangular lattices exhibits exactly the same energy per site for both quantum and classical ground states, and the Kagomé lattice indicates an energetic preference for the quantum ground state. Hence, this argument does not seem conclusive in the case of the triangular lattice but reveals how the coordination of a given lattice plays a role: the lower the coordination, the likelier is a lattice to favor a dimerized state. Both thermal and quantum fluctuations may act to move the ground state in one or the other manifold, however at zero Kelvin, only quantum fluctuations are able to perturb the spins in the required manner, and are maximal for spin half spins: explaining the early historical focus on spin half systems to find actual realizations of such physics. In 1973, P.W. Anderson formally stated the Resonating Valence Bond (RVB) state[66], in a study of the frustrated triangular lattice.

An important point can be made regarding usual the statistical physics: in principle, at a given temperature, one only thinks that populated states are those with energy smaller than the temperature of the system. This is most of the time right, since the states with energy higher than the temperature of the system are exponentially suppressed. However, in highly frustrated systems, the degeneracy scales with systems sizes and may be exponential as well: the RVB state on the Kagomé lattice consists in  $2^{N/3+1}$  different coverings. In that case, states

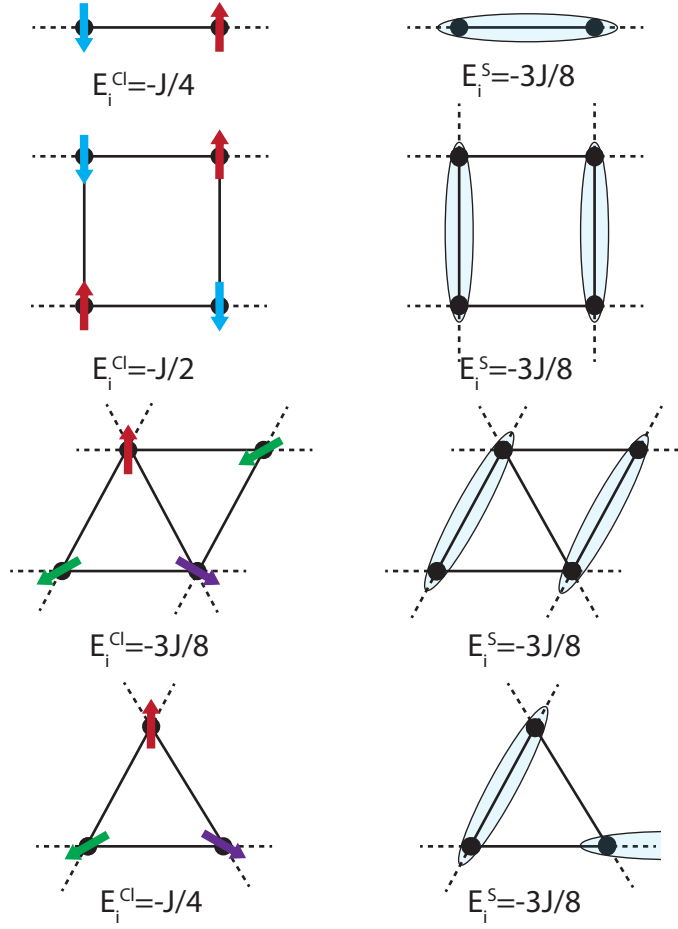


Figure 3.3: Pictorial representation of the classical (left hand side) and quantum (right hand side) ground states of the Heisenberg Hamiltonian on several lattices: a 1D chain (top), the square lattice (second row), the triangular lattice (third row), and the Kagomé lattice (fourth row). The energy per spin of each state is indicated.

with "high" energy can actually dominate the behavior of the systems, the massive degeneracy, compensating their exponential suppression in the partition function. This phenomenon is often called fluctuations domination, and is of course temperature dependent. The lower the temperature, the larger must be the degeneracy. In many frustrated cases, at arbitrarily small temperatures, the properties of the systems are determined by the ground state properties exclusively, and thus present usual magnetic long-range order. The "delay" in the transition temperature can be attributed to frustration and the high degeneracy of states, giving some credit to the idea of frustration ratio.

The experimental search for spin liquid states saw a burst[67] in the proposed number of candidates around 2005, when the first actual realization of a compound hosting a spin liquid ground state was synthesized and measured[68] in Herbertsmithite. This material is made of decoupled Kagomé planes formed by spin half atoms of copper. Examples also appeared in two

dimensions, on the frustrated square lattice [69, 70]. Some limitations quickly became clear. For example, distortions of the perfect triangular geometry can perturb the high symmetry required to stabilize the RVB state. In Herbertsmithite, it appeared that chemical poisoning was also a real experimental limitation: even though it has been established theoretically that the Kagomé lattice hosts a spin liquid as a ground state[71], it is quite frequent when synthesizing Herbertsmithite that copper atoms are replaced by zinc, creating vacancies and faults in the magnetic lattice, making the analysis of results hard to attribute to either the spin liquid behavior or chemically -accidentally- induced disorder. Finding spin liquids nowadays remains a hot topic dragging considerable attention[72]. Recent research includes, but is not limited to, a search of spin liquids in three dimensions and with spins higher than spin half. In the vast field of research dedicated to the study of the spin liquid state, it appears that a distinction has to be made between quantum and classical spin liquids. In the case of classical spin liquids, a large ground state degeneracy typically exists, and thermal fluctuations can drive a transition between the distinct ground states. This typically results for example in a spin ice system. For many of such systems, at very low temperatures, stray fields become important and cause the spins either to order or to form a spin glass. On the other hand, the quantum spin liquid also corresponds to a highly fluctuating state, with fluctuations finding their origin in the quantum realm: the commutation relations of spin operators give rise to quantum fluctuations, which can be strong and can occur at 0 K, and prevent the stabilization of long range order. These states cannot be associated to broken symmetries and can thus not be described by the usual Landau theory of phase transitions.





## **Experimental background Part II**



## 4 Magnetometry

When trying to assess the quantum phase diagram of a novel compound, many techniques can be used. Among the most used ones are DC and AC temperature dependent and field dependent magnetization, and also heat capacity. Heat capacity measurements are particularly well suited to confirm second order-phase transitions, for example, transitions to a state with magnetic long range order. Measurements performed with magnetometers are extremely well suited to study magnetic phase transitions of both first and second order. One of the most basic experiments that can be done when analyzing magnetic properties of a compound is called magnetometry. The idea of magnetometry is to measure the magnetization of a sample, at different experimental conditions: in an external field, at different temperatures and also possibly at different applied pressures. This field is quite well established and several commercial companies, such as Quantum Design and Cryogenic limited propose fully integrated measurement systems such as the Magnetic Properties Measurement System (MPMS), Physical Properties Measurement System (PPMS, which can also measure physical properties other than magnetization). A wide variety of magnetometers exists, ranging from Hall probes and torque measurements to more accurate Superconducting QUantum Interference Device (SQUID) based techniques. The latter are among the most precise ways of determining the magnetization of magnetic samples and are often a part of many condensed matter physics laboratories.

### 4.1 Superconducting Quantum Interference Devices

The Superconducting Quantum Interference Device (SQUID) relies on the principle of the Josephson junction. A loop using a superconducting material, typically niobium, with two insulating Josephson junctions, typically made of aluminum oxide. A current  $I$  is applied and flows through that loop. If no external field is applied, then the current splits equally between the two branches as  $I/2$ . In the case of displacement of a nearby external field, for example due to the movement of a magnetic dipole moment close to the SQUID, a screening current will appear,  $I_s$ , and a magnetic field is induced that cancels the external magnetic flux. In order to create a counterbalancing magnetic flux, the current flows in the loop, resulting in a

current of  $I/2 + I_s$  in one of the two branches and  $I/2 - I_s$  in the other. This functioning principle is illustrated in Fig. 4.1.

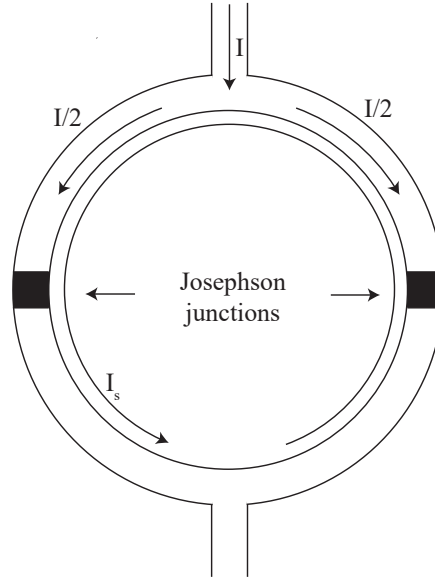
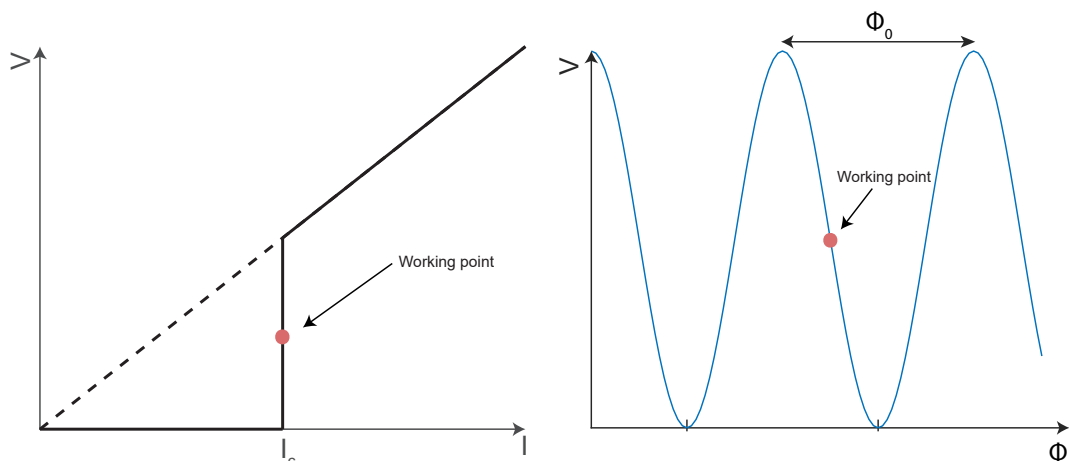


Figure 4.1: Basic design of a SQUID: two Josephson junctions and an applied current  $I$ .  $I_s$  is the current created to compensate for the external flux.

Once the current in either loop exceeds  $I_c$ , the critical current of the Josephson junction, a voltage appears across the junction, as shown in Fig. 4.2a. Moreover, the flux in each loop has to be quantized, and equal to an integer number times the flux quantum  $\Phi_0 = 2.067 \cdot 10^{-15}$  Wb, with  $1\text{T} = 1 \text{ Wb/m}^2$ . If the external flux is greater than  $\Phi_0(n+1/2)$  for some integer  $n$ , instead of trying to cancel the flux, the induced current tries to force the new flux to be  $\Phi_0(n+1)$ . The sign of the induced current thus changes and the total current  $I/2 + I_s$  thus decreases until the total flux reaches  $\Phi_0(n+1)$ . If the input current  $I$  is greater than  $I_c$ , then the measured electric potential difference between each end of the loop is a periodic function of the field, with period equal to  $\Phi_0$ , as shown in Fig. 4.2b.

There are therefore two options to effectively measure the magnetic field creating the change of flux. The first option is to simply count how many quanta of flux are necessary to stabilize the system. However, it turns out that another method provides better accuracy: instead, the idea is to work at a specific voltage-flux and voltage-current working point, and effectively change the induced current to balance the change of flux in the sample. This working point is chosen in such a way that the derivative of the voltage with respect to both flux and current is maximum, which enables to maximize the accuracy. A real SQUID is often used in an actual instrument in the way described in Fig. 4.3.

A detection coil is placed near the sample. The change of flux at the sample position is transmitted to another coil, placed next to the SQUID. The loop itself is placed next to a compensation loop, that is controlled through a pre-amplification system. The use of a lock-



(a) V-I curve of a Josephson junction. Once the current reaches  $I_c$ , a voltage develops. (b) Periodicity of the loop voltage in function of the applied flux.

Figure 4.2: Voltage developing at a Josephson junction in function of applied current and external magnetic flux.

in and many different resistance ranges result in precise and adaptive measurements. The sensitivity of such a SQUID can go down to  $10^{-7}$  emu, much smaller than the Earth's magnetic field.

## 4.2 Magnetometers

The basic measurement principle is to translate the sample in a set of coils. Assuming that, to first the order, the sample is a perfect magnetic dipole (typical samples are much smaller than the detection coil), the theoretical voltage observed for a sample going through a given set of coils can be calculated. Fig. 4.4a shows the signal measured when moving a magnetic dipole through a given set of loops. The two loops in the middle are hosting a current flowing in one direction. The current flows in the two other loops in the opposite direction. In practice, all of it is made of a single wire, with one current and different loops are present to make the gradiometer work in one way or the other. The individual contributions are indicated in blue and red for the two loops, and the total signal is represented in purple. The exact shape depends on the sample geometry but the measured curve can nonetheless be fitted to extract the value of the magnetic moment. The vertical axis refers to the field direction. In practice, during a measurement, the sample is moved up and down in the loops, which allows to correct for a potential SQUID drift.

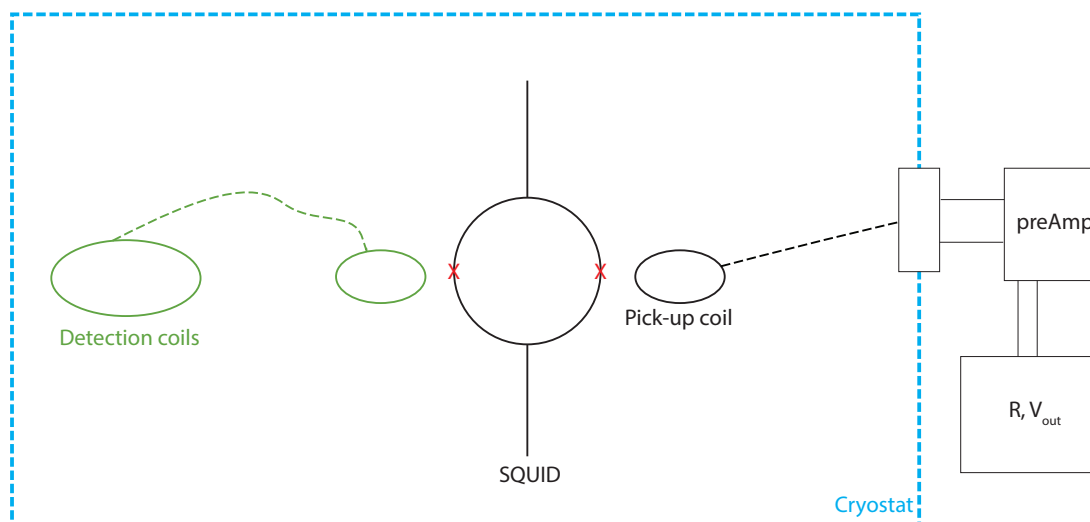
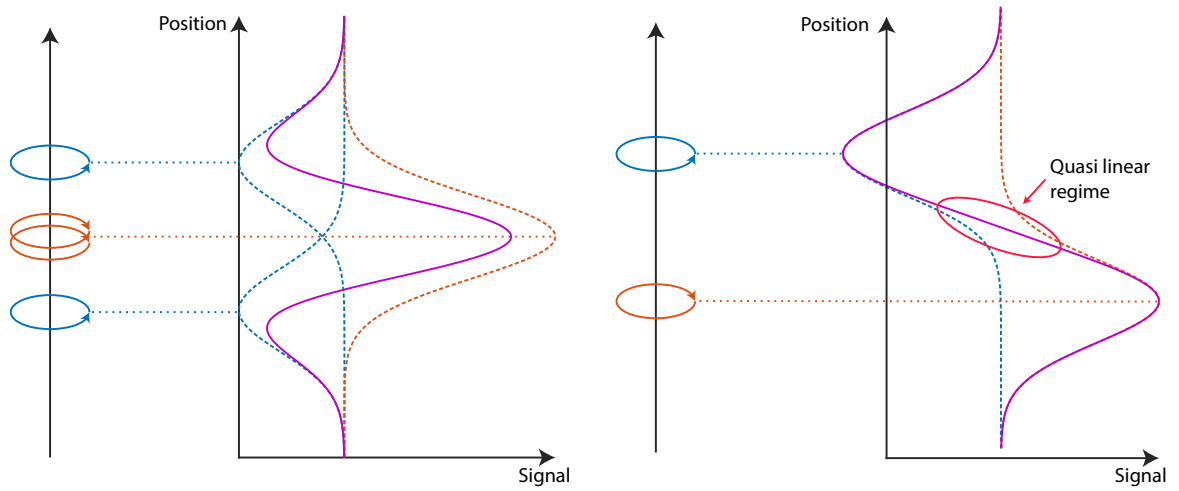


Figure 4.3: Schematic portraying the conventional use of a SQUID: pick-up loop, cryostat, and compensation loop.

### 4.3 Vibrating Sample Magnetometers

The Vibrating Sample Magnetometer (VSM) takes advantage of a geometry of loops that differs from that of the SQUID. Instead of four loops, only two are used. Fig. 4.4b presents how the combined use of two loops with currents flowing in opposite directions result in an area where the measured response to the sample displacement is linear. By having an oscillating movement (typically 10–100 Hz) of the sample in this region, the response is thus also oscillating. The amplitude of oscillation is mathematically connected to the magnetization of the sample. The accuracy of VSM is slightly lower than that of the SQUID. Both instruments enable to measure quantum phase diagrams in function of temperature and magnetic fields. Commercial solutions routinely propose options to measure with a DC field of up to 14 T and down to 2 K. A wide variety of options also include cryogen-free, re-condensing systems. Since the magnetometers are so accurate, shielding from the surrounding magnetic fields, including the earth's, is paramount. The sample holders are also typically made of plastic, with small, assumed temperature independent diamagnetic component. Samples are usually fixed using GE varnish, low temperature grease, or are wrapped in teflon tape. The samples are then placed in long straws, providing a homogeneous background or fixed onto a plastic plate.



(a) SQUID configuration: second order gradiometer: two current loops are circulating in one direction, in the middle and the two outer loops are circulating in the opposite direction.  
 (b) VSM configuration: first order gradiometer: two current loops are circulating in opposite direction, creating a linear region in between the two loops.

Figure 4.4: Signal measured when passing a magnetic dipole through a set of coils, with current flowing in one direction (blue), in the other, (red) and the total, measured signal (purple).





## 5 Heat Capacity measurements

### 5.1 Principle

Heat capacity is a measurable quantity that is really practical to observe second order phase transitions. In practice, heat capacity measurements are slightly less adequate to identify first order phase transitions even though it can still be used for such purpose. Many magnetic systems undergo structural first order phases transitions that reduce the symmetry of the system and help magnetic order to be stabilized, or simply modify its details when already settled[73].

The heat capacity is defined as the quantity of energy that has to be furnished to a system to increase its temperature by one Kelvin per unit mass, and is stated in equation (5.1).

$$c_{p,V} = \frac{1}{m} \left( \frac{\partial Q}{\partial T} \right)_{p,V} \quad (5.1)$$

When undergoing a phase transition, a system requires additional energy to change its internal structure, and energy is not exclusively converted into a temperature rise. Once the phase transition point is passed, the system no longer reorganizes and the available energy is used exclusively to heat the sample. This is the fundamental physical mechanism explaining why a phase transition creates a peak in the specific heat. Even though in theory a transition could be very sharp, in practice peaks can be broaden by a variety of effects. The simplest of effects is due to the intrinsic behavior of the observed phase transition. In the Landau theory of phase transitions, a critical exponent describes how the heat capacity diverges in the vicinity of the transition. Depending on the universality class of the transition, this exponent may take different values, and thus result in different peak widths. Additionally to that, other phenomena can be at play, such as: impurities, non uniformity of the structure, slightly different temperatures of different parts of the system during the measurement, and so on. In order to acquire the heat capacity experimentally, several techniques are commonly used such as: the relaxation method, the Alternative Current (AC) method and the long range method. The Physical Properties Measurement System (PPMS) uses a variation of the heat pulse method, called the relaxation method, particularly suitable for measurements of crystalline samples.

## 5.2 Measurements in practice

In a first step, the heat capacity of the sample,  $C_s$  can be computed using equation (5.2). In that equation,  $K_e$  refers to the heat conductivity of the weak link, and  $C_0$  is the specific heat without the sample. Indeed, the sample is placed on a plate that contributes to the total heat capacity as a rather systematic background. However, an additional contribution to the measured signal comes from the amount and shape of the grease that is used, which varies from experiment to experiment. Each heat capacity measurement is thus preceded by an "empty puck" measurement of the so-called addenda, in order to subtract this signal and discriminate between signal coming from the grease and from the sample. Coefficient  $K_e$  can be deduced from the heat added to the system,  $\Delta P$ , by the following mathematical relation:  $K_e = \Delta P / \Delta T$ .

$$C_s = K_e(a_1\tau_1 + a_2\tau_2) - C_0 \quad (5.2)$$

The sample can be either a powder, pressed into a pellet, or a single crystal, placed on a holder. The typical sample mass is of the order of one milligram. The holder is made of a material with high thermal conductivity, and is equipped with a thermometer and heater. The whole system is embedded in a thermal reservoir, kept at a constant temperature and typically made of copper, and connected to the sample plate through a weak link. The sample is fixed onto the sample holder with low temperature grease. The grease facilitates the thermal contact between holder and sample, but also creates a background signal, its use is typically restricted to the least possible amount. The whole system is placed under vacuum with a view to preventing heat losses through convection, as shown in Fig. 5.1. Ideally, the heat capacity of the grease is negligible, and its heat conductivity is a lot higher than that of the weak link. Under these hypothesis, the heat provided by the heater can be assumed to be fully transferred to the sample first, and then in a second process dissipated through the weak link.

During a measurement, the sample is heated for a certain time, until its temperature is steady and reaches a balance between supplied heat from the heater and losses through the weak link. Fig. 5.2 summarizes this process.

It is however practically faster to heat the sample and measure only the beginning of the heating curve. Based on that principle, the steady state temperature can be computed from fitting a model to the data. A similar process can be performed for the temperature relaxation part. The formula describing the temperature change is given by equation (5.3), where  $T$  stands for the temperature,  $\Delta T$ , the total temperature rise,  $t$  the time,  $\tau_1$  and  $\tau_2$  relaxation constants, and  $a_1$  and  $a_2$  are amplitude coefficients.

$$T(t) = T_0 + \Delta T \left( a_1 e^{-\frac{t}{\tau_1}} + a_2 e^{-\frac{t}{\tau_2}} \right) \quad (5.3)$$

The lowering of the temperature is fitted with equation (5.3), which allows to extract experi-

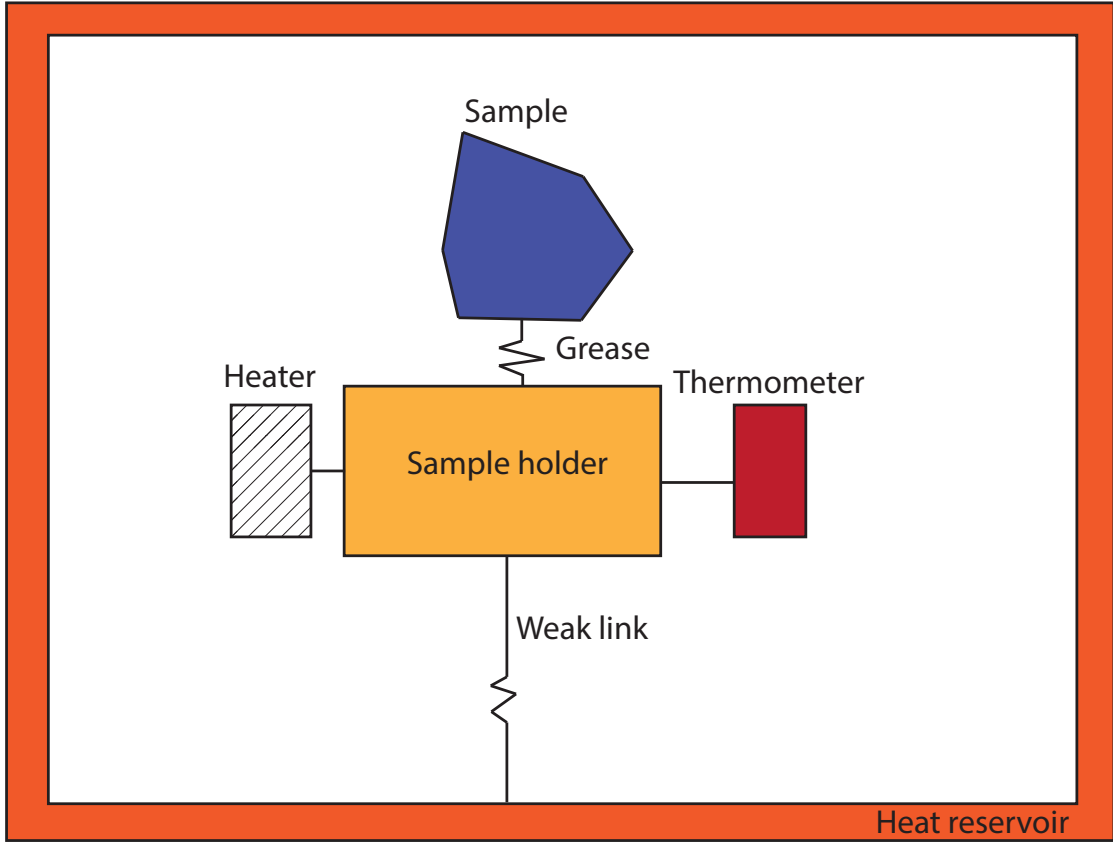


Figure 5.1: Schematic of a PPMS heat capacity measurement stage

mental values of  $a_1$ ,  $a_2$ ,  $\tau_1$  and  $\tau_2$ .

The temperature of the temperature reservoir is then modified to a new  $T_0$ , and the process is repeated. The measurement can also be done in an external magnetic field. Since the method is based on the thermal relaxation of the sample, and since the relaxation depends on the temperature, the measurement time varies substantially across the whole temperature range, which should be kept in mind when planning experiments.

### 5.3 Applications

The heat capacity is closely related to entropy. The mathematical relation between these quantities is stated in equation (5.4), where  $S$  is the entropy.

$$C_V = T \left( \frac{\partial S}{\partial T} \right)_V \quad (5.4)$$

When a phase transition occurs, as mentioned previously, some energy is used to reorganize the internal structure of the material. This can be associated to a non negligible change of the atomic structure and in particular its symmetry, giving rise to a structural phase transition.

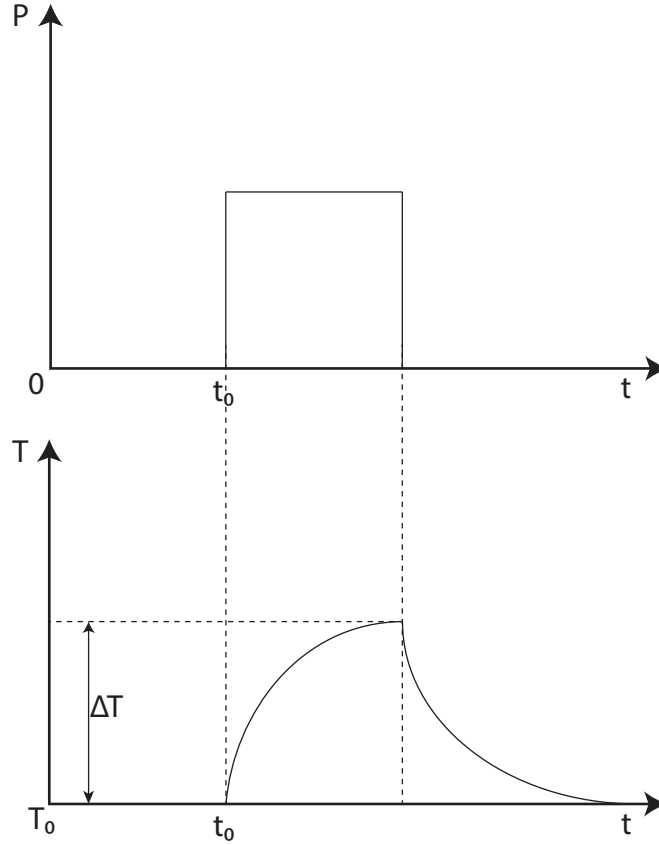


Figure 5.2: Top: power in the heater for heat capacity measurements. The heating is maintained for a time  $t_0$  until the steady state is reached. Bottom: the temperature gradually increases after  $t_0$ , then the heater is switched off, and the temperature relaxes down to its initial value.

More interestingly, in the case of magnetism and a usual second order phase transition to a state exhibiting magnetic long range order, the spin of each atom freezes and some entropy is locked in the transition, in order to orient the spins as they are frozen into a given state. The amount of entropy required depends on the spin value, and can be expressed as  $S = k_B \ln(2S + 1)$ . In contrast with non frustrated systems, where it is quite common to capture the whole entropy in the transition in a rather sharp peak occurring at a temperature close to that of the transition in frustrated systems, it is quite common to have a significant contribution of the heat capacity explained the correlations building up in the system, over a wide temperature range, and sometimes less than 20% of the total entropy purely associated to the ordering of spins[39]. In the case of a highly frustrated system, these correlations develop over a wide range of temperatures, due to the fact that the characteristic interactions in the system are comparable to thermal fluctuations.

Another quite instrumental application of the measurement of heat capacity took place in the frame of the study of the so-called spin ice systems [74].  $\text{Dy}_2\text{Ti}_2\text{O}_7$  hosts such physics. Its name comes from water ice. In the usual water ice ( $I_h$ ) obtained by transition of liquid ice

below 273.15 K at standard atmospheric pressure. Atoms settle in a structure showing a long range order, and geometrical frustration leads to O-H bond distances to vary significantly, giving rise to the ice rules: out of the four hydrogen surrounding an oxygen atom, two are sitting closer to the central atom than the other two. Since the tetrahedra are corner sharing, there are six ways of satisfying these rules. In the case of spin ice, these tetrahedra are also present and corner linked, with magnetic atoms at the corners. There are similar ice-rules with spins pointing either in or out of the tetrahedra. In a similar fashion, no long range magnetic order arises, and the magnetic spin orientation plays the same role as the atomic position in ice, with the "two in two out" state: two spins pointing inside the tetrahedron and two pointing outside. This high macroscopic state degeneracy gives rise to an extensive entropy, and thus the existence of a residual entropy, as evidenced by Pauling[75]. A similar residual entropy has been evidenced in several spin ice systems. The phenomenon has been studied and has resulted in the observation of magnetic monopoles in  $\text{Ho}_2\text{Ti}_2\text{O}_7$ [76], in the form of spin excitations of the system.



## 6 Resonance techniques

Resonance techniques are spectroscopy methods frequently used in condensed matter physics. It can be split into three subcategories: Electron Spin Resonance (ESR), also known as Electron Paramagnetic Resonance (EPR), Nuclear Magnetic Resonance (NMR), and Muon Spin Rotation ( $\mu$ SR), also named Muon Spin Resonance for its similarities with the other two techniques. These three spectroscopy techniques share in common that they are local techniques, and are sensitive to magnetic fields. They are thus a powerful tool to study magnetism in compounds, and act as a local probe. Additionally, all these techniques are quite sensitive to chemical environments. The main difference between these three ways of probing matter are the time scales of the fluctuations actually probed, their degree of sensitivity to small magnetic moments, and the size and geometry of possible external magnetic fields involved. Last but not least, another non negligible difference is the fact that while ESR and NMR can be both performed in a regular laboratory,  $\mu$ SR requires the production of an intense muon beam, and is thus only available at a few dedicated large scale facilities. The physical mechanisms on which NMR and ESR are based are analogous so only ESR and  $\mu$ SR will be described in more details.



## 6.1 Electron Spin Resonance

ESR stands for the Electron Spin Resonance technique, which is a measurement taking advantage of the ability of electrons to absorb and re-emit the energy coming from an electromagnetic wave, when placed in an external magnetic field. In the case of Nuclear Magnetic Resonance, it is the spin of the spin of the atomic nuclei that plays this role, instead of that of the electron. Only unpaired electrons can behave in such a way, thus this method is very useful to study transition metal based compounds. The other name of the technique, Electron Paramagnetic Resonance implies that paramagnets can be studied, however, ferro and antiferromagnetic spin resonance do exist and can be studied using the same principles and experimental setups.

The basic principle on which ESR relies is the Zeeman splitting[77]: when embedded in an external magnetic field  $B_0$ , the degenerate energy levels of a spin  $S$  split into  $2S + 1$  states, according to their  $m_S$  quantum number:  $-S, -S+1, \dots, S-1, S$ . The splitting is proportional to the field strength  $B_0$ . In the case of an ion with a single unpaired electron, there are two resulting energy levels, corresponding to  $m_S = +1/2$  and  $m_S = -1/2$ , as summarized in Fig. 6.1 The

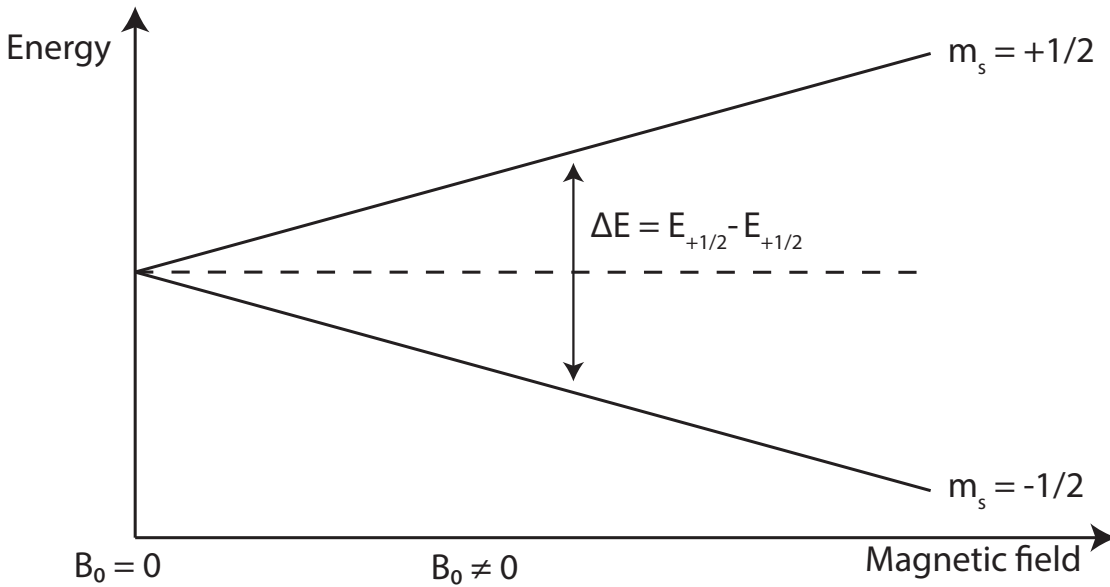


Figure 6.1: Zeeman splitting scheme of an ion with a single unpaired electron, resulting in two states:  $m_S = +1/2$  and  $m_S = -1/2$ .

resulting splitting is given by the magnetic energy and can be written  $m_S g \mu_B B_0$ , where  $m_S$  is the spin quantum number,  $g$  the Landé factor[78],  $\mu_B$  the bohr magnetron,  $9.2741 \cdot 10^{-24} \text{ J} \cdot \text{T}^{-1}$ . The electrons in the system can occupy these two electronic levels. The macroscopic distribution of the electrons is given by the Maxwell-Boltzmann distribution shown in equation (6.1), where  $k_B$  is the Boltzmann constant and  $T$  the temperature.

$$\frac{n(m_S = +1/2)}{n(m_S = -1/2)} = \exp\left(-\frac{E(m_S = +1/2) - E(m_S = -1/2)}{k_B T}\right) = \exp\left(-\frac{\Delta E}{k_B T}\right) \quad (6.1)$$

This implies that the  $m_S = -1/2$  state is populated by more electrons than the other level. At 298 K, and in a field of 3350 Gauss, the ratio between the two populations is 0.998, meaning that the perturbation induced by the field is small.

In the presence of an external electromagnetic wave of frequency  $\nu$ , perpendicular to the first magnetic field pulse, and of much smaller intensity, a photon can be absorbed if its energy  $h\nu$  is equal to the difference between the  $m_S=+1/2$  and the  $m_S=-1/2$  energy levels:  $g\mu_B B_0$ . The resonance condition thus reads as in equation 6.2, where  $h$  is the Planck constant,  $h = 6.6261 \cdot 10^{-34} \text{J}\cdot\text{s}$ .

$$h\nu = g\mu_B B_0 \quad (6.2)$$

For optical transitions in general, with more than two states, the Fermi Golden rule implies that the only allowed transitions are the ones with  $\Delta S = 0$  and  $\Delta m_S = \pm 1$ , the other transitions being forbidden, unless in the specific case of a system mixing quantum states[79]. The resonance condition can be reformulated using the gyromagnetic ratio of the electron as shown in equation (6.3).

$$\nu = \gamma_e B_0 \quad (6.3)$$

In practice, a measurement consists in acquiring a set of resonance spectra. An experiment can be performed as in typical NMR, by fixing the magnetic field  $H$ , and varying the electromagnetic wave's frequency,  $\nu$ . However, in most typical ESR modern setups, the frequency is fixed, and the magnetic field is varied. A standard result of an experiment is thus what is shown in Fig. 6.2. The majority of ESR spectrometers use a magnetic field oscillating about a mean value:  $B = B_0 + B_1 \cos(\omega t)$ . The Taylor expansion of the absorption signal to first order thus reads as in equation (6.4).

$$A = A(B_0) + \left( \frac{dA}{dB} \right)_0 \cos(\omega t). \quad (6.4)$$

This justifies the relevance of considering the derivative of the absorbance. The usefulness of these spectra can be better apprehended by considering the Bloch equations, governing the time evolution of the magnetization,  $M(t) = (M_x(t), M_y(t), M_z(t))$ . The set of equation can be found in equation (6.5). In that set of equations,  $B(t) = (B_1 \cos(\omega t), -B_1 \sin(\omega t), B_0)$ . The  $z$  component of the applied field  $B(t)$  is split into two: a time independent one,  $B_0$  and an oscillating one, with amplitude  $B_1$ . The two relaxation times defined in equation (6.5) are the key components of the model, for both ESR and NMR.  $T_1$  describes the longitudinal relaxation in the field, and  $T_2$  the transversal relaxation. These two relaxations correspond to the fact that when applying an additional field, the spins of the magnetic atoms align in that field. In a second step, the system relaxes to go back to its original state with characteristic time  $T_1$ , and if the field direction is not exactly that of the moments, an additional Larmor precession

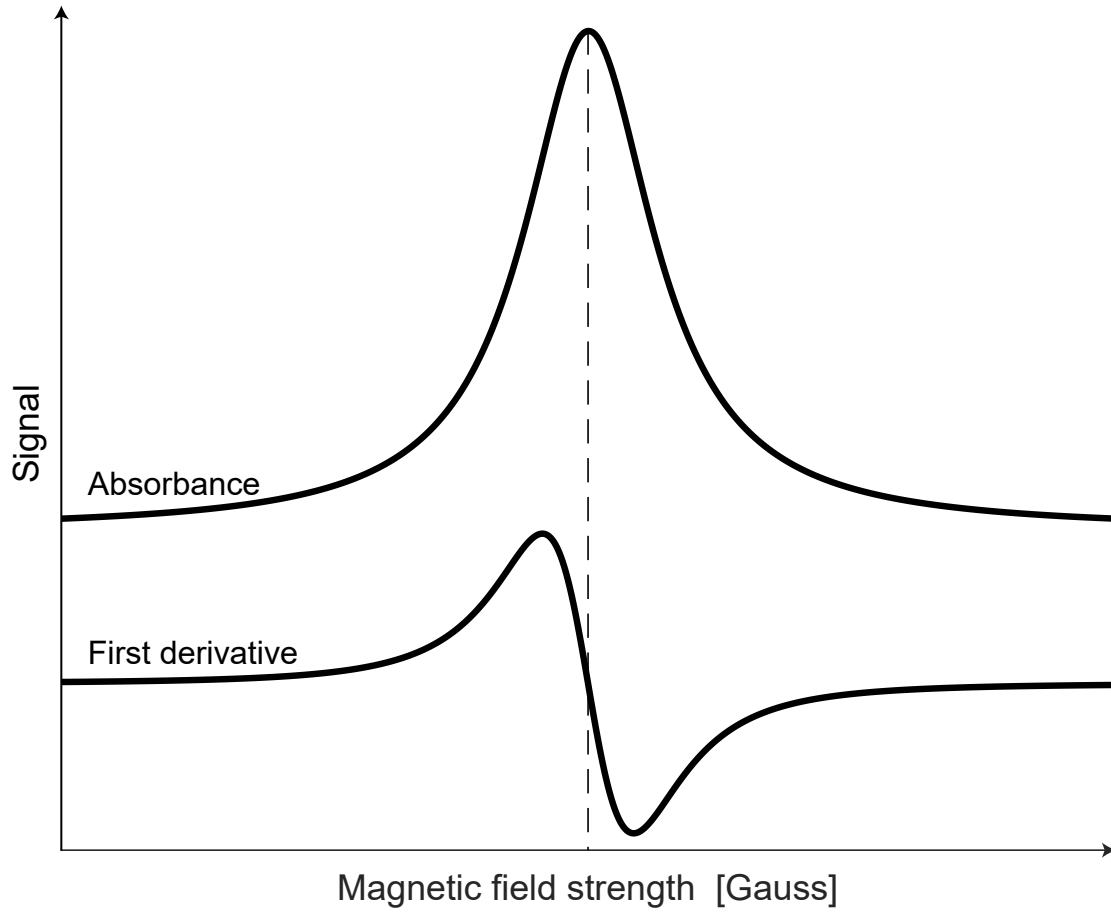


Figure 6.2: Signal measured by ESR: absorbance curve and its first derivative. The frequency is kept constant and the field is swept.

occurs, of characteristic time  $T_2$ .

$$\begin{aligned}
 \frac{dM_x(t)}{dt} &= \gamma_e(M(t) \times B(t))_x - \frac{M_x(t)}{T_2} \\
 \frac{dM_y(t)}{dt} &= \gamma_e(M(t) \times B(t))_y - \frac{M_y(t)}{T_2} \\
 \frac{dM_z(t)}{dt} &= \gamma_e(M(t) \times B(t))_z - \frac{M_z(t) - M_0}{T_1}
 \end{aligned} \tag{6.5}$$

$T_1$  is often associated to the spin-lattice relaxation, and is the result of the change of energy of the spins, released to the surrounding system, to go back to the thermodynamic equilibrium.  $T_2$  is called the spin-spin relaxation. The spin echo method consists in the application of two pulses, at ninety degrees, separated by a short time period. It gives the possibility to separate inhomogeneity coming from macroscopic dephasing from that originating from a

local dephasing due to true spin-spin relaxation. These inhomogeneities are induced by the local inhomogeneities in the magnetic field that result in slightly different Larmor frequencies, causing a different precession period about the z-axis. After a mathematical treatment of equations (6.5) called the rotating reference frame, one obtains equation (6.6). Despite this naming, it should not be understood that the apparatus produces a rotating field: the field is oscillating linearly.

$$\frac{dM}{dt} = \begin{pmatrix} -\Omega_S M_y - M_x / T_2 \\ \Omega_S M_x - \omega_1 M_z - M_y / T_2 \\ \omega_1 M_y - (M_z - M_0) / T_1 \end{pmatrix} \quad (6.6)$$

The Bloch equations with  $\Omega_S = \omega_0 - \omega$  and  $\omega_1 = \gamma B_1$  can be solved and the obtained results are visible in equation (6.7).

$$\begin{aligned} M_x &= M_0 \omega_1 \frac{\Omega_S T_2^2}{1 + \Omega_S^2 T_2^2 + \omega_1^2 T_1 T_2} \\ M_y &= -M_0 \omega_1 \frac{T_2}{1 + \Omega_S^2 T_2^2 + \omega_1^2 T_1 T_2} \\ M_z &= M_0 \frac{1 + \Omega_S^2 T_2^2}{1 + \Omega_S^2 T_2^2 + \omega_1^2 T_1 T_2} \end{aligned} \quad (6.7)$$

By measuring  $M_x$ ,  $M_y$  and  $M_z$ , the different characteristic of a physical system can be fitted and extracted. The value of the resonance field gives information on the Landé g factor of the magnetic ion. The area below the absorbance curve is proportional to the number of spins contributing to the signal, the half-width-half-maximum of the absorbance curve provides insights on the interactions between the spins.

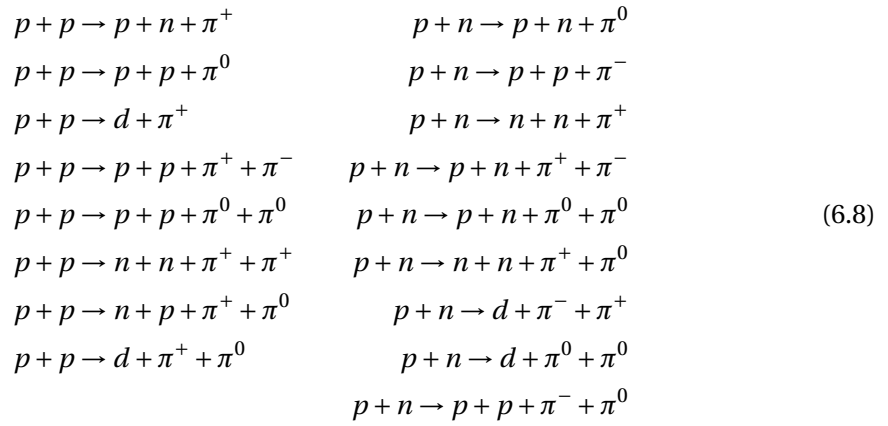
The ESR instruments use a microwave cavity and a lock-in amplifier, in order to obtain the best possible accuracy. With a view to detecting a signal, an ESR device typically needs about  $10^{12}$  spins participating. Since a spin half carries a moment of  $2.1 \cdot 10^{-27}$  emu, this means that a moment of  $2 \cdot 10^{-15}$  emu can be detected, which is 7 orders of magnitude more sensitive than a SQUID, that can detect moments of about  $5 \cdot 10^{-8}$  emu. When compared to NMR, the sensitivity that can be achieved is the same, however, due to the fact that the magnetization depends on the gyromagnetic ratios, it turns out that ESR requires a lot less sample than NMR: a decent signal can be obtained with a couple of nanograms, whereas the NMR technique requires measuring a micro-gram or milligram sample.

Due to the intrinsic local character of the technique, ESR, probes with greater accuracy the susceptibility of materials than a SQUID in the sense that in the case of a low susceptibility, the signal may be dominated by impurity coming from the sample. ESR is able to discriminate between the two signals, whereas a SQUID can only measure the total contribution[80]. The same comment applies to NMR: a diverging susceptibility could be attributed to an impurity in spin half, copper based Kagomé system Herbertsmithite[81] in which a suspected spin liquid ground state has been both theorized and measured. In some cases, it appeared that a substitution of paramagnetic copper at zinc sites hindered the stabilization of spin liquids, or at least could be associated to a macroscopic divergence of the magnetic susceptibility. In order to separate collective from local magnetic susceptibility, resonance techniques were successfully used and this resulted in the identification of a small and finite intrinsic susceptibility that could be obtained from the NMR line shift. ESR proves to be useful also in the study of antifer-

romagnets, for example  $\delta$ -[EDT-CONMe<sub>2</sub>]<sub>2</sub>AsF<sub>6</sub>, a quasi-1D charge ordered antiferromagnet. In this compound magnetic atoms are placed in chains with a complicated magnetic lattice involving three main couplings, including inter-chain coupling. ESR helped to reveal that a combination of the effects of the coupling between the frustrated chains combined to defects restores a three dimensional order[82]. Another compelling use of ESR also took place in the study of the spin lattice interaction in the quasi-one dimensional helimagnet LiCu<sub>2</sub>O<sub>2</sub>[83]. ESR was essential in the study of the field dependence of the compound: measuring around a critical transition and establishing a spin gap of 1.4 meV in zero field. It helped establishing a comprehensive model for magnons in the system.

## 6.2 Muon Spin Rotation

The idea behind muon spin rotation, also called  $\mu$ SR is to take advantage of the muon that, once implanted in a sample, has a spin rotating around the local fields present in the compound. Certain figures in this work are inspired from a book by prof. Blundell[84]. The muons can be implanted into a sample, they are stopped easily by matter, so the thickness of the sample plays an important role in the experiments. The muon has a magnetic moment antiparallel to its momentum and decays radioactively with a lifetime of  $2.2 \mu\text{s}$ . Muons are typically produced by the following process: a high energy proton beam collides onto a graphite target. A wide variety of reactions between the incoming protons and the target produce pions[85], as shown in equation (6.8).



Such pions decay into a muon and a neutrino, through equation (6.9). This pion has a lifetime of 27 ns.



The obtained muon can be collected and guided towards the sample, thanks to the regular combination of dipolar and quadrupolar magnets. While penetrating into a sample, the muon loses kinetic energy in less than a tenth of a nanosecond and settles in interstitial sites. The precise knowledge of the so-called muon stopping sites is a whole field of research in itself, and can involve a lot of computations, using Density Functional theory (DFT)[86]. In order to investigate thin films, several facilities offer a low energy muons option, providing muons[87] of energy comprised between 0.5 and 30 keV allowing to investigate 1-300 nm thin films[88, 89, 90], rather than millimeter thick samples.

The muon has a mass and magnetic moment between that of the proton and that of the electron, its gyromagnetic ratio is 13.5 kHz/G. This value has to be compared to 2800 and 4.26 for the electron and proton respectively. This gives  $\mu$ SR experiments a great sensitivity to low magnetic moments, smaller than one Bohr magneton, and access to a fluctuation window of  $10^{-5}$  to  $10^{-11}$  seconds. The muons implanted in a sample share the same momentum direction and decay radioactively into a positron and two neutrinos, as shown in equation

(6.10).



The muon decays on average at the end of its lifetime and the products of its decay can be detected. In practice, it is very hard to measure neutrinos in conventional detectors since they interact very weakly with matter, but it is quite easy to detect positrons. The decay is heavily non anisotropic, as represented in Fig. 6.3.

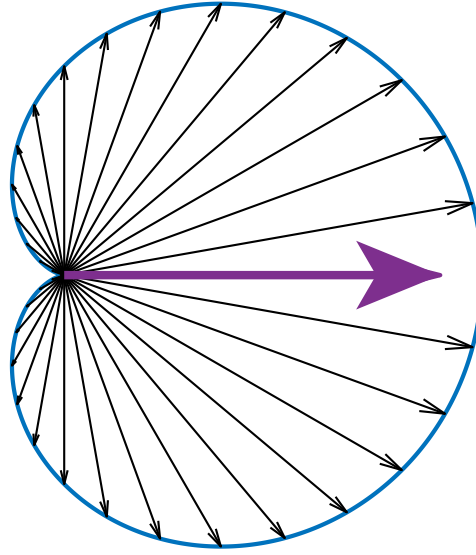


Figure 6.3: Muon decay: positron emission direction underlying the asymmetry. The purple arrow describes the muon spin direction and the black arrows the possible emitted positrons.

The positrons are in majority emitted in the direction of the muon spin (antiparallel to its momentum). In the presence of any magnetic field, applied or internal, the spin of the muon precesses with a characteristic frequency proportional to the gyromagnetic ratio  $\gamma_\mu$  as stated in equation (6.11), where B is the magnetic field.

$$f = \frac{\gamma_\mu}{2\pi} B\tag{6.11}$$

One can thus place detectors, labeled forward and backward, with respect to the initial muon momentum, and define the asymmetry function as in equation (6.12), where t is the time,  $N_B$  the number of positrons collected in the backward detector, and  $N_F$  the number of positrons

collected in the forward detector.  $A$  is the total asymmetry.

$$A(t) = \frac{N_B(t) - N_F(t)}{N_B(t) + N_F(t)} \quad (6.12)$$

As a function of time, the number of detected positrons decays with time, but since the total asymmetry is normalised, it is expected to oscillate. The positron counts in any detector globally decays exponentially. Due to the anisotropic decay of the muon, more positrons are detected by the detector in the direction in which points the spin of the muon.

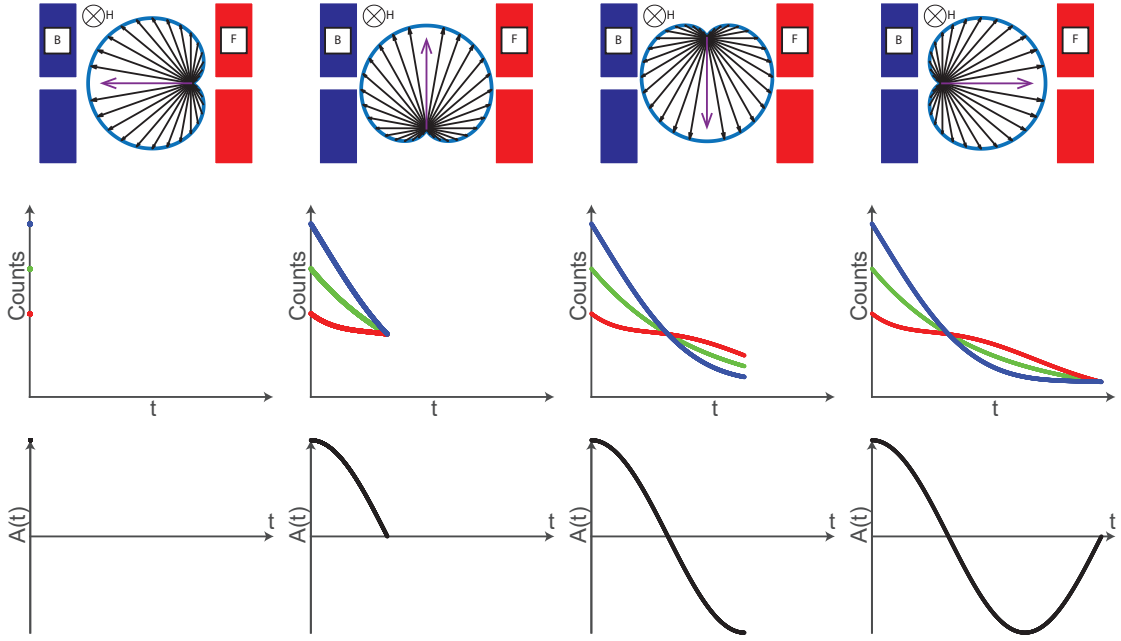


Figure 6.4: Rotation of a muon spin in a magnetic field  $H$ . The forward and backward detector are shown on the second line. The third line shows the asymmetry in function of time.

Fig. 6.4 underlines the idea behind a  $\mu$ SR measurement. In a first step the muon is implanted in the sample and reaches a stopping site, at  $t = 0$ . Due to the presence of a field, its spin rotates. After some time, given on average by the muon lifetime, the muon decays into a positron, measured by the detector. This is a statistical process which is repeated for all muons directed at the sample. When a muon decays with its spin perpendicular to its initial direction, both forward and backwards detectors record a positron with the same probability. If the muon is given enough time to rotate 180 degrees, then the forward detectors record more positrons than the backward one. Globally, the total number of measured positrons decays exponentially, due to the exponential decay of the muon. The asymmetry function is normalized and thus theoretically oscillates as a cosine function (Fig. 6.4, third row). The measured signal,  $G$ , is given by equation (6.13).

$$G(t) = \frac{1}{3} + \frac{2}{3} \cos(\gamma_\mu B t) \quad (6.13)$$

This is the case when a single field is dominant in a system, and equation (6.13) models what



happens in a real material, when applying a field larger than all other relevant fields in a given sample. When no external field is applied, a wide variety of internal fields can combine effects. Indeed, each nuclear spin has a moment, creating a small field with arbitrary direction in which implanted muons can precess. A very small external magnetic field of a couple of Gauss is sufficient to quench these internal fields but their effect is worth mentioning, even from a pedagogical point of view. Indeed, since muons stop at different sites, muSR is greatly sensitive to local environments. In magnetically long range ordered systems, several magnetic atoms can create different local fields, depending on the magnetic structure. For instance, a ferromagnet creates a rather homogeneous field, while a helicoidal structure results in many different fields. The total measured signal is a combination of all these contributions from individual fields. Since the measured signal for one field is a cosine with frequency proportional to the field, the sum of signals presented in Fig. 6.5 is acquired. In that figure, one can observe a superposition of oscillating curves with many different oscillating frequencies, corresponding to the different local fields present in the sample.

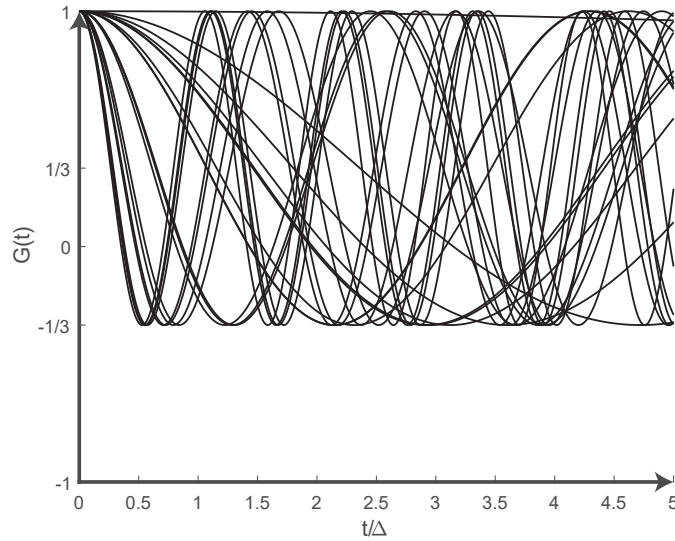


Figure 6.5: Overlay of muon asymmetries for a Gaussian distribution of local fields.

In the specific case of a field taking values according to a Gaussian distribution, the total signal takes the form of the Kubo-Toyabe function stated in equation (6.14). The static Kubo-Toyabe function is represented in Fig. 6.6. The function starts from its maximum and then rapidly decreases to reach its minimum at time  $t = \sqrt{3}/\Delta$ , where  $\Delta/\gamma_\mu$  is the standard deviation of the distribution of fields.

Such a behavior had been measured for example in skyrmion compound MnSi[91], and also the heavy fermion system with non-Fermi-liquid behavior CeCu<sub>5.9</sub>Au<sub>0.1</sub> [92]. This shape can be

understood as coming from the fact that, while many different cosine functions are combined with different frequencies, they all share the same phase, so the limit for small times converges to 1, while the limit for large times averages to a finite value.

$$G(t) = \frac{1}{3} + \frac{2}{3} (1 - \Delta^2 t^2) \exp(-\Delta^2 t^2 / 2) \quad (6.14)$$

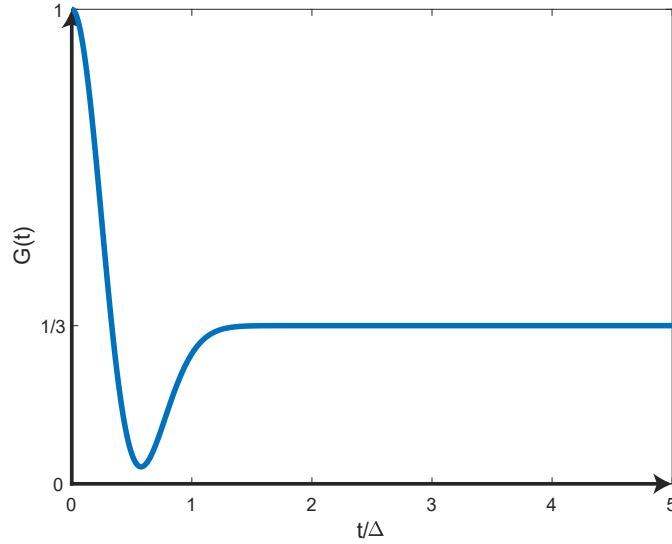


Figure 6.6: Kubo-Toyabe curve arising from a normal distribution of static fields, normally distributed around zero, with standard deviation  $\Delta/\gamma_\mu$ .

The Kubo-Toyabe distribution describes the case of muons stopping in an environment of normally distributed fields, with an average of zero field. The distribution of fields can however be different, and may for example follow a Lorentzian distribution, rather than a normal distribution. The distribution can even be some mixture of Gaussian and Lorentzian. This gave rise to the stretched exponential Kubo-Toyabe function given in equation (6.15), where  $\beta$  corresponds to the stretching exponent. If  $\beta = 1$ , the distribution is purely Lorentzian, and purely Gaussian if  $\beta = 2$ .

$$G(t) = \frac{1}{3} + \frac{2}{3} \left(1 - (\lambda t)^\beta\right) \exp\left(-\frac{(\lambda t)^\beta}{\beta}\right) \quad (6.15)$$

In magnetically ordered systems, the average magnetic field,  $B_L$  is typically finite. The behavior of the observed asymmetry is more complex and presented in Fig. 6.7, in function of the ratio of the field strength divided by the distribution width. For high values of fields, the long time limit averages to one, significantly different from the 1/3 value characteristic of the zero-field Kubo-Toyabe limit.

Unlike zero kelvin moments, which can only experience quantum fluctuations, at finite temperature, in almost every system the spins experience at least thermal fluctuations. Depending

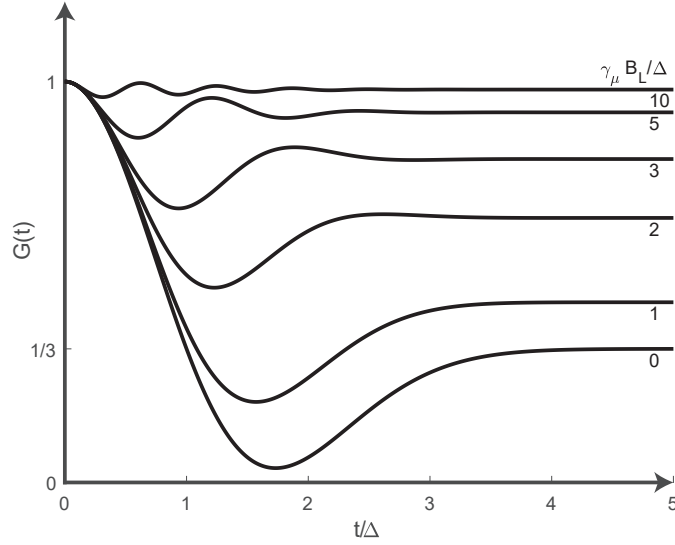


Figure 6.7: Kubo-Toyabe distribution for gaussian-distributed field with center  $B_L$  and standard deviation  $\Delta/\gamma_\mu$ . The shape of the function depends on the ratio  $\gamma_\mu B/\Delta$ .

on how the fluctuations are occurring (time scale and distribution), a very different asymmetry can be measured. In the strong collision approximation, it is assumed that the field changes its magnitude and orientation with a fluctuation rate  $\nu$ : after "collision", the new field is arbitrarily chosen from a probability distribution, completely disregarding its former state: this is a Markov process. A general equation for sufficiently fast fluctuations, when  $\nu > 3\Delta$  is given by equation (6.16) which is the so-called Abragam formula in zero field.

$$G(t) = \exp \left( -2 \frac{\Delta^2}{\nu^2} [\exp(-\nu t) - 1 + \nu t] \right) \quad (6.16)$$

In the quasi-static limit, where  $\nu \ll \Delta$ , the asymmetry takes the form given in equation (6.17).

$$G(t) = \frac{1}{3} \exp \left( -\frac{2}{3} \nu t \right) + \frac{2}{3} (1 - \Delta^2 t^2) \exp \left( -\frac{\Delta^2 t^2}{2} \right) \quad (6.17)$$

In resonance techniques, the notion of motional narrowing is important. The muons spins rotate in the local fields. These fields can be very inhomogeneous and vary from point to point creating a finite range of oscillating frequencies. Diffusing entities in this scheme then feel lower variations of the fields than if they were stationary (due to the central limit theorem): this phenomenon is called motional narrowing. For a Gaussian distribution of fields, in the extreme motional narrowing limit, the asymmetry can be described by equation (6.18).

$$G(t) = \exp\left(-\frac{2\sigma^2}{\nu} t\right) \quad (6.18)$$

The quasi-static limit and the extreme motional narrowing limits are represented in Fig. 6.8. The extreme motional narrowing describes well the thermal fluctuations of magnetic spins in paramagnetic samples.

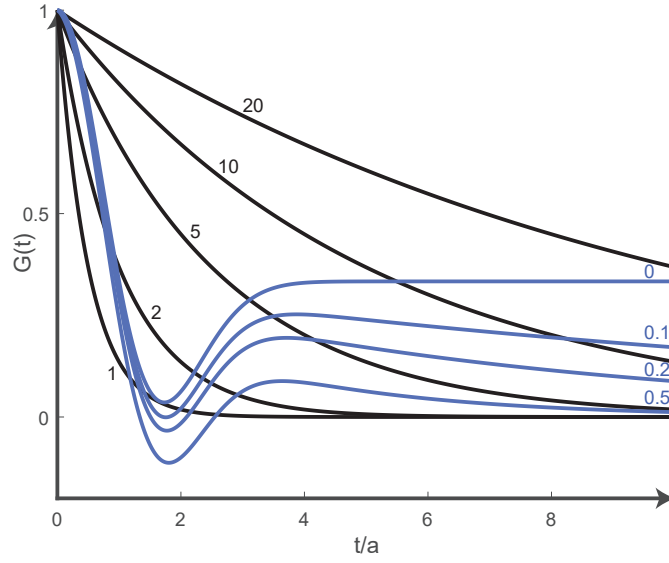


Figure 6.8: Extreme motional narrowing (in black) and quasi-static limit (blue) asymmetries. The numbers are indicating values of the  $\nu/\Delta$  ratio, corresponding to the strength of the fluctuation rate, relative to the width of the (Gaussian) distribution of magnetic fields.

In real materials, these local fields can arise from either nuclear moments, as seen before, long range ordered moments, a dipolar or hyperfine field, or even a demagnetization field, an applied field or a combination of these. In practice the instruments are not always well calibrated, and a significant influence from sample environment, sample position, and detector efficiency can result in an experimental normalization factor,  $\alpha$  that enters calculations as in equation (6.19), with  $\alpha \neq 1$ . The proper value of alpha is determined at the beginning of each experiment by applying a large transverse field.

$$G(t) = \frac{N_F - \alpha N_B}{N_F + \alpha N_B} \quad (6.19)$$

It was mentioned that  $\mu$ SR has been used to measure the relaxation of MnSi[91], and that a gaussian distribution of field was believed to be found to be responsible for the Kubo-

Toyabe-like observed behavior of the asymmetry, similar to  $\text{CeCu}_{5.9}\text{Au}_{0.1}$  [92]. Researchers managed to track the oscillating signal in ferromagnet  $\beta\text{-UB}_2\text{C}$  [93] and study the criticality in the system from the muSR data. Another example of useful information that can be obtained from muSR data concerns superconductivity: in a type II superconductor it is possible to obtain the London penetration depth from muSR measurements [94]. Muons spectroscopy is a probe extremely sensitive to local fields and can be used to unveil a subtle transition from 2D magnetic order to 3D magnetic order [95], or conversely to help to resolve the absence of magnetic long range order [62] and try and reconcile observations of spin liquid behavior in Kagomé compound Herbertsmithite.

## 7 X-ray techniques

X-ray techniques group the set of measurements that are performed with photons on samples. Several techniques are quite useful for basic characterization of samples: purity assessment, determination of number of phases, crystal orientation, twinning, while others give deep insight on the nature of the compound: space group determination, lattice parameters, atomic positions, strain and stress, particle size, and so on. The most basic structural properties of a compound can be established from X-ray diffraction of a powder sample. In the frame of quantum magnetism, where one wants to measure direction-dependent properties on a large single crystal, or a co-alignment of single crystals, using neutron scattering, it is quite common to use a Laue diffractometer in combination with a single crystal diffractometer, in order to fully characterize the orientation of the crystals beforehand.

## 7.1 Basic elements of X-ray diffraction

The whole idea behind X-ray diffraction comes from the Bragg's law[96]. A crystalline compound is made of lattice planes and an incoming X-ray, pictured as a wave, scatters on the sample.

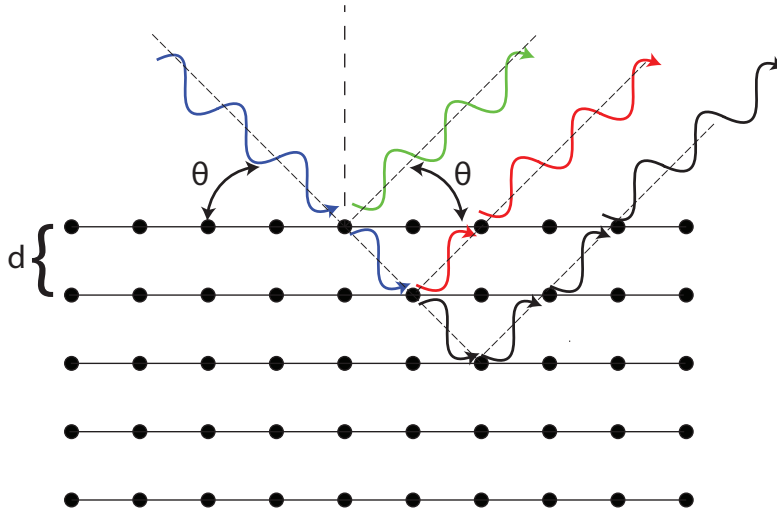


Figure 7.1: Incoming wave diffracting on an atomic lattice. Part of the wave is reflected (green) and part of it is transmitted (black). The transmitted wave in turn transmits and reflects on the next atomic plane. The diffraction angle,  $\theta$  is indicated.

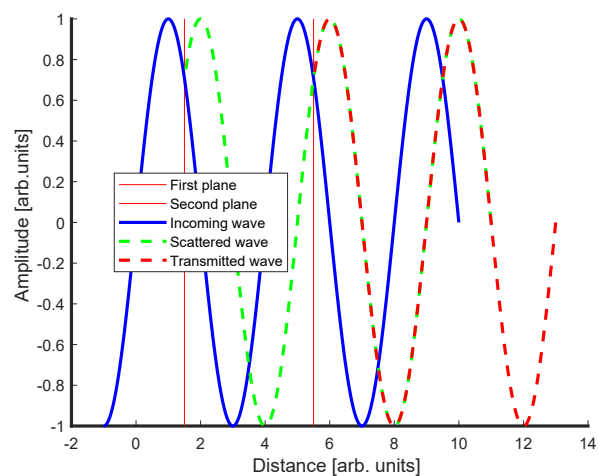
Fig. 7.1 shows a typical diffraction configuration. Lattice planes are separated by a given distance  $d$ . The incoming wave is characterized by an angle  $\theta$ , and the outgoing wave is scattered at the same angle. Part of the incoming wave is transmitted, while the other is scattered. This process repeats for the scattered wave. Depending on the incoming wave angle  $\theta$ , the phase difference in the outgoing waves may create constructive, destructive or no interferences. This is the essence of Bragg's law stated in equation (7.1), which stipulates that if the difference of optical paths between waves is a multiple of the wavelength, a constructive interference, i.e., a peak, is measured.

$$2d \sin \theta = n\lambda \quad (7.1)$$

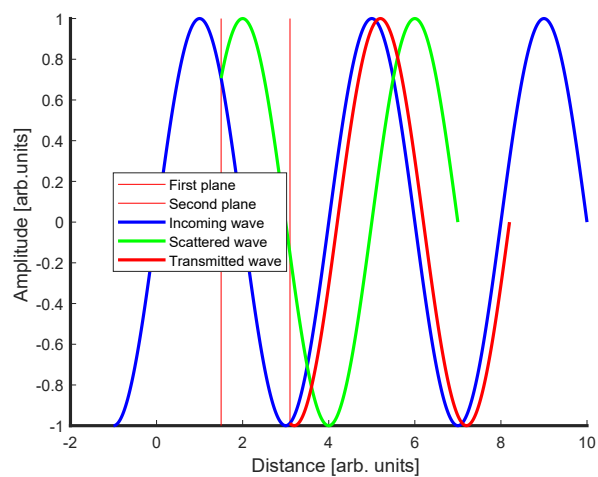
This behavior is illustrated in Fig. 7.2. This figure shows two examples: Fig. 7.2a shows the case where the optical path is proportional to the frequency of the wave, and Fig. 7.2b the case where it is not. In both cases, the incoming wave is shown in blue, and the first vertical red line corresponds to the first lattice plane. Part of the wave is scattered, with a phase shift, shown in green, and part of it is transmitted, without any phase shift, shown in blue. The same process occurs at the next lattice plane. In the case the interlayer distance is fulfilling Bragg's condition, the phase change of the wave obtained from the scattering of the wave transmitted at the first lattice plane is such that it is constructively interfering with the first scattered wave,

as shown in Fig. 7.2a this is not the case if Bragg's condition is not fulfilled, as shown in Fig. 7.2b where the waves are out of phase. The total contribution to a detector comes from the contribution of a supposed infinite number of lattice planes. Each and every time a crystal satisfies Bragg's condition, a spike in the recorded intensity appears, indicating that a family of lattice planes is creating constructive interferences. The subtlety when doing crystallography is that these planes are actually made of any periodic unit, which can be atoms, but also whole unit cells: each dark spot in Fig. 7.1 does not necessarily represent a single given atom. Indeed, diffraction is the result of the scattering on a periodic object and it does not matter what are the inner constituents of this periodic object, at least not to when it comes to predicting peak positions. The arrangement of atoms within unit cells contributes to the intensity of the given reflection in the diffraction pattern. The position of the atoms within the unit cell contribute to the so-called structure factor of the peak, which is the main contribution to the intensity of measured peaks. The actual quantity describing the intensity of a given peak and is called the structure factor because it arises from the crystal structure of the compound. This quantity takes a slightly different form for neutrons and is discussed in more details and written explicitly in another chapter. The most important piece of information being that it is derived thanks to global translational symmetry, and depends mainly on atomic positions and atomic (thermal) displacements, due to phonons. Constructive and destructive waves may combine in a way that a peak associated to a certain family of lattice planes is forbidden (destructive interference) according to space group rules: this effect is called a systematic absence. A real measurement can be performed on either a powder or on single crystals. A powder consists in a collection of randomly oriented microscopic single crystals.





(a) Fulfilling Bragg's criteria: constructive interference.



(b) Not fulfilling Bragg's criteria: no constructive interference.

Figure 7.2: Interference between transmitted and scattered wave with Bragg's condition being fulfilled or not.

Since the wave picture has been introduced for the X-ray photons, it is worth mentioning the definition of the scattering vector. The incoming wave can be represented by a wave vector  $k_i$  of length  $2\pi/\lambda_i$  and the outgoing wave by a wave vector  $k_f$ , with  $Q = k_f - k_i$  the scattering vector. Such a vector can be seen in Fig. 7.3.

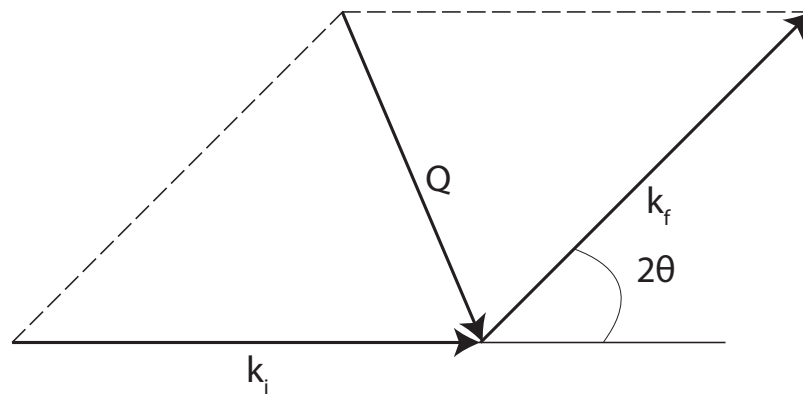


Figure 7.3: Definition of the scattering vector  $Q$ , in terms of incoming and outgoing wave vectors,  $k_i$  and  $k_f$ .

## 7.2 Powder X-ray diffraction

In the field of quantum magnetism, large single crystals are often required, as the neutron scattering cross section is small and the measurement of a signal with good statistics needs a significant counting time. However, for many different compounds, obtaining a high quality powder is a prerequisite to the growth of single crystals[97], and quite often, obtaining single crystals proves to be experimentally challenging and impossible. Hopefully this does not preclude from studying novel materials, since a lot of information can be extracted from powder measurements. Most of the information that can be extracted relies on the powder averaging principle. High quality powders are produced from polycrystalline materials which are then grained into powders. The powder grown by various methods can contain grains of different size which would create anomalies in the measurements. This is why when preparing a sample, unless measuring nanoparticles, one grinds in a mortar the result of a growth process. In some cases and to guarantee purity of the sample, the powder may be obtained from grinding large single crystals. Once a homogeneous powder is obtained, it can be reasonably assumed that the measured substance contains an arbitrary large number of crystallites, and that every crystalline orientation is represented.

The powder can be placed in a capillary, or layed down on a flat surface, typically a glass plate, giving low, amorphous background. If air or water sensitive, the capillary can be sealed, or the sample embedded in grease, preventing contact with air, and contributing to the signal in low amounts. Temperature control of the sample stage is usually ensured by a nitrogen jet, down to 80 K, or a Helium jet, down to 5 K. Due to the fact that X-rays do not penetrate deeply into matter, it is hard experimentally to measure below 5 K, and not typically available. Indeed, most sample environments require bulky sub-parts.

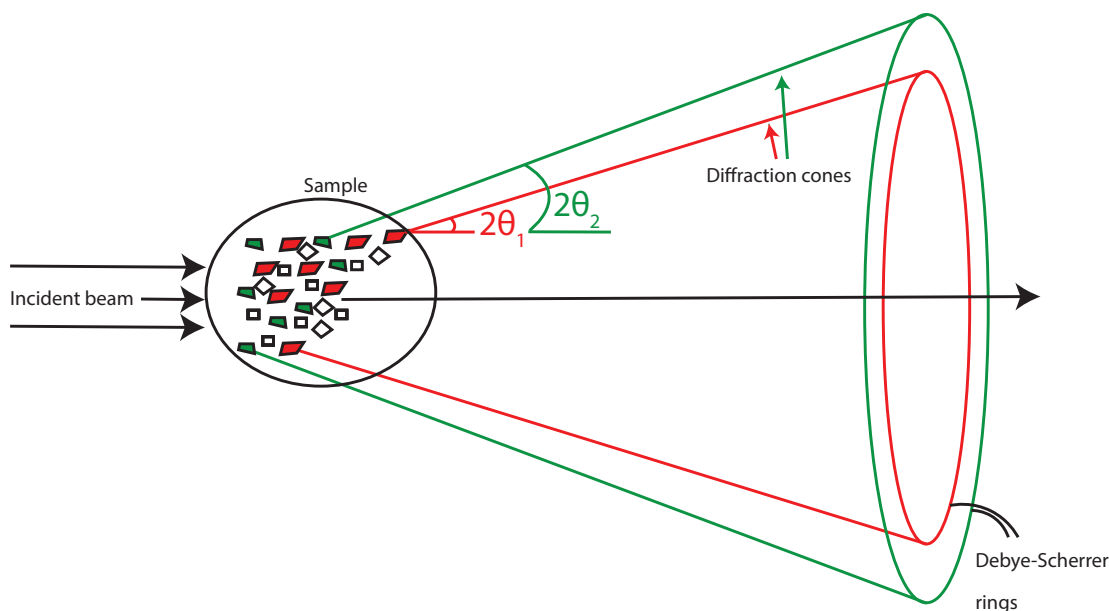


Figure 7.4: Incoming X-ray beam scattering on a polycrystalline sample. Several crystalline orientations correspond to different two theta angles. This creates Debye-Scherrer cones.

Fig. 7.4 shows how Debye-Scherrer cones are created. When the incoming beam hits the sample, X-ray get scattered. Since many crystallites are fulfilling Bragg's equation for different angles, a cone of scattering opens up, with angle associated to the  $2\theta$  of each crystallite. These cones intersect a 1D detector as lines or a flat 2D detector as circles. The radius of these circles can then be directly linked to the d-spacing of the associated lattice plane family.

There exists two ways of producing X-rays for such scattering experiments. The most common way is with an X-ray tube. This presents the advantage of being available for in-house X-ray sources and setups. However, since this type of X-ray production is based on the transition-emission lines of an element, typically copper, it is quite frequent to have an incoming beam containing photons of different wavelengths. The functioning principle of a typical laboratory X-ray source can be seen in Fig. 7.5.

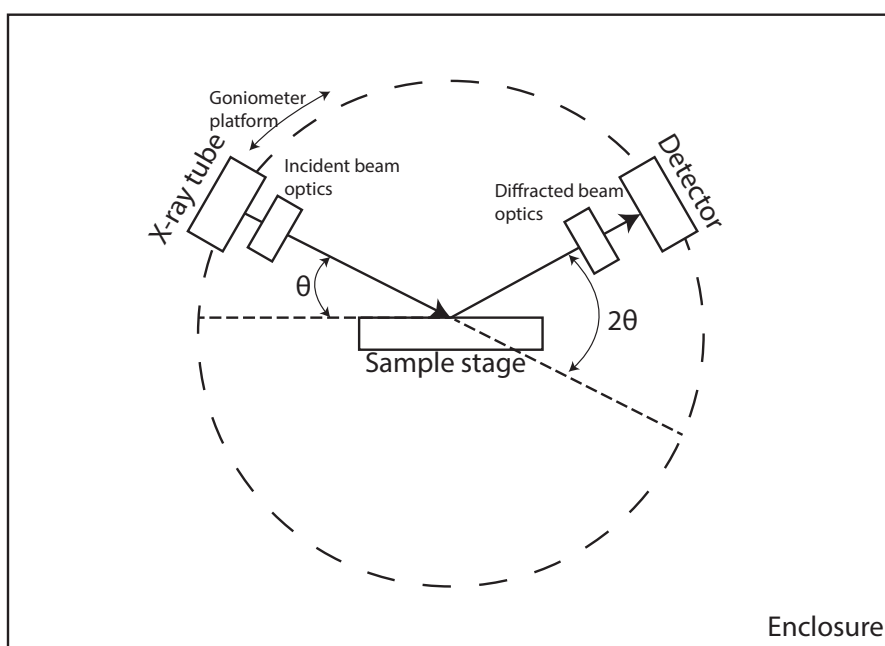


Figure 7.5: X-ray tube, incident and diffracted beam optics, detector, and sample stage. The sample stage is fixed, while a goniometer platform rotates both the source and the detector.

The source is a X-ray tube, that can be rotated around the sample stage thanks to a goniometer platform. The detector is also mobile. Both incident and diffracted beam paths can be equipped with various optical elements. These include a monochromator, divergence slits, a beam attenuator, beam masks, anti scatter slits, Soller slits and collimators.

Another way of obtaining an X-ray beam is from a synchrotron: electrons are accelerated up to 99.9% the speed of light. When deflected by a magnetic field, the electron will adopt a curved trajectory and emit X-rays. After passing through the beam-line optics, these X-rays are used to measure X-ray diffraction (and other types of X-ray scattering) on samples.

The collected pattern contains information on the crystal structure and on the atomic placement, and is convoluted to an instrumental resolution that broadens peaks. In order to refine and fit an atomic model to the data, one typically uses a software, of which the Fullprof suite[98] is a good example. In a few words, one can mainly perform two tasks. The first one is called a LeBail fit[99] (LBF). All structural information embedded in the peak intensity is discarded. The only relevant information that is kept is the peak position. With the known space group, the unit cell parameters and profile parameters are refined to match the measured powder diffraction pattern. A more advanced method available in the Fullprof suite deals with the determination of atomic positions and is the so-called Rietveld refinement[100]. The method consists in simulating the diffractogram from a crystalline model of the sample. The model takes into account various parameters such as: instrumental peak shape, crystal structure, atomic positions within the unit cell, absorption coefficients, preferred orientation, and so on. Once all the desired parameters have been selected, a fitting is performed, with a weighted reliability factor, defined as in equation (7.2), where  $w_i$  is the weight of the  $i$ th measurement, and  $I_i^{\text{exp}}$  and  $I_i^{\text{cal}}$  the measured and calculated intensities.

$$R_{\text{wp}} = \sqrt{\frac{\sum_i w_i (I_i^{\text{exp}} - I_i^{\text{cal}})^2}{\sum_i w_i I_i^{\text{exp}^2}}} \quad (7.2)$$

$R_{\text{wp}}$  corresponds to a weighted reliability factor that compares the difference between the modeled and measured data. For a perfect simulation the reliability still depends on the signal to noise ratio. One can determine the minimum of the reliability factor,  $R_0$ , with the ratio  $R_{\text{wp}}/R_0$  going to one.

A typical example of this analysis can be seen in a copper based system[39], where the authors measured synchrotron powder diffraction and could track the evolution of lattice parameters with temperatures. The observed regular lattice contraction down to a temperature of 50 K. The system undergoes a magnetic transition to a state with long range order at 20 K. They successfully used the LeBail method to keep track of the magnetic effects on the lattice close to 20 K: magnetic order, which sets in, affects the position of the atoms and a weak, but clear, magnetostriction was reported. In some other cases, it can lead to even more remarkable macroscopic properties. This phenomenon has indeed been observed in the frame of multiferroic compounds: in orthorhombic manganites[101] a colossal magnetostriction effect was observed and correlated to a finite polarization of the sample.

### 7.3 Single crystal X-ray diffractometer

If single crystals of a given compound are available, measuring X-ray scattering on single crystal often provides more insight on the crystalline symmetries than measuring on powder. Equivalent reflections can be collected and consistency checks between them can be performed. Modern single crystal diffractometers are equipped with lights and rotating stages, and enable to fully resolve the morphology of a given crystal. This provides a method far more unequivocal and consistent than using a Laue diffractometer (described in the next section). A picture of a single crystal diffractometer can be seen in Fig. 7.6.

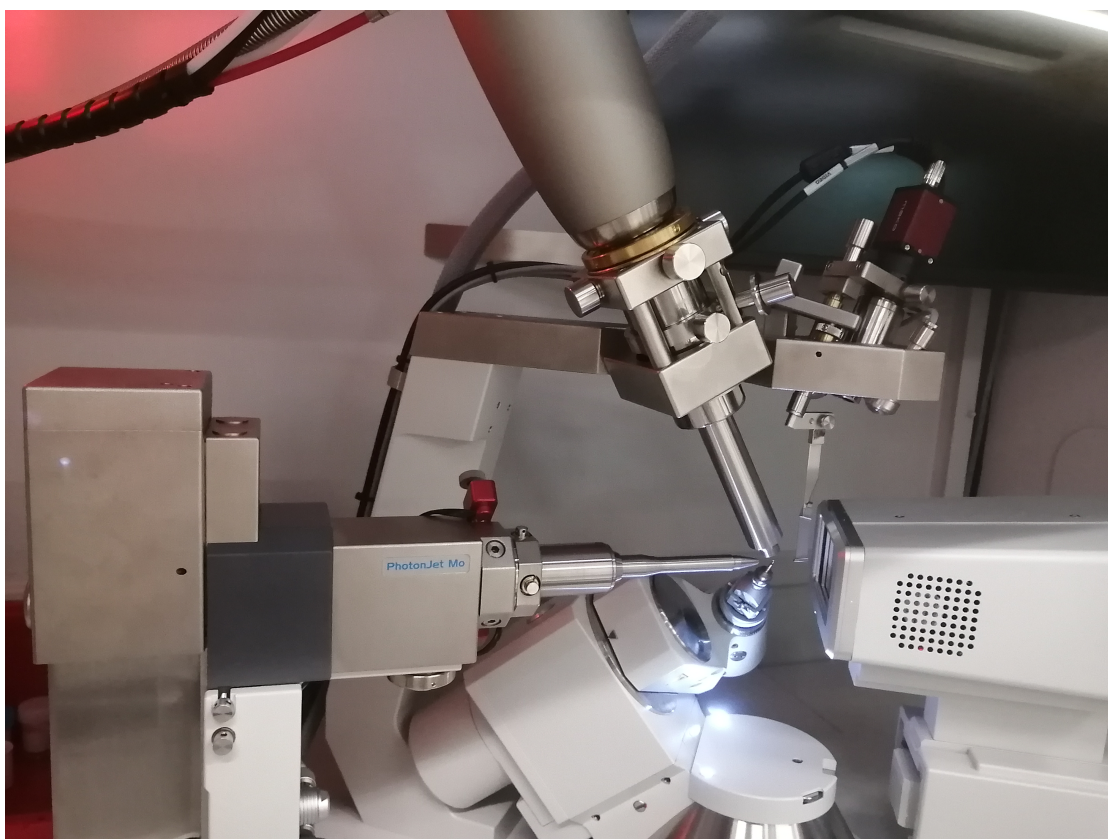


Figure 7.6: X-ray tube, collimator, nitrogen jet, sample goniometer and detector.

On the left hand side, encapsulated in a metal frame, stands a molybdenum tube which is the X-ray source. The beam is directed towards the right hand side and goes through a collimator. The other metallic tube is guiding nitrogen to cool the sample to the desired temperature, down to a base temperature of 80 K. The sample is glued on a pin, typically with plasticine. A very thin beam stop ensures that the incoming beam does not damage the detector, without losing too many scattered photons. The crystal and detector can be both rotated, allowing for the collection of multiple configurations, necessary step to properly refine the crystal structure of a compound, including all the atomic positions. Indeed, many compounds contain tens of

inequivalent atomic positions, which generates many inequivalent positional and thermal parameters that have to be refined. Having a large number of independent measured quantities is thus paramount to obtain publication quality results. Quite frequently however, when a compound is already quite well known, the precise knowledge of the inner structure of the unit cell is not desired anymore. A popular goal for an experiment is thus the determination of the morphology of a crystal. Many crystals naturally present facets, the knowledge of the orientation of a crystal is the first step of the measurement of a direction-dependent physical quantity. Fig. 7.7. present the results of a morphology identification of a  $\text{K}_2\text{Ni}_2(\text{SO}_4)_3$  crystal.

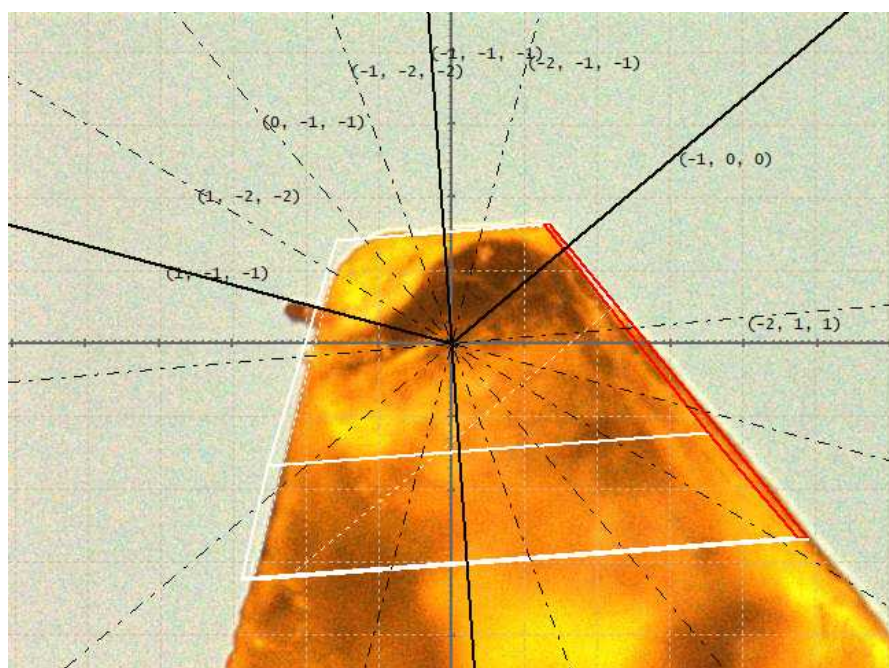


Figure 7.7: Facet identification of a  $\text{K}_2\text{Ni}_2(\text{SO}_4)_3$  crystal.

After having collected about 200 images by rotating the sample, the unit cell of this specific  $\text{K}_2\text{Ni}_2(\text{SO}_4)_3$  crystal could be reconstructed. Moreover, the knowledge of the relative angles allowed to additionally identify clear facets and assign them simple Miller indices. The  $(\bar{1}00)$  facet and the  $(1\bar{1}\bar{1})$  are both having their normal vectors in the plane of the picture, and, as theoretically predicted, differ by an angle of  $125^\circ$ . Many other facets have been spotted, as indicated directly on the figure. In several different cases the indexing process gives unreliable results: for example in the case of an orthorhombic space group with lattice parameters barely different from one another. In some other cases, the crystal cannot be detached from its holder, and the diffractometer can then not be used at all. In such cases, the use of a complimentary tool, a Laue diffractometer, proves to be extremely efficient.



## 7.4 Laue diffractometer

The Laue diffraction is a method that consists in obtaining diffraction images from a white beam of either X-rays or neutrons, scattered on a non moving single crystal. For practical purposes: flux (X-rays are easier to generate), and safety (neutrons are hard to stop), X-rays Laue instruments are more widespread, since they can be installed in a regular laboratory. The white beam of X-rays contains photons with a wide range of wavelengths. This beam is typically generated by a tube on which a certain voltage and current are applied. An example of choice in the Laue diffractometer at EPFL are tungsten tube on which is applied a voltage of 40 kV and a current of 10 mA. Quite naturally many settings exist depending on the machine and objectives. The electrons are decelerating on the anode and produce photons through Bremsstrahlung. Synchrotron photons can even go beyond the X-ray range, providing an even wider range of available wavelengths.

The detectors are two-dimensional, and can be either a CCD detector, or an image plate (stimulated photoluminescence). Two configurations are possible: transmission and reflection. In the transmission geometry, the measured signal comes from photons transmitted through the sample, while in the reflection geometry, the measurement comes from backscattered X-rays. The advantage of using the reflection geometry is that since X-rays interact strongly with matter, it is more suited for large single crystals. Scattering in the Laue geometry may be considered as represented in Fig. 7.3. The method consists in considering only elastic processes, meaning that  $k_i$  and  $k_f$  have the same norm. The direction in which the scattered photons interact constructively are given by the Laue condition: the scattering vector has to coincide with a reciprocal lattice node. The possible outgoing wave vectors thus form a sphere of radius  $2\pi/\lambda$ , called the Ewald sphere. Since the crystal is not moving, the reciprocal lattice points are also fixed, and it is convenient to think of potential scattering as the locus of the tip of the scattering vector  $Q$ . By taking into account all the different wavelengths in the incoming white beam, a family of Ewald spheres have to be used to satisfy the Laue condition. All the reciprocal lattice points in that sphere can thus be reached and appear in the measured diffraction pattern. Once a pattern is measured, a typical way of analyzing the image is by comparison to a well known, generated pattern. Several softwares allow to do this, including OrientExpress and QLaue.

Fig. 7.8 shows an example of how to use Laue measurements, QLaue, and what information can be extracted from it. The figure shows in black and white the acquired Laue pattern of a specific crystal orientation of  $\text{Cu}_2\text{OSO}_4$ , a monoclinic system. The blue dots correspond to the pattern calculated by the software. Since the theoretical pattern matches the measured one, it can be concluded that the facet perpendicular to the beam (referred to as "X axis") is the (001) facet. Moreover, the horizontal axis can be identified as the [0 -1 0] direction. This work is paramount for neutron scattering spectroscopic studies where, most of the time, the limiting factor is the mass of the sample, directly proportional to the measurement time. Knowing the morphology of crystals of the same compound enables to create co-alignments made



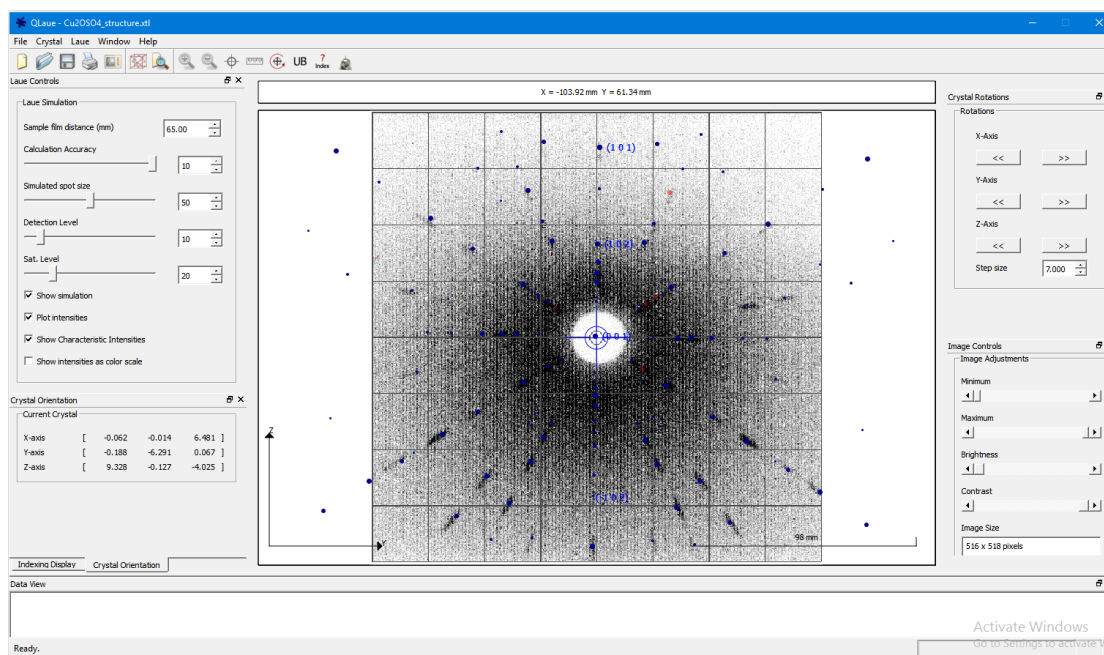


Figure 7.8: Laue pattern imported in QLaue: identifying crystal facets.

of several distinct crystals glued on the same support and aligned together with a similar orientation in order to create an higher effective mass than that of individual crystals, playing a key role in reducing measurement time. A picture of such a co-alignment can be seen in Fig. 7.9, where a set of five crystals of  $\text{Cu}_2\text{OSO}_4$  were co-aligned, to provide a sample with total mass of 747 mg, whereas the biggest crystal was weighing 175 mg.



Figure 7.9: Co-alignment of crystals of  $\text{Cu}_2\text{OSO}_4$ . The crystals (in black) are co-aligned on top of aluminum posts. The brass-made base encapsulates goniometers, whose screws enable for fine tuning of the each of the orientation of each crystal.

## 8 Neutron scattering techniques

### 8.1 Brief elements of scattering theory

The explanations on neutron scattering are based on a set of typewritten notes written by Prof. Kim Lefmann, distributed by Prof. Henrik M. Rønnow in the frame of one of his lectures on condensed matter physics. Neutrons are electrically neutral particles of the same mass as the proton, that interact weakly with matter. Since they are chargeless, they interact weakly with magnetic fields. A neutron however, does possess a magnetic moment[102], making it sensitive to the local magnetic moments present in typical condensed matter systems, as shown in equation (8.1).

$$\mu_n = -\gamma_n \mu_N \quad (8.1)$$

Where  $\gamma_n = -1.91 \text{ rad s}^{-1} \text{ T}^{-1}$  is the gyromagnetic ratio of the neutron, and  $\mu_N = 5.05 \text{ J/T}$  the nuclear magneton. The fact that neutrons interact weakly with matter enables to perform perturbative expansion studies and obtain quantitative agreements between experiments and theory. On the contrary to X-rays, neutrons primarily interact with the nucleus, in a fashion that depends greatly on the details of the content on the nucleus. In that aspect, neutron present the great advantage over X-rays that they are able to resolve light elements, like hydrogen, even when placed close to heavy elements, for example uranium. The probability of interaction of a neutron with a nucleus also presents an isotopic effect[103]. The neutron has a magnetic moment of a spin half, antiparallel to its nuclear spin. Unlike the neutron-nucleus interaction which is mediated by the nuclear force, the interaction of neutrons with the electronic clouds is a process involving the electromagnetic force, and is less significant. This is why the magnetic signal obtained from neutron scattering is in many cases far less strong than the one obtained from nuclear scattering. There are roughly five main reasons why neutrons are a very interesting tool to probe solid state systems:

- They are useful to study *magnetism* in great details, with the full power of potential polarization analysis.
- Thermal neutrons are produced at an *energy* of 25 meV, that is perfectly suited to study

with sufficient resolution crystal structures and their excitations.

- They are enabling *quantitative* comparisons between experiments and theory.
- They are penetrating matter easily, and thus it is possible to study samples in *extreme conditions*: very low temperatures (millikelvin), high magnetic fields (several to tens of Teslas), and high pressures (several gigapascals).
- *Isotopes* of the same atom present very different neutron scattering interactions. For example, naturally abundant boron absorb neutrons, but it is quite easy, even though expensive, to simply isotopically replace the natural boron with another isotope, not absorbing. Moreover, since different isotopes scatter neutrons very differently, this also opened up the idea of using isotopic replacements as markers, as has been performed with deuterium-hydrogen substitution. Additionally, light atoms in crystal structures can be resolved, even when mixed with other heavy atoms.

The neutron behaves as any other particle, and in particular, can be considered in the particle-wave duality realm. The neutron is a particle that can be considered as a propagating plane wave, with a certain wavelength. The relation between its wavelength and energy is given in equation (8.2).

$$\lambda = \frac{2\pi\hbar}{mv} \quad (8.2)$$

Since most physical processes happen in the reciprocal space, it is also quite convenient to define the neutron wave number,  $k$ , by  $k = 2\pi/\lambda$ , with  $E = \frac{\hbar k^2}{2m}$ . When plugging the actual numbers of the Planck constant, and the neutron mass, the following constants appear:  $E[\text{meV}] = 2.072 k^2$ ,  $k$  in [ $\text{\AA}^{-1}$ ] and  $E[\text{meV}] = 81.81 / \lambda^2$ ,  $\lambda$  in [ $\text{\AA}$ ]. The study of neutron scattering requires a bit of terminology. The first important notion is that of the cross section, usually noted  $\sigma$ , defined in equation (8.3)

$$\sigma = \frac{\text{surface perpendicular to beam direction} \cdot \# \text{ of scattered neutrons per second}}{\# \text{ of incoming neutrons on a surface per second}} \quad (8.3)$$

The cross section naturally describes how well a given sample scatters neutrons, and its unit is that of an area. When performing condensed matter physics experiments, recording the energy and direction of the outgoing neutrons is paramount. This induces the need for an angle-dependent and an energy difference-dependent cross section, namely the differential scattering cross section and the partial differential scattering cross section. The former is defined in equation (8.4) while the latter is defined in equation (8.5).

$$\frac{d\sigma}{d\Omega} = \frac{\text{surf. perp. to beam direction}}{\# \text{ of inc. neutrons on a surf. per sec.}} \cdot \frac{\# \text{ of scatt. neutrons per sec. in } d\Omega}{d\Omega} \quad (8.4)$$

$$\frac{d^2\sigma}{d\Omega dE_f} = \frac{\text{surf. perp. to beam direction}}{\# \text{ of inc. neutrons on a surf. per sec.}} \cdot \frac{\# \text{ of scatt. neutrons per sec. in } d\Omega \text{ with energy in } [E_f; E + dE_f]}{d\Omega dE_f} \quad (8.5)$$

When integrating over the whole solid angle, one recovers the full scattering cross section:  $\sigma = \int \frac{d\sigma}{d\Omega} d\Omega$ , and similarly:  $\frac{d\sigma}{d\Omega} = \int \frac{d^2\sigma}{d\Omega dE_f} dE_f$ . The processes considering only  $E_f = E_i$  is called elastic scattering, while the process that is the integral over all energy and retains only the angular dependence of the scattering, the differential scattering cross section, is called diffraction. There is a subtle difference between the two of them, even though the majority of the measured signal comes from nuclear scattering, even in diffraction.

In the wave picture, an incoming neutron is described by a wavefunction  $\psi_i$  given in equation (8.6), where  $A$  is a normalization constant, and  $\vec{k}_i$  the neutron wavenumber, related to its velocity by  $v = \frac{\hbar k_i}{m_n}$ .

$$\psi_i(\vec{r}) = \frac{1}{A} \exp(i\vec{k}_i \cdot \vec{r}) \quad (8.6)$$

When scattering on a single nucleus located at position  $\vec{r}_j$ , the outgoing neutron can be modeled by a spherical wave, with waveform given in equation 8.7.

$$\psi_i(\vec{r}) = \psi_i(\vec{r}_j) \frac{-b_j}{|\vec{r} - \vec{r}_j|} \exp(i\vec{k}_f \cdot |\vec{r} - \vec{r}_j|) \quad (8.7)$$

The quantity  $b_j$  has a unit of length, and is nucleus dependent, it is called the scattering length. In the specific case of elastic scattering, defined by  $|\vec{k}_i| = |\vec{k}_f|$ , it can be proven that  $\frac{d\sigma}{d\Omega} = b_j^2$  and thus that  $\sigma = 4\pi b_j^2$ .

The scattering from several nuclei, located at a set of positions  $\{\vec{r}_j\}$  results in the total differential cross section stated in equation 8.8, with  $\vec{q} = \vec{k}_i - \vec{k}_f$ , called the scattering vector. The final form comes from the interference between the scattered waves on each nuclei, a pictorial representation of vector  $\vec{q}$  is shown in Fig. 8.1. There is a debate in the community on the sign of the scattering vector. The chosen convention here is widely used by spectroscopists and slightly less popular among diffraction experts.

$$\left. \frac{d\sigma}{d\Omega} \right|_{\text{nucl}} = \left| \sum_j \exp(-2W_j) b_j \exp(i\vec{q} \cdot \vec{r}_j) \right|^2 \quad (8.8)$$

There is an additional term in equation (8.8),  $\exp(-2W_j)$ , called the Debye-Waller term. This term arises from the fact that atoms are actually moving due to phonons, and relates to the mean square atomic displacement:  $W_j = -\frac{1}{2} \langle \vec{q} \cdot \vec{u}_j \rangle$ , where  $\vec{u}_j$  is the displacement of atom at site  $j$ . Even though this displacement is related to phonons, it is non zero at low temperature

because of zero point fluctuations and evolves with temperature.

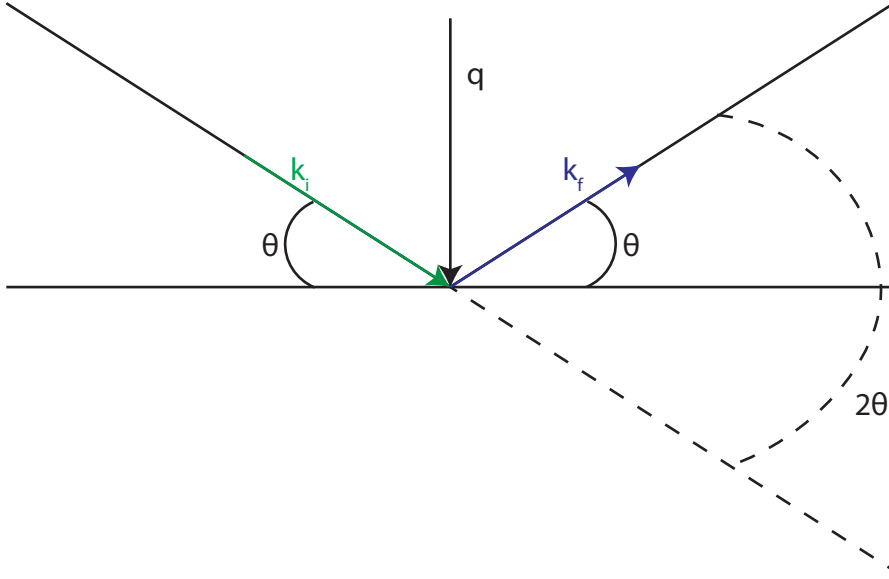


Figure 8.1: Definition of the scattering vector  $Q$ , in terms of incoming and outgoing wave vectors,  $k_i$  and  $k_f$ , the scattering angle,  $2\theta$  is indicated.

In the case of elastic scattering,  $||\vec{k}_i|| = ||\vec{k}_f|| := k$ . It entails, that  $||\vec{q}|| = 2k \sin(\theta)$ . This equation together with an additional equation  $q = 2\pi/d$  that holds information on the sample, form a set of equations that are equivalent to the Bragg equation for scattering. In a typical diffraction or elastic experiment, the use of  $\theta$  as a scattering variable is thus widespread. For inelastic processes, however, it is quite handy to add another quantity, the energy transfer, that directly relates to the change in energy between the incoming and outgoing neutron, and can be straightforwardly linked to the difference of the norms of their wavenumber, as shown in equation (8.9).

$$\Delta E = \hbar\omega = \frac{\hbar(k_i^2 - k_f^2)}{2m_n} \quad (8.9)$$

More details about inelastic scattering will be given in another section, treating the full quantum cross section of the scattering.

The nuclear spin of each nucleus can be varying with time, there can be also non negligible variations due to the fact that different isotopes of the same element are present in the sample, or because different elements are considered. This results in a static disorder responsible for the so-called incoherent scattering. It can be assumed that the scattering length at site  $j$  has a time dependent value,  $b_j = \langle b \rangle + \delta b_j$ , where  $\langle b \rangle$  is the average (stochastic) value of the scattering length and  $\delta b_j$  its variance. It is moreover assumed that the variation are not correlated between sites:  $\langle \delta b_i \delta b_j \rangle = 0$ ,  $i \neq j$ . The final result for the differential cross section is

given in equation (8.10), where  $\sigma_{\text{inc},i} = 4\pi \langle (\delta b)^2 \rangle$ .

$$\left\langle \frac{d\sigma}{d\Omega} \right\rangle = \frac{\sigma_{\text{inc},i} + \sigma_{\text{inc},j}}{4\pi} + |\langle b_i \rangle \exp(i\vec{q} \cdot \vec{r}_i) + \langle b_j \rangle \exp(i\vec{q} \cdot \vec{r}_j)|^2 \quad (8.10)$$

The so-called incoherent scattering appears to be direction-independent, and contributes in the form of a background at every angle, while the right hand-side term in equation (8.10) is angle dependent. The incoherent scattering is a considerable, atom dependent, source of background. While in many cases the scattering cross section is dominated by the coherent signal, it can happen, for example in the case of vanadium and hydrogen atoms, that the incoherent scattering is more intense than the coherent scattering. In the case of vanadium, the coherent scattering length is close to zero, effectively making it close to impossible to see Bragg peaks of pure vanadium. Importantly, samples (or glues) containing hydrogen are thus usually avoided (or deuterated) to get rid of this large background.

## 8.2 Quantum scattering processes

In order to grasp the effects of magnetic scattering, one has to go through the quantum mechanical treatment of the neutron scattering cross section, stated in equation (8.11), established thanks to the Fermi golden-rule[104].

$$\frac{d\sigma}{d\Omega} = Y^2 \frac{k_f}{k_i} \left( \frac{m_n}{2\pi\hbar^2} \right)^2 |\langle \psi_i | \hat{V} | \psi_f \rangle|^2 \quad (8.11)$$

Y is a normalization constant ensuring the plane waves are normalized, and operator V is the interaction potential, which can be describing nuclear as well as magnetic scattering. Nuclear scattering is described by the Fermi pseudo-potential[105] in equation (8.12).

$$\hat{V}(\vec{r}) = \sum_j \frac{2\pi\hbar^2}{m_n} b_j \delta(\vec{r} - \vec{r}_j) \quad (8.12)$$

In the case of inelastic scattering, the neutron can transfer energy to the sample. It is thus important to also consider initial (before the neutron hits) and final (once the neutron is scattered) sample states:  $|\lambda_i\rangle$ ,  $|\lambda_f\rangle$ . The suited cross section is the partial differential cross section, stated in equation (8.13).

$$\left. \frac{d^2\sigma}{d\Omega dE_f} \right|_{\lambda_i \rightarrow \lambda_f} = \frac{k_f}{k_i} \left( \frac{m_n}{2\pi\hbar^2} \right)^2 |\langle \lambda_i \psi_i | \hat{V} | \psi_f \lambda_f \rangle|^2 \delta(E_{\lambda_i} - E_{\lambda_f} + \hbar\omega) \quad (8.13)$$

### 8.2.1 Diffraction from a crystal

A crystal is described by a unit cell and a set of inequivalent atomic positions. The unit cell and lattice parameters describe how tessellation creates the whole lattice. The atomic positions

are the minimum set of parameters that one needs to describe the compound arrangement of atoms within the unit cell. In every case but in that of very low symmetry (triclinic space group  $P1$ ), the symmetry operators of a given space group generate more atoms than the number of inequivalent lattice positions. Each atomic position in a compound,  $\vec{r}_{i,j}$  can thus be described as the sum of a vector pointing to its unit cell,  $\vec{R}_i$  with another vector, describing the relative position in the unit cell,  $\vec{\Delta}_j$ :  $\vec{r}_{i,j} = \vec{R}_i + \vec{\Delta}_j$ . The translational symmetry enables us to rewrite the differential cross section to take this symmetry into account, as in equation (8.14).

$$\left. \frac{d\sigma}{d\Omega} \right|_{\text{nuc.el.}} = N \frac{(2\pi)^3}{V_0} \exp(-2W) |F_N(\vec{q})|^2 \sum_{\vec{\tau}} \delta(\vec{q} - \vec{\tau}) \quad (8.14)$$

Here  $\vec{\tau}$  is any reciprocal lattice vector, and  $F_N(\vec{q}) = \sum_i b_i \exp(i\vec{q} \cdot \vec{\Delta}_i)$  is the nuclear structure factor. Equation (8.14) encapsulates all the elements required to understand diffraction data. The last term,  $\delta(\vec{q} - \vec{\tau})$  is responsible for the presence of peaks in diffraction patterns, it is a reformulation of Bragg's law. The nuclear structure factor, describes how intense is a given peak, and depends on the details of the atomic positions with the unit cell.

A single crystal consists in a stacking of lattice planes. In a typical single crystal diffraction experiment, the crystal is placed within the desired sample environment and placed in the beam. One or several detectors are placed to detect outgoing neutrons. For a given orientation of the crystal, Bragg law describes at which angles a peak is expected to be observed. The crystal, or detectors, are then moved to change the scattering condition. The only accessible reflections are the ones in the scattering plane defined by the source-sample and sample-detector vectors. This strongly constrains the set of reflections that can be accessed, and even though four-circles geometry instruments exists, enabling to rotate the crystal in all three dimensions and access the full reciprocal lattice, when looking for preliminary information about a sample, it is more handy to start by performing powder diffraction.

### 8.2.2 Diffraction from a powder

In the field of crystal synthesis, it happens that most crystal growth processes require the preparation of a high quality powder sample. Moreover, the purest powders are always obtained from crushing crystals to ensure that the contamination is as low as possible, and the stoichiometry remains the expected one throughout the whole sample. Additionally, as mentioned previously, a powder experiment presents the advantage of accessing all scattering planes at once, without having to rotate the sample. Indeed, a powder sample effectively behaves as a infinitely large number of small single crystals with as many different orientations. Rotating the detector then simply corresponds to changing the angular range that is measured. Another important parameter that can be changed in actual experiments is the wavelength of the incoming neutrons  $\lambda_i$  (in the case of monochromatic beams): this impacts what is the maximum reachable  $2\theta$  angle. It is always required to balance the resolution, which strongly depends on  $\lambda_i$ , with the flux of neutrons. Another typical setup for experiments is the time of flight configuration. Instead of creating a monochromatic beam, a white beam containing a

wide range of frequencies is sent to the sample, all the neutrons being synchronized before the sample at a certain time, in a pulse. As many detectors as possible surround the scattering area, trying to record every scattered neutron. The time-of-flight of the recorded neutrons is analyzed and each detector corresponds to a given scattering angle. In this setup there is therefore no need to rotate any element.

### 8.3 Magnetic scattering

Magnetic scattering takes into account the interaction between the neutron and the magnetic field created by the electrons in the outer electronic shells. The interaction term is given by the Zeeman Hamiltonian:  $H_Z = -\boldsymbol{\mu} \cdot \vec{B} = -\gamma \mu_N \hat{\sigma} \cdot \vec{B}$ , with  $\vec{B}$  being the field of a single spin, assumed to be a dipole:  $\vec{B} = \mu_0 / (4\pi) \nabla \times (\vec{\mu}_e \times \vec{r} / r^3)$ , with  $\mu_e = -g \mu_B \mathbf{s}_j$ . The total interaction is written in equation (8.15).

$$\hat{V} = \sum_j \frac{\mu_0}{4\pi} g \mu_B \gamma \mu_N \hat{\sigma} \cdot \nabla \times \left( \frac{\mathbf{s}_j \times (\mathbf{r} - \mathbf{r}_j)}{|\mathbf{r} - \mathbf{r}_j|^3} \right) \quad (8.15)$$

A usual trick to obtain an expression for the neutron scattering cross section is to use the Fourier representation of the rotational operator:  $\nabla \times \left( \frac{\mathbf{s} \times \mathbf{r}}{r^3} \right) = \frac{1}{2\pi^2} \int \hat{\mathbf{q}}' \times (\mathbf{s} \times \hat{\mathbf{q}}') \exp(i\mathbf{q}' \cdot \mathbf{r}) d^3q'$ . A number of mathematical operations follow, but what is important here is that the quantity that enters the equation is  $\vec{q} \times (\vec{s} \times \vec{q})$ . This quantity is actually the projection of the spin,  $\vec{s}$  on the direction perpendicular to  $\vec{q}$ :  $\vec{s}_\perp$ . This has the drastic consequence, often mentioned in neutron scattering literature and experiments, that the only component of the spin perpendicular to the scattering vector is accessible. The partial differential cross section that has to be computed is stated in equation (8.16)

$$\begin{aligned} \frac{d^2\sigma}{d\Omega dE_f} &= \frac{k_i}{k_f} \left( \frac{\mu_0}{4\pi} \right)^2 \left( \frac{m_N}{2\pi\hbar^2} \right)^2 (g\mu_B\gamma\mu_N)^2 \sum_{\lambda_i, \lambda_f, \sigma_i, \sigma_f} p_{\lambda_i} p_{\sigma_i} \\ &\times \left| \left\langle k_f \lambda_f \sigma_f \left| \sum_j \sigma \cdot \nabla \times \left( \frac{\mathbf{s}_j \times (\mathbf{r} - \mathbf{r}_j)}{|\mathbf{r} - \mathbf{r}_j|^3} \right) \right| k_i \lambda_i \sigma_i \right\rangle \right|^2 \delta(\hbar\omega + E_{\lambda_i} - E_{\lambda_f}) \end{aligned} \quad (8.16)$$

Additionally to keeping track of the sample state before and after the scattering, and the neutron wavenumber, it is required to also record the spin state of the neutron,  $\sigma_{i,f}$ .  $p_{\lambda_i}$  and  $p_{\sigma_i}$  describe the probability for the individual states. For unpolarized neutrons,  $p_\uparrow = p_\downarrow = 1/2$ , and the sum can be carried out to finally yield the final magnetic cross section that reads as in equation (8.17).

$$\begin{aligned} \frac{d^2\sigma}{d\Omega dE_f} &= (\gamma r_0)^2 \frac{k_f}{k_i} \left[ \frac{g}{2} F(q) \right]^2 \sum_{\alpha\beta} (\delta_{\alpha\beta} - \hat{q}_\alpha \hat{q}_\beta) \\ &\times \sum_{\lambda_i \lambda_f} p_{\lambda_i} \sum_{j,j'} \left\langle \lambda_i \left| \exp(-i\vec{q} \cdot \vec{r}_j) \vec{s}_j^\alpha \right| \lambda_f \right\rangle \left\langle \lambda_f \left| \exp(i\vec{q} \cdot \vec{r}_{j'}) \vec{s}_{j'}^\beta \right| \lambda_i \right\rangle \\ &\times \delta(\hbar\omega - E_{\lambda_i} - E_{\lambda_f}) \end{aligned} \quad (8.17)$$



In this complicated equation,  $F(\vec{q}) = \int \exp(i\vec{q} \cdot \vec{r}) s(\vec{r}) d^3\vec{r}$  is the magnetic form factor, where  $s(\vec{r})$  is the spin density. This term is maximal at  $q = 0$  and decays for finite values of  $q$ , and is the main reason why magnetism is predominantly present at low values of  $q$  (in most cases). The sum upon  $\alpha$  and  $\beta$  accounts for the fact that only the component of the spin perpendicular to the scattering vector is accessible.  $\lambda_{i,f}$  correspond to the state of the sample, and finally, the last term,  $\delta(\hbar\omega - E_{\lambda_i} - E_{\lambda_f})$  ensures that the energy is conserved.

In the case of diffraction, the equation can be simplified to become equation (8.18).

$$\left. \frac{d\sigma}{d\Omega} \right|_{\text{el. mag.}} = (\gamma r_0)^2 \left[ \frac{g}{2} F(q) \right]^2 \exp(-2W) \times \left| \sum_j \exp(-i\vec{q} \cdot \vec{r}_j) \langle \vec{s}_{j,\perp} \rangle \right|^2 \quad (8.18)$$

This equation can be applied to two cases of interest: the diffraction on paramagnetic structures (8.19), where spins fluctuate in an uncorrelated fashion, and the diffraction on magnetically ordered states (8.20).

$$\left. \frac{d\sigma}{d\Omega} \right|_{\text{el. paramag.}} = \frac{2}{3} N (\gamma r_0)^2 \left[ \frac{g}{2} F(q) \right]^2 \exp(-2W) s(s+1) \quad (8.19)$$

The paramagnetic cross section does not present any  $q$ -dependence, except for the Debye-Waller factor,  $W$ , coming from the phonons, and the magnetic form factor. This is a  $q$ -dependent background term.

$$\left. \frac{d\sigma}{d\Omega} \right|_{\text{el. mag. ord.}} = (\gamma r_0)^2 \left[ \frac{g}{2} F(q) \right]^2 \exp(-2W) \frac{N(2\pi)^3}{V_0} |F_M(\vec{q})|^2 \sum_{\vec{\tau}} \delta(\vec{q} - \vec{\tau} - \vec{Q}) \quad (8.20)$$

In equation 8.20  $F_M(\vec{q}) = \sum_i \exp(-i\vec{q} \cdot \vec{\Delta}_i) \langle \vec{s}_{i,\perp} \rangle$  are the magnetic structure factor,  $\vec{\Delta}_i$  is the relative positions of atoms within the unit cell, and  $\vec{Q}$  is the ordering vector of the magnetic structure. It appears that, similarly to the periodic nuclear structure that creates structural Bragg peaks, the last term in equation (8.20) is responsible for the creation of purely magnetic Bragg peaks. Depending on the ordering vector  $\vec{Q}$ , these magnetic peaks can coincide with nuclear ones ( $\vec{Q} = \vec{0}$ ), but may also appear at incommensurate positions ( $\vec{Q} \neq \vec{0}$ ). The intensity of such peaks is given by the magnetic structure factor, very similarly to the nuclear structure factor for nuclear peaks.

## 8.4 Neutron spectroscopy

Spectroscopy refers to the study of inelastic processes, and is used, among others, to study magnetic excitations in materials. A typical excitation is a spin wave, but the partial differential cross section enables to study phenomena that are not limited to excitations in ordered systems. Starting with equation (8.17) the Dirac function encapsulating the energy conservation

can be transformed into an integral of an exponential and then interpreted as the time evolution of the Hamiltonian, yielding the final formula for inelastic magnetic scattering, presented in equation (8.21)

$$\begin{aligned} \left( \frac{d^2\sigma}{d\Omega dE_f} \right)_{\text{magn.}} &= (\gamma r_0)^2 \frac{k_f}{k_i} \left[ \frac{g}{2} F(q) \right]^2 \exp(-2W) \sum_{\alpha\beta} (\delta_{\alpha\beta} - \hat{q}_\alpha \hat{q}_\beta) \\ &\times N \frac{1}{2\pi\hbar} \int_{-\infty}^{\infty} dt \exp(-i\omega t) \sum_{j'} \exp(i\vec{q} \cdot (\vec{r}_j)) \langle s_0^\alpha(0) s_{j'}^\beta(t) \rangle \end{aligned} \quad (8.21)$$

This equation reflects the fact that the quantity measured by inelastic neutron scattering is the Fourier transform of the spin-spin correlation function: it gives access to both time and space correlations. The second line in equation (8.21) is called the dynamic structure factor, and usually written  $S(Q, \omega)$ :  $S^{\alpha\beta}(\vec{q}, \omega) = \frac{1}{2\pi\hbar} \int_{-\infty}^{\infty} dt \exp(-i\omega t) \sum_j \exp(i\vec{q} \cdot \vec{r}_j) \langle \vec{s}_0^\alpha(0) \vec{s}_j^\beta(t) \rangle$ . An important property that it obeys is called the sum rule, stated in equation (8.22), relating the total intensity measured to  $S$ , the spin of the system.

$$\int_{-\infty}^{\infty} \sum_{\alpha, \beta, \vec{q}} S^{\alpha\beta}(\vec{q}, \omega) d\omega = \frac{1}{\hbar} NS(S+1) \quad (8.22)$$

A typical neutron scattering instrument is the so-called triple axis spectrometer (TAS). A pictorial description of the instrument layout can be found in Fig. 8.2.

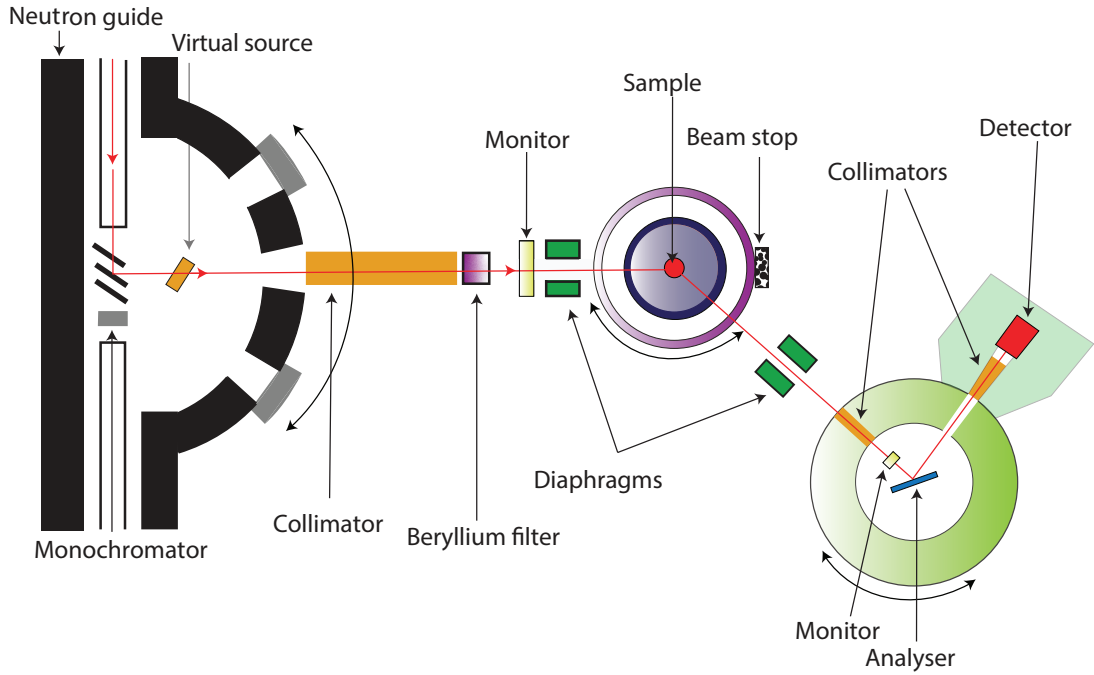


Figure 8.2: Example of a triple axis spectrometer.

The name triple axis comes from the fact that three axes can be moved. Essentially, this kind of instrument selects an incoming  $k_i$ , and through the sample rotation and analyzer angle, enables of choosing both the relative direction and magnitude of  $k_f$ , providing an option to aim for any point in the (Q,E) space. Kinematic conditions as well as instrument geometries and sample parameters of course constrain this accessible space but the general principle of functioning remains the same. The other kind of spectrometer consists in a very large array of detector tubes, replacing the single analyzer shown here in Fig. 8.2. The incoming neutrons arrive at a defined  $E_i$  thanks to a combination of choppers, and the angular information as well as the time-of-flights of neutrons are used to back-engineer the scattering vector and energy of each neutron. In this kind of geometry, the detector banks are too massive to be move but give access to hundreds, if not thousands of (Q,E) points at once. This is called direct time-of-flight. The indirect time-of-flight geometry also exists and consists in fixing the energy of the outgoing neutrons, rather than the energy of the incoming neutrons.

### 8.5 Polarized neutron scattering

It has been supposed in the previous discussion that neutrons are unpolarized, with an equal probability of having spin up and spin down neutrons. In practice however, one can take advantage of the spin of the neutrons to study condensed matter systems. It can indeed be used to conduct for example spherical neutron polarimetry. This technique uses elastic scattering to determine with great accuracy the direction of the moments of antiferromagnets[106](ferromagnets tend to depolarize neutron beams). It can also be used for inelastic signals to distinguish longitudinal from transverse magnetic excitations[107]. Several polarization analysis can be considered.

In many cases, it is sufficient to analyze the polarization of the outgoing neutron along the same axis as the polarization of the incoming neutron. This is called longitudinal polarization analysis. The essence of the idea is to separate the processes in two categories: the spin-flip and non-spin-flip channels. A non-spin-flip process is associated to a spin up sent at the sample, and a spin up detected, or inversely, a impinging spin down, and a detected spin down. The spin-flip channel corresponds to a change in the spin: up-to-down, or down-to-up. For nuclear scattering, the coherent scattering manifests itself purely in the non-spin-flip (NSF) channel, while the spin incoherent scattering is split in between the NSF channel (one third), and the spin-flip (SF) channel (two thirds). The cross sections for nuclear scattering are summarized in equation 8.23.

$$\begin{aligned} \left(\frac{d\sigma}{d\Omega}\right)_{++} &= \left(\frac{d\sigma}{d\Omega}\right)_{--} = \left(\frac{d\sigma}{d\Omega}\right)_{\text{coh+II}} + \frac{1}{3} \left(\frac{d\sigma}{d\Omega}\right)_{\text{inc}} \\ \left(\frac{d\sigma}{d\Omega}\right)_{+-} &= \left(\frac{d\sigma}{d\Omega}\right)_{-+} = \frac{2}{3} \left(\frac{d\sigma}{d\Omega}\right)_{\text{inc}} \end{aligned} \quad (8.23)$$

The advantages of these techniques appear already in a striking fashion: the different cross

sections help to discriminate between background and signal. In the very common case of magnetic scattering, one only accesses the component of the moments perpendicular to the magnetic moment. There is one more subtlety at play, since the polarization direction is a priori not related to the moment direction. It happens that the component of the moment parallel to the polarization axis contributes to the NSF channel, and conversely, the component perpendicular to the polarization axis contributes to the SF channel[108]. For disordered moments, the cross sections are stated in equation

$$\begin{aligned}\left(\frac{d\sigma}{d\Omega}\right)_{++} &= \left(\frac{d\sigma}{d\Omega}\right)_{--} \propto 1 - (\hat{Q} \cdot \hat{P}_i)^2 \\ \left(\frac{d\sigma}{d\Omega}\right)_{+-} &= \left(\frac{d\sigma}{d\Omega}\right)_{-+} \propto 1 + (\hat{Q} \cdot \hat{P}_i)^2\end{aligned}\tag{8.24}$$

In the case of a long range ordered system, the cross sections are more complicated and  $\left(\frac{d\sigma}{d\Omega}\right)_{++} \neq \left(\frac{d\sigma}{d\Omega}\right)_{--}$ , but the principle remains the same: by measuring the four different scattering cross sections, one can dis-intricate signal coming from the magnetic channel, from the incoherent channel and from spin coherent. The use of such techniques has been instrumental in the separation of broad, magnetic signal from incoherent background in frustrated systems[109]. An example of an actual instrument (D7 at the ILL) can be found in Fig. 8.3. The monochromator is responsible for the monochromatic beam which is then collimated and filtered to avoid high harmonics. The wide array of analyzers and detectors is indicated, collecting scattered neutrons. Several polarization elements can be placed on the beam path, such as spin flippers, or beam polarizing elements. Three main techniques are used to produce a polarized beam: filters, using preferential absorption by polarized  $^3\text{He}$  nuclei, polarizing mirrors using preferential reflections, or polarizing crystals, such as Heusler crystals ( $\text{Cu}_2\text{MnAl}$ ) using preferential Bragg reflections. Once generated, the polarized beam is manipulated with adiabatic or non adiabatic techniques. Examples of adiabatic manipulations of the polarization include guide fields and field rotators. The Drabkin spin flipper and the Dabbs foil are example of non-adiabatic spin-flippers. For example a Dabbs foil uses a current loop generating a field that rotates the polarization of the beam by  $180^\circ$ .

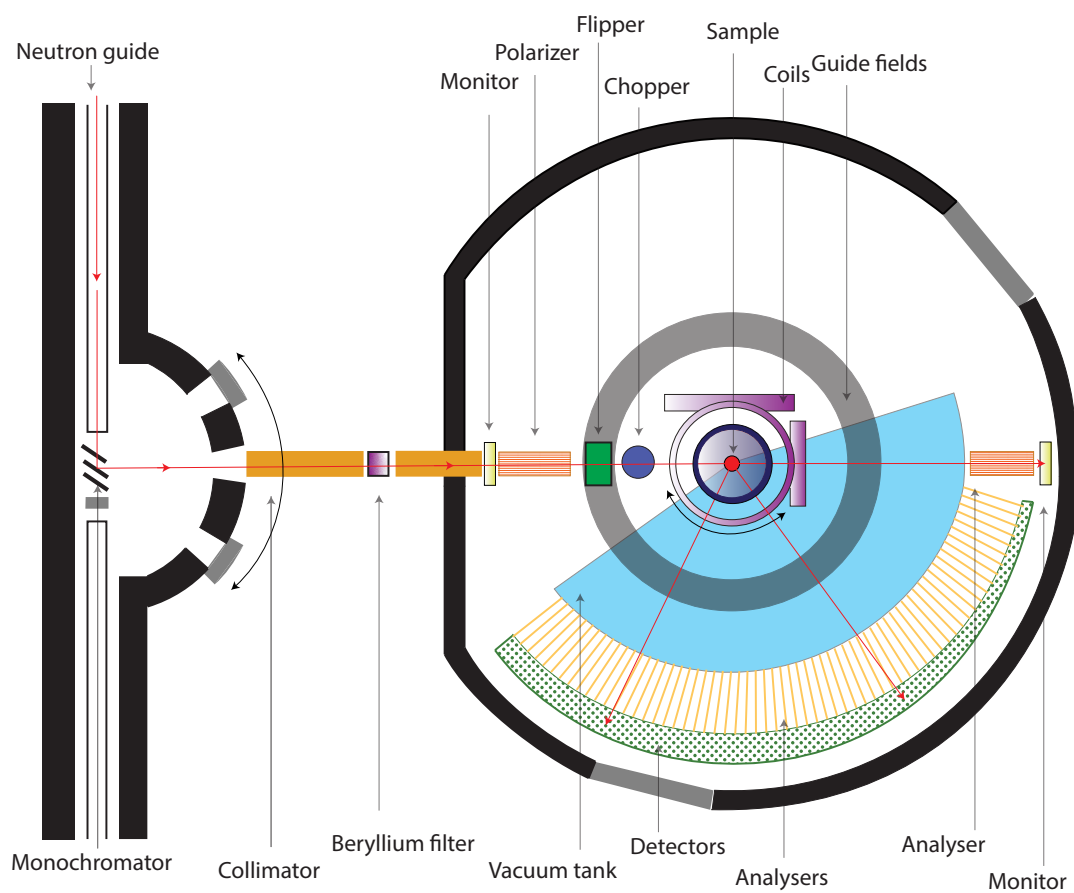


Figure 8.3: Example of neutron scattering instrument: D7 at the Institut Laue Langevin: polarized diffractometer.

# Quantum magnets and methods **Part III**



## 9 $\text{Cu}_2\text{OSO}_4$ : a playground for low dimensional quantum magnetism

As mentioned before, the notion of spin liquid was introduced by P.W. Anderson in 1973, in order to solve the complex problem of the ground state of the spin half Heisenberg Hamiltonian on the triangular lattice[110, 111]. Further studies actually evidenced that the state with lowest energy for that system exhibits magnetic-long-range order, in the form of the so-called  $120^\circ$  configuration[112]. This state is both the quantum and classical ground state of the system. The hunt for quantum spin liquids extended to other systems and models than the simple triangular lattice[113, 114]. The Kagomé lattice attracted considerable attention from both the experimental[115, 116, 117, 118], and theoretical sides[119, 120, 121]. The square lattice with second nearest neighbor interactions can be viewed as a triangular lattice, in the same type of thinking, the Kagomé lattice can be thought of as a triangular lattice, with missing interstitial sites, effectively lowering the coordination of the lattice: each site neighbors four sites instead of six. It has been theoretically postulated that the ground state of the spin half Kagomé Heisenberg antiferromagnetic Hamiltonian is the long sought-for spin liquid[122, 123, 124] and it is still debated whether the excitation spectrum is expected to be gapped or not [125, 126, 127]. Numerous attempts tried to discover compounds hosting this rich Kagomé physics [128, 129, 130, 131, 132] and up to date, Herbertsmithite[133] remains one of the best candidates. Another notable candidate of a Kagomé magnetic lattice has been long studied in mineral Jarosite[134], studied for over three decades. It turns out that numerous candidates failed to reproduce the simple Kagomé model: because of further neighbor interactions[135], non-negligible out-of-plane couplings, significant antisymmetric Dzyaloshinskii-Moriya interaction (DM)[136, 137], structural distortions, or chemical poisoning. These significant deviations from the model perturb the extremely high degeneracy required to obtain a quantum-spin-liquid and result in a ground state with magnetic-long-range order.

Even though order prevails, the question of whether or not, and to what extent, some of the quantum spin liquids properties can survive and coexist with ordered states still is relevant. This burning question of frustrated magnetism does not have, to-date, a clear and well defined answer, and goes way beyond Kagomé systems[138]. It is thus interesting to study lattices



created from triangular buildings blocks, other than the pure triangular and Kagomé lattices. In that context, the study of  $\text{Cu}_2\text{OSO}_4$  [139], a mineral named *dolerophanite*, also known as *copper oxysulfate*, has been carried out. The magnetic lattice describing the arrangement of copper atoms in the compound can be described by a quasi-two-dimensional combination of triangular motifs. The compound can be described as a Kagomé lattice, with one third of the atoms replaced by a pair of atoms (dimers) with  $S = 1$ . Another way of characterizing the compound is to state that it consists of chains, coupled by pairs of spins giving rise to a frustrated triangular model.

As evidenced in a further section, the spin pairs seem to align in a ferromagnetic fashion, meaning that the compound can be described as a Kagomé lattice with  $S = 1/2$  for two-thirds of the sites, and  $S = 1$  on the remaining  $1/3$  of the sites.

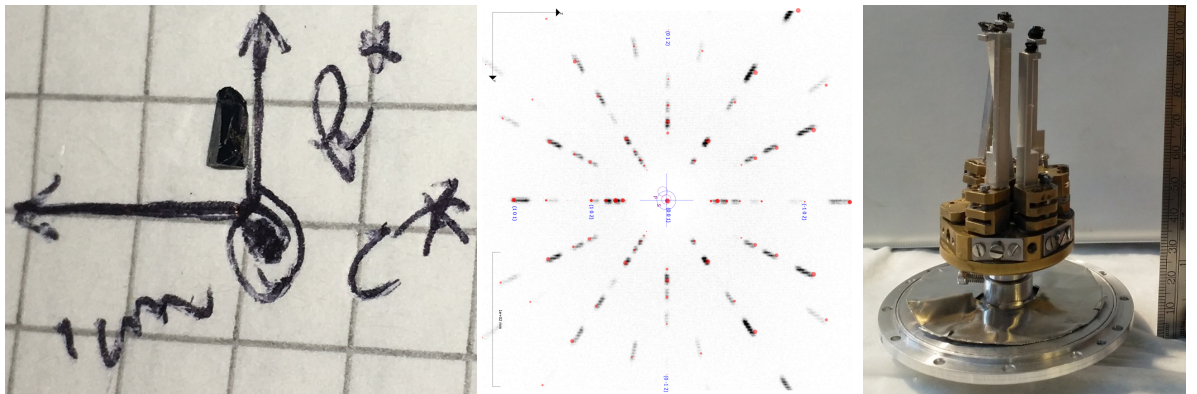
No previous successful single crystal growth has been published, and previous powder studies reported [140, 141] the DC susceptibility of the compound and found evidence for a transition to a state with magnetic-long-range order at 20 K. The DM interaction in the system has been estimated by careful analysis of Electron Spin Resonance (ESR) data [142]. Based on bulk measurements, an canted antiferromagnetic ground state has been proposed [143]. The growth process of single crystals of  $\text{Cu}_2\text{OSO}_4$ , and the details of the ground state of the compound are presented, obtained from DC-susceptibility, heat capacity, and also X-ray and neutron scattering. Many results presented here are already published in a peer-reviewed article [39].

### 9.1 Synthesis process

Single crystals of  $\text{Cu}_2\text{OSO}_4$  were grown by chemical vapor transport (CVT), by Arnaud Magrez [39]. A very high quality polycrystalline sample has been synthesized using anhydrous  $\text{CuSO}_4$  as precursor, placed in a quartz ampoule. The ampoule has been placed in a muffle furnace and heated up to a temperature of  $740^\circ\text{C}$ . Two chemical transport agents have been encapsulated in a quartz ampoule at ambient temperature:  $\text{Cl}_2$  and  $\text{NiBr}_2$ , as well as a small quantity of the  $\text{Cu}_2\text{OSO}_4$  powder. Both ampoules were placed in a two-zone gradient furnace. The best temperatures for the charge and the growth zone were respectively  $650^\circ\text{C}$  and  $550^\circ\text{C}$ . After five weeks, several semi-transparent, dark-brown crystals were visible. A typical set of dimensions for the obtained crystal is  $4 \times 2 \times 0.5 \text{ mm}^3$ . An example of crystal is shown in Fig. 9.1a.

Most of the crystals present regular facets. Some of these facets could be identified thanks to a combination of X-ray Laue measurements, shown in Fig. 9.1b, as well as single crystal diffraction. In the majority of cases, one could identify a (001) facet, with one of the edges being the  $b^*$  axis. This identification has been instrumental in measuring crystal direction-dependent properties. The purity of the compound has been established thanks to single crystal X-ray diffraction. A given representative crystal is rotated in the beam of X-rays, and

one diffraction pattern is recorded at each angle. The combination of all patterns gives a three dimensional view of the purity of the crystal: it is used both to refine the unit cell parameters and verify at the same time that a reasonable amount of outliers are observed. Because of the surface-character of X-ray measurements, this is of course not a definitive proof that the bulk of the crystals is a single crystal but is nevertheless a solid first step towards ensuring decent crystal quality. In a second step, the surface deterioration, and the orientation of the sample can be determined using X-ray Laue scattering. Once the orientations of the crystals are known, one can glue the crystals together onto the same sample holder, as shown in Fig. 9.1c.



(a) Example of single crystal with typical dimensions. (b) Laue pattern confirming crystal orientation and surface state. (c) Example of co-alignment of samples for neutron scattering.

Figure 9.1: Example of single crystal (left), with dimensions. The Laue pattern (middle) in the center confirms the surface is rather clean, and the orientation of the sample. Several crystals can then be co-aligned by gluing them on top of aluminum posts (right) to increase the signal-to-noise ratio of the neutron scattering signal.

The solid brass base ensures good thermal contact with the temperature controller. This setup is optimized for experiments above 1.2 K, temperature at which the aluminum becomes superconductor. The crystals, at the very top, are mounted on aluminum posts. For this range of temperature, the thermal conductivity of aluminum, as well as the presence of an exchange gas -a couple of millibars of Helium- surrounding the sample, are enough to thermalize properly in a reasonable time the sample: it takes a couple of minutes. Aluminum is a material providing rather low neutron scattering background, compared to copper, and also known and easily recognizable inelastic features: phonons, and thus can be disentangled from the signal coming from the sample in a rather straightforward manner. The aluminum posts are mounted on small brass platforms, effectively machined to act as goniometers. With the help of a set of ingeniously placed screws, these platforms provide a control and a possibility to correct with high precision -less than a degree- the relative orientation of each of the six crystals mounted on the holder. With a view to minimizing undesired elements in the beam, it is quite important to try and get rid of absorbing elements, or those that create strong inco-

herent scattering. Of that class is hydrogen, one of the strongest incoherent scatterers, which happens to enter in significant amounts the composition of most glues, in particular widely used low temperature GE-varnish[144]. In order to minimize undesired signals, it has been chosen to use cytop, an *almost* hydrogen free glue[145, 146]. The aluminum posts have been carved out of a substantial amount of matter, to try and reduce the background as much as possible. The crystal placement has been thought through to minimize the horizontal spread, contributing in an undesirable manner to the resolution by broadening features. Each crystal is also slightly offset vertically from one another to try and optimize for the vertical dimension of the neutron beam: typically two to four centimeters. Slits made of an absorbing material (Boral) are typically mounted on the instrument to narrow the beam size both vertically and horizontally.

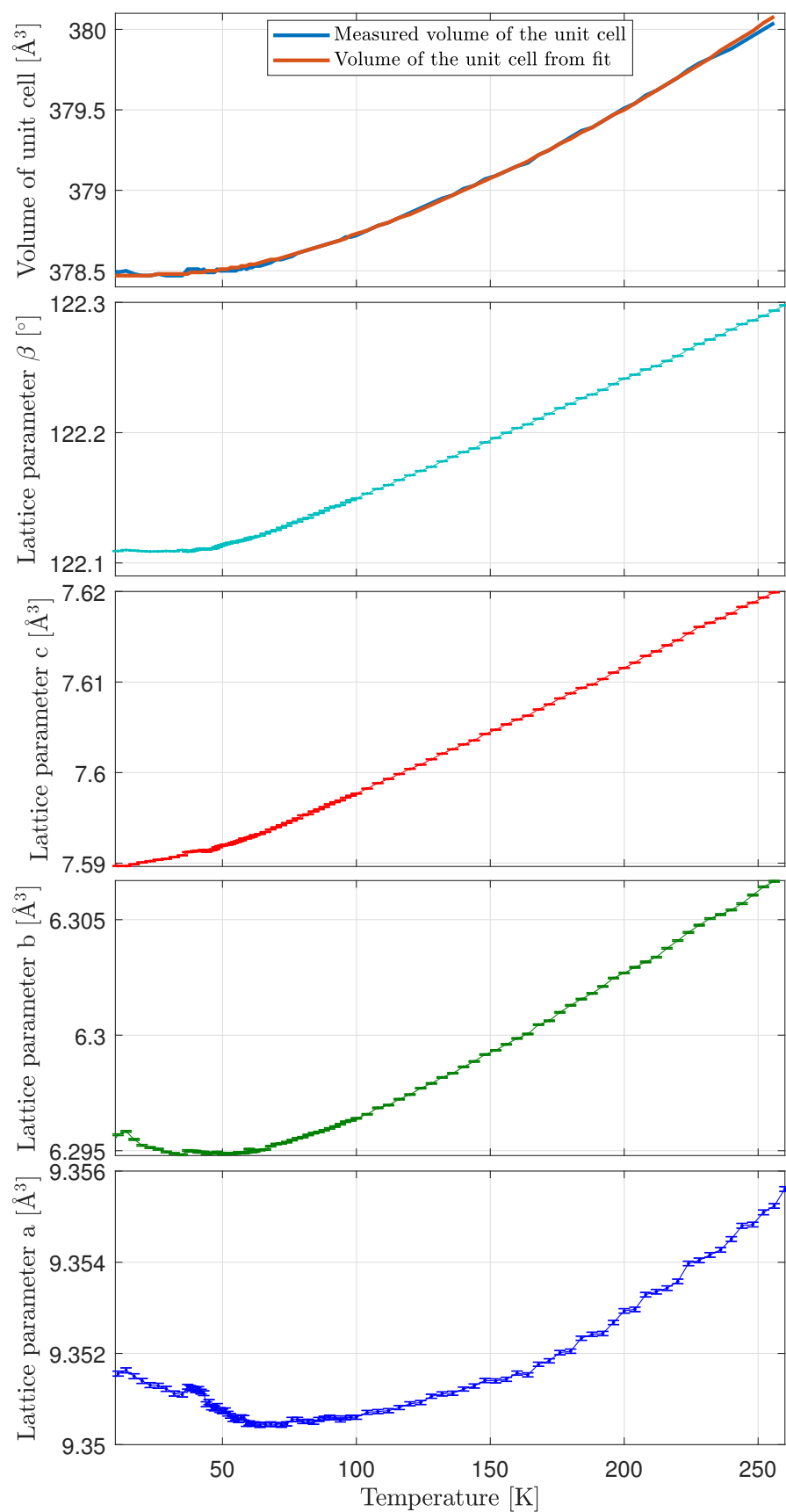
## 9.2 Bulk measurements: a potential ferrimagnet

### 9.2.1 X-ray diffraction and crystal structure

According to a previous study[139], the compound synthesizes in a crystal structure described at room temperature by a monoclinic space group:  $C 2/m$  (space group number twelve), with lattice parameters given by  $a = 9.355(10) \text{ \AA}$ ,  $b = 6.312(5) \text{ \AA}$ ,  $c = 7.628(5) \text{ \AA}$ ,  $\alpha = \gamma = 90^\circ$ , and  $\beta = 122.29(2)^\circ$ . The unit cell contains two inequivalent copper sites. The details of the atomic placements of atoms are to be discussed in another section.

The crystal structure thus appears to be a relatively low symmetry one. Even in this case, the question of whether there is a transition to another structure when cooling down the sample is of great importance. Indeed, a symmetry lowering, or even a simple distortion of the sample can impact severely the symmetry of the exchange paths in the sample and perturb perfect Heisenberg couplings, or the delicate equilibrium that is necessary to stabilize the spin-liquid state. In order to determine the behavior of the nuclear structure in function of temperature, temperature dependent synchrotron X-ray diffraction on a powder sample was carried out at the material science MS-X04SA beam line at the Swiss Light Source (SLS) at the Paul Scherrer Institut (PSI) in Switzerland. The powder was packed in a 0.5 millimeter capillary, slightly wider than the usual 0.3 millimeters one. This was necessary because of the high stickiness of the obtained powder. The target energy was 21.99 keV, corresponding to a wavelength of  $0.5637 \text{ \AA}$ . Each temperature was measured for roughly 10 minutes. The temperature was controlled thanks to a helium jet and a heater, giving a base temperature near 5 K. The sample was consisting in a few milligrams of powder obtained from crushing in small pieces in a agate mortar several single crystals. The grinding was performed in a constantly-flushed nitrogen glove bag to ensure that no contamination resulted of the contact between the sample the water in the air. The capillary was sealed by fire. The dependence of lattice parameters and the unit-cell volume could be extracted thanks to a LeBail fit (LBF), carried out using the Fullprof suite, and is shown in Fig. 9.2.

It appears that the usual global thermal contraction of the lattice was observed down to a temperature of 50 K, with an observable minimum of the lattice parameters  $a$  and  $b$  around 60 K. This non-monotonic dependence of the lattice parameters may find its origins in the slow build-up of magnetic correlations coupling to the lattice, similar to what has already been reported in multiferroic compound  $\text{HoMnO}_3$ [147], explained in that case by a magnetoelastic origin.



96 Figure 9.2: Lattice parameters of  $\text{Cu}_2\text{OSO}_4$  obtained from LeBail fit of powder diffraction data.

Evidence for such magnetoelastic couplings in  $\text{Cu}_2\text{OSO}_4$  have been identified in the low-temperature variations of lattice parameters for temperatures below the magnetic transition, confirmed by neutron diffraction and visible in Fig. 9.3.

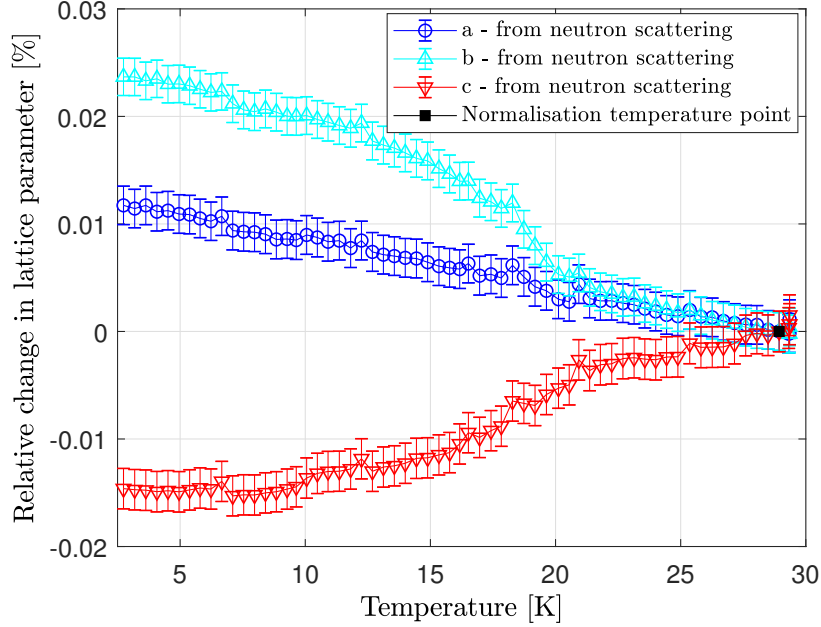


Figure 9.3: Relative change in lattice parameters of  $\text{Cu}_2\text{OSO}_4$  obtained from LeBail fit of powder neutron diffraction data. The black dot is the normalization point.

A thermal diffractogram, set of diffraction patterns measured at many different temperatures was measured at the D20 diffractometer in the Institut Laue Langevin neutron source (ILL) in Grenoble, France. The sample consisted of 1.5 grams of high quality powder obtained from crushed small single crystals in a Helium glove box, sealed in a vanadium can with indium wire and helium acting as exchange gas. The high resolution option with neutron take-off angle of  $90^\circ$  degrees and a wavelength of  $2.41 \text{ \AA}$  was used. Four hour measurements were taken at a base temperature of 1.5 K and at 30 K, intermediate temperature points were obtained using a ramp, with approximately 0.45 K between subsequent runs. The relative change in lattice parameters was established by normalizing data to the data measured at 29 K, indicated as a black square in Fig. 9.3. It can be observed that there is a small change in lattice parameters from 30 K to 20 K, and that a sizable change occurs when decreasing the temperature below 20 K, which corresponds to the magnetic transition to a state exhibiting magnetic-long-range order. The lattice contraction is anisotropic, but does not significantly change the magnetic lattice.

### 9.2.2 Structure and lattice

The magnetic lattice inherited from the crystal structure of dolerophanite is quite complex and deserves some clarification. The magnetic arrangement of copper atoms is based on two non equivalent atomic positions, with a total of eight atoms per unit cell. The atoms are placed in the crystallographic  $ab$ -plane, with atoms from inequivalent site 1, labeled  $\text{Cu}_1$ , exactly in the plane, while atoms constructed from inequivalent position 2, labeled  $\text{Cu}_2$  are shifted slightly out-of-plane, symmetrically above and below. Fig. 9.4b. shows how the different planes are then connected by sulfur tetrahedra[148].

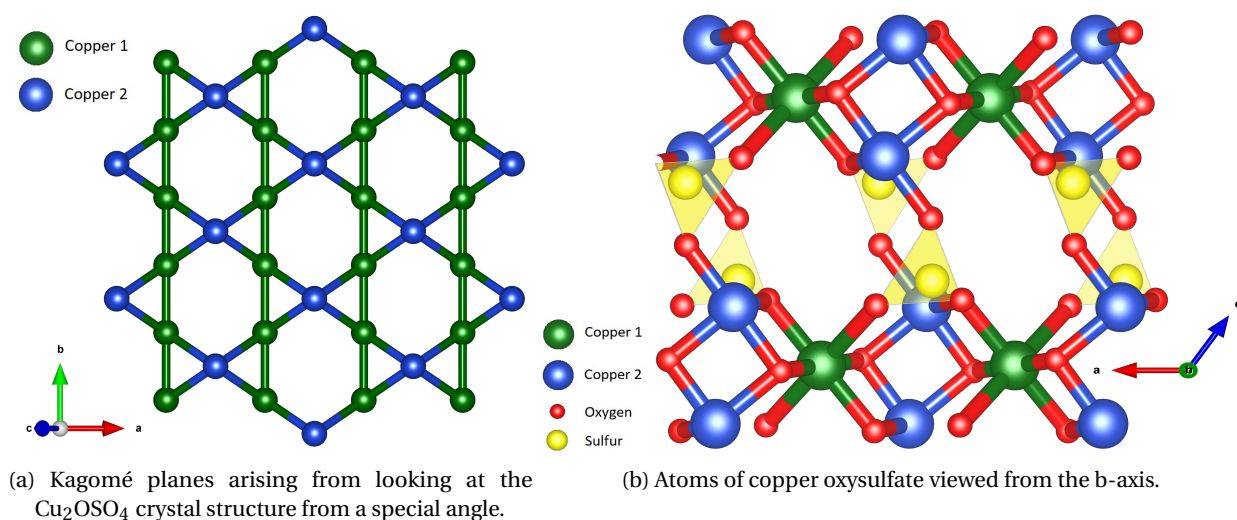


Figure 9.4: Crystal structure of copper oxysulfate. Blue and green atoms are inequivalent copper positions. The Kagomé layers are apparent when looking at the structure from a direction close to  $c^*$  (left). The right-hand side picture reveals how blue copper atoms are shadowing each other in the picture on the left, as well as the magnetic decoupling between two consecutive layers, caused by intercalation of sulfur tetrahedra.

The placement of  $\text{Cu}_1$  and  $\text{Cu}_2$  ions in the planes is quasi two-dimensional, and can be described either as  $\text{Cu}_1$  chains along the crystallographic  $b$ -axis, interconnected by  $\text{Cu}_2$  dimers in a frustrated zig-zag pattern; or as a Kagomé lattice, with a third of the sites replaced by  $\text{Cu}_2$ . Fig. 9.4a reveals the Kagomé planes that arise when shadowing one of the out-of-plane  $\text{Cu}_2$  atom by the other. To achieve this, one has to tilt the point-of-view by an angle of  $8.5^\circ$  from the  $c^*$  direction. Fig. 9.12b shows how the lattice appears when looking from the crystallographic  $c^*$  direction. A concise discussion about exchange paths giving rise to the potential couplings in the systems seems to be required and is the focus of another chapter dealing with inelastic neutron scattering experiments and modeling.

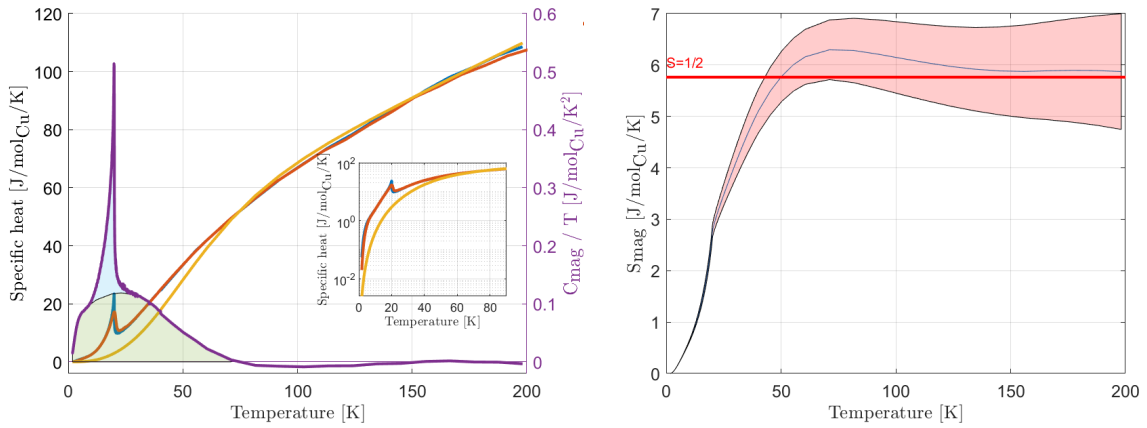
What is in essence important to realize is that there are plausible exchange paths linking  $\text{Cu}_1$

atoms with each other within the Kagomé plane, and also exchange paths linking  $\text{Cu}_2$  to  $\text{Cu}_2$  atoms, as well as paths connecting the two sublattices. Moreover, it does not appear that any simple superexchange path connects atoms between Kagomé like layers, without involving sulfur atoms. It is thus expected that these give rise to weaker couplings, because the orbital overlaps involving sulfur orbitals should be less significant. This tends to confirm the validity of a rather two dimensional model. A careful analysis of bond angles and distances is necessary to claim more and is to be discussed in the analysis of the inelastic neutron scattering results. Another point worth mentioning is that of the geometry. It appears that the Kagomé-like lattice is actually very close to a perfect Kagomé, in the sense that its triangular unit constituents are not deformed, nor twisted, which is a typical problem of Kagomé systems[149] and triangular units in general. Additionally, it seems that even though a sizable magnetoelastic coupling has been observed, it is not associated to significant deviations from the original Kagomé-like structure.



### 9.2.3 Heat capacity

Heat capacity  $C_p$  was measured by Markus Kriener at the Riken Center for Emergent Matter Science in Japan, using the specific heat option of a Physical Properties Measurement System (PPMS, Quantum design, inc.) on a powder sample, pressed to form a pellet of mass 1.2 milligrams. The sample as well as the addenda were measured from 2 K to 200 K in zero field. Subtraction of the addenda signal provides a complete view of the sample's self heat capacity, from 2 K to 200 K in zero field as well as in a field of 9 T. The results can be observed in Fig. 9.5a.



(a) Specific heat in function of temperature in zero field (blue) and in 9T (red). The yellow curve shows the modeling of the lattice contribution, and purple the subtraction, accounting for magnetic heat capacity, divided by temperature. The inset shows a zoom on the low temperature part where the fitted lattice contribution differs significantly from the measured signal.  
(b) Recovered entropy as a function of temperature, plateauing to the entropy of a spin half system. The red shading corresponds to the confidence interval.

Figure 9.5: Measured heat capacity on a  $\text{Cu}_2\text{OSO}_4$  pellet(left), extracted magnetic entropy(right).

The figure shows the specific heat per copper atom in zero field (in blue), and in a field of 9 T (in red). The yellow curve is a fit to a lattice model that results in the separation of the contribution of the specific heat that is coming purely from magnetic processes. The purple curve shows this magnetic specific heat, divided by the temperature. The inset is a zoom on the contribution at temperatures lower than 90 K, showing the sensible difference between measured data and the modeled contribution.

Fig. 9.5b shows the total magnetic entropy in function of temperature, with error-bars corresponding to the red area. The horizontal red line is a guide-to-the-eye, showing for reference the entropy expected for a purely spin-half system.

## 9.2. Bulk measurements: a potential ferrimagnet

It appears that  $C_p$  above 70 K is similar for both fields, increasing monotonically with temperature. In the zero field data, a sharp  $\Lambda$ -like peak is observed around 20 K, indicative of a magnetic transition towards a state exhibiting magnetic long range order, which is confirmed by other experimental data presented in the next sections. The peak shifts to a slightly higher temperature in a field of 9 T, and its intensity seems to be marginally reduced.

In order to disentangle the purely magnetic contribution to the heat capacity,  $C_{\text{mag}}$ , with a view to extracting the corresponding transition entropy,  $S_{\text{mag}}$ , the lattice effects have been modeled using the hypothesis that the high temperature data is of exclusive lattice origin. Indeed, the differences between in-field and zero field data indicate that the effect of magnetism is irrelevant above 70 K, and that thus, magnetic correlations do not contribute in a significant way to the total, measured heat capacity. The full lattice model has been determined taking into account contributions from Einstein and Debye branches, as is routinely done for many compounds[150]. There are subtleties when this method is applied to magnetic systems that are the topic of a whole chapter of this thesis. Dolerophanite has been modeled using contributions from one Debye branch ( $C_D$ ) and several Einstein branches ( $C_{E,i}$ ). In order to maximize the accuracy of the results, and since both the heat capacity and the volume of the unit cell derive from the same physical quantity: the internal energy of the system, a combined fit was used to obtain reasonable parameters. The volume of the unit cell is obtained from the X-ray measurements. The total lattice contribution is given by equation (9.1)

$$C_p = C_D + \sum_i C_{E,i} \quad (9.1)$$

With the Debye contribution written in equation (9.2)

$$C_D = 9n_D R \left( \frac{T}{\Theta_D} \right)^3 \int_0^{\Theta_D/T} \frac{x^4 e^x}{(e^x - 1)^2} dx \quad (9.2)$$

And the Einstein contribution stated in equation (9.3).

$$C_E = 3n_E R \frac{y^2 e^y}{(e^y - 1)^2}, y \equiv \Theta_E / T \quad (9.3)$$

$R$  is the gas constant[151],  $8.31 \text{ J mol}^{-1} \text{ K}^{-1}$ .  $\Theta_D$  and  $\Theta_E$  stand respectively for the Debye and Einstein temperatures.  $n_D$  and  $n_E$  are the Debye and Einstein weights, describing the relative importance of each branch. Their sum,  $n_D + n_E$  accounts for the total number of atoms per formula unit. The Debye and Einstein contribution can be explicitly related to the internal energy of a solid. The relation between the energy and the unit cell volume[152, 153, 154] can be found in equation (9.4).

$$V(T) = \gamma U(T) / K_0 + V_0 \quad (9.4)$$

$V_0$  stands for the volume of the unit cell at zero Kelvin,  $K_0$  is the bulk modulus, and  $\gamma$  the Grüneisen parameter. The dependence of the internal energy  $U(T)$  on the temperature can be

written, using Einstein and Debye terms, as in equation(9.5).

$$U(T) = U_D(T) + U_E(T) \quad (9.5)$$

With the Debye contribution written as follows and is shown in equation (9.6).

$$U_D(T) = 9n_D k_B T \left( \frac{T}{\Theta_D} \right)^3 \int_0^{\Theta_D/T} \frac{x^3}{e^x - 1} dx \quad (9.6)$$

And the Einstein component written in equation (9.7).

$$U_E(T) = \frac{3}{2} k_B \sum_i n_{E,i} \Theta_{E,i} \coth\left(\frac{\Theta_{E,i}}{2T}\right) \quad (9.7)$$

The best result obtained from a combined fitting of both unit cell volume and heat capacity yields the following Debye and Einstein temperatures:  $\Theta_D = 171$  K,  $\Theta_{E,1} = 245$  K and  $\Theta_{E,2} = 939$  K. These results are obtained with a Debye weight of  $n_D = 1$ , and two Einstein branches, with respective weights of  $n_{E,1} = 3$  and  $n_{E,2} = 4$ . In order to fit the lattice model onto the data, only points associated to a temperature that is larger than 70 K have been used, with a view to making sure that there is no more contribution from magnetic correlations to the measured heat capacity. As mentioned before, this temperature has been chosen because it corresponds to a significant overlap of in-field versus zero field data, and the robustness of the results does not depend strongly on the chosen range, as long as the starting temperature is at least 70 K. The fitted volume of the unit cell at 0 K has been found to be  $V_0 = 373.65 \text{ \AA}^3$ . The result of the fit can be observed in Fig. 9.2

Fig. 9.5a shows on the right axis the obtained magnetic heat capacity, divided by the temperature  $C_{\text{mag}}/T$ , in zero field. Fig. 9.5b reveals the corresponding magnetic entropy, obtained by integrating the magnetic heat capacity over temperature. The magnetic entropy reaches saturation, with a saturated value of 101(19)% of  $R \ln 2$  per formula unit. This is in excellent agreement with the entropy recovered by a system with two degrees of freedom. A similar analysis was performed on the in-field data and confirmed that the field does not significantly change the results. The magnetic contribution to the entropy can be separated in two categories: between the short range correlations, in green, in Fig. 9.5a, and the transition, in blue in Fig. 9.5a. The entropy from the transition accounts for the thermal energy used to reorganize the internal degrees of freedom that are the spins, while the entropy in green develops in a rather wide peak, over a large range of temperatures, compatible with the onset of magnetic correlations over the whole temperature range. It has been estimated that 18(5)% of the magnetic entropy contributes to the phase transition, and the rest takes the form of correlations.

### 9.2.4 DC susceptibility and magnetization

Fig. 9.6 shows the inverse of the DC-susceptibility, measured on a single crystal in a field of 0.1 T. Several single crystals have been used to confirm the results. The presented data used a single crystal of 25.1 milligrams. The measurements were done using a combination of Vibration Sample Magnetometer (VSM) included in the PPMS instrument, as well as a SQUID magnetometer, part of a Magnetic Properties Measurement System (MPMS, Quantum Design, inc.)

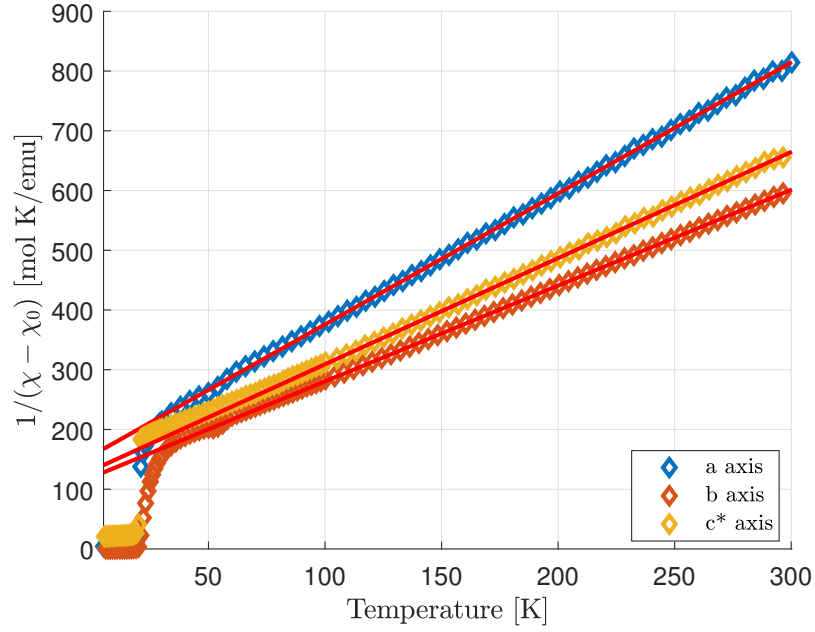


Figure 9.6: Inverse susceptibility, corrected for the constant component of DC susceptibility in function of temperature, measured on a single crystal along the three crystallographic directions. The red line corresponds to Curie-Weiss fits, performed at high temperature.

The DC-susceptibility has been measured along the three most relevant crystallographic directions: the a- and b-axes, which are spanning the Kagomé plane, and the c\*-axis, direction along which the planes are stacked. The fitted values of the Curie Weiss temperature  $\Theta_{CW}$ , the diamagnetic background  $\chi_0$  and the effective moment  $\mu_{eff}$  are presented in table 9.1.

direction	$\Theta_{CW}$ [K]	$\chi_0$	$\mu_{eff}$ [ $\mu_B$ ]
a	-71(4)	5.4e-05	1.91(25)
b	-75(1)	4.7e-04	2.23(25)
c*	-70(1)	-7.6e-05	2.11(11)

Table 9.1: Results of Curie-Weiss fits for measurements along the a-, b- and c\*-axes

The starting temperatures for the fits of the Curie-Weiss fits presented in the form of red lines in Fig. 9.6 have been checked to have no effect on the fit results: fits were performed on many different temperature ranges, and fit results are selected in a region of temperature providing so-to-say constant values of the resulting parameters, ensuring fit stability. The Curie-Weiss temperature appears to be isotropic, within its errorbars, and negative. This is indicative of a predominant antiferromagnetic interaction in the system. The slope of the linear Curie-Weiss part given by parameter  $C$ , is anisotropic, indicative of a slightly anisotropic  $g$ -tensor, with easy axis along the crystallographic  $b$ -axis. Below 20 K, the susceptibility develops rapidly to a non-negligible value. This indicates a transition to a long-range ordered state, with a ferromagnetic component. The magnetization of the sample was measured in function of temperature with two protocols: cooling down to base temperature in a field, and then measuring by increasing the temperature (Field Cooled Warming (FC)), but also by cooling down in zero field, and then again, measuring when increasing the temperature (Zero Field Cooled Warming (ZFC)). When cooled in a field, the field strength and direction that were used are the same as those of the measurement field. A finite field cooled - zero field cooled splitting was observed below the transition temperature, which is typical of the opening of a small hysteresis. The transition is occurring at a temperature much lower than the Curie-Weiss temperature. This suppression of the transition for a given range of temperatures is indicating that the establishment of magnetic-long-range order is suppressed. This is typically due to a combined effect of both frustration and fluctuations in a low dimensional system. Fig. 9.7 shows the difference in magnetic susceptibility between FC and ZFC protocols.

The presented magnetization has been measured along the crystallographic  $b$ -axis, only direction developing a strong magnetization below 20 K. Different values of field have been used for the measurement:  $H = 5$  mT,  $H = 10$  mT,  $H = 20$  mT,  $H = 50$  mT.

The susceptibility along other relevant crystallographic axes ( $a$  and  $c^*$ ) have also been measured, and are shown in Fig. 9.8. The inset shows a zoom on the susceptibility below 20 K. The magnetic susceptibility measured along the  $a$  and  $c^*$ -axes show a similar temperature dependence to the one measured along the  $b$ -axis, but with a much lower value of projected zero Kelvin limit. This is evidenced in the inset of Fig. 9.8. It has actually been found that the component developed is due to a misalignment of the crystal when measuring: achieving a precision of less than a degree is actually close to impossible on such small crystals, and the measured signal along other relevant directions picks up a partial contribution from the  $b$ -axis: they are still one or more order of magnitude less intense. Additionally, gluing the crystal with a low-background glue limits the force that maintains the crystal in place. It has been observed that the crystal tends to rotate to align its  $b$ -axis in the applied field. This also explains why the alignment, despite the best efforts, is not perfect.

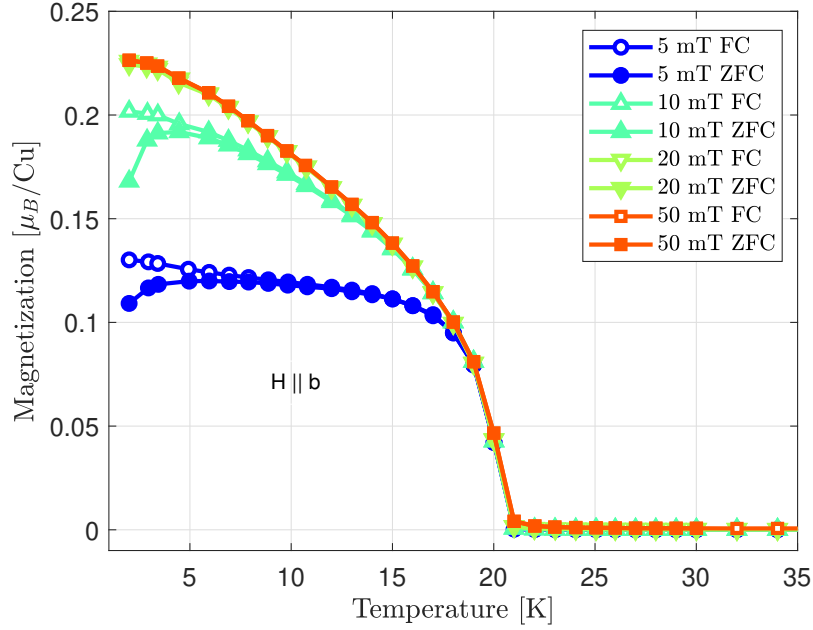


Figure 9.7: Magnetization measured on a single crystal along the crystallographic b-axis, for different values of the measurement field strengths, highlighting Field Cooled - Zero Field Cooled splitting for small fields. The strongest splitting occurs for a field strength of 5 mT.

Fig. 9.9 shows fixed-temperature magnetization measured along the crystallographic b-axis and the a- and c\*-axes in the inset. For temperatures greater than 20 K, the curves are linear, which corresponds to the usual paramagnetic response: thermal fluctuations are dominating, the field aligns the spins, but a very high field is required to reach full theoretical moment, the greater the temperature, the larger the field needs to be. Below 20 K, a small hysteresis opens up. This corresponds to the transition to a magnetically long-range ordered state that was evidenced with other measurements. The field required to saturate the magnetization increases when lowering the temperature, reaching 40 mT at 2 K. No comparable hysteresis has been observed along other crystallographic directions (a (which shows a way smaller hysteresis, due to misalignment) and c\*). The hysteresis is yet another indication of a non-negligible ferromagnetic component of the ground state, with a moment of  $\approx 1/4 \mu_B$  aligned with the crystallographic b-axis. The hysteresis curve happens to be slightly asymmetric and presents a weak time dependence: it is wider when measured on the PPMS in the scanning field mode, while on the MPMS, where a steady, stabilized field is waited for at each field, sometimes taking up to minutes, the hysteresis is narrower: it seems that the ferromagnetic component is thus relatively soft. This exchange-bias like phenomenon may reflect the fact that the resulting state is a ferrimagnetic ground state, stabilized by competing ferromagnetic and antiferromagnetic interactions. The exchange bias is the result of the coupling between sub-units from both interaction types. Fig. 9.10 shows the behavior of the magnetization for high values of applied field, up to 14 T, measured on a single crystal, along the crystallographic

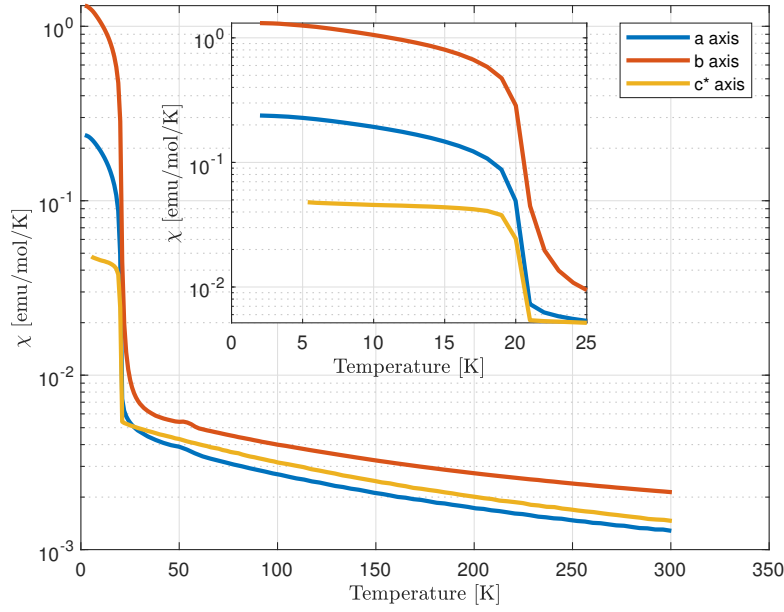


Figure 9.8: Susceptibility measured on a single crystal along the crystallographic a, b and  $c^*$ -axes, in a field of 0.1 T. The inset shows how the susceptibility develop below 20 K, with its most significant contribution clearly along the b-axis.

b-axis. The inset shows the results of the measurement along the a and  $c^*$  crystallographic axes. There is no transition detected up to 14 T. The value of the moment reached at 14 T, and 2 K is  $0.32 \mu_B$  per copper atom. The linear slope observed at 2 K is indicative of slowly rotating moments that are gradually aligning in the field. The M-H curves acquire a curvature for higher temperatures. The base temperature data could be extrapolated to calculate at which field the moments would be reaching a fully polarized state. The calculated slope is of  $3.56 \text{ m}\mu_B \text{ T}^{-1}$ , with an intercept of  $0.267 \mu_B$ . This would correspond to an external applied field of 205 T, along the crystallographic b-axis. It remains possible, however that the system undergoes a brutal transition to the field polarized state. This happens in the case of the so-called spin flop transition[155, 156]. In that scenario, usually occurring when a magnetic field is applied parallel to collinear, antiferromagnetic moments, the energy of the system cannot be lowered significantly by a small deviation of spins around their zero Kelvin positions. When the external applied magnetic field is strong enough, it overcomes the anisotropy energy that was constraining the moments and the spin rotate rapidly "in plane", by ninety degrees, still presenting an antiferromagnetic alignment. In that configuration, only the Zeeman energy from the external field and the anisotropy are frustrated. In a second step, the spins then slowly rotate to align with the field, and reach the field (fully) polarized state. Since this corresponds to a jump in the M-H curve, the saturation field has to be lower or equal to the predicted one. The inset of Fig. 9.10 shows the behavior of the magnetization at 2 K, with an applied field along the crystallographic a- and  $c^*$ -axis. It appears that the magnetization along the

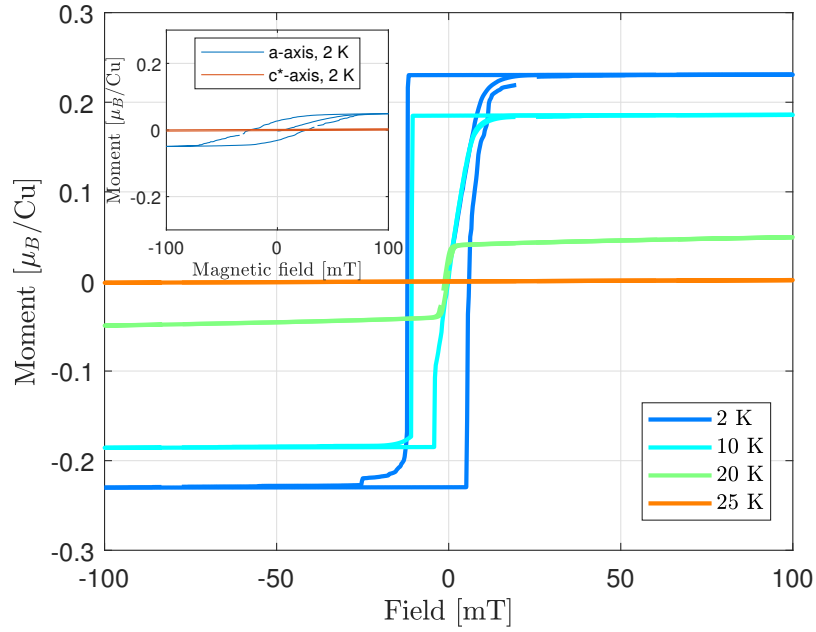


Figure 9.9: Isothermal magnetization curves, with applied field parallel to the crystallographic b-axis. The inset shows, for comparison the same data along the crystallographic a and c\*-axes.

crystallographic c\*-axis is purely linear, confirming the zero component of the magnetization in the c\*-direction. The spins are simply aligning in the field. The same behavior is observed along the crystallographic a-direction, however it seems that the measurement also picks up a small component from the crystallographic b-axis. Reaching one  $\mu_B$  by applying a field along the crystallographic c\*-axis would require applying a field of 183 T, by linear extrapolation. Since the measurement along the crystallographic a-axis is influenced by the behavior along the crystallographic b-axis, it is hard to get such a conclusion, however, simple eyeballing of the curve would lead to a value around 200 T as well.



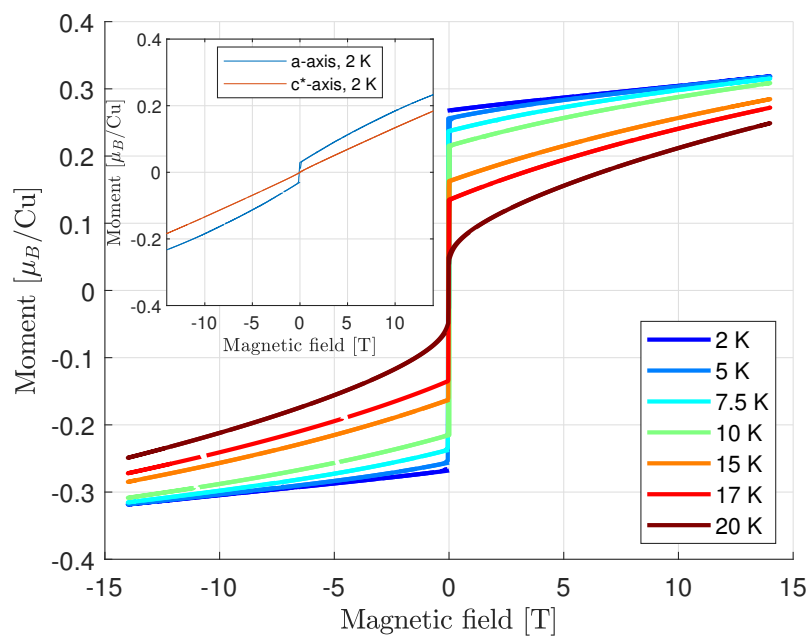


Figure 9.10: Isothermal magnetization curves, for large values of fields, along the b-axis. The inset shows measurement results along the a and c\*-axes at base temperature.

## 9.3 Neutron diffraction unveils 120° magnetic order

In order to determine with certainty the details of the magnetic ground state, neutron scattering diffraction was performed on a powdered sample. Fig. 9.11 shows the results of the measurements. One can see the data measured at a base temperature of 1.5 K, presented in blue.

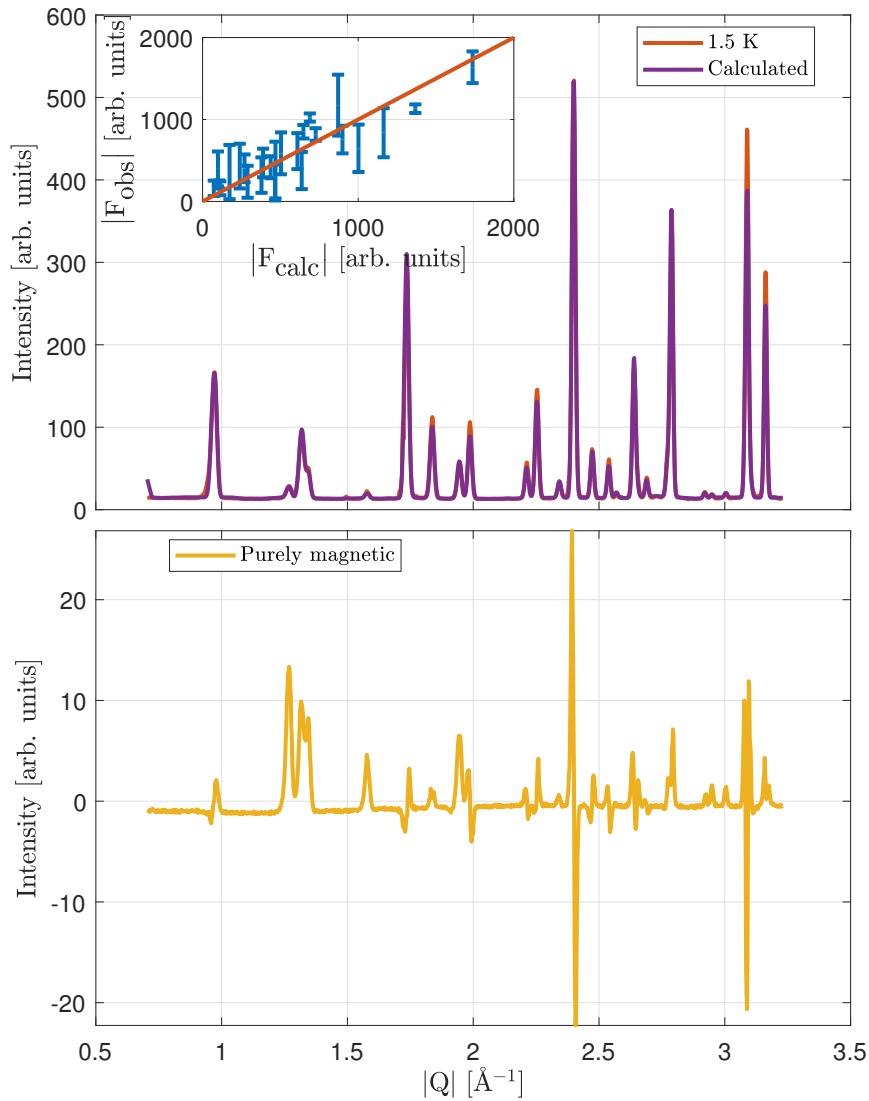


Figure 9.11: Refinement of neutron scattering data measured at the D20 powder diffractometer at a base temperature of 1.5 K (red). The result of the fit of the magnetic model is shown in purple. The purely magnetic signal has been obtained by subtracting data measured above the transition from the base temperature data and is shown in yellow. The inset shows the result of the magnetic refinement of data measured in the magnetic sector at the ZEBRA single crystal diffractometer, with Irreps  $\Gamma_1$  at a base temperature of 1.5 K. The graph shows the observed structure factors vs the calculated structure factors. The best fit shows a reasonable qualitative agreement between the data and the model

The part of the signal originating from purely magnetic scattering could be separated by measuring a similar pattern with similarly high statistics above the transition temperature, at 30 K, where the phonons are already frozen. The result of the subtraction is shown in yellow in Fig. 9.11. This pattern shows a negative background due to the reduction of paramagnetic scattering. Several peaks appear with a clear positive intensity. On the other hand, many other peaks are presenting up-down features: this is typical of a system whose lattice parameters change by a small amount, slightly changing the peak position. The relevant parameter in the subtracted pattern is thus more than ever the integrated intensity. The up-down feature is asymmetric for most peaks, showing that some intensity is present, and the maximum is placed either left or right of the peak position, indicative of asymmetric lattice parameter changes: one or several lattice parameter is reducing while one or the others are increasing. All of the separated magnetic intensity is located on top of a nuclear position. This is indicative of a magnetic propagation vector of  $\vec{k} = (0\ 0\ 0)$ . The analysis of the magnetic data was carried out using magnetic symmetry analysis software BasIreps[157, 158, 159] on this magnetic propagation vector, for Wyckoff sites 4e (Cu<sub>1</sub>) and 4i (Cu<sub>2</sub>), with space group C2/m. Table 9.2 shows the predicted possible irreducible representations (Irreps) written as  $\Gamma_1 - \Gamma_4$ . Irreducible representation analysis relies on the position of magnetic atoms and on the magnetic propagation vector. Basis vector of the allowed magnetic structure, as well as transformations linking magnetic moments on sites are given as a result of the symmetry analysis. Basis vectors components are written as (u,v,w) for the site 1, and (r,s,t) for the site 2, and specifies how magnetic moments on symmetry equivalent sites x,y,z and -x,y,-z are constrained and transformed by the different predicted Irreps.

	Cu <sub>1</sub> : x,y,z	Cu <sub>1</sub> : -x,y,-z	Cu <sub>2</sub> : x,y,z	Cu <sub>2</sub> : -x,y,-z
$\Gamma_1$	(u,v,w)	(-u,v,-w)	(0 s 0)	(0 s 0)
$\Gamma_2$			(r 0 t)	(-r 0 -t)
$\Gamma_3$	(u, v, w)	(u, -v, w)	(r 0 t)	(r 0 t)
$\Gamma_4$			(0 s 0)	(0 -s 0)

Table 9.2: Basis functions for irreducible representation (Irreps)  $\Gamma_\nu$  for magnetic propagation vector  $\vec{k} = (0\ 0\ 0)$ . The only relevant components are the real part, since the imaginary component vanishes. The indicated symmetry operations enable to construct both copper sites by application of the shown operator.

Here again, the Fullprof software was used[157] to perform the magnetic refinements. In a first step, paramagnetic data, measured at 30 K, was refined to verify and adjust the atomic structure. The scale factor from that refinement was then kept to a fixed number and used to perform the refinement of the subtracted data, purely magnetic. For both experiments on ZEBRA and D20, the paramagnetic and ordered phase data were measured with similarly high statistics. By subtracting the two patterns, one effectively eliminates the nuclear component, thus technically increasing the focus that the fit puts on the magnetic part, contributing to significantly reducing the errorbars on the fitted magnetic moment components. Ideally, this subtraction is performed between temperatures at which the phonons are already frozen,

meaning the Debye-Waller factor is constant and no peak broadening is observed. In practice, even if that situation is true, lattice parameters can still vary by a small amount, creating up-down features. The refinement processes the integrated intensity of a given peak so it does not matter that peaks appear as heartbeat-like curves, since the information on the magnetic contribution is held in the integrated intensity.

The experiment on ZEBRA used the four-circle geometry to access a wide range of nuclear reflections of a single crystal. The crystal used for the experiment turned out to present a rather strong mosaic behavior with up to three different crystallites that were identified as contributing to the signal, with an angular spread of up to two degrees (peak-center to peak-center angular distance). This did not enable a systematic collection of intensity for Bragg-nuclear reflections in all of the reciprocal space directions, despite using a combination of the four circle geometry to the advantage of the experiment and the two dimensional detector of ZEBRA. A total of 55 reflections were used to collect nuclear intensity at a temperature of 25 K. This data has been used to refine the nuclear structure. A total of 42 inequivalent reflections overlapping with the ones used for the crystal structure were collected at a base temperature of 1.5 K to study magnetic scattering and refine the magnetic structure. The result of the refinement of the most conclusive magnetic model is presented in the inset of Fig. 9.11. The selected irrep is  $\Gamma_1$  on both inequivalent copper sites.

Several combinations of irreps have been tried.  $\Gamma_2$  and  $\Gamma_4$  are not defined on copper site 1, and it turns out that it is not possible to obtain a stable magnetic refinement when using any of these two possibilities on site 2. Slightly more generally, it appears that no refinement could be performed using  $\Gamma_\mu$  on site 1, and  $\Gamma_\nu$  on site 2, with  $\mu \neq \nu$ . Indeed, all these combinations have been tried and fail to produce a solution converging to a local minimum of any goodness-of-fit metric, but rather strongly diverging. This leaves only two possible combinations available:  $\Gamma_1$  or  $\Gamma_3$  on each site. It appears that using  $\Gamma_3$  does not fit properly all the magnetic peaks with no up-down feature, main signature of magnetism in the sample,  $\Gamma_3$  has thus been discarded. The best refinement is obtained by using  $\Gamma_1$  on both sites. Fig. 9.11 shows in purple a prediction of the base temperature data, using as input the result of both magnetic and nuclear fits. The associated ground state is shown explicitly in Fig. 9.12.

Fig. 9.12a. shows the resulting magnetic ground state when observing the crystal structure from the crystallographic b-axis, while Fig. 9.12b shows the in-plane configuration of moments. Table 9.3 contains the result of the fits of Irrep  $\Gamma_1$  on both copper sites. The second line in the table indicates the components of the magnetic moments when forcing the moments to be in the ab-plane. This slightly reduces the total moment along the crystallographic b-axis. When setting the Irreps coefficients to the result obtained from refining the magnetic data obtained from the powder diffraction experiment, one can constrain the refinement of the single crystal experiment carried out at ZEBRA, which then gives free parameters that can be

### 9.3. Neutron diffraction unveils 120° magnetic order

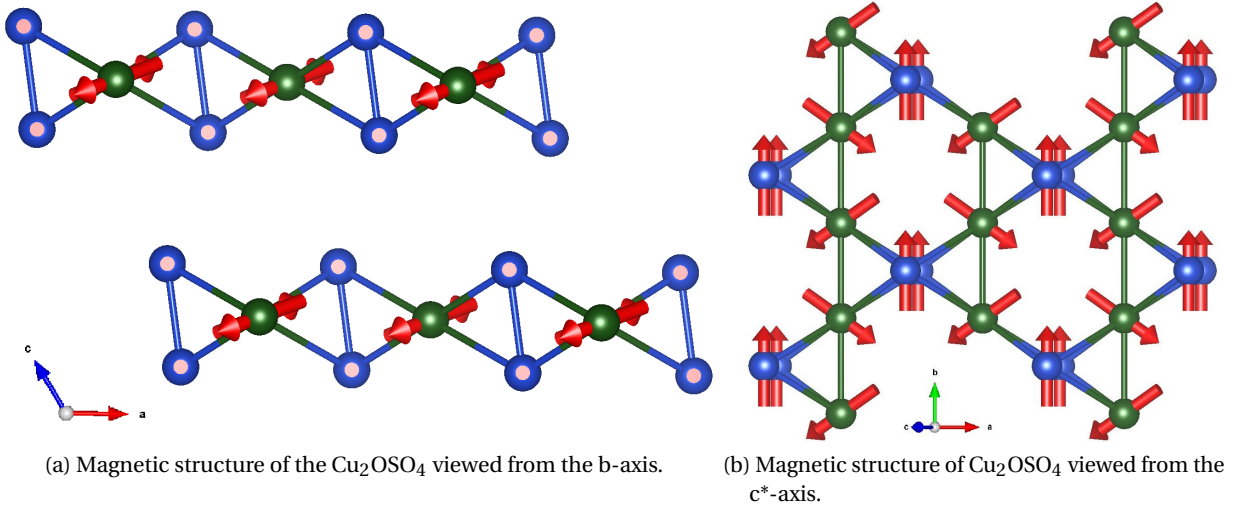


Figure 9.12: Magnetic ground state of dolerophanite, showing long-range order. Spins on the  $\text{Cu}_2$  position are parallel and along the b-axis, while those at the  $\text{Cu}_1$  position alternate both left and right of the a-axis, and up and down of the ab-plane. The spins do not alternate between planes. This creates a state with a small effective moment along the b-axis, all the moments along a and  $c^*$  being canceled by symmetry.

	u [ $\mu_B$ ]	v [ $\mu_B$ ]	w [ $\mu_B$ ]	s [ $\mu_B$ ]	$  \vec{\mu}_{\text{Cu}_1}  $ [ $\mu_B$ ]	$  \vec{\mu}_{\text{Cu}_2}  $ [ $\mu_B$ ]
w $\neq$ 0	0.83(5)	-0.47(4)	0.30(9)	0.86(5)	0.98(4)	0.86(5)
w = 0	0.70(4)	-0.45(5)	0	0.91(6)	0.83(8)	0.91(6)

Table 9.3: Fit result using  $\Gamma_1$  to model the magnetic ground state of Dolerophanite. There is no guarantee that moments should have out-of-plane components. The last row corresponds to moments constrained to be lying in the ab-plane.

reasonably adjusted and lead to a magnetic structure in agreement with that obtained from refinement of the D20 data.

The magnetic structure consists in a ferromagnetic alignment of spins on the  $\text{Cu}_2$  sites, with moments constrained by symmetry to lie along the crystallographic b-axis. The moments on copper site 1 are non-collinear, and alternating along the crystallographic a- and c-axes in a fashion that cancels moments in these two directions, contributing to a finite moment exclusively along the crystallographic b-axis. The moments on the  $\text{Cu}_1$  sites can be described as an alternating, non-collinear, antiferromagnetic chain. It corresponds to the configuration that would satisfy the Hamiltonian of a regular antiferromagnetic chain, embedded in an external magnetic field, with field direction along the chain, and a field strength of half the field fully polarizing the spins of the sample. The  $\text{Cu}_2$  dimers can be viewed as acting as a link between the different copper chains. Each triangular unit forms a structure consisting in

four spins, approximately creating a  $120^\circ$  configuration. The net moment along the crystallographic a- and c-directions cancels out, resulting in a net moment along the crystallographic b-axis. By using the values of the moments given by best-fitting Irrep  $\Gamma_1$ , provided in table 9.3, the moment along the crystallographic b-axis has been estimated to  $0.23(3) \mu_B$ , which effectively corresponds to a quarter of the sum of the moments on  $\text{Cu}_1$  and  $\text{Cu}_2$ . This value is in perfect agreement with the previously measured magnetization curves at base temperature presented in Fig. 9.9.

In order to study the way magnetic order sets in the system, temperature dependent neutron diffraction was carried out on the D20 diffractometer. Using the LBF technique, one can extract the lattice parameters temperature dependence. This change is presented in Fig. 9.3. The evolution of lattice parameters in function of temperature is consistent with a weak magneto-elastic effect occurring at, and below the same temperature as the transition to a magnetically long-range ordered state. Fig. 9.13 shows the temperature dependence of the magnetic moments from both copper sites in  $\text{Cu}_2\text{OSO}_4$ .

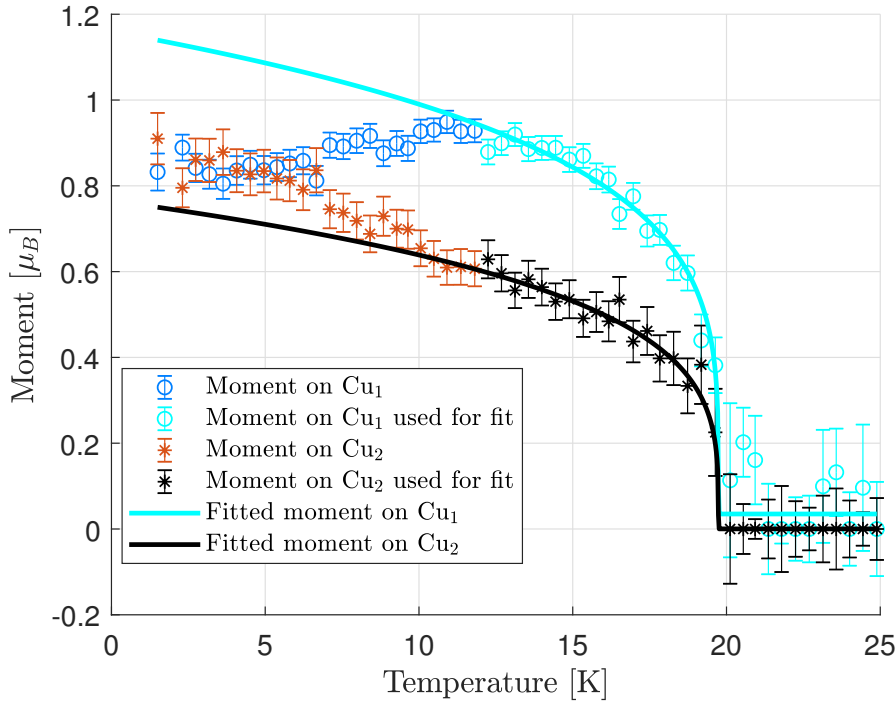


Figure 9.13: Temperature dependence of magnetic moments in Dolerophanite, obtained from refining data at finite temperature with Irrep  $\Gamma_1$ . Solid lines correspond to a power-law fit used to model the critical behavior of the moments:  $\mu(T) \propto (T_N - T)^{2\beta}$ . To better model the behavior, the fitting was performed on a restrained temperature range (black and cyan data points).

Irrep  $\Gamma_1$  has been used to fit the temperature dependent data in a cyclic refinement. Critical

behavior was modeled using equation(9.8).

$$\mu(T) \propto (T_N - T)^{2\beta} \quad (9.8)$$

Fitting has been restrained to a temperature range close to the transition, to better model the critical description, only valid in the vicinity of the phase transition. In Fig. 9.13 data in black and cyan markers correspond to data used for the fit, which yields  $T_N = 19.7$  (07) K, shared by the two sites, and  $\beta = 0.11$ (1) for site 1 and  $\beta = 0.24$ (2) for site 2. These critical exponents are very different, showing that both inequivalent sites, despite ordering at the same temeptrature, may order in a very different way.



## **9.4 Discussion on static properties of $\text{Cu}_2\text{OSO}_4$**

Materials with magnetic spins on the Kagomé lattice have long been at the forefront of the research in experimental condensed matter physics. For a long time, Herbertsmithite was one of only candidates exhibiting a regular Kagomé lattice and its physics, with the realization of a spin liquid state. Multiple studies concluded that small perturbations to ideal conditions quickly destabilized the spin-liquid physics. In that context, copper oxysulfate presents a new lattice, two dimensional, offering multiple possibilities to study the stability of spin-liquids, the delicate balance between long-range order and quantum fluctuations. In that spirit,  $\text{Cu}_2\text{OSO}_4$  can be considered as a playground where significant perturbations to the Kagomé lattice can help quantify the effects of fluctuations and strong frustration -denoted by its finite frustration ratio  $|\Theta_{\text{CW}}|/T_N \sim 3.75$ - and provide better understanding on their experimental and theoretical effects on the quantum spin-liquid state.

The magnetic structure determined by means of neutron scattering is supported by the analysis of the crystal structure and exchange paths. There exists a  $\text{Cu}_2 - \text{O} - \text{Cu}_2$  exchange path, connecting the two closest  $\text{Cu}_2$  ions with an oxygen atom, used as ligand. According to the Goodenough-Kanamori-Anderson rule, the  $\text{Cu}_2 - \text{O} - \text{Cu}_2$  bond angle of  $\sim 93.0^\circ$  appears to be supporting weak ferromagnetism, associated to a coupling noted  $J_{22} < 0$ . The interactions along the chain, involving the two closest  $\text{Cu}_1$  ions, can be associated partly to a  $\text{Cu}_1 - \text{O} - \text{Cu}_1$  exchange path with bond angle of  $114.9^\circ$ . GKA rules predict that such an angle favors dominant antiferromagnetic interactions combined into a coupling noted,  $J_{11} > 0$ . There are exchange paths that couple copper atoms from the chains to other copper atoms from the dimer. Two symmetry inequivalent superexchange paths may be responsible for that coupling. One of them forms a  $\text{Cu}_1 - \text{O} - \text{Cu}_2$  angle of  $104.9^\circ$ , while the other is of  $117.3^\circ$ . Once more, GKA rules predict that these couplings are antiferromagnetic. They are noted  $J_{21a} > 0$  and  $J_{21b} > 0$ .

Many other exchange paths exist, but none of them links copper atoms with the mediation of a single oxygen atom, giving rise to regular superexchange with a single ligand. Additional exchange paths, in-plane or out-of-plane involve hopping spins through (at least) a sulfur tetrahedron. These  $\text{Cu} - \text{O} - \text{S} - \text{O} - \text{Cu}$  super-superexchange paths help creating a coupling that connects  $\text{Cu}_2$  atoms of the dimer across Kagomé units,  $J_{2nn}$ , as well as an out-of-plane coupling, connecting planes with each other. It is quite possible that this predicted weak coupling is responsible for the establishment of magnetic order by effectively increasing the dimensionality of the systems, in accordance with the Mermin-Wagner theorem (copper atoms usually present no single ion anisotropy[160, 161, 162], even though it has been evidenced that it can in practice happen[163].). Estimating the relative strength of that coupling, with respect to the dominant in-plane interaction is a task that can be performed correctly by neutron scattering spectroscopic studies, and a precise modeling of measured dispersion relations. The long range order can be settling in two dimensional systems when a considerable source of anisotropy is relevant. Even though it has been mentioned that copper atoms usually do

not produce sizable single ion anisotropy, it is now quite established that another anisotropy mechanism plays a role in many copper-containing systems. It has been experimentally evidenced that a non negligible Dzyaloshinskii-Moriya interaction (DMI) is present in the system [164], supported by careful symmetry analysis of the crystal structure. Its intensity has been estimated to be  $D \sim 7$  K. The relative importance of this antisymmetric interaction can be estimated by taking the Curie-Weiss temperature as a measurement of the interaction strength in the system, one obtains  $D/J \gtrsim 0.1$ . It has been predicted that in the case of the Kagomé lattice, DMI anisotropy may induce a quantum phase transition stabilizing the  $120^\circ$  order above  $D_c = 0.1J$  [165, 166]. These two relative orders of magnitudes tend to suggest that the DMI may be responsible for the establishment of the  $120^\circ$  in copper oxysulfate, and that subsequently, the system locates itself close to a quantum phase transition. Such a transition could potentially be reached by tuning external parameters, such as the pressure of the system, or chemical substitution.

A small, time dependent and asymmetrical hysteresis has been noted to open up at low temperatures. The time dependent character was observed by a significant difference between results obtained from measurements with a ramping field showing the hysteresis, while measurement with a settled field at each field-point showed little to no hysteresis. This time dependence deserves further studies, and the asymmetry of the hysteresis has been tentatively attributed to the exchange bias phenomenon, consistent with a potential couplings between sub-units from both ferromagnetic and antiferromagnetic interactions.

To summarize, from bulk measurements and neutron diffraction, a solid understanding of static properties of the ground state of dolerophanite could be built up. It has been confirmed that the compound retains its structural properties down to temperatures as low as 1.5 K, and that the spin half picture models the susceptibility and heat capacity data with good agreement. The Curie-Weiss temperatures are rather isotropic, pointing towards Heisenberg interactions, and are of the order of 70 K, considerably higher than the transition temperature. This indicates a competition between interactions in the system, resulting in the suppression of long range order for a wide temperature range. Long range order does get established below 20 K, with neutron scattering revealing the details of the magnetic ground state, corresponding to the  $120^\circ$  state. It is quite interesting that this specific ground state is selected, even though the model is far away from an ideal Kagomé or triangular lattice: one third of the sites is replaced by a set of ferromagnetic dimers. Finally, the relatively small entropy associated to the transition, most of it being encapsulated in correlations, suggests that subtle dynamical effects may take place in the system, associated to the formation of ferromagnetic dimers,  $120^\circ$  triangles, and relative alignment of such sub-units. Inelastic neutron scattering studies have been performed and are detailed in the next section, shedding even more light on the system.

## **9.5 Spin dynamics: two decoupled sub-lattices and a mean field**

In quantum magnetism, the process of describing faithfully the physics governing a given compound most of the time comprises the essential step of finding a Hamiltonian describing the magnetism in the sample[167]. In order to try and establish the proper Hamiltonian that describes the physics of copper oxysulfate, the most natural tool that comes to mind is inelastic neutron scattering. This type of measurement gives access to the dynamical structure factor at several different reciprocal lattice points, and for different energy transfer values[168, 169, 170]. The results of these experiments provide a way of probing spin excitations in quantum magnets, that can then be described by a model and in many cases are related to spin waves. In this specific case, experiments have been carried out on a co-alignment of five Cu<sub>2</sub>OSO<sub>4</sub> crystals, that accounted for a total sample mass of around 700 milligrams. The measurements were carried out using triple axis spectrometers: the EIGER and IN22 spectrometers at SINQ, PSI and at the ILL in Grenoble, using thermal neutrons and giving optimized energy resolution and flux for energy transfers of about 10 meV, and the TASP triple axis, at SINQ, PSI, using cold neutrons and giving more insights on lower values of energy transfer. In a regular experiment, the sample is oriented in a scattering plane, defined by two inequivalent and non parallel lattice reflections. Barring kinematic conditions restrictions and instrument design, virtually any point in the reciprocal lattice defined by a linear combination of these two reflections can be reached. Several scattering planes have been studied. For practical reasons, due to the shapes of the crystals and their usable facets, the (2L K -L) scattering plane has been the most studied. It contains the [0 K 0] direction, which is that of the chains of Cu<sub>1</sub> atoms, the perpendicular direction however [2L 0 -L] is not in the Kagomé plane, but rather corresponds to a mixture between the in-plane, perpendicular direction, and the out-of-plane direction. The Kagomé plane is the crystallographic ab-plane, and has thus little physical sense. Indeed, Dolerophanite is a monoclinic compound, implying that in the usual choice of unit cell, the crystallographic b\* and b-axes are parallel to each other, however the a and a\*-axes are not. Since actual physical processes take place in the reciprocal lattice rather than in the direct one, trying to measure the ab\*-plane makes little sense. It appears that the a\* direction is roughly that of the projection of the Cu<sub>1</sub>-Cu<sub>2</sub> nearest neighbor bond, projected on the plane perpendicular to b, while the c\* direction is perpendicular to the Kagomé planes. Since there are clear, bright, and well defined excitations in the [0K0] direction (shown below), this motivated the choice of the [0K0] as a reference, and the subsequent choice of the (HK0) plane to study the in plane dispersion and the (0KL) scattering plane to elucidate the out-of-plane scattering.

### 9.5.1 Experimental evidence for magnons

Results are presented in Fig. 9.14. Fig. 9.14a and Fig. 9.14b show measured spin wave dispersions along the chain direction. The red dots correspond to fits of individual scans by Gaussian functions that enable to track the position of the spin wave modes in the (Q,E) space.

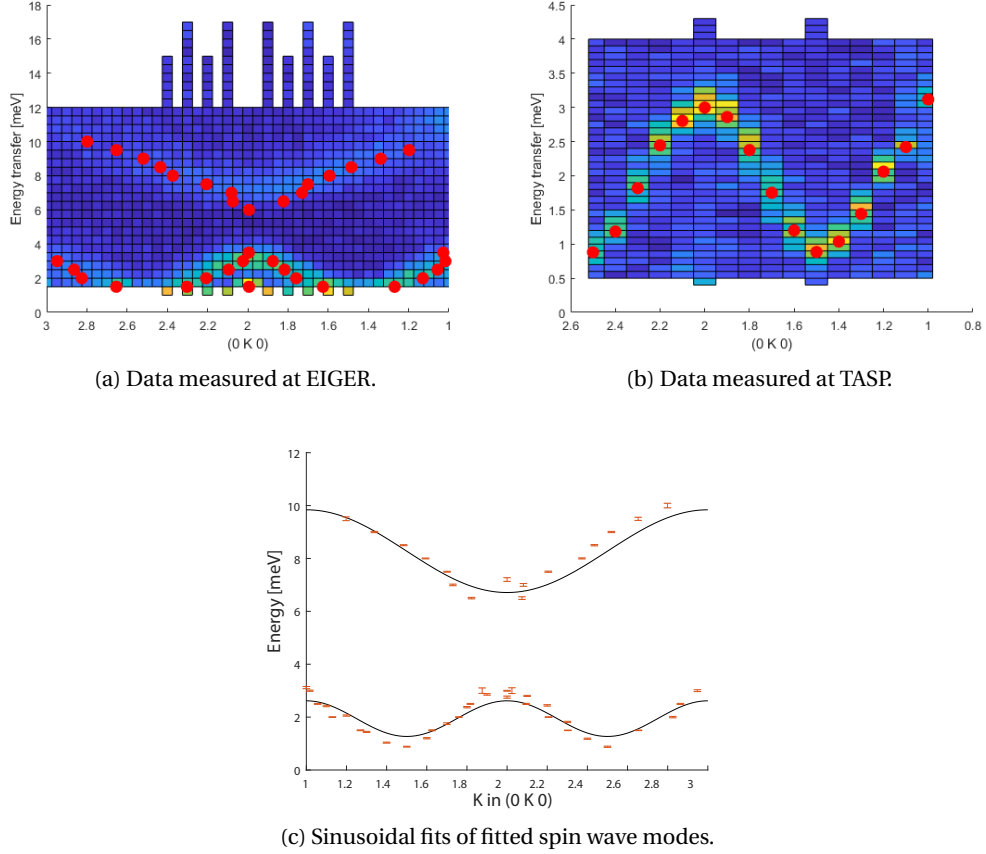


Figure 9.14: Inelastic neutron scattering data consisting of constant energy scans. The x axis is expressed in reciprocal lattice units. The red dots correspond to the position of gaussian curves fitted to each individual scan. The color corresponds to the neutron normalized intensity.

It appears that two modes of excitation are clearly visible and dispersive in the [0K0] direction. The lower mode is gapped, and reaches its maximum at the Brillouin Zone Center, and is repeated two times for a single Brillouin Zone. The upper mode presents a different periodicity, double of that of the lower mode. Moreover it reaches its minimum at the zone center and maximum at the zone boundary. The inelastic neutron scattering scans could be well fitted, as shown in Fig. 9.14 and the position of the mode could be fitted as well.

Fig. 9.14c. shows sinusoidal fits of the obtained spin wave dispersion. These fits yields the

following parameters:  $J = 1.57 \pm 0.29$  meV for the upper mode,  $J = 0.67 \pm 0.08$  meV for the lower mode and a gap of  $\Delta = 1.94 \pm 0.06$  meV for the lower mode and  $\Delta = 8.28 \pm 0.20$  meV for the upper mode. The upper mode seems to present the same periodicity as the one expected for the  $J_1$  coupling, linking  $\text{Cu}_1$  atoms. The lower mode's period is half of that of the upper mode, which would be consistent with a coupling linking atoms separated by twice the distance of atoms in the  $\text{Cu}_1$  chain. This distance is consistent with a coupling between  $\text{Cu}_2$  atoms from the dimers, across the whole Kagomé unit.

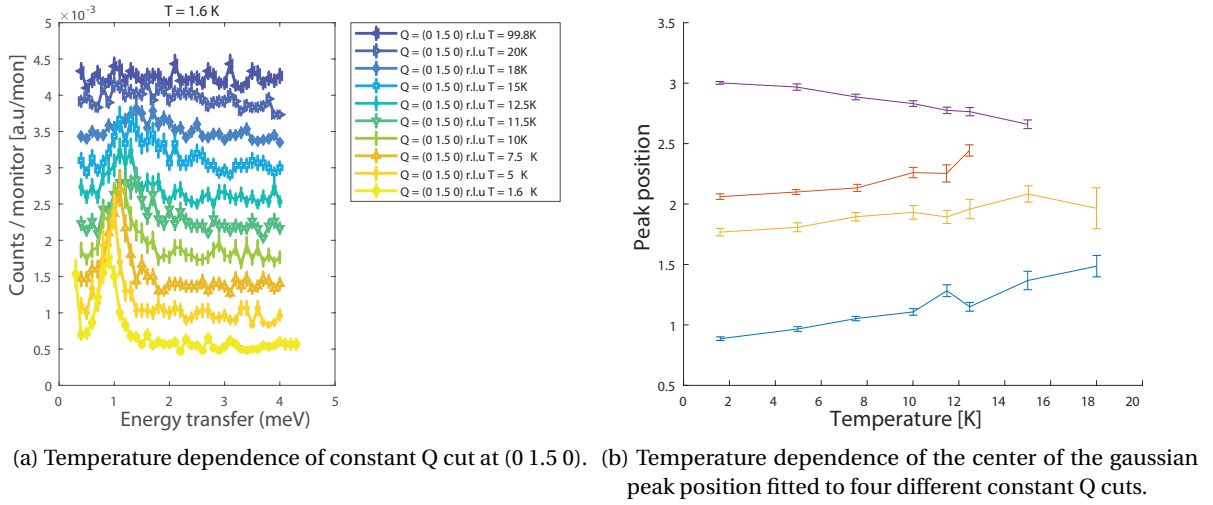
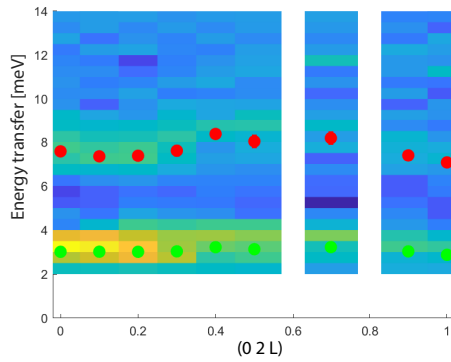


Figure 9.15: Temperature dependence of different constant Q cuts.

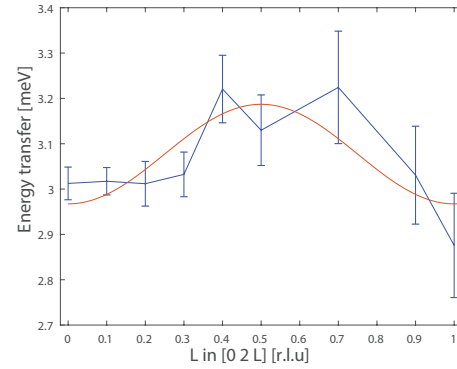
Fig. 9.15 shows that these scans are temperature dependent, with peaks that vanish at the transition temperature, confirming their magnetic origin. It seems that the temperature narrows down the bandwidth of the excitation, in a similar fashion to hard-core bosons[171, 172, 173].

Fig. 9.16 shows the result of scans along the direction perpendicular to the Kagomé planes for a representative direction. Fig. 9.16a shows the data measured in the [02L] direction for different values of L, and in red and green the respective fits of the dispersion. Fig. 9.16b and Fig. 9.16c present sinusoidal fits of the obtained dispersions.

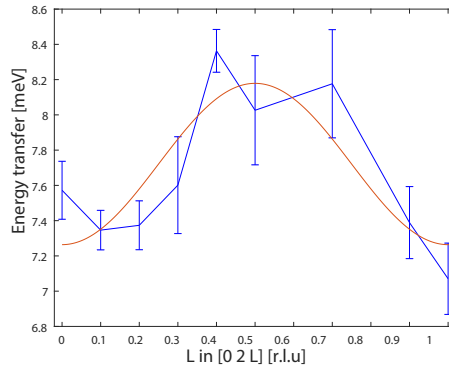
It has thus been shown that when fitting such observed features to a dispersive out-of-plane excitation, one obtains an upper bound on the strength of the potential coupling responsible for that dispersion. It can hence be concluded that the planes can be thought of as magnetically decoupled, since the two couplings between them have been estimated to  $J = 0.45 \pm 0.13$  meV for the upper mode and  $J = 0.11 \pm 0.04$  meV for the lower mode. Indeed, in that crystal structure, the planes are stacked along the  $c^*$ -crystallographic axis, so measurements along [01L] and [02L] exhibiting a very small dispersion in the L-direction reasonably leads to the



(a) Representative inelastic neutron scattering data of Dolerophanite in the out-of-plane direction. The color scale corresponds to the normalized neutron counts.



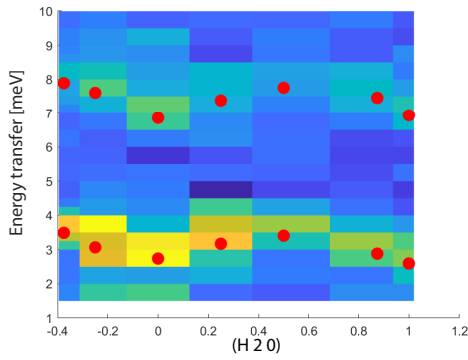
(b) Fits of the lower mode.



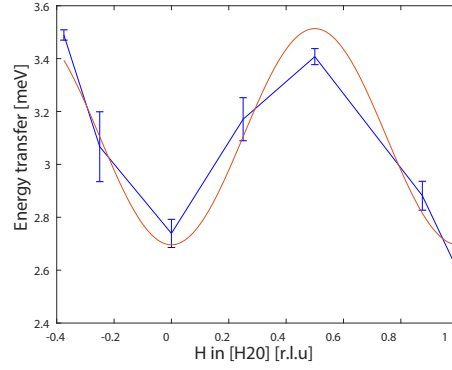
(c) Fits of the upper mode.

Figure 9.16: Inelastic neutron scattering data in the  $[02L]$  direction, representative of out-of-plane scattering.

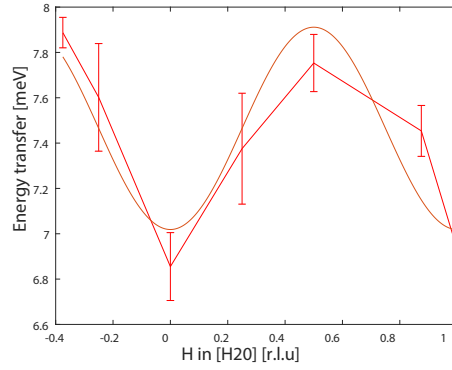
conclusion that the compound is mostly two dimensional, with the main dispersion in the  $ab$ -plane. The periodicity of the observed modes is consistent with a coupling that would link atoms separated by a distance of half a unit cell. Such a bond distance is in full agreement with interactions supported by bonds between atoms from two different Kagomé planes.



(a) Representative inelastic neutron scattering data of Dolerophanite in the Kagomé plane, perpendicular to the  $\text{Cu}_1$  chain. The color scale corresponds to the normalized neutron counts.



(b) Fits of the lower mode.



(c) Fits of the upper mode.

Figure 9.17: Inelastic neutron scattering data in the  $[\text{H}20]$  direction, representative of in-plane scattering, perpendicular to the  $\text{Cu}_1$  chains.

There is also evidence for dispersive features in the  $[\text{H}00]$  direction, as presented in Fig. 9.17. The observed features along  $[\text{H}00]$  are clearly dispersive. The intensity is presented as a color scale in Fig. 9.17a. The two excitation modes, already visible in the  $[0\text{K}0]$  direction are dispersing in the  $[\text{H}00]$  direction. The results of the fit of the lower and upper mode are presented in Fig. 9.17b and Fig. 9.17c respectively. A sinusoidal fit provides the following values for the potential couplings:  $J = 0.44 \pm 0.13$  meV for the upper mode and  $J = 0.41 \pm 0.06$  meV for the lower mode. The mode periodicity is consistent with having a coupling linking two atoms separated by half a unit cell in the  $[\text{H}00]$  direction. The only atoms separated by such a distance in the  $[\text{H}00]$  direction are neighboring  $\text{Cu}_1$  atoms from neighboring  $\text{Cu}_1$  chains.

**9.5.2 Modelling**

The excitations and periodicity observed along the [0K0] direction are consistent with a coupling between atoms separated by half a unit cell for the higher mode, and a full unit cell for the lower mode. This naturally tends to associate the higher mode to a coupling that would be hosted by the Cu<sub>1</sub>-Cu<sub>1</sub> nearest-neighbor bond, predicted to be antiferromagnetic by inspection of the superexchange path. The lower mode could be associated to a different bond length: it could be a second nearest neighbor Cu<sub>1</sub> interaction, or a dimer-dimer interaction between Cu<sub>2</sub> atoms across Kagomé units. Despite best efforts using the spinW MATLAB package[174], providing a way of computing numerically spin wave spectra from linear spin wave theory[175, 176, 177], it seems that no simple spin wave model with interactions between Cu<sub>1</sub> and Cu<sub>2</sub> sub-lattices describes truthfully the excitations along the [0K0] direction. Indeed, no scheme of coupling seems to reproduce the fact that the maximum of the dispersion of the lower mode is reached at the Brillouin Zone Center, with a periodicity such that the maximum is also reached at the Zone Boundary. However, this type of mode shows a surprising similarity to the dispersion of an antiferromagnetic chain embedded in a magnetic field[178, 179, 180, 181, 182]. That magnetic field would here be generated by the effects of the spins of the Cu<sub>1</sub> atoms. At the level of the modeling, the magnetic field exerted by Cu<sub>1</sub> on Cu<sub>2</sub> would thus be the same as the one exerted by Cu<sub>2</sub> on Cu<sub>1</sub>, the field being thus staggered. The lower mode would thus be described by a coupling between Cu<sub>2</sub> atoms across Kagomé units, called  $J_{2nn}$ , the effect of the magnetic field exerted by atoms of the Cu<sub>1</sub> chain produces an effective mean field that aligns the spins ferromagnetically along the crystallographic b-axis. In this coupling scheme, the Cu<sub>1</sub> atoms are coupled by a strong  $J_1$  nearest neighbor interaction, and embedded in the reciprocal mean field generated by Cu<sub>2</sub> atoms. An appropriate field strength is thus the field corresponding to approximately half the saturation field, creating the 120° degree configuration. Additional couplings have been added to stabilize both the magnetic structure and the upper mode dispersion: a  $J_{cross}$  coupling, linking Cu<sub>1</sub> atoms diagonally across the Kagomé units, and a  $J_2$  coupling, creating an interaction between Cu<sub>1</sub> atoms from neighboring chains. This complex coupling scheme has been summarized in Fig. 9.18.



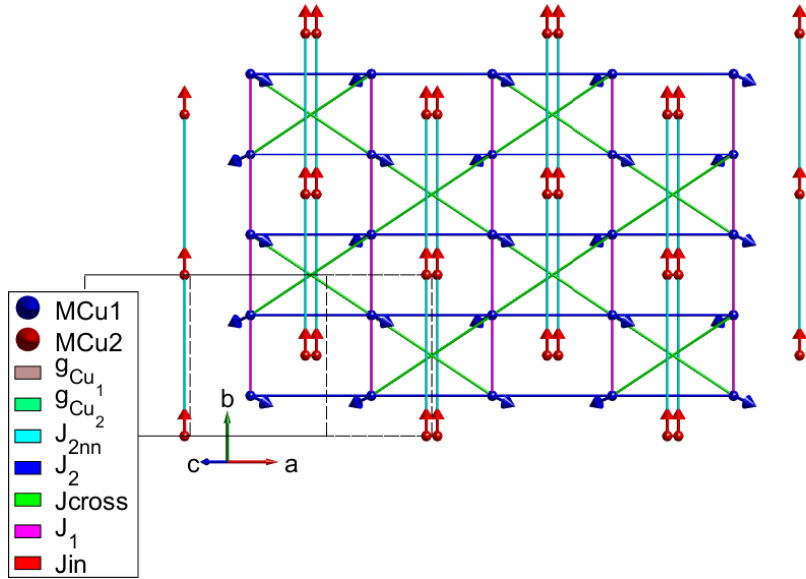


Figure 9.18: Coupling scheme best describing magnetic excitations in the  $\text{Cu}_2\text{OSO}_4$  along the crystallographic  $b$ -axis.  $\text{Cu}_1$  atoms are shown in blue and  $\text{Cu}_2$  atoms are shown in red. The main couplings are  $J_1$  (purple) and  $J_{2\text{nn}}$  (cyan). The other couplings are stabilizing the magnetic structure that is shown by the arrows. The view shows the  $ab$ -plane in which lie most of the couplings.  $J_{\text{in}}$  couples  $\text{Cu}_2$  atoms in the dimer with each other and there is no other out-of-plane coupling. The magnetic field is applied along the crystallographic  $b$ -axis.

The g-tensor has been slightly modified to push the higher mode to higher energies so that it lies in the correct, experimentally measured energy range. The current model can be characterized as a model with two decoupled sub-lattices made of  $\text{Cu}_1$  and  $\text{Cu}_2$  atoms, coupled through a mean field. The predicted dispersion around the magnetic ground state can be seen in Fig. 9.19 and matches the experimental dispersion to a very satisfactory qualitative level and in decent quantitative agreement.

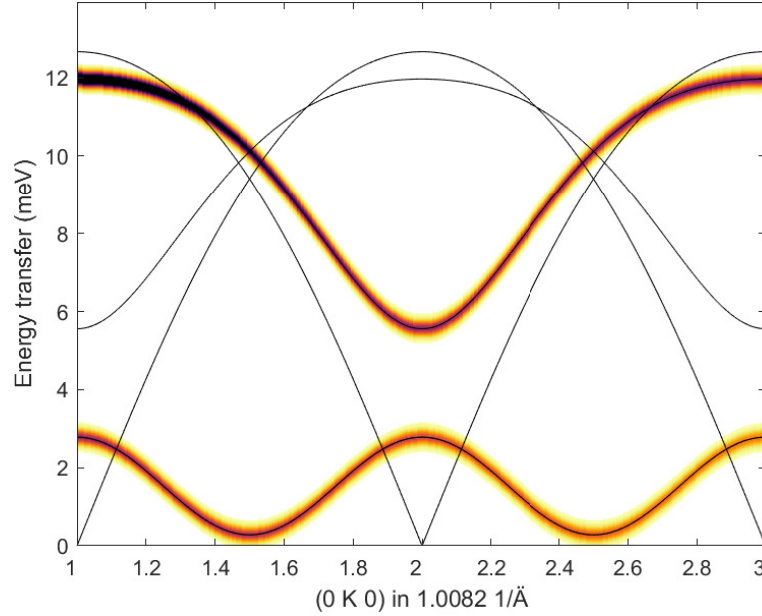


Figure 9.19: Excitations along the [0K0] chain predicted by mean field model of  $\text{Cu}_2\text{OSO}_4$  with the following parameters:  $J_1 = 5$  meV,  $J_{2nn} = 1.25$  meV,  $J_2 = 2.5$  meV,  $J_{\text{cross}} = -2.5$  meV,  $J_{\text{in}} = -0.005$  meV, and a field of 6 T in the crystallographic b direction.

The presented curve corresponds to the following values of coupling parameters:  $J_1 = 5$  meV,  $J_{2nn} = 1.25$  meV,  $J_2 = 2.5$  meV,  $J_{\text{cross}} = -2.5$  meV,  $J_{\text{in}} = -0.005$  meV. A very small ferromagnetic coupling  $J_{\text{in}}$  has been introduced for the sake of calculations stability. The ground state has been calculated by optimization of the energy by steepest decent and the excitations have been predicted by linear spin wave theory.  $J_1$  is assumed to be the dominant interaction since it seems to be the strongest from superexchange paths considerations. The second important coupling is  $J_{2nn}$  that creates the lower excitation mode. The coupling between  $\text{Cu}_1$  chains and  $\text{Cu}_2$  atoms has been replaced with a mean-field. This explains why the model does not truthfully represent the dispersion in other directions. When considering the case of a quantum interaction between sub-lattices and no mean field, a line of zeroes appeared as a mode predicted by the spin wave theory: this is a hint that the system is close in parameter space to a point where spin wave theory breaks down and cannot describe the physics correctly.

The next step to fully model quantum interactions in the problem is to change the model

to replace this mean field by an interaction that couples the two sub-lattices. Unfortunately no such coupling could be identified. It is worthwhile noting that the key ingredient in this mean field model is the presence of a virtual field along the crystallographic  $b$  direction. For that reason, magnetic excitations of the compound in other directions cannot be truthfully obtained from the model and are thus not presented.

## 10 $\text{K}_2\text{Ni}_2(\text{SO}_4)_3$ : frustration at its finest

### 10.1 Indications of 3D, $S=1$ quantum spin liquid

As previously mentioned, the search for spin liquids has been a burning issue of condensed matter physics[183, 184, 185] with the focus of low-dimensional systems without magnetic long-range order[186, 187, 188, 64]. The most promising realizations were found in quasi two dimensional antiferromagnetic systems, where considerable frustration coming from competing antiferromagnetic interactions suppresses the long range order. Such realizations are found in triangular system  $\text{YbMgGaO}_4$ [189], and in famously known Herbertsmithite[190, 191]. Three dimensional structures supporting spin-liquids candidates started to appear, such as in  $\text{Na}_4\text{Ir}_3\text{O}_8$ , whose structure can be described as a hyper-Kagomé model. In that compound, no evidence for long range order was observed down to 20 mK[192], pointing to a certain ubiquity of quantum spin liquids. A single compound has been evidenced as being a 3D lattice with a spin half quantum spin liquid ground state:  $\text{PbCuTe}_2\text{O}_6$ [193]. Most efforts were concentrated on spin half systems, but more recent contribution also demonstrated that spin one systems, in the likes of  $\text{NaGa}_2\text{S}_4$  may also be a fruitful playground to explore this physics[194], by the means of biquadratic contributions. Novel physics, such as the Kitaev model has also been realized with a lot of emphasis put on  $\alpha\text{-RuCl}_3$  and its field stabilized spin liquid ground state[195, 196]. An important example of three dimensional lattices that proved to challenge the rich quantum spin liquid physics is the trillium lattice where atoms are placed in equilateral corner-sharing triangles with complete three dimensional geometry. Previous work on  $\text{MnSi}$ , a compound realizing this lattice evidenced a pressure induced quantum phase transition with non-Fermi liquid behavior above the transition[197, 198]. Further developments proved that even though the trillium lattice presents the key ingredient of geometrical frustration, the system still develops magnetic long-range order [199, 200].

$\text{K}_2\text{Ni}_2(\text{SO}_4)_3$  belongs to a family of sulfates of the langbeinite type  $\text{K}_2\text{TM}_2(\text{SO}_4)_3$  realizing interconnected trillium lattices, which have been studied due to their ferroelectric behavior and related structural transition[201]. At high temperatures all the members of the langbeinite

family exhibit a high-symmetry cubic structure (space group  $P2_13$ ) while at low temperatures some of them sustain a transition to an orthorombic phase (space group  $P2_12_12_1$ ), ranging from 125 K in TM = Co to 457 K in TM = Ca. On the other hand  $\text{K}_2\text{Ni}_2(\text{SO}_4)_3$  does not show any indication of the structural transition, in accordance with the observed dependence of distortions on ionic radius[201].

First single crystals of the compound were synthesized using the Bridgman method[202]. This opened the way for intensive studies of this interesting compound: nickel atoms typically carry a spin one and the non centrosymmetric space group allows for non-trivial topological spin configurations(similar to the observed skyrmions in MnSi[203] and  $\text{Cu}_2\text{OSeO}_3$ [204]). Fingerprints of spin liquids can be detected in many ways, none of them however being a smoking gun signaling with certainty that the spin liquid is the ground state. A combination of techniques is typically used to show the absence of magnetic long-range order: this usually consists in a combination of susceptibility measurements,  $\mu\text{SR}$ , and neutron scattering. In that context being able to grow single crystals of the compound is paramount, since it opens up the possibility of measuring directional dependent inelastic neutron scattering and the potentiality of looking for continuous diffuse scattering patterns that have already been revealed in 1D and 2D systems[205].

### 10.1.1 Structure

It has been evidenced that in the frame of the study of spin-liquids, an essential ingredient on which physics relies may take the form of geometrical frustration. Compounds with complex lattices present many inequivalent bonds, exchange paths, and thus many inequivalent couplings. This asymmetry gives rise to complicated frustration patterns that are typically not balanced enough to break long range order, which prevails when cooling the system to a cold enough temperature. This comment also holds for complex, three dimensional interactions: in real compounds, one does not really control which couplings are relevant and more often than not, three dimensional compounds end up presenting couplings poisoning the precise equilibrium required to stabilize the spin liquid phase. This is why main searches focused on systems of lower dimensionality. Three dimensional lattices such as the pyrochlore lattice gained a lot of traction since they are remarkably well behaved in terms of couplings. In that context,  $\text{K}_2\text{Ni}_2(\text{SO}_4)_3$  appears to be both promising but at the same time already non-trivial. Indeed, its crystal structure is described by a very high symmetry, non centrosymmetric,  $\text{P2}_13$  cubic space group. Table 10.1 shows all the inequivalent positions necessary to construct the unit cell of  $\text{K}_2\text{Ni}_2(\text{SO}_4)_3$ , with fractional coordinates X, Y, Z. Both nickel and both potassium atoms are placed at highly symmetrical positions, while oxygen atoms are occupying less symmetrical positions.

Atom label	Oxydation state	Wyckoff position	X	Y	Z
K1	K1+	4 a	0.8149(2)	0.8149(2)	0.8149(2)
K2	K1+	4 a	0.0488(2)	0.0488(2)	0.0488(2)
Ni1	Ni2+	4 a	0.3354(1)	0.3354(1)	0.3354(1)
Ni2	Ni2+	4 a	0.5992(1)	0.5992(1)	0.5992(1)
S1	S6+	12 b	0.2171(2)	0.3764(2)	0.0191(2)
O1	O2-	12 b	0.3079(6)	0.2731(6)	0.9616(6)
O2	O2-	12 b	0.0756(6)	0.3293(6)	0.0035(6)
O3	O2-	12 b	0.2410(7)	0.5013(7)	0.9415(7)
O4	O2-	12 b	0.2465(6)	0.4050(7)	0.1614(6)

Table 10.1: Inequivalent atomic positions in  $\text{K}_2\text{Ni}_2(\text{SO}_4)_3$ .

The unit cell is however described by two inequivalent Nickel ions, and the formed magnetic lattice develops in a complex three dimensional structure. The two crystallographically nonequivalent  $\text{Ni}^{2+}$  ions form an intricate 3-D magnetic lattice in which individual  $\text{NiO}_6$  octahedra are separated and connected by  $\text{SO}_4$  tetrahedra, as shown in Fig. 10.1.

Fig. 10.1a shows the crystal structure with atoms in the first unit-cell, there are eight nickel atoms, with two inequivalent positions, and thus four symmetry operators creating the whole

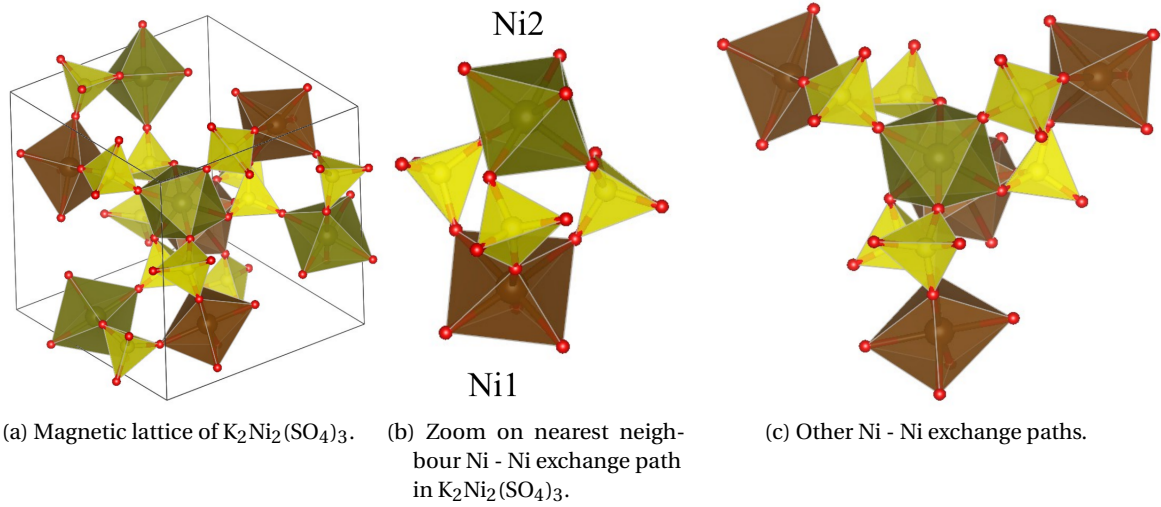


Figure 10.1: View of the crystal structure of  $\text{K}_2\text{Ni}_2(\text{SO}_4)_3$ . A full unit cell is shown (left). The nickel atoms are shown in brown, oxygen atoms in red, and sulfur atom in yellow. The solid line corresponds to the limits of the unit cell. The simplest examples of Ni - Ni exchange paths are also shown (middle), as well as more complex ones (right).

unit cell. Fig. 10.1b shows how nearest neighbor interactions are formed in the compound: it is supported by a Ni - O - S - O - Ni exchange path. In one instance there are three symmetrically identical bridges between  $\text{Ni}_1$  and  $\text{Ni}_2$  while in other there are double and single bridges, such as shown in Fig. 10.1c. Without a prior knowledge of the strength of individual magnetic interactions it is hard to classify this material and hypothesize whether it belongs to a 'standard' 3-D material or maybe the reduction of the effective dimensionality and/or geometrical frustration plays some role to lower the complexity of the lattice to form a simpler one, both from the dimensionality and from the couplings point of view. From the purely magnetic lattice point of view, a list of bonds could be extracted from the crystal structure. These bonds can be classified according to their lengths, and are shown in Table 10.2. It appears that the main characteristic distances can be grouped in five different classes that can be associated to five different Heisenberg couplings labeled:  $J_1, J_2, J_3, J_4, J_5$ . These classes of bonds are presented in Fig. 10.2.

Label	$J_1$	$J_2$	$J_3$	$J_4$	$J_5$
Distance [Å]	4.429	4.901	6.084	6.121	6.127

Table 10.2: Bond lengths in  $\text{K}_2\text{Ni}_2(\text{SO}_4)_3$ .

The effects of the different bonds can be apprehended from these images. The gray and purple atoms are nickel atoms created by the two crystallographically inequivalent positions. Fig.

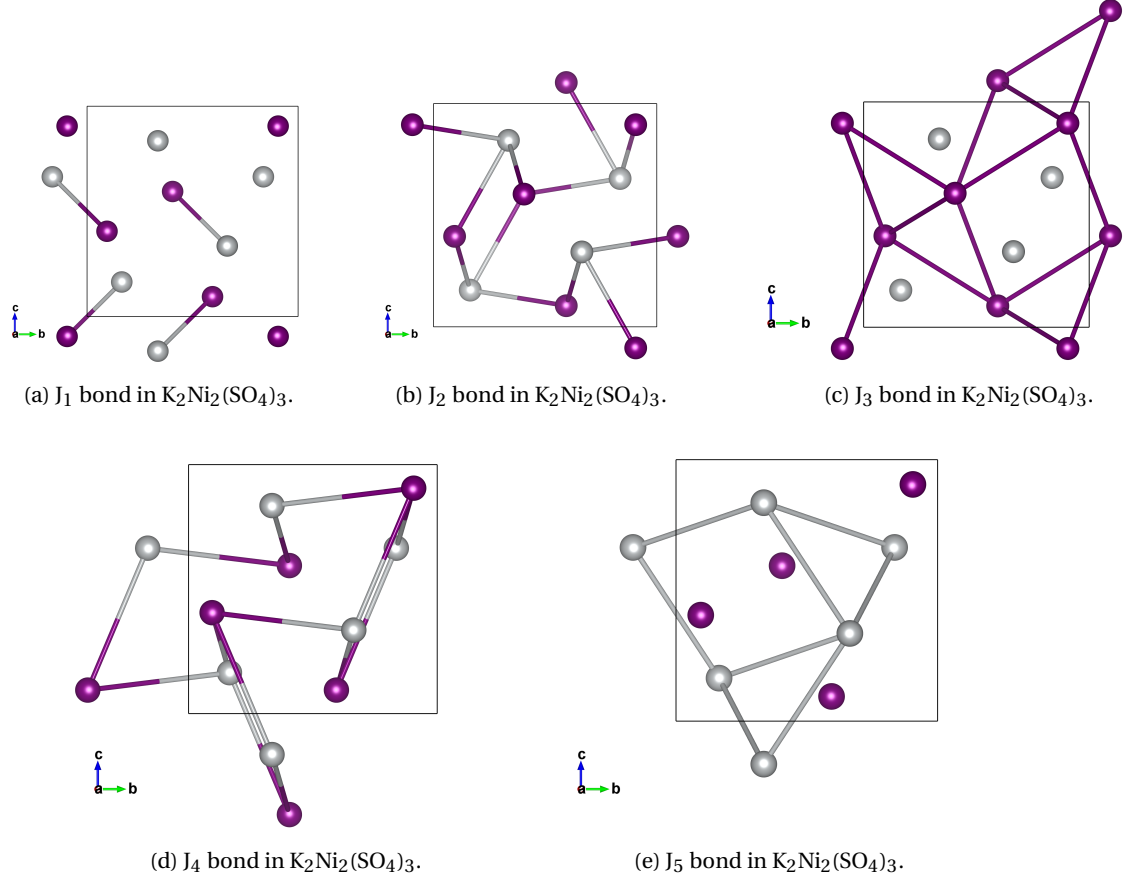


Figure 10.2: Nearest neighbor magnetic bonds in  $K_2Ni_2(SO_4)_3$ . Only the magnetic (nickel) atoms are shown, colors correspond to different inequivalent sites. The black, solid line is the unit-cell, the structure is viewed from the crystallographic  $a$ -axis.

10.2a shows that the  $J_1$  coupling indeed is the nearest neighbor bond, however using only this bond does not form a lattice. Fig. 10.2b and Fig 10.2d show other bonds that create couplings linking the whole lattice. Finally, Fig. 10.2c and Fig. 10.2e show other bonds that link atoms exclusively within a single sublattice, formed by atoms from only one of the two crystallographically inequivalent positions. As a final note, Density Functional Theory (DFT+U) calculations with the Generalized Gradient Approximation (GGA) indicate that the bond supporting strongest, and antiferromagnetic interaction is the  $J_4$  bond, which should thus be thought of as the primary source of magnetic interaction in the system, in any kind of modeling.  $J_4$  connects the two trillium lattices formed by couplings  $J_3$  and  $J_5$ , and would lead to antiferromagnetic order if it was the sole source of magnetic interaction in the system. The trillium lattices are made of triangular units, arranged in a corner-sharing fashion in a three dimensional pattern. It is the main source of frustration in the system. A single trillium lattice has been theoretically predicted to not be frustrated enough to have a spin-liquid ground state[206, 207]. In this system, two trillium lattices are interconnected through



another interaction, which has been predicted by DFT+U calculations to be the strongest, and antiferromagnetic, seconded by the two antiferromagnetic trillium interactions. It can also be noted that the coupling associated to the nearest neighbor bond is not the strongest one, this can be explained by the variety of exchange paths linking the nearest neighbor nickel atoms, resulting in a reduction of the coupling strength due to quantum-mechanical interference between the different paths.

## 10.1.2 Heat Capacity

The specific heat  $C_p$  was measured from a base temperature of 85 mK to 50 K. The measurements were carried out on a powder sample pressed into a pellet, using a combination of PPMS, and in-house dilution fridge heat capacity measurement system. The results are presented in Fig. 10.3. Fig. 10.3a shows the raw data, in black the zero field measurement, in red the measurements with an applied field of 1 T, and in blue with a field of 3 T.

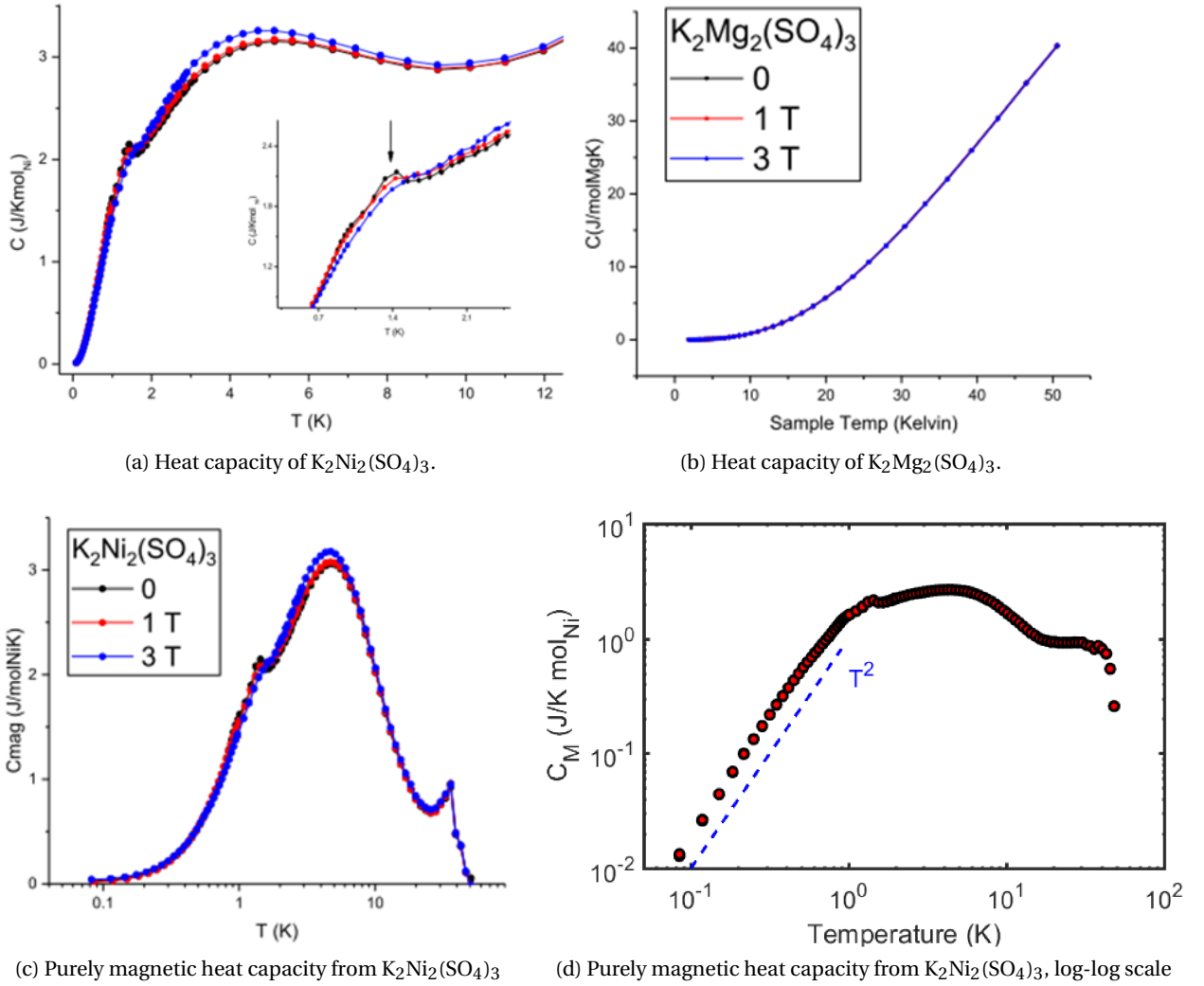


Figure 10.3: Subtraction of non magnetic analogue  $K_2Mg_2(SO_4)_3$  heat capacity to separate magnetic heat capacity from  $K_2Ni_2(SO_4)_3$ , the different colors refer to different field strengths: 0 T (black), 1 T (red), 3 T (blue).

A small peak was detected in the heat capacity, around 1.14 K. Moreover, this peak is suppressed by a magnetic field, pointing towards its magnetic origin. Additionally, another feature appears in the form of a very broad peak, with maximum located around 5 K. With a view to try

and separate the magnetic heat capacity from the lattice specific heat, a similar measurement was carried out on non-magnetic  $\text{K}_2\text{Mg}_2(\text{SO}_4)_3$ , whose result is presented in Fig. 10.3b. The chemical substitution of nickel by magnesium does not change the symmetry of the compound, but has the effect of removing any magnetism taking place in the system, magnesium being a non magnetic ion. The obtained heat capacity can then be subtracted from the one of the parent compound, after re-normalizing to take into account the fact that the atomic masses are slightly different, and thus the phonon contribution differ accordingly. The results of the obtained heat capacity are presented in Fig. 10.3c and in Fig. 10.3d on a log-log scale. It is quite clear that both peaks identified in the unsubtracted data remain a major feature of the subtracted heat capacity, and are thus of confirmed magnetic origin.

Single crystal growth opened up possibilities for new measurements and direction dependent measurements. The heat capacity was thus once again measured, at the Helmholtz-Zentrum Dresden-Rossendorf. The results are presented in Fig. 10.4.

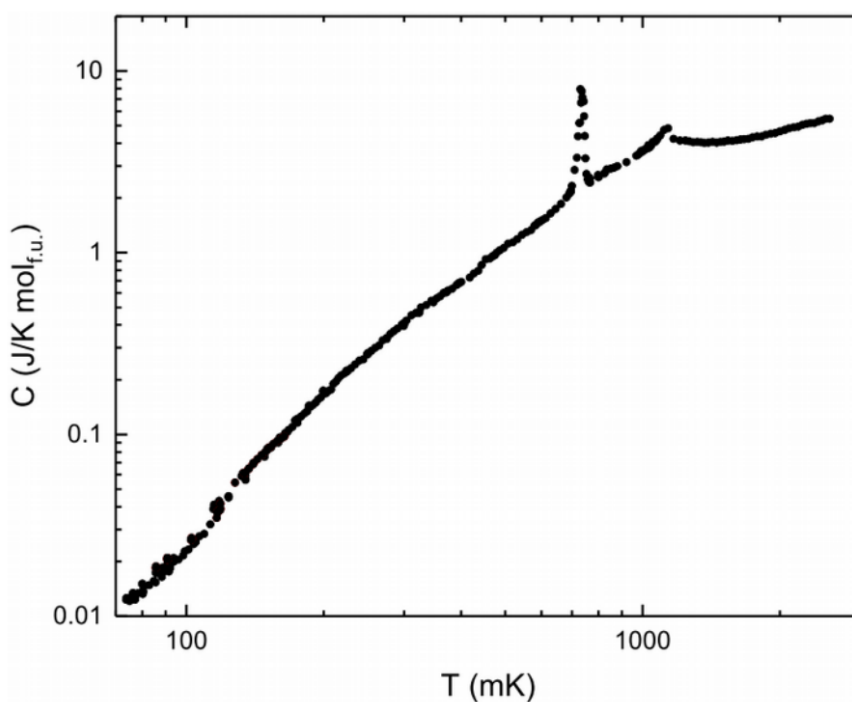


Figure 10.4: Single crystal heat capacity of  $\text{K}_2\text{Ni}_2(\text{SO}_4)_3$ .

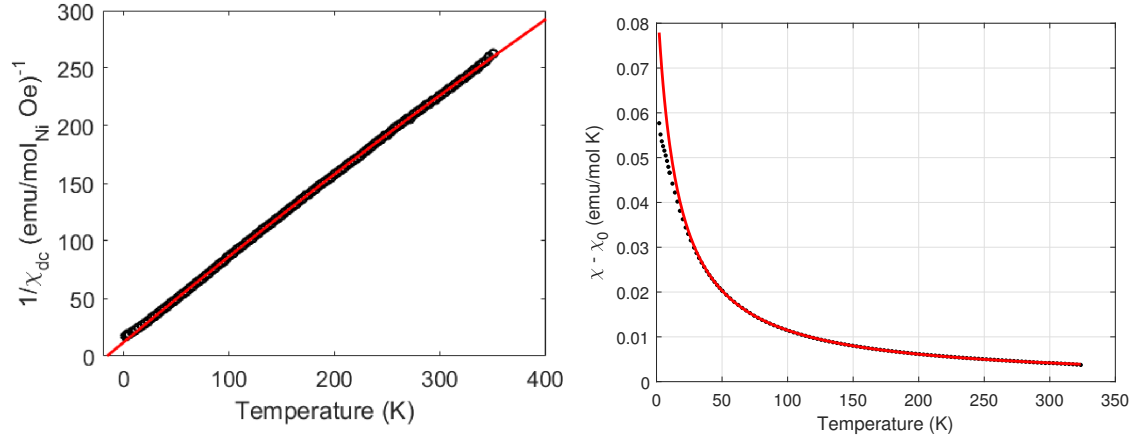
The single crystal heat capacity turns out to be very conclusive. It appears that the peak previously observed in the powder measurement is once again present in the single crystal data. More importantly, another sharp peak appeared at 740 mK. This is indicative of a potential transition to a long-range-ordered phase, that could be observed and confirmed by other measurement methods. It appears that the area of the peak is still quite small, indication that if long-range-order is confirmed, it should be quite weak, and that significant correla-

tions participate in the magnetic entropy. Finally, the log-log representation behavior of the magnetic specific heat, shown in Fig. 10.3d matches a power-law behavior, with a quadratic temperature dependence. This phenomenon has been observed in numerous long range order-suppressed systems, among others quantum spin-liquids candidates[208, 209, 210, 211] and differs considerably from the cubic temperature dependence observed and expected in systems presenting an antiferromagnetic ground state[194, 212, 200, 213, 201]. The low temperature part of the purely magnetic specific heat could be fitted with a polynomial form so that the model overlaps with a data up to 10 K. This enables to calculate the total recovered entropy which, at 50 K, corresponds to 98% of the entropy expected for a spin one system. The convergence of the entropy towards the expected value shows that there is little room for residual entropy that could be associated to a high degeneracy of frozen states. The difference between single crystal and powder heat capacity can be explained by mainly two theories, at least for the peak at 1.14 K, which seems to be completely absent from the powder measurement. A first theory may attribute the observed peaks to an impurity phase. The second hypothesis is that they are intrinsically related to the magnetic phase observed at low temperatures, and that the temperature resolution in the powder experiment was not sufficient to fully resolve the very sharp peaks.

The power law used to describe the low temperature data remains a good description of data obtained from measurements in external applied field strengths of up to 14 T, without a visible crossover to gapped polarized state that has been evidenced in  $\text{YbMgGaO}_4$ [214]. This detailed analysis of the heat capacity data has been performed by Dr. Ivica Živković.

### 10.1.3 Magnetization - Susceptibility

The DC-susceptibility has been measured on a powder sample using a MPMS, with a field of 0.1 T. The results are shown in Fig. 10.5. The data presented in black is the inverse DC-susceptibility, and the red solid line corresponds to the Curie-Weiss fit.



(a) Inverse DC-susceptibility of  $K_2Ni_2(SO_4)_3$  (black) and (b) DC-susceptibility of  $K_2Ni_2(SO_4)_3$  (black) and Curie-Weiss fit (solid red line).

Figure 10.5: DC-susceptibility of  $K_2Ni_2(SO_4)_3$ .

Fig. 10.5a shows the inverse DC-susceptibility, together with the inverse Curie-Weiss fits. An excellent agreement is obtained at high temperatures, and small deviations appear to be more clearly visible in the low temperature DC-susceptibility, presented in Fig. 10.5b. Starting at a temperature of 50 K and lower, the sample susceptibility starts to develop slower than the ideal Curie-Weiss, but with no anomaly whatsoever down to 100 mK. The results of the fit yield a Curie-Weiss temperature of  $\Theta_{CW} = -14.9$  K, and an effective moment of  $\mu_{eff} = 3.24 \mu_B$ , obtained for a Landé g-factor of 2.28. This value of the effective moment is fully consistent with that of a  $S = 1$  system. No feature at temperature similar to the ones corresponding to peaks observed in the heat capacity are detected, and thus no obvious transition to a magnetically long-range ordered phase can be identified solely from this data. The negative sign of Curie-Weiss temperature confirms that antiferromagnetic interactions play a significant role in the system.

AC susceptibility at low temperatures has also been measured by Dr. Ivica Živković's intern, using an AC magnetometer that was developed in the Laboratory for Quantum Magnetism, and then the AC-susceptibility measurement was reproduced on another instrument. The results are presented in Fig. 10.6, where the inset shows a zoom on data close to 1.5 K where confirmation measurements showed evidence for a peak.

No indication of any kind of ordering has been observed down to a temperature of 100 mK

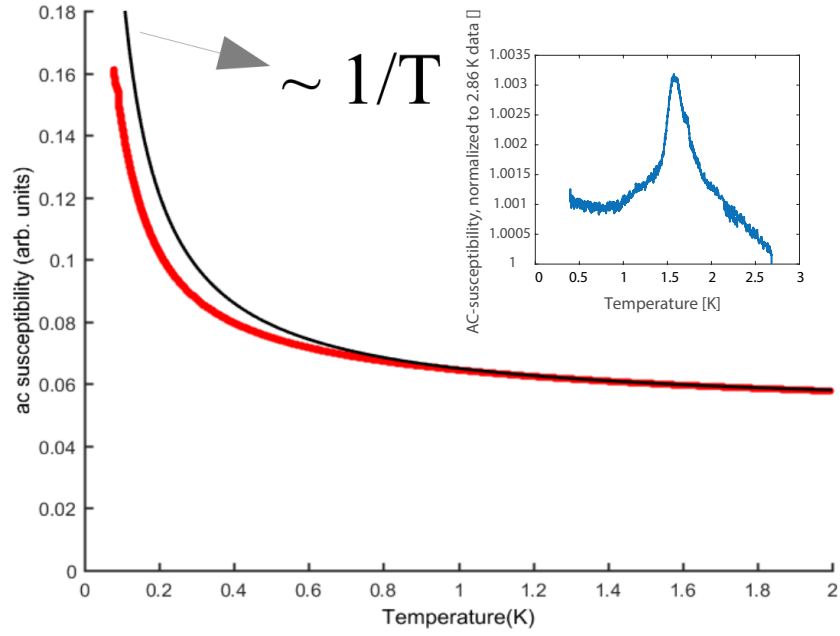


Figure 10.6: AC susceptibility at low temperatures for  $K_2Ni_2(SO_4)_3$  (red), the black curve is a guide to the eye presenting  $1/T$  free spin behavior. The inset shows the details of a peak that did not appear in the first measurement, located above 1.5 K.

except for the peak above 1.5 K. Here again, Fig. 10.6 shows that the susceptibility develops slower than an inverse temperature law, and that this increase in the paramagnetic response cannot be attributed to free spins, since the sample response is smaller than a  $1/T$  contribution coming from hypothetical free spins.

Additional measurements on single crystals confirmed the behavior inferred from the powder measurements, and were carried out with fields in the [111], [110], and [100] directions. No significant change between the measured DC-susceptibility could be observed, and the Curie Weiss temperature fitted to each of the data showed a fairly isotropic behavior.

### 10.1.4 ESR

In order to confirm or disprove the absence of magnetic long range order in the system, Electron Spin Resonance was carried out on a powder sample of high purity of  $\text{K}_2\text{Ni}_2(\text{SO}_4)_3$ . Measurements were carried out by Balint Nafradi at EPFL. The results of the ESR linewidth can be observed in Fig. 10.7. Even though ESR does not reveal any sign for a transition to a

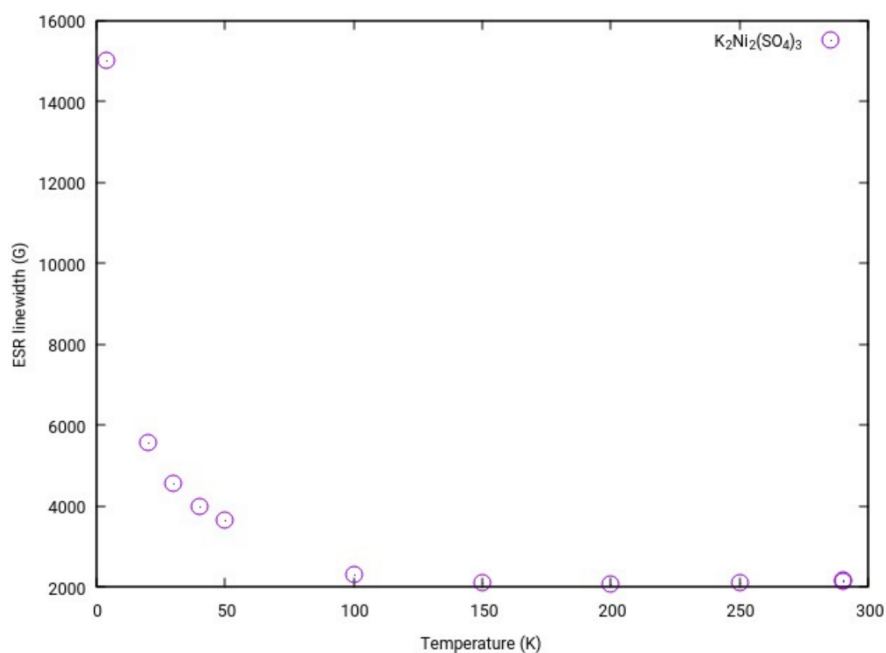


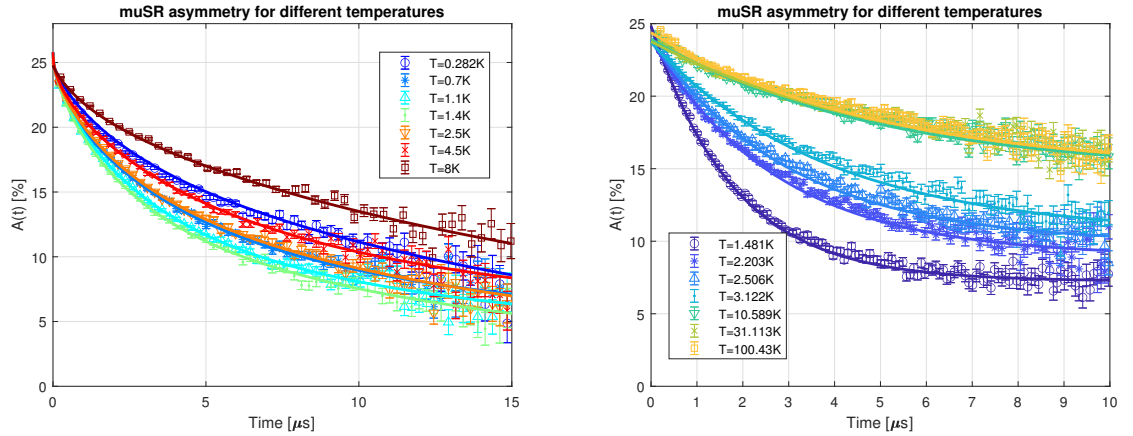
Figure 10.7: Temperature dependence of the ESR linewidth of  $\text{K}_2\text{Ni}_2(\text{SO}_4)_3$ .

magnetically long range ordered state, the measurement does confirm that the g-factor of the sample is 2.28, reinforcing the argument from DC-susceptibility that the results are consistent with a spin 1 system. Additionally, the ESR linewidth starts to increase significantly for temperatures lower than 100 K, which has not yet been attributed to any physical mechanism. A broad linewidth is typically associated to a state that is decaying fast (as opposed to a state with narrow linewidth which is decaying faster). For a given system, a broadening may occur due to the interaction with neighboring spins, a more detailed analysis is required.

### 10.1.5 muSR and the absence of magnetic long range order

The establishment of magnetic-long-range order in the system at this point is thus everything but sure. Indeed, even though heat capacity points towards one or several transitions occurring around one Kelvin, dedicated magnetic measurements did not show any conclusive sign of a magnetic transition. Muons being an tool with extreme sensibility to magnetism, and fairly easy to combine with dilution fridges experiments, muSR is thus a must-do experiment to confirm or disprove the potential quantum spin-liquid behavior of the compound. MuSR has indeed been used by many different peers with this view[215, 216, 217, 218, 219, 220].

The first experiments took place at the ISIS muon source. The sample consisted in a large amount of high purity powder and was cooled down to base temperature of 280 mK, then heated back up to 10 K. No wiggles, characteristic of the rotations of the muon spins around the local magnetic fields were ever observed while cooling down to 280 mK. Moreover, no wiggles were observed in any measurement at any different constant temperature, but only relaxing curves, corresponding to an exponential decay. This means that long range ordered static moments are not obviously visible in the sample. All measurements using the  $^3\text{He}$  cooling system enable to measure the low temperature muon asymmetry spectra, while the Variable Temperature Insert (VTI) allowed for measurements at higher temperatures: up to 100 K. Results for some representative temperatures are shown in Fig. 10.8a for the  $^3\text{He}$  fridge and for the VTI in Fig. 10.8b, both in zero field.



(a) Muon asymmetry of  $\text{K}_2\text{Ni}_2(\text{SO}_4)_3$  measured in  $^3\text{He}$  probe. (b) Muon asymmetry of  $\text{K}_2\text{Ni}_2(\text{SO}_4)_3$  measured in Variable Temperature Insert.

Figure 10.8: Zero field muon asymmetry of  $\text{K}_2\text{Ni}_2(\text{SO}_4)_3$ . Solid lines indicate a modeling (fit) of the relaxation data.

On the qualitative side of the measurements, it can be mentioned that the relaxation rate is obviously decreasing with temperature. Further analysis is required to confirm this result.



In a second step longitudinal field experiments were performed. Indeed, one way to look for static moments is to study the evolution of the relaxation rate with a longitudinal field, since random distributions of static moments, being of nuclear or electronic origins may contribute to facilitate the relaxation : these moments can be decoupled by applying a given strength of longitudinal field. Quite naturally, the dynamics of spins can also contribute to the relaxation, however, these time dependent processes typically involve applying a larger field. By applying a longitudinal field, one can check if the static moments are dominating. The results of longitudinal field measurements are presented in Fig. 10.9.

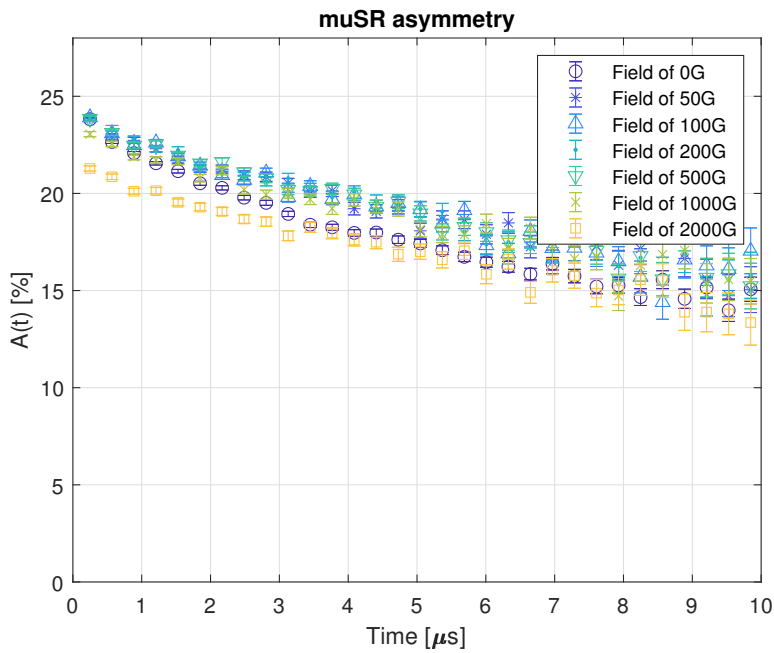


Figure 10.9: Longitudinal field dependence of  $\text{K}_2\text{Ni}_2(\text{SO}_4)_3$  muSR asymmetry at 10 K.

It appears that the muSR asymmetries do not exhibit noticeable changes in relaxation rate upon application of longitudinal fields of up to 2000 G, the relaxation rate remaining practically the same, there is thus no evidence for static moments. The slow decreasing in the relaxation rate for large fields can be explained by instrument calibration.

Another fingerprint of static moments, if frozen, is an effect similar to the eventual Knight shift observed in Nuclear Magnetic Resonance[221, 222, 223, 224], occurring when looking at transverse field measurements. A transverse field of 20 G has been applied and studied from 0.3 K to 5 K. No significant shift in the muon asymmetry can be observed. This means that there is no evidence for frozen static moments. The results can be seen in Fig. 10.10.

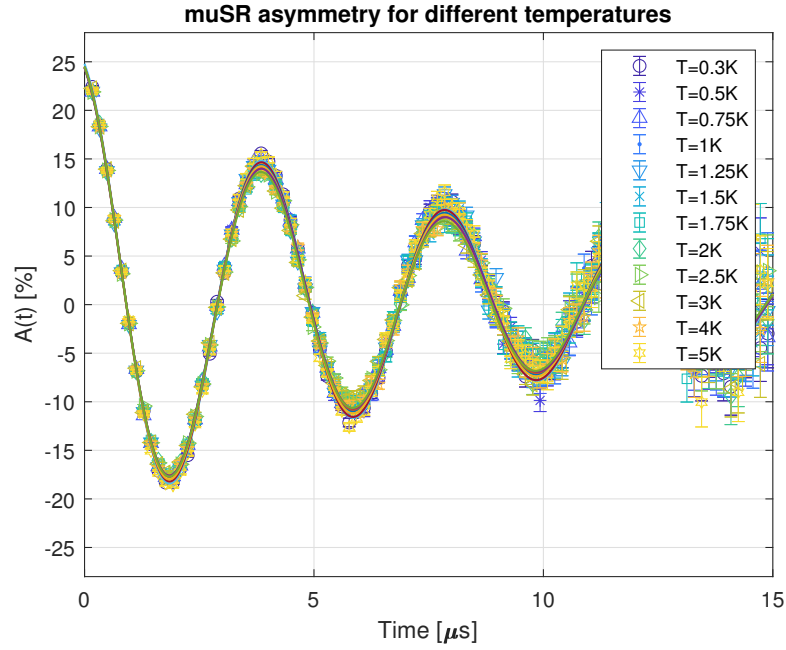


Figure 10.10: Transverse field dependence of  $\text{K}_2\text{Ni}_2(\text{SO}_4)_3$  muSR asymmetry. Solid lines correspond to fits to an oscillating function, attenuated by an exponential: no significant shift is observed.

A general formula of the muon spin relaxation rate used to model the asymmetry in the absence of static moments or transverse fields creating wiggles in the muon asymmetry is written as in equation (10.1).

$$A(t) = A \exp(-(\lambda t)^\beta) + B \exp(-\lambda_{bg} t) \quad (10.1)$$

Where  $\lambda$  is the relaxation rate,  $\beta$  the stretching exponent,  $\lambda_{bg}$  the background relaxation, and A and B respectively the relaxing and baseline (background) coefficients. Several methods have been used to try and fit the data:

1. Simple exponential, free constant background
2. Stretched exponential, free constant background
3. Stretched exponential, shared constant background
4. Stretched exponential, simple exponential background

These fitting methods have been used to fit both  $^3\text{He}$  fridge and VTI data. Regardless of our choice of fitting schemes, there is a peak in  $\lambda$  around  $T=1.4$  K, which corresponds to the temperature found by the specific heat.

The fits giving the best results have been obtained by the following routine. The 10 K temperature has been chosen as reference for several reasons. First, the  $^3\text{He}$  probe had problems to stabilize the temperature around 1.6 K, up to 2.3 K. The VTI set temperature was differing by generally 0.3 K from the sample temperature (below 10 K). 10 K was the first point for which the sample temperature recorded using VTI was close to one of the sample temperatures recorded when using the  $^3\text{He}$  probe. Moreover,  $T = 10$  K corresponds to a region in which  $\lambda$  is still decreasing, but not varying too rapidly. So one can have good confidence in the fact that the value of  $\lambda$  obtained from fitting the VTI data can be used as value expected for the  $^3\text{He}$  probe data, due to the small difference in temperatures. A strategy to obtain consistent results between VTI and  $^3\text{He}$  probe is the following.

1. Use the data measured in the VTI lowest temperature.
2. Fit to find single exponential background.
3. Fix a single exponential background.
4. Fit all VTI points
5. Use the  $^3\text{He}$  data at 10 K.
6. Free the background amplitude coefficient, while at the same time fixing the relaxation rate and stretching exponent as equal to the values found for the VTI.
7. Fit  $^3\text{He}$  data at 10 K.
8. Fix background coefficients and set as free the relaxation rate and stretching exponent.
9. Fit all Helium 3 temperature points.

The relaxation curves obtained by this procedure can be seen in Fig. 10.11, where the relaxations rates obtained with the two different measurements were set to match, but the data overlap also continues to higher temperatures. Representative fits of low temperature data are shown in Fig. 10.8.

A divergence occurs at 1.4 K which is an indication that the physics changes around this point. It appears quite strikingly that there is a large discrepancy between the fitted relaxation rates obtained from the VTI and fridge data. This discrepancy is believed to be due to temperature calibrations, explaining the overlap of finite to diverging values. The data from the Helium

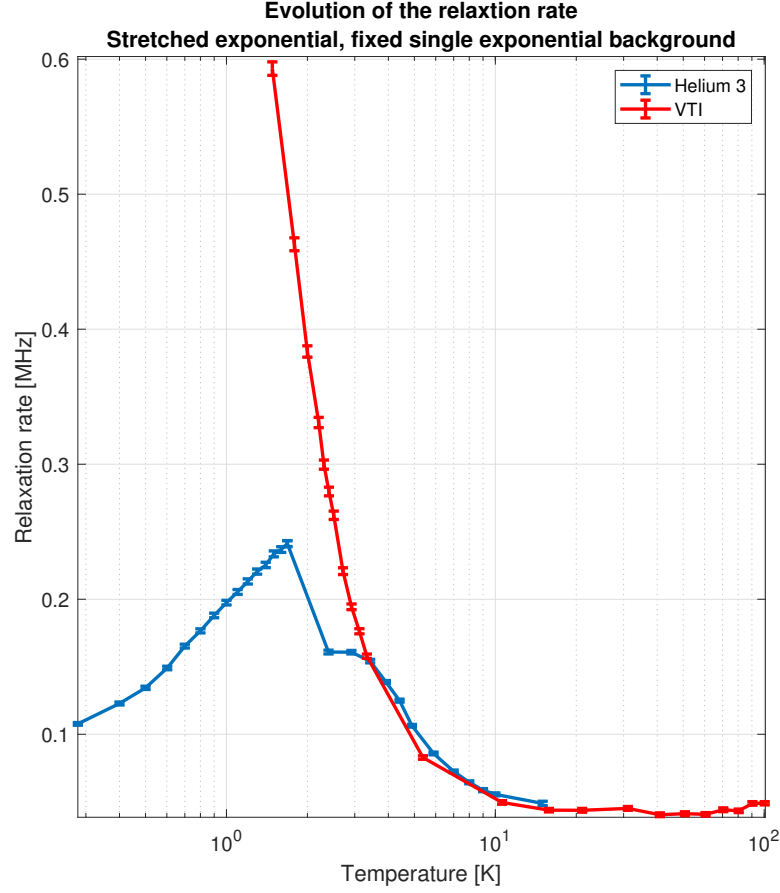


Figure 10.11: Relaxation rate in  $\text{K}_2\text{Ni}_2(\text{SO}_4)_3$  showing a clear peak at 1.5 K.

3 fridge does not fully diverge, this is believed to be due to a lack of statistics, but more importantly, as was evidenced further, due to a modeling issue.

Indeed, measurements at PSI, where muons give access to a shorter time scale, and also lower temperatures were performed by our collaborators in a second step. The experiments were carried out on a high quality powder sample, down to a base temperature of 20 mK. No significant fingerprint of large ordered moments has been observed, similarly to what has been reported from the aforementioned experiments at ISIS. Data and fits to the data can be seen in Fig. 10.12. The data has been modeled with two different asymmetry functions: one describing the low temperature behavior of the system, given by  $A_{\text{low temp}}(t) = A_0 \left( f e^{-(\lambda_1 t)^{\beta_1}} + (1-f) e^{-(\lambda_2 t)^{\beta_2}} \right) + A_{\text{BG}}$  and another function describing the high temperature data:  $A_{\text{high temp}}(t) = A_0 e^{-(\lambda t)^{\beta}} + A_{\text{BG}}$ . These correspond to the usual stretched exponential modeling with a constant background. It appeared that the low temperature data, down to 20 mK, is better described by the sum of two stretched exponential functions. In order not to over-constrain the fit, parameters  $f$  and  $\beta_1$  have been fixed to 0.5 and 1 respectively. The two relaxing components then describe both the dynamics due to sporadic spinon excitations

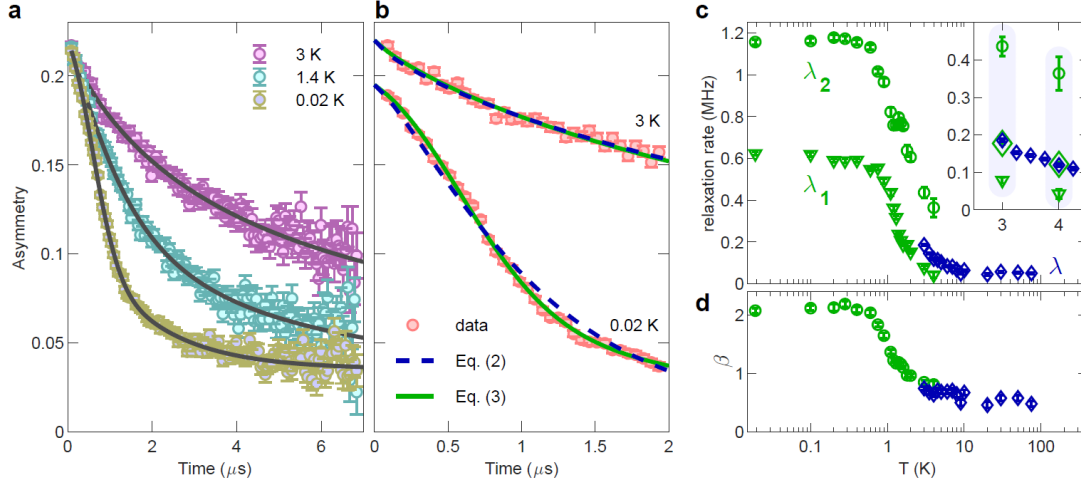


Figure 10.12:  $\mu\text{SR}$  measurements carried out at PSI with corresponding analysis. a) show measured data with the model. b) shows a comparison between models. c) and d) show the temperature dependence of fit parameters.

and a partial order of the sample. This partial order would be due to the existence of a sporadically incomplete covering of the lattice by singlets that leaves some spins unpaired. These isolated spins would then survive a certain time, much shorter than the average muon lifetime. Fig. 10.12 shows the result of the fits. The fact that the two-asymmetry function models better the low temperature data is showcased in sub-figure b). The temperature dependence of the different fit parameters is shown in panels c) and d). Parameters in green correspond to data measured in a dilution fridge, whereas parameters in blue correspond to data measured in a VTI. Circles and triangles correspond to data modeled with the low temperature asymmetry functions while diamonds correspond to results obtained modeled using the high temperature asymmetry function. The fact that the low temperature asymmetry function models better the low temperature data is shown in sub-panel b): and a significant overlap (over a wide temperature range) of the fit parameters obtained by the two methods can also be observed in sub-panels c) and d), confirming the validity of the models. At high temperature, the stretched exponent reaches a plateau at one, effectively turning the low temperature asymmetry equation into the high temperature one. The saturation of the stretched exponent at low temperatures at the value of two is characteristic of a specific type of a correlated spin system based on spin-singlets[225].

The results are quite interesting and point towards a highly dynamical ground state with potential partial ordering. It thus seems that there is some room for magnetic long range order, but that it is strongly suppressed by the system to a point where even muons arguably detect its presence. More experiments are thus required to characterize fully the low temperature state of the system. Neutron scattering stands out as the natural tool to perform such additional

investigations.

## 10.2 Frustration-suppressed magnetic long range order

### 10.2.1 Elements of a magnetic ground state

In order to study the potential magnetic ground state of  $\text{K}_2\text{Ni}_2(\text{SO}_4)_3$ , several neutron scattering experiments have been carried out, the first of which was performed at the DNS instrument, in the FRMII neutron scattering center in Munich.

#### DNS

DNS is a polarized neutron scattering instrument, with a time-of-flight neutron scattering option that was available at the time of the experiment. The goal of the measurement was thus two-fold: using the polarized diffraction option to separate nuclear from magnetic signal at the base temperature, and start studying the inelastic spectrum associated to the magnetic excitations of the compound. A dilution fridge with a base temperature of 500 mK was used, the sample was placed in a can with exchange Helium gas to ensure reasonable temperature thermalization. After collecting several high statistics pattern at different temperatures, the nuclear coherent, the magnetic and the spin incoherent cross sections could be separated. The measurements were repeated at 0.5 K, 17 K, and 80 K, in order to keep track of the observed signal and study its temperature evolution. The results of the base temperature data are shown in Fig. 10.13.

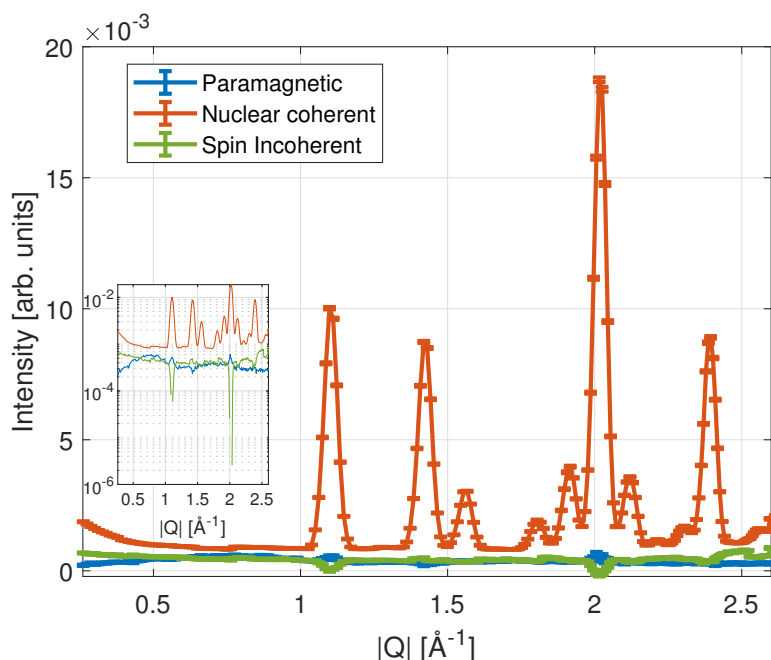


Figure 10.13: Base temperature (500 mK) separation of cross section of  $\text{K}_2\text{Ni}_2(\text{SO}_4)_3$  diffraction pattern. The inset shows a y-axis log scale to apprehend fully the ratios between cross sections.

Fig. 10.13 shows that as expected, the nuclear coherent scattering is dominant in the sample. It originates from the scattering of neutrons on the crystal structure. The results of a fit of the nuclear structure, using the Fullprof suite can be seen in Fig. 10.14. The room temperature space group has been used, and even though the fitted pattern (in red) matches fairly well the measured data points (in blue) with a small difference (in yellow), the peaks are so broad that there is room for a structural transition to another phase with space group and lattice parameters that would be confirmed by peak splittings. In that case, these splittings may just be small enough not to be resolved properly by this measurement.

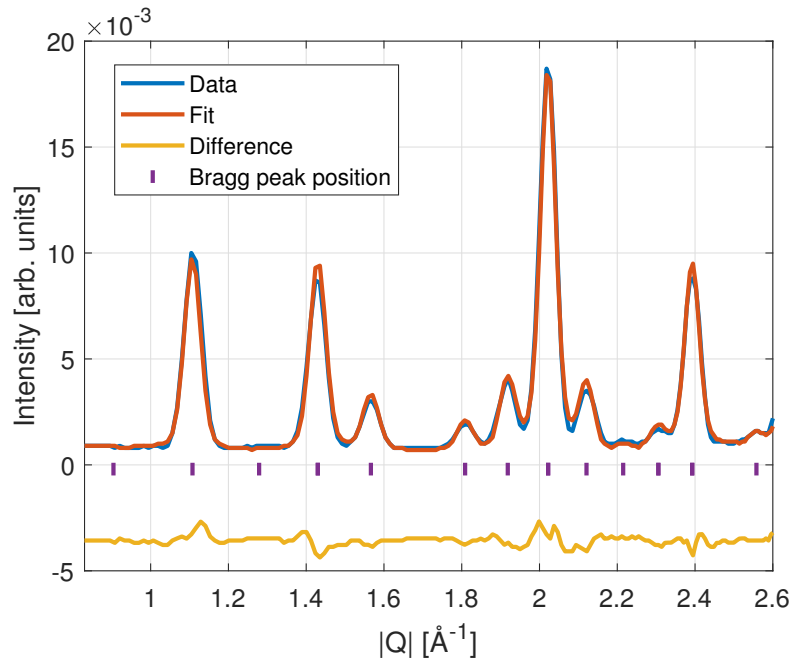


Figure 10.14: Base temperature (500 mK) separation of cross section of  $\text{K}_2\text{Ni}_2(\text{SO}_4)_3$  diffraction pattern: nuclear coherent scattering and fit of the data.

More importantly, the purely magnetic scattering could be separated thanks to the polarization analysis. The magnetic signal is presented in Fig. 10.15. Fig. 10.15a shows the magnetic cross-section, the solid curve corresponding to a Reverse Monte-Carlo (RMC) fit of the data. In essence, RMC fits spin orientations, fixing the spin positions, in order to match a given diffuse scattering data set. The quantity that is minimized throughout the refinement is not given by the energy of the system, but rather by the square of the deviation of the difference between experimental and modeled data. In that sense, the spinvert software[226] does not model magnetic interactions, but rather magnetic correlations. A typical outcome of the system is given by the spin-pair correlation function, which is a measure of how spin correlations change in function of the distance between spins. Fig. 10.15b shows the pair correlation function associated to the RMC fit. The data presents strong peaks around  $Q = 1$  and  $2 \text{ \AA}^{-1}$  which have been ignored by the fit: they are located at strong nuclear peaks positions and most probably correspond to a small error in the flipping ratio, main parameter responsible



for the proper separation of nuclear and magnetic intensities. Aside of these nuclear peaks, the magnetic scattering presents a broad peak up to  $1 \text{ \AA}^{-1}$ , and another one located at  $1.75 \text{ \AA}^{-1}$ , much less intense. One could arguably claim that many peaks are observed, slightly above the strong broad peak at low  $Q$ . This deserve further studies and is addressed by another experiment. The main conclusion that can be obtained from this data is that there is no sharp magnetic peak, that would be associated with magnetic long range order, but rather broad features. Diffraction measures the time-integral of the dynamic structure factor, meaning that these observed peaks may find their origins in fluctuations of the sample, which could take the form of diffuse scattering, magnetic continua, or spin waves. The pair correlation function obtained by the Reverse Monte-Carlo fit shows an oscillation, which can be understood as confirming that the system is globally antiferromagnetic. The amplitude of the positive and negative peaks are different, which suggests a level of competition between interaction in the system, each maxima corresponding to a different nickel - nickel interaction distance.

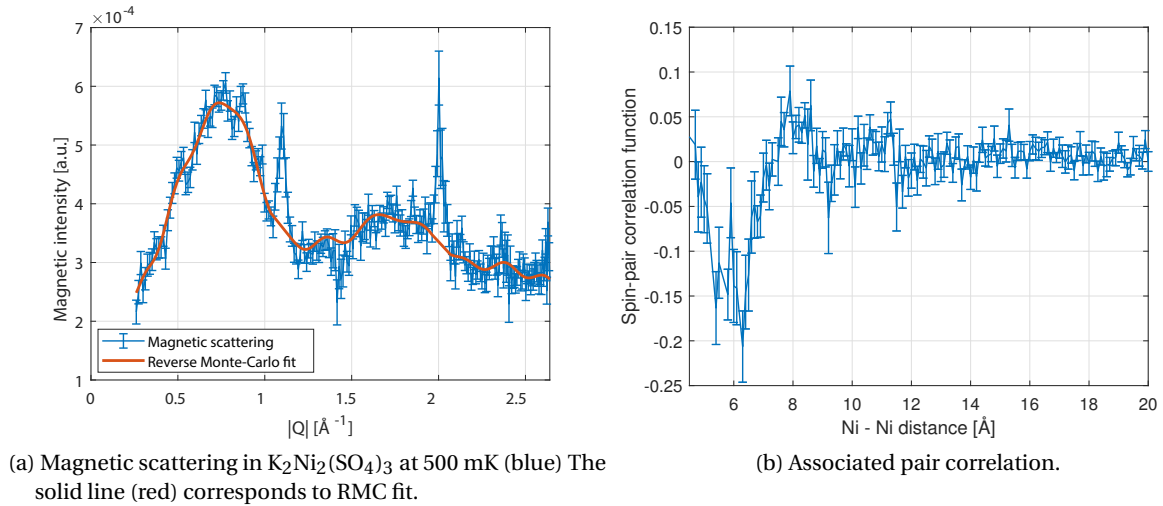


Figure 10.15: Magnetic scattering in  $\text{K}_2\text{Ni}_2(\text{SO}_4)_3$  at 500 mK.

The temperature dependence of the magnetic scattering has been studied with measurements at various temperatures, presented in Fig. 10.16. The data at a base temperature of 500 mK is shown in blue, at 17 K in red, and at 80 K in black. It appears that the broad peak of magnetic origin is still present at 17 K, however with reduced intensity. The same comment can be made for the other peak, which has an even lower intensity. At 80 K, the broad peaks seem to have completely disappeared.

The purely magnetic scattering at 80 K does not show any indication of neither long-range, nor short range magnetic order. Its dependence on momentum can be reasonably well matched to that of the square of the magnetic form factor of a  $\text{Ni}^{2+}$  ion, as shown in Fig. 10.17, in full agreement with paramagnetic moments.

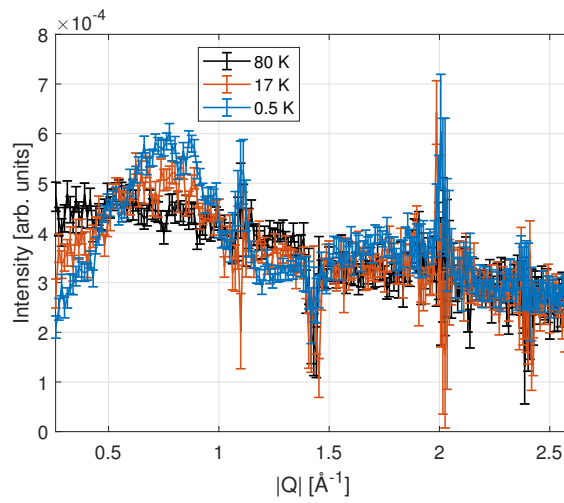


Figure 10.16: Temperature dependence of magnetic scattering in  $\text{K}_2\text{Ni}_2(\text{SO}_4)_3$ .

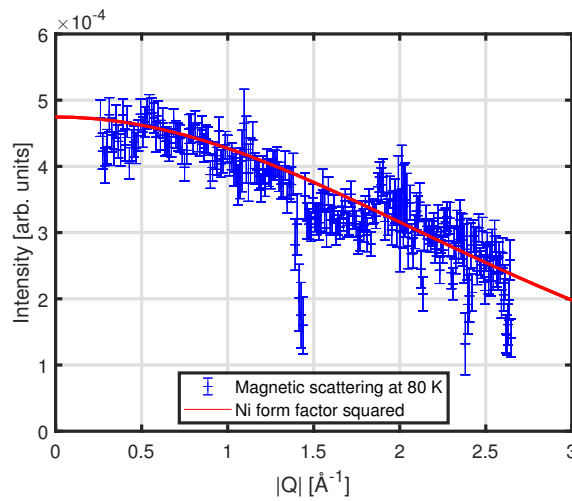


Figure 10.17: Magnetic scattering of  $\text{K}_2\text{Ni}_2(\text{SO}_4)_3$  at 80 K (blue) and square of  $\text{Ni}^{2+}$  magnetic form factor (red solid line).

The final measurement that was carried out at DNS corresponds to time-of-flight inelastic neutron scattering. The inelastic spectrum collected at 500 mK is shown in Fig. 10.18.

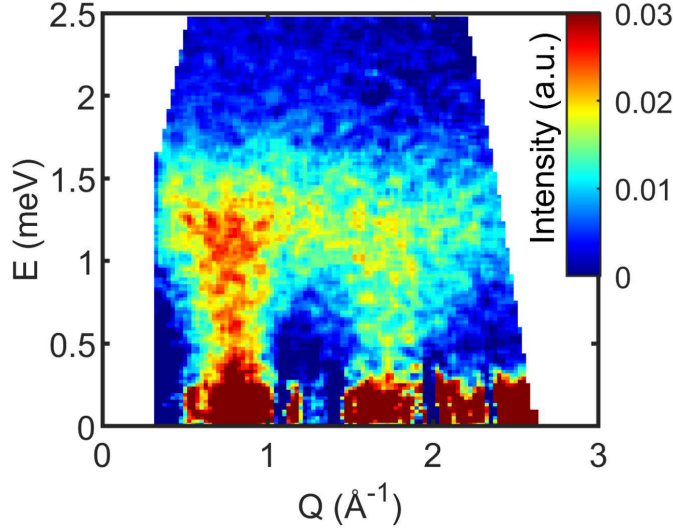


Figure 10.18: Powder inelastic neutron scattering in  $\text{K}_2\text{Ni}_2(\text{SO}_4)_3$ .

This inelastic spectrum, even though measured on powder, turns out to be quite informative. It appears that bright, dispersive features are observed as originating from the elastic line at positions below  $1 \text{ \AA}^{-1}$  and around  $1.7 \text{ \AA}^{-1}$ . These positions are fully consistent with the signal measured in the diffraction data, showing broad peaks located at the same positions. The upper limit of the spin excitation is about 1.8 meV, consistent with the order of magnitude of the Curie-Weiss temperatures obtained from the DC-susceptibility fits. A careful analysis seems to expose the gapless nature of the excitation spectrum, as shown in Fig. 10.19.

Indeed, this analysis consists in the observation of the energy dependence of the measured integrated intensity for two different  $Q$  ranges. In particular, Fig. 10.19 shows for a narrow integration range given by  $0.65 < Q < 0.85 \text{ \AA}^{-1}$ , a continuum of excitations is observable down to the elastic line, in complete accordance with the power law behavior observed in the low temperature heat capacity data. Moreover, the observed dispersion spectrum seems to be quite sharp, and may very well correspond to spinwave related features. Spinwaves are the typical inelastic entities observed in magnetically long range ordered systems, and correspond to perturbations around the ordered ground state. It is therefore extremely peculiar for such spin wave to appear without ordering, and one thus has to look for signs of magnetic order. The intensity observed in the powder averaged data seems to point towards more than just the usual spinwave picture, indeed, such a continuum of intensity would be consistent with a spinon-like behavior that is a signature of disordered magnetic states and cannot be predicted by usual spinwave theory. In order to address that issue, another diffraction experiment was performed, at the WISH beam line in the ISIS facility, the spin wave spectra being ideally

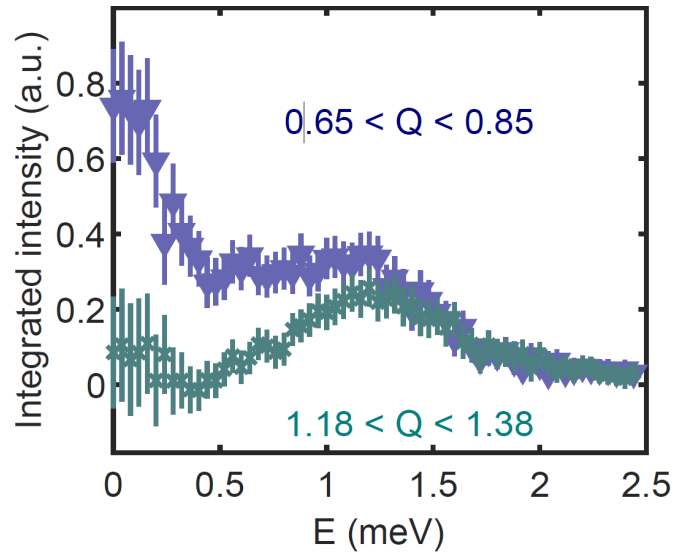


Figure 10.19: Energy dependence of the integrated intensity, for two different Q-ranges.

measured on a single crystal to confirm couplings in an unequivocal way.

## WISH

In the general theory of magnetism, a critical notion is that of the magnetic propagation vector, describing how to obtain the magnetic unit cell from the crystalline unit cell. Magnetic propagation vectors with small norms show potentially many magnetic peaks at lower values of  $Q$  than those of the nuclear peak at lowest  $Q$ , depending on the details of the magnetic structure factor. It can thus be stated that the magnetism associated to short magnetic propagation vectors shows interesting contributions at low values of the modulus of the scattering vector. Even though the experiment at DNS provided many important information about potential ordering at 500 mK, it lacked a crucial component required for a more detailed quantitative analysis: good resolution in the low  $q$  range. The WISH diffractometer at the ISIS neutron source in Didcot UK is a time-of-flight diffractometer. Its great advantage is the presence of ten detector banks placed around the sample, allowing for great resolution in  $q$ , for both nuclear and magnetic scattering. Unlike on DNS there is no polarized option that helps to separate intrinsic magnetism from nuclear scattering but both the accessible  $q$ -space and the  $q$ -resolution are much greater and hopefully provide much more insight on low- $q$  phenomena. The measurements were carried out using a dilution fridge and one bar of helium acting as exchange gas in the sample can to thermalize the sample, allowing for measurements at up to 1.3 K, and a VTI to verify potential structural transitions at higher temperatures.

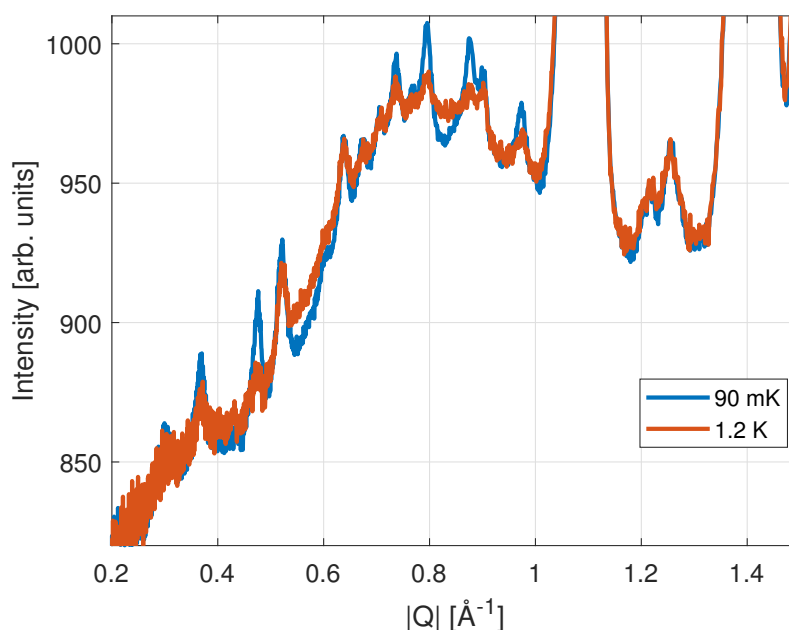


Figure 10.20: Zoom on low  $Q$  neutron diffraction in  $\text{K}_2\text{Ni}_2(\text{SO}_4)_3$ .

The low temperature data presented in Fig. 10.20 shows a clear broad background peak with maximum around the same position as the one detected in the DNS data. However, additionally, many more peaks can be observed on top of the broad maximum, and also

other peaks at lower values of  $q$ . These peaks are located at a position where they cannot be attributed to purely nuclear peaks and have to be of some magnetic origin. Their intensity is very small, relative to that of the broad peak which confirms that the magnetic order is originating from a frustrated configuration and is very weak. These peaks disappear with temperature as shown in Fig. 10.21. This figure show a comparison of 90 mK data with data measured with a thermometer indicating the same temperature but without exchange gas. In the absence of exchange gas, the sample is not able to thermalize properly, so the actual sample temperature is effectively higher than the temperature recorded by the thermometer, and corresponds to an unknown temperature. In this case, the broad, diffuse background is clearly visible, and the small magnetic peaks disappeared.

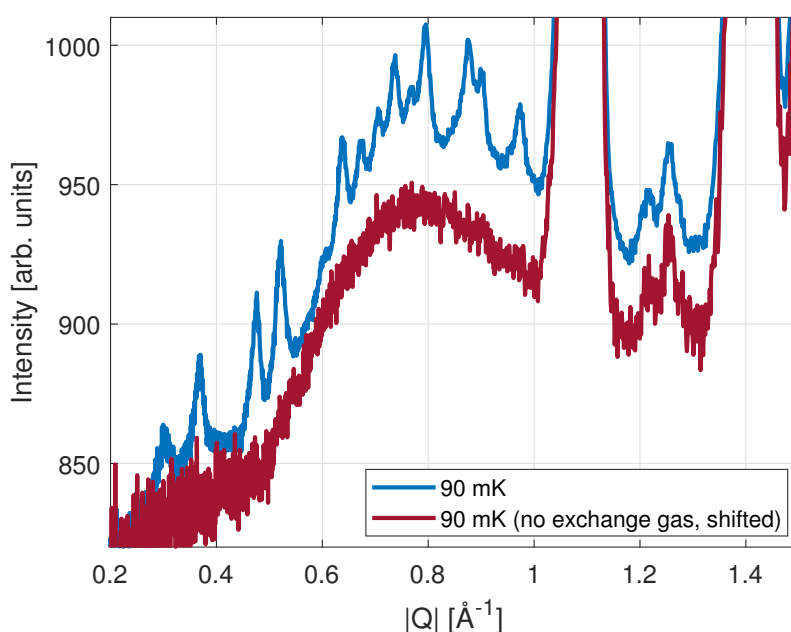


Figure 10.21: Zoom on low  $Q$  neutron diffraction in  $K_2Ni_2(SO_4)_3$ . The curve without exchange gas (dark red) has been shifted for clarity and corresponds to effective high temperature since the sample is not thermalized.

The temperature dependent data does not show any convincing sign of transition to any other nuclear space group. A slight shift appears to happen for some peaks, but no peak splitting is observed. The analysis of the magnetic data proves to be more complicated. Using the  $k$ -search algorithm in the Fullprof suite the magnetic propagation vectors creating the observed magnetic Bragg peaks could be identified. The results are presented in Fig. 10.22.

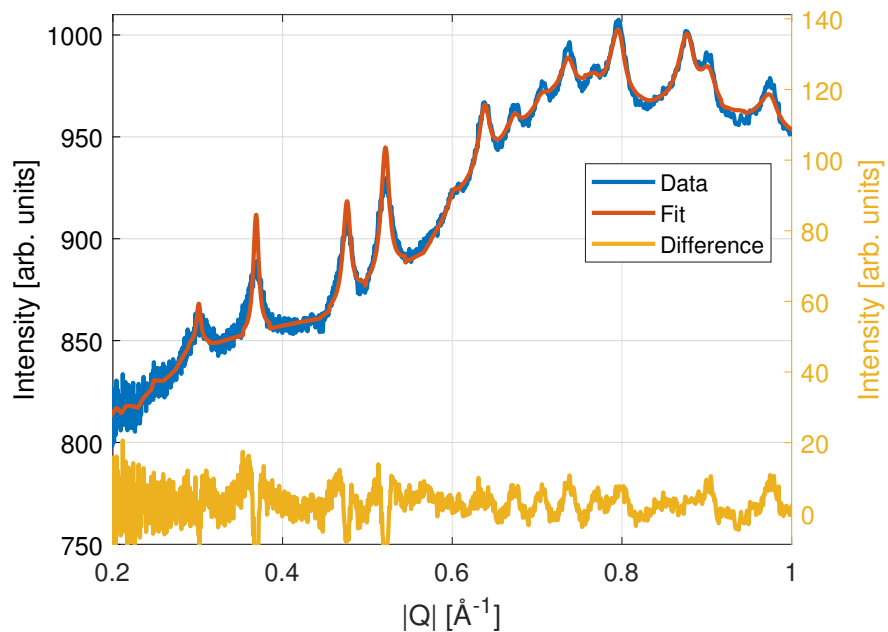


Figure 10.22: Zoom on low  $Q$  diffraction in  $\text{K}_2\text{Ni}_2(\text{SO}_4)_3$ . The blue data is the measurement, and the red curve corresponds to a LBF using several propagation vectors:  $(1/3 \ 0 \ 0)$ ,  $(1/3 \ 1/3 \ 0)$  and  $(1/3 \ 1/3 \ 1/3)$ . The difference is shown in yellow.

## 10.2. Frustration-suppressed magnetic long range order

The data is shown in blue and the red curve corresponds to a LeBail fit using three different magnetic propagation vectors at the same time:  $(1/3\ 0\ 0)$ ,  $(1/3\ 1/3\ 0)$  and  $(1/3\ 1/3\ 1/3)$ . A combination of these three vectors is necessary to describe all observed peaks, as shown in Table 10.3. The magnetic ordering vectors are of the 3-sublattice type. The origin of this is yet to be understood.

Peak position $ Q  [\text{\AA}^{-1}]$	Nuclear peak	Magnetic propagation vector
0.3018	(0 0 0)	$(1/3\ 1/3\ 0)$
0.3696	(0 0 0)	$(1/3\ 1/3\ 1/3)$
0.4267	(1 0 0)	$(-1/3\ 0\ 0)$
0.4771	(0 1 0)	$(-1/3\ -1/3\ 0)$
0.5226	(0 0 1)	$(-1/3\ -1/3\ -1/3)$
0.6034	(1 1 0)	$(-1/3\ -1/3\ 0)$
0.6400	(1 0 0)	(0 0 0) (purely nuclear)
0.6746	(0 1 0)	$(1/3\ 0\ 0)$
0.7075	(0 0 1)	$(1/3\ 1/3\ 0)$
0.7390	(1 1 1)	$(-1/3\ -1/3\ -1/3)$
0.7982	(-1 0 1)	$(1/3\ 1/3\ 0)$
0.8533	(1 0 0)	$(1/3\ 0\ 0)$
0.8796	(-1 -1 1)	$(1/3\ 1/3\ 0)$
0.8796	(0 0 1)	$(1/3\ 0\ 1/3)$
0.9051	(1 1 0)	(0 0 0) (purely nuclear)
0.9051	(1 0 0)	$(1/3\ 1/3\ 1/3)$
0.9299	(0 -1 1)	$(1/3\ 0\ 0)$
0.9540	(1 -1 0)	$(-1/3\ -1/3\ 0)$
1.0006	(1 1 1)	$(-1/3\ 0\ 0)$
1.0450	(1 -1 1)	$(-1/3\ -1/3\ -1/3)$
1.0666	(2 0 0)	$(-1/3\ 0\ 0)$
1.0666	(1 1 0)	$(1/3\ 0\ 0)$
1.0877	(0 2 0)	$(0\ -1/3\ -1/3)$
1.0877	(1 0 1)	$(1/3\ 1/3\ 0)$

Table 10.3: Magnetic propagation vectors required to construct magnetic Bragg peaks observed in neutron diffraction patterns of  $\text{K}_2\text{Ni}_2(\text{SO}_4)_3$ .

By modeling the broad contribution to the magnetic signal originating from short range order correlations, one can try and extract a bound on the magnetic moment strength. It can thus be estimated that the static contribution to the intensity amounts to roughly 11% of the total magnetic intensity. This value can nonetheless be used to still conclude that the long range order is evidently suppressed and supports the theory that the ordered state in the compound is dominated by spin fluctuations and that this state is located close to a quantum critical point.



**10.2.2 Diffuse scattering**

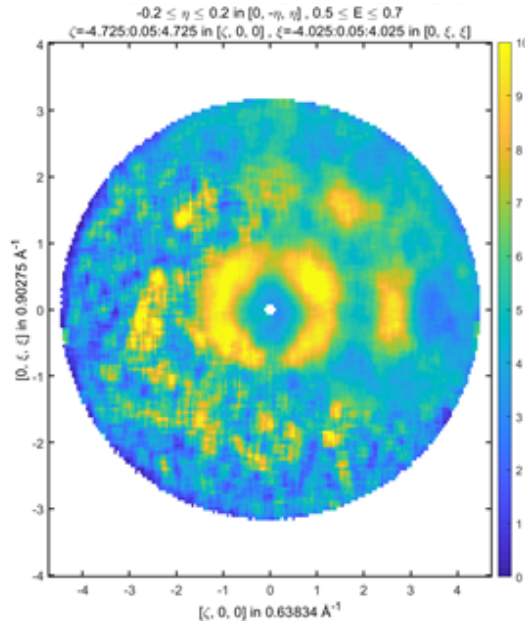
A single crystal inelastic neutron scattering experiment was carried out at the LET spectrometer at the ISIS neutron source in Didcot, UK. The sample consists in a co-alignment of four different crystals co-aligned on aluminum posts. Each individual crystal weighs about 100 mg, accounting for a total sample mass of 450 mg. A picture of the sample can be seen in Fig. 10.23.



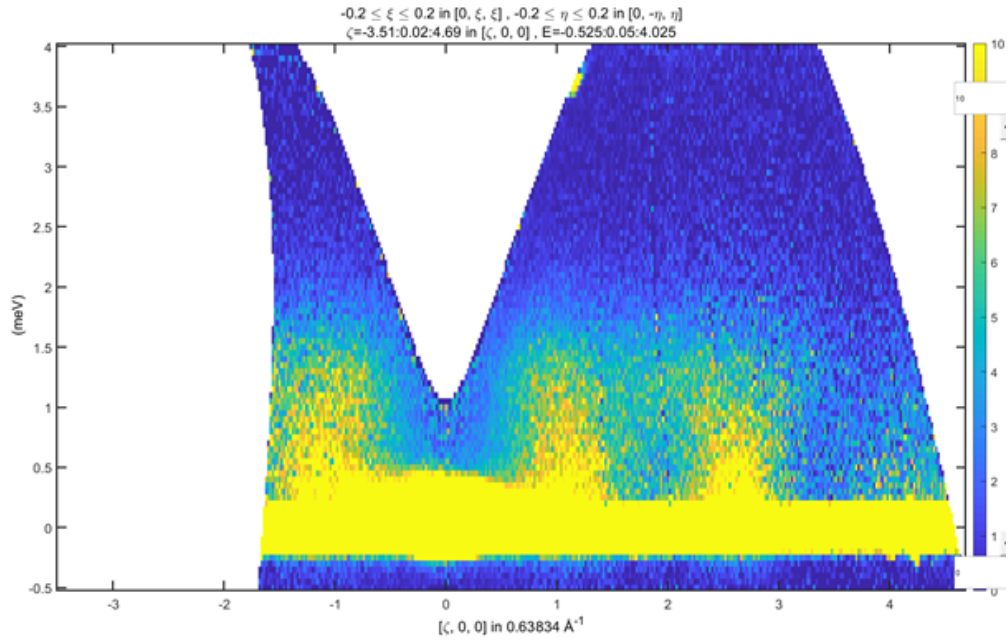
Figure 10.23: Co-alignment of four crystals of  $\text{K}_2\text{Ni}_2(\text{SO}_4)_3$ , used for an inelastic neutron scattering experiment at LET.

The data, measured at 2 K, is presented in Fig. 10.24. Fig. 10.24a shows a representative constant energy slice with evidence for broad, diffuse scattering peaks. This diffuse scattering pattern is confirmed in a constant- $q$  cut, presented in Fig. 10.24b. The observed features appear to be broad and energy independent, with an energy scale of 1.5 meV.

## 10.2. Frustration-suppressed magnetic long range order



(a) Constant energy slide of inelastic neutron scattering data in  $K_2Ni_2(SO_4)_3$ .



(b) Constant  $q$  cut of inelastic neutron scattering data in  $K_2Ni_2(SO_4)_3$ .

Figure 10.24: Neutron spectroscopy results on  $K_2Ni_2(SO_4)_3$ .

The positions of the measured features qualitatively agree with the calculations from the Pseudofermion Functional Renormalization Group (PFFRG). The PFFRG computations were performed by Johannes Reuter and his team. PFFRG is based on a fermionic formulation of the Hamiltonian, with spin one operators represented by two spin half operators. Many body physics is then used, with typical treatments using Feynmann diagrams, an infrared frequency cutoff, and vertices undergoing a renormalization group flow with the standard functional renormalization group scheme. The main result is given by the zero-frequency part of the magnetic susceptibility that is momentum dependent, and that can be linked to the dynamical structure factor using the Kramers-Kronig relations. PFFRG predicts a spin-liquid behavior at finite temperature and a weak magnetic ground state at zero Kelvin. The results are presented in Fig. 10.25. Fig. 10.25a shows the result of the PFFRG computation, while Fig. 10.25b shows the structure factor calculations associated to an antiferromagnetic, frustrated exchange coupling  $J_4$ . This is the bond that DFT calculations predict to be the one hosting the strongest interaction. Several scattering features appear to be predicted correctly by the structure factor of spins coupled by this  $J_4$  bond, but the details do not match perfectly. This simple model tends to indicate that the  $J_4$  bond is indeed relevant, a couple of other bonds have been tried with no success, this work would be better performed by Reverse Monte Carlo than choosing the strength of the exchanges empirically. In order to gain more insight on the couplings in the system, one should try to acquire single crystal inelastic data at dilution temperature, and verify results from the DNS experiment predicting spinons and continuous excitations. The shape and Q-dependence of such continuous excitations will certainly provide crucial information on the couplings responsible for the ground state of the system including the small long range ordered component, the strong dynamical part, and also the complex excitation spectrum. In principle, applying an external field in an inelastic neutron scattering experiment may give important information on what is the manifestation of the long range ordered component of the ground state in the spectrum.

## 10.2. Frustration-suppressed magnetic long range order

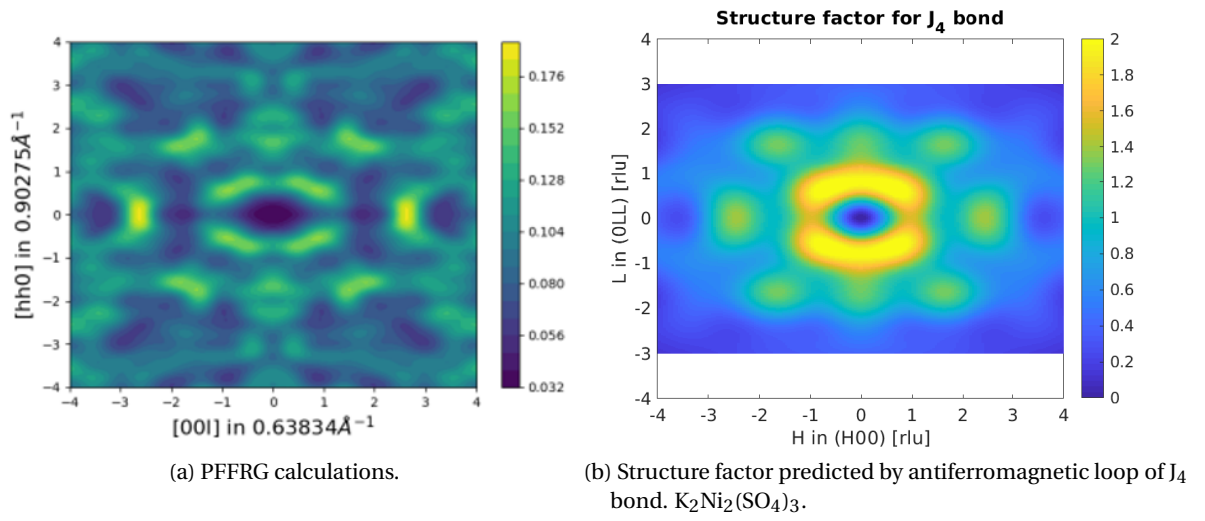
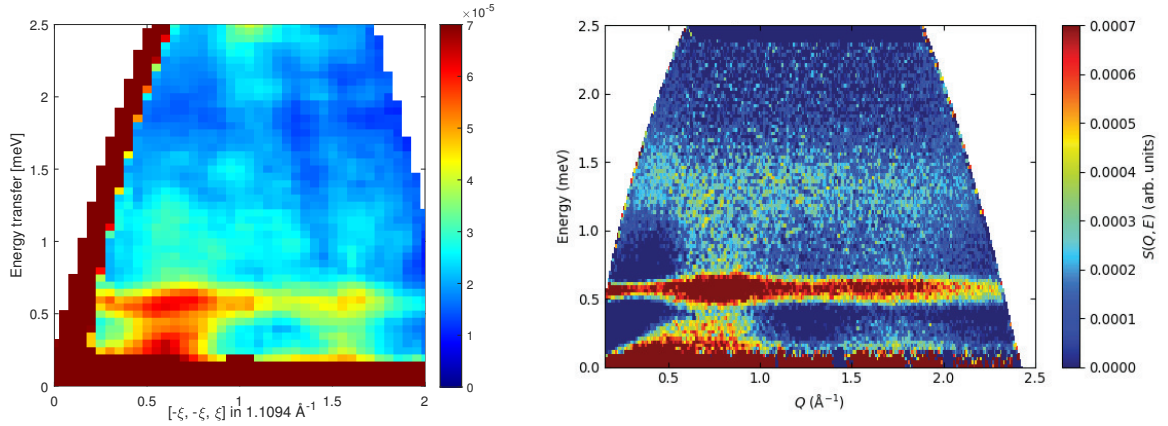


Figure 10.25: Computations trying to model observed inelastic spectrum in  $K_2Ni_2(SO_4)_3$ .

### 10.2.3 Dispersive excitations and continua

In order to study the dispersive and potentially gapped character of the magnetic excitations in the system, inelastic neutron scattering was carried out on a single crystal of 105 mg of  $K_2Ni_2(SO_4)_3$ , at the IN5 spectrometer at the ILL neutron source in Grenoble. The crystal was placed in a dilution fridge, giving access to scattering at a base temperature of 50 mK. The results are presented in Fig. 10.26.



(a) Neutron scattering cross section of  $K_2Ni_2(SO_4)_3$  in a selected direction. (b) Powder average of inelastic neutron scattering data measured at 50 mK of  $K_2Ni_2(SO_4)_3$ , subtracted from 30 K data.

Figure 10.26: Inelastic neutron scattering results on  $K_2Ni_2(SO_4)_3$  at 50 mK.

Figure 10.26a shows the observed inelastic features along a selected direction of interest. It appears that a clear dispersive feature is observed, reaching its maximum at 0.6 meV, and emerging from the elastic line at a position similar to the observed features in the DNS and in the WISH data. The intensity of the excitations looks to be continuous all the way up to 0.6 meV. The intensity above 0.6 meV is significantly smaller, but quite notably, not completely suppressed. It indeed seems that there is some other continuum of intensity present up to 1.5 meV, energy above which the excitation does not seem to survive. This is seen in a better fashion in the powder averaged data, shown in Fig. 10.26b, where the 30 K powder averaged data has been used as background and subtracted. The dispersion looks strikingly similar to the dispersion already acquired in the DNS experiment, with an energy scale of 1.5 meV and highlighting the importance of the 0.6 - 1.5 meV energy range. Moreover, a clear line of very intense scattering above 0.5 meV is visible, and may be associated to singlets populating the system. The q-dependence of this feature is very interesting and should be further studied.

Overall, these new results have not yet been analyzed in details but certainly show very interesting features of the physics at play in the system and deserve a full, in-depth dedicated

study.

**10.2.4 Discussion on  $\text{K}_2\text{Ni}_2(\text{SO}_4)_3$** 

Numerous experiments were carried out on  $\text{K}_2\text{Ni}_2(\text{SO}_4)_3$  and all of them seem to point towards the same direction: the low temperature ground state of  $\text{K}_2\text{Ni}_2(\text{SO}_4)_3$  shows hints of long range order, strongly suppressed by the quantum fluctuations of its spin-one nickel constituents. Low temperature heat capacity,  $\mu\text{SR}$ , and diffuse neutron scattering data show compelling evidence of strong frustration and spin-liquid like behavior of the ground state, even though neutron diffraction reveals unambiguously that a very weak static magnetic moments settles at dilution temperature.

Application of a magnetic field seems to liberate the system from the static component and drive the system in a pure quantum spin liquid state, similar to the field induced stabilization of quantum spin liquids in  $\alpha\text{-RuCl}_3$  [227]. This hypothesis may be tested by measuring in field neutron diffraction, confirming the disappearance of the static contribution from the long range ordered moments to the magnetic cross section.

This novel three dimensional compound, based on two interconnected trillium lattices thus shows a configuration of magnetic moments that successfully hosts a quantum spin liquid ground state at low temperature, with several questions remaining unanswered: what are the details of the magnetic structure of the weak static moment observed in zero field? What are the details of the dispersion spectrum at dilution temperature? Can it be described by a spinon model? Does the spin wave picture describe faithfully the observed excitations, similar to spin liquids in one dimension, where spin waves "only" fail to describe the continuum?

## 11 Combining heat capacity and X-rays: a new way to investigate spins systems

As discussed in previous chapters, the heat capacity offers a unique way of obtaining numerous insights on condensed matter systems. Indeed it overcomes local effects, inhomogeneity for example, and grabs also collective information on the investigated system. Heat capacity is sensitive to first and second order phase transitions, and is thus a remarkable tool, helping to establish the phase diagrams of various compounds. It was for example instrumental in determining the crystalline electric field in  $\text{CeMg}_3$ [228], in the determination of residual entropy in spin ice systems[229], or even in the study of high temperature superconductivity[230, 231, 232, 233, 234]. The need for specific heat data analysis is thus really present, even more since measuring it is quite simple, as it is typically performed on small samples, of less than five milligrams. Powders of this size can be obtained fairly easily, or at least more easily than obtaining sizable single crystals. Small single crystals are also way easier to obtain than millimeter-sized chunks of single crystal, and very relevant for heat capacity measurements that only required a couple of milligrams of sample.

There are three main possibilities to extract purely magnetic information from a heat capacity measurement. One of them implies fitting heat capacity at high temperature (compared to the magnetic energy scale) with a given lattice model. Alternatively one can measure a non magnetic analogue, and correct the heat capacity by re-normalizing to a new phonon mass. Lastly, one can use Density Functional Theory (DFT) to predict the phonon dispersion of a given lattice, and thus predict the phononic contribution to the heat capacity.

In a first step such experimentally educated methods are described through the Debye and Einstein models, and how the internal energy of a solid can be described by such models. From the internal energy the heat capacity and the unit cell volume can both be derived and predicted. In a second step, the measurements of non magnetic analogues and how this information can be used to analyze condensed matter systems are discussed. The relation between magnetic entropy and heat capacity is finally discussed, with numerous examples coming from research at the forefront of condensed matter physics. Finally, numerical methods and



## **Chapter 11. Combining heat capacity and X-rays: a new way to investigate spins systems**

---

their predictions are discussed and compared to other modeling methods: the case of non magnetic silicon is presented, as well as the study of  $\text{MnF}_2$ , a strongly correlated magnetic system. These two basic examples are complimented by measurements of the heat capacity and comparison between the numerical and experimental results. Room for improvements of the method and further numerical aspects are also discussed, in order to provide a robust systematic way of analyzing the data. The work on the combination of heat capacity and volume of the unit cell to better determine phonon parameters of a sample is an exclusive work, while the last part on numerical calculations has only been supervised, hence the small emphasis put on it.

## 11.1 Experimentally educated methods

### 11.1.1 Theory: Debye and Einstein

Both the heat capacity and the unit cell volume can be estimated using the internal energy of a solid,  $U$ . The relation between the energy and the unit cell volume is stated in equation (11.1).

$$V(T) = \gamma U(T) / K_0 + V_0 \quad (11.1)$$

This temperature dependent equation denotes the fact that the unit cell volume has the same temperature dependence as the internal energy, up to a factor given by the ratio of the Grüneisen parameter  $\gamma$ , divided by the bulk modulus  $K_0$  plus an offset, called  $V_0$ , playing the most important role for the unit cell volume at zero Kelvin. The relationship between the energy and the heat capacity is even simpler and is stated in equation (11.2).

$$C_p = \left( \frac{\partial U}{\partial T} \right)_p \quad (11.2)$$

Thus the determination of the internal energy of a solid appears yet once again paramount. In the simplest approximation, only the contribution coming from the quantized vibrations of the lattice, the phonons, is considered. This contribution is dominant at high temperatures ( $\propto T^3$ ), whereas the purely electronic contribution is more relevant at very low temperatures (linear in  $T$ ). The internal energy from the phonons is given by equation 11.3.

$$U = \sum_{\vec{k}} \sum_p \langle n_{\vec{k}p} \rangle \hbar \omega_{\vec{k}p} \quad (11.3)$$

In that equation,  $\vec{k}$  is the phonon momentum,  $p$  its polarization,  $\langle n_{\vec{k}p} \rangle$  the occupation factor of such a phonon, and  $\hbar \omega_{\vec{k}p}$  its associated energy. The brackets stand for thermal equilibrium using a distribution function. The Debye and Einstein model consists of an set of approximations used to model the dispersion relations, i.e., the dependence of the phonon energy on the momentum. Indeed, even though this quantity can be predicted theoretically -this is the topic of another section-, remarkable predictions can often be made by using drastic, yet realistic simplifications[235, 236]. In the Debye model, the phonon dispersion relations are linearly depending on the temperature, with a finite slope, directly related to the Debye temperature. This models best acoustic modes, which can be present up to a number of three: one longitudinal, and two transverse. The other interesting modes of a lattice are the optical modes, They present relatively lower dispersion, and in the Einstein model, they correspond to a flat band, located at a certain energy transfer defined by the Einstein temperature.

## Chapter 11. Combining heat capacity and X-rays: a new way to investigate spins systems

The internal energy can be separated in its Debye and Einstein contributions, as specified in equation (11.4).

$$U(T) = U_D(T) + U_E(T) \quad (11.4)$$

The Debye contribution is explicitly written in equation (11.5), and the Einstein contribution is stated in equation (11.6).

$$U_D(T) = 9 \sum_i n_{D,i} k_B T \left( \frac{T}{\Theta_{D,i}} \right)^3 \int_0^{\Theta_{D,i}/T} \frac{x^3}{e^x - 1} dx \quad (11.5)$$

$$U_E(T) = \frac{3}{2} k_B \sum_j n_{E,j} \Theta_{E,j} \coth \left( \frac{\Theta_{E,j}}{2T} \right) \quad (11.6)$$

This set of equation has direct implications on the mathematical description of heat capacity.

### Heat Capacity

The lattice contribution to the specific heat can thus be expressed as the sum of the Debye contributions, noted  $C_{D,i}$  [237, 238], with  $i = 1, 2, 3$  and the Einstein contributions  $C_{E,j}$ , with  $j = 1, 2, \dots, N - 3$ , where  $N$  is the number of atoms per unit cell, as in equation (11.7).

$$C_p = \sum_i C_{D,i} + \sum_j C_{E,j} \quad (11.7)$$

The details of the Debye contribution are given in equation (11.8).

$$C_{D,i}(T) = 9 n_{D,i} R \left( \frac{T}{\Theta_{D,i}} \right)^3 \int_0^{\Theta_{D,i}/T} \frac{x^4 e^x}{(e^x - 1)^2} dx \quad (11.8)$$

The explicit form of the Einstein component is shown in equation (11.9).

$$C_{E,j}(T) = 3 n_{E,j} R \frac{y^2 e^y}{(e^y - 1)^2}, y \equiv \Theta_{E,j}/T \quad (11.9)$$

In this set of equations,  $R$  stands for the gas constant, and the Debye and Einstein temperatures

are written as  $\Theta_D$  and  $\Theta_E$  respectively. There is a sum rule, accounting for the total weights of the Debye and Einstein branches respectively, written as  $n_{D,i}$  and  $n_{E,j}$  respectively. The rule stipulates that the total weight of both contributions has to match the total number of atoms in the unit cell. In a typical fit routine, the heat capacity is measured, for a wide range of temperature, but only the high temperature part is used to fit Debye and Einstein temperatures. Indeed, the lower temperature data often contains contributions from magnetic transitions, in the form of a sharp  $\Lambda$ -like peak, or broad peaks, associated to correlations building up. Once the fit has been performed, one can subtract the fitted specific heat from the experimental data, which corresponds to the purely magnetic heat capacity. This heat capacity is related to the entropy of the system by equation (11.10).

$$S_{\text{mag}} = \int_T \frac{C_{p,\text{mag}}}{T} dT \quad (11.10)$$

In systems dominated by a given quantized spin  $S$ , thus corresponding to a  $2S+1$  level system, the total entropy expected to be recovered by a system is given by equation (11.11).

$$S_{\text{mag}} = R \ln(2(S+1)) \quad (11.11)$$

Even though this fitting can be performed on a set of data with many different points, there is no well defined way of determining which Debye and Einstein weights are reasonable. The way a typical fit is performed is the following: first one establishes all the configurations allowed for integer values of the weights, and satisfying the sum rule. In a second step, the fit is performed for these fixed values with many different random initial conditions. Finally, only physical solutions are retained: heat capacity cannot be negative, and the obtained parameters have to be weakly dependent on the chosen temperature range for the fit. There are still many solutions left, even though the fits do not necessarily converge for each choice of weights. The user can then choose a solution of his liking, a typical choice being to retain solutions that predict an entropy close to that of an expected spin  $S$  system. Of course, this solution cannot be used to make strong claims on the spin state of the system, but should rather be viewed as a self consistency check. In order to try and make the fit process more robust, one can use additional information from the volume of the unit cell. Indeed, this quantity is related to the internal energy of the solid, which means it can be modeled by a Debye and Einstein approximation as well. Moreover, on the experimental side, obtaining the lattice parameters of a sample is not considerably time nor resource-expensive[239, 240]. Many in-house, laboratory X-ray diffractometers exist, providing temperature control from room temperature to several Kelvins. Synchrotron measurements are always more precise, as they use a beam made of a single and well-defined wavelength, but are not required. Extracting lattice parameters from a diffraction pattern is one of the simplest tasks, since one only has to

do a LeBail Fit (LBF) to extract peak positions. Finally, this is also compatible with neutron scattering experiments, offering a rather simple way of double checking results from sole heat capacity fits.

### Unit cell volume

The volume of the unit cell is related to the internal energy by equation (11.1)[152, 153, 154]. This set of equations can be used as well as the heat capacity formulae to fit the Einstein and Debye temperatures. As a starting point, the initial version of the developed code only contained one Debye branch, leaving obvious room for improvement. The fitting is performed by taking as input both heat capacity and unit cell volume data, with a possible correction factor for the fitting weights. Traditionally, the fit weights are taken as the inverse of the square of the measured standard deviation. This intuitively gives great importance to measurements that are more precise. When combining two different data sets, the typical uncertainty of one measurement may however be very different from that of the other, and since the measured quantities are also different, there is no guarantee that measurements with higher uncertainty are actually of lesser quality. To reflect that when the fitting is performed, the possibility of scaling the measurement uncertainty of the whole set of unit cell volume data has been introduced. Quite naturally, this leaves a free parameter for the user to choose, but since this method is intended to be a confirmation method, confirming the magnetic data is consistent with a certain expected spin, this is deemed to be a reasonable decision to make in the overall fitting scheme. In that regard, another option has been implemented to the overall fitting scheme: the possibility of taking the expected value of entropy as a fit parameter. This option enables the user to specify the expected entropy, with a certain weight, so that the fit converges to a solution that corresponds to the required magnetic entropy, with the strength of the requirement corresponding to the weight of the desired entropy.

### 11.1.2 Chemical substitution

Another solution to the problem of extracting the heat capacity from a sample uses the non magnetic analogue route. This solution is based on the idea that it is a magnetic ion that induces a magnetic phase transition in a sample, detected by specific heat. However, if a non magnetic element substitutes the magnetic ion, the magnetic transition does not happen and hence can obviously not be measured by heat capacity. If, additionally, the crystal structure remains the same, the contribution of the lattice to the heat capacity has to also be similar, up to the mass of the atoms, resulting in different phononic constants. This method has been used with some success[241, 242, 243] and presents the advantage of getting rid of the uncertainty of models and numerical fits artifacts. It is however not possible for every compound to just substitute out the magnetic element, and even when it is indeed feasible, the obtained crystal structure sometimes does change significantly. Any correction due to strong deviations from the original crystal structure presents the disadvantages of introducing again modeling and numerical uncertainties in the studies.

### 11.1.3 Results

#### MoOPO<sub>4</sub>

The notion of fitting the heat capacity with one Debye branch and several Einstein branches, using the total magnetic entropy as a guide to the goodness-of-fit, was first used in 2017[237]. This study was performed in the frame of the study of MoOPO<sub>4</sub>, an orbitally quenched insulator. The authors used two Einstein branches and one Debye branch, and found an excellent agreement between the entropy recovered by the system and that of a two levels system. Cross checking these predictions with effective moments from DC-susceptibility measurements, the consistency of the fit was claimed. Errorbars were small, and left little room to misinterpretation from the mathematical point of view. From the point of view of physics, however, it appeared that this method was systematically producing solutions with large Debye temperatures, which brings up a question mark: the Debye contribution and the Einstein ones are valid for high temperature, compared to the interactions in the system. Within this high temperature region, the Debye contribution is expected to be more relevant at temperatures lower than the Einstein ones, simply because the Debye term is proportional to  $T^3$ , while the Einstein term explains the heat capacity behavior at extremely high temperatures, mainly responsible recovering the Dulong-Petit law. With the obviousness of the overwhelming importance of the Devye term, tt was thus felt that a more robust way of fitting the data was needed, which is why later uses of that method combine heat capacity information with unit cell volume data.

#### Cu<sub>2</sub>OSO<sub>4</sub>

Another example of use of that method took place in copper oxysulfate, Cu<sub>2</sub>OSO<sub>4</sub>, as discussed in chapter 9, dedicated to this material. The information is repeated here for the sake of grouping. This compound is a copper based Kagomé compound, presenting a transition to a magnetically long range ordered state at 20 K. This manifests in the form of a sharp  $\Lambda$  peak in the heat capacity, that shows a weak magnetic field dependence. The lattice parameters were measured by synchrotron X-ray diffraction at many different temperatures, enabling to provide both a complete view of high temperature heat capacity and unit cell volume.

Fig. 11.1a shows the measured heat capacity in zero field (blue), and in 14 T (red) on a powder sample. The yellow curve shows the result of the fit of the lattice model, for temperatures above 80 K. The inset shows a y-axis logarithmic scale zoom on the heat capacity to better grasp that the magnetic field effects are not present above 80 K. The purple curve shows the subtraction of the fitted heat capacity from the experimental data, divided by the temperature. The blue and green shadings correspond to the part of the entropy that are respectively locked in the transition and by correlations. The green area shows a strong temperature dependence up to 70 K. Fig. 11.1b corresponds to the magnetic entropy, plateauing to the value of a  $S = 1/2$ . The red shading corresponds to the uncertainty. Fig. 11.1c shows the result of the fit of the unit cell volume, in red, and the extracted data in blue. The help of the unit cell volume helped

## Chapter 11. Combining heat capacity and X-rays: a new way to investigate spins systems

---

selecting the final configuration, with one Debye branch with weight  $n_D = 1$  and a Debye temperature of  $\Theta_D = 171$  K, and two Einstein branches, with weights  $n_{E1} = 3$  and  $n_{E2} = 4$  and temperatures  $\Theta_{E1} = 245$  K and  $\Theta_{E2} = 939$  K. This is again fully consistent with DC-susceptibility measurements on the sample, in agreement with a spin half system.

### **$K_2Ni_2(SO_4)_3$**

$K_2Ni_2(SO_4)_3$  is a nickel based, three dimensional,  $S = 1$  spin liquid candidate. In this complex quantum magnet, the heat capacity was measured down to dilution temperature. It happens that chemical substitution was possible, and resulting in a compound with similar structure to the parent compound. Such a substitution consists in a replacement of nickel atoms by non magnetic magnesium atoms. The measured heat capacity for different values of field is shown in Fig. 10.3a, that of non magnetic analogue  $K_2Mg_2(SO_4)_3$  is shown in Fig. 10.3b and the subtraction is shown in Fig. 10.3c. The resulting heat capacity could be integrated to extract the overall spin, but its most interesting feature remains its low temperature behavior, corresponding to a  $T^2$  law, often observed in other spin-liquid candidates[244]. This result is visible in the log-log plot of the extracted magnetic heat capacity and shown in Fig. 10.3d.

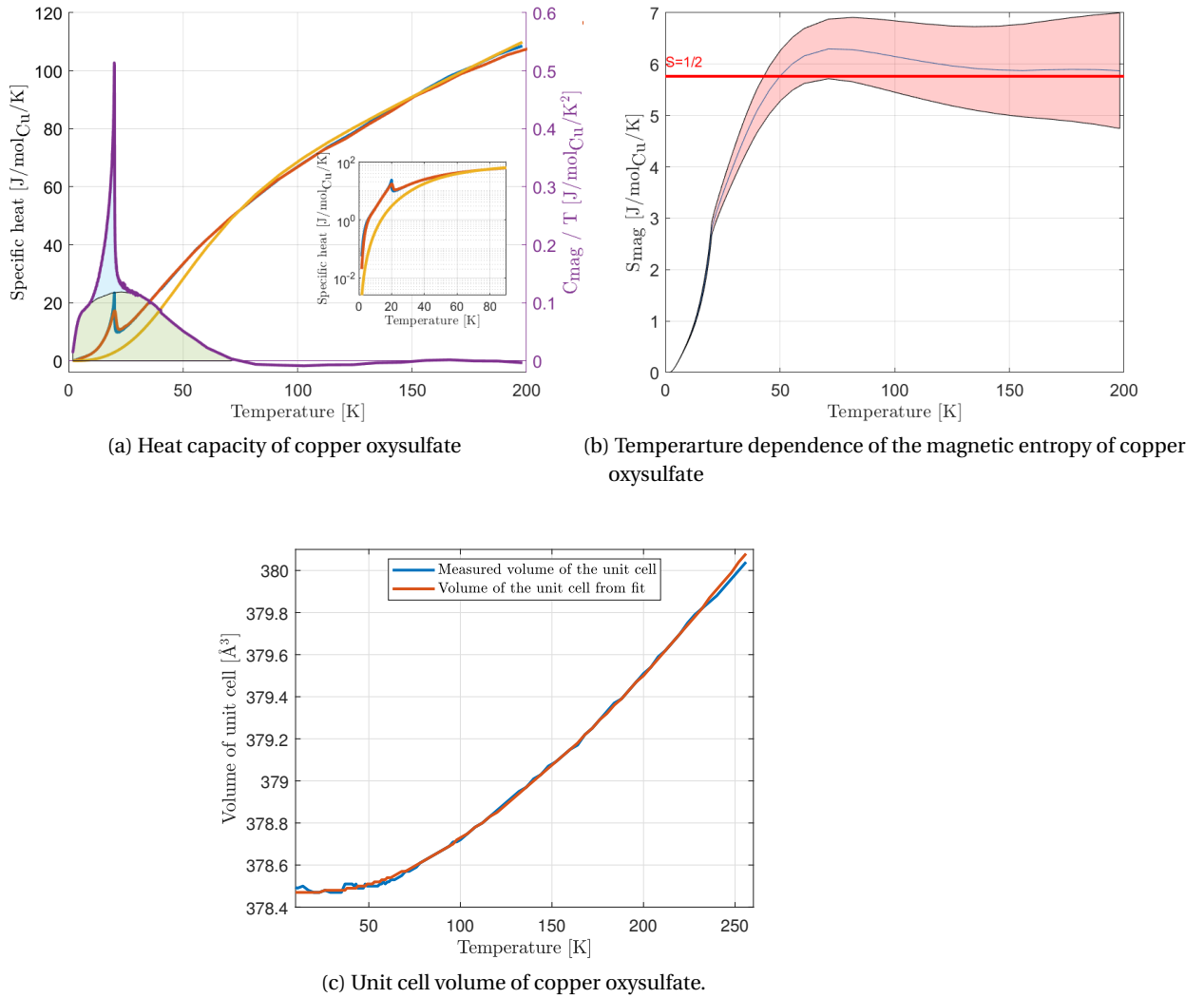


Figure 11.1: Result of combined fitting of heat capacity and unit cell volume for copper oxysulfate.



$\text{Co}_{4-x}\text{Ni}_x\text{Nb}_2\text{O}_9$

Last but not least, this method was used to investigate potential ferroelectric materials member of the nickel-doped cobalt niobate family:  $\text{Co}_{4-x}\text{Ni}_x\text{Nb}_2\text{O}_9$ . The parent compound is a known ferroelectric material, with a weakly non collinear antiferromagnetic ground state below a transition temperature of 27.4 K. It has been predicted that Nickel substitution in this compound may enhance both the magnetic transition temperature and the ferroelectric coupling strength. In order to study the ferroelectric coupling strength in two members of this family, labeled CN1 for  $x = 1$ , and CN2 for  $x = 2$ , it was first required to probe the spin configuration of the ground state. Neutron scattering was carried out on a powder sample of both compounds, and gave access to the ground state configuration, the transition temperature, and the values of lattice parameters at several temperatures. Fig. 11.2 shows data and analysis for samples of CN1 in the middle panel, and CN2 in the right one. The left panel corresponds to CN0, the parent compound, which was used as a sanity check since it is quite known from the literature[245].

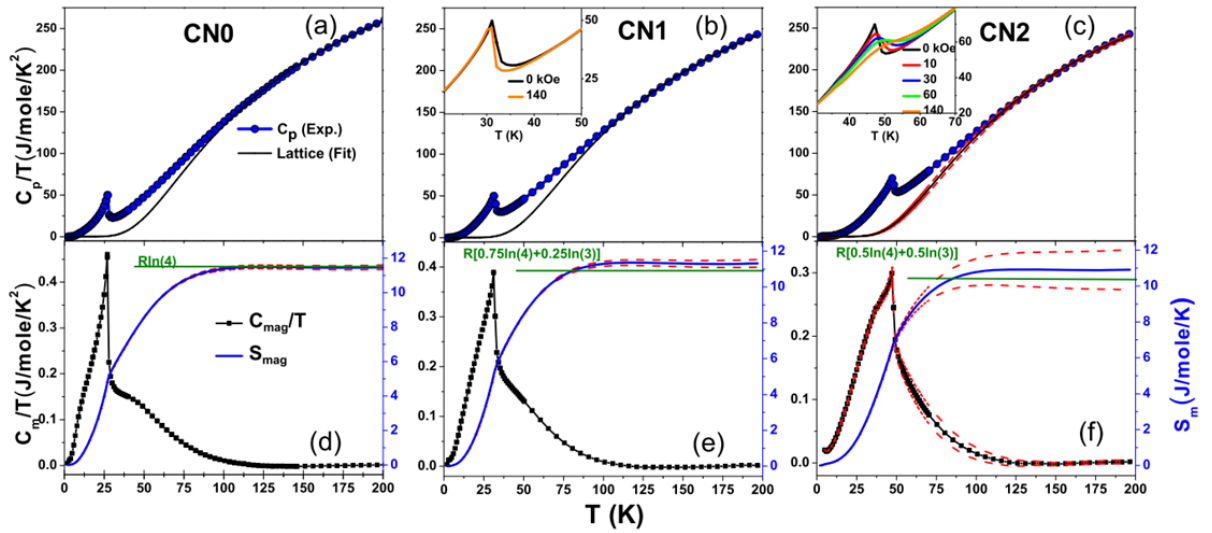


Figure 11.2: Heat capacity of  $\text{Co}_{4-x}\text{Ni}_x\text{Nb}_2\text{O}_9$  for  $x = 0$  (left),  $x = 1$  (middle),  $x = 2$  (right).

Results presented in Fig. 11.2 correspond to the heat capacity measurements in blue, and the lattice model in black (top row). The insets show the magnetic field dependence of peaks, confirming their magnetic origin. It appears that CN1 undergoes a magnetic transition at 31 K, slightly above CN0, and CN2 also shows a transition to a long range ordered state, at 47 K[238]. The bottom row in Fig. 11.2 corresponds to the subtraction providing the magnetic heat capacity divided by temperature. The blue curve shows the integral, the magnetic entropy plateauing to  $R \ln 4$ ,  $R(0.75 \ln 4 + 0.25 \ln 3)$  and  $R(0.5 \ln 4 + 0.5 \ln 3)$  for CN0, CN1, and CN2 respectively. These values of the entropy are consistent with a spin 3/2 for the Cobalt and a spin 1 for the Nickel atom, in their respective proportions. The red dashed lines show the uncertainty on the fit showing good confidence in the final value of the entropy. These fits are

obtained using one Debye and one Einstein branch, with respective weights of 5 and 10 for both CN1 and CN2. The associated Debye and Einstein temperatures are  $\Theta_D = 1083(16)$  K and  $\Theta_E = 312.5(1.5)$  K for CN1 and  $\Theta_D = 1047(65)$  K and  $\Theta_E = 322.5(10)$  K for CN2. These results have been consolidated by performing the usual combined fit where not only heat capacity data is used, but also the unit cell volume. The result of the fit of the unit cell volume is shown in Fig. 11.3.

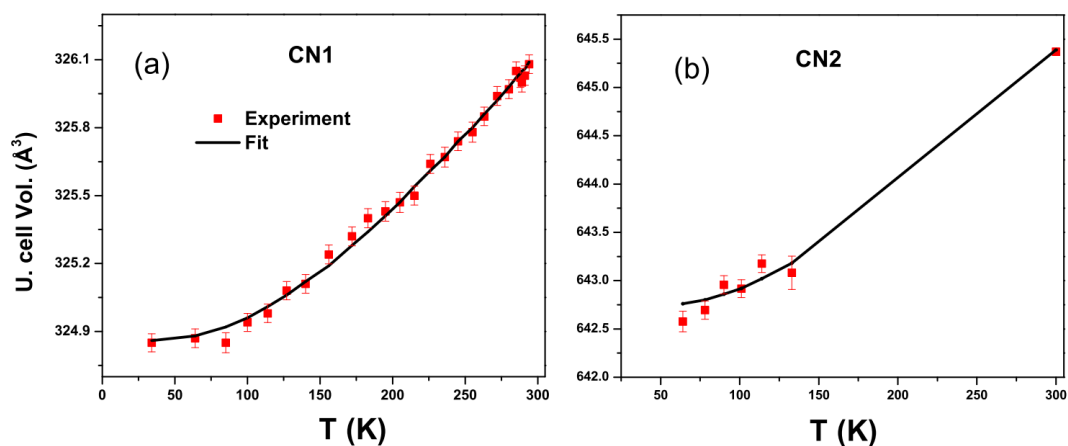


Figure 11.3: Unit cell volume of  $\text{Co}_{4-x}\text{Ni}_x\text{Nb}_2\text{O}_9$  for  $x = 1$  (left) and  $x = 2$  (right).

In Fig. 11.3, the experimental data is shown in red, obtained from refining neutron diffraction patterns. The black curve corresponds to the result of the fit from the combined fitting method. Fig 11.4 shows the stability checks that were performed to ensure that the fit was actually physical.

Fig. 11.4 shows for CN1 on the left hand side and for CN2 on the right hand side, the stability of some relevant parameters of the fit. In order to fit the heat capacity, one has to first select a temperature range over which the fit has to be performed. The basic rule is to try and keep the highest temperature points. However, in practice, in many heat capacity experiments, one has to change to a new grease to fix the sample above 200 K. This induces a contamination of the sample's own specific heat, and even though this should be subtracted from careful addenda measurements, it is frequently far from being perfect. This is the reason why many specific heat measurements stop around 200 K. The starting temperature for the fit can also not be too low, otherwise one risks using data mixing lattice contributions with some part of the magnetic entropy.

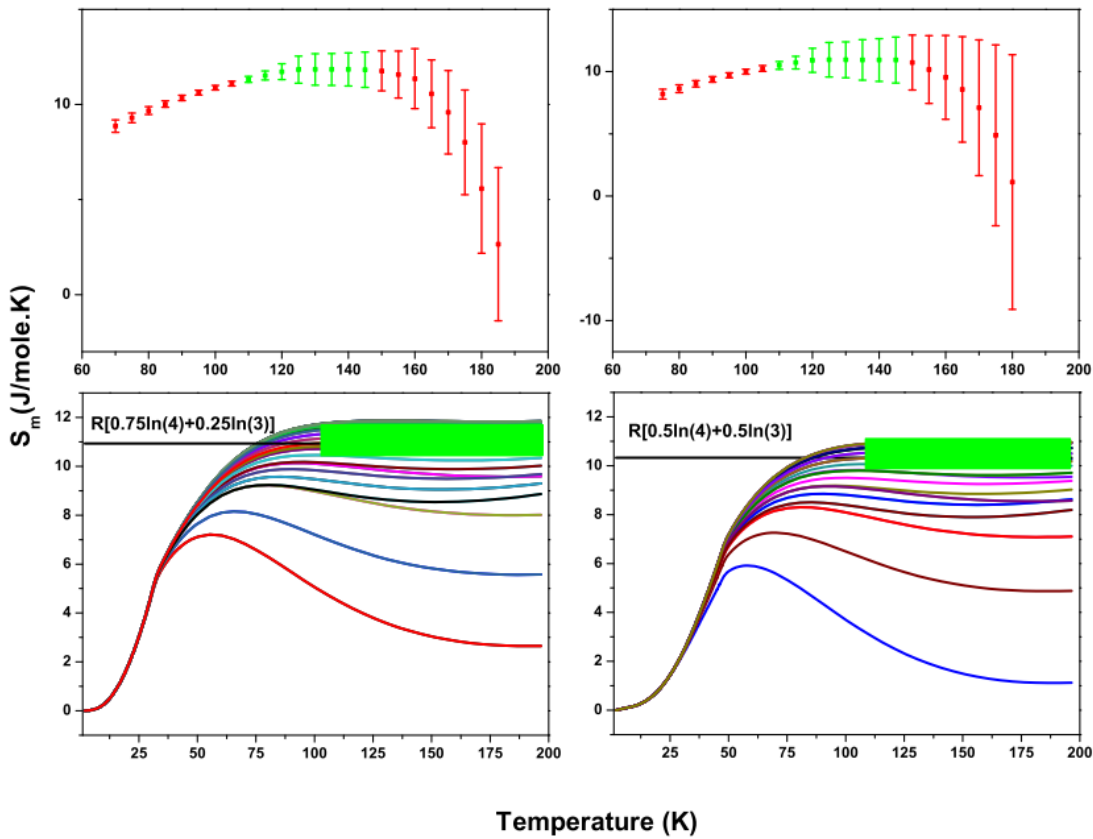


Figure 11.4: Entropy of  $\text{Co}_{4-x}\text{Ni}_x\text{Nb}_2\text{O}_9$  for  $x = 1$  (left) and  $x = 2$  (right).

A good consistency check that can be performed is thus to vary the fit range, typically only the lower temperature bound and check how this impacts the resulting entropy: a starting temperature that is too low results in failing to capture the whole magnetic entropy from the sample. It is expected that then, there is a region in the parameter space where the obtained parameters (entropy, and Debye and Einstein temperatures) are rather constant, with reasonable errorbars. Finally, when increasing too much the starting temperature of the fit, it is expected that, at some point, too few measurement points are used and the fits start

to be unstable, with large uncertainties in the obtained parameters. This is exactly what is happening in Fig. 11.4, where only the entropy is shown, for simplicity (and not the Debye or Einstein temperatures). The graphs in the top row show that for both compounds, the fit is providing a rather stable and reasonable entropy, for a certain range of parameters, and finally, when increasing too much, the fits become unstable. The left hand side of the graphs shows that when changing (by increasing) the starting temperature of the fit from 60 K to 100 K, the resulting entropy also changes (and increases). This is indicative that the starting temperature of the fit is too low, and that it impacts the resulting parameters. The graphs in the second row present all the temperature-dependent entropy curves for both compounds. The green rectangle shows the region of parameters for which the fit is considered stable.

A method helping to extract spin information from heat capacity measurements has been developed by fitting a model lattice. The fit routine has been made more robust by adding additional information and constraints from the volume of the unit cell. An ideal solution would be to confirm this way of fitting the data works more simple compounds, where the lattice contributions can be predicted, for example from Density Functional Theory (DFT). These results were obtained by Xavier Boraley during his master thesis, supervised by Virgile Y. Favre, and are briefly mentioned thereafter, for completeness.

### 11.2 Calculations predicting heat capacity

#### 11.2.1 Density Functional Theory

As mentioned before, an ideal solution to the heat capacity problem is to model theoretically compounds with a method predicting Debye and Einstein temperatures, weights, and thus contributions with reasonable confidence. This study needs to involve many different approximations, as the many body systems that have to be solved are both non trivial and computationally very expensive, the number of states of a spin half system increasing as  $2^N$ ,  $N$  being the number of simulated sites. One such vastly used method is the Density Functional Theory (DFT). DFT involves a way of simplifying the Schrödinger equation in the frame of many-body physics. The basic hypothesis of the theory states that the Hamiltonian of the system contains four different terms: the kinetic energy, and interactions between electrons and ion: ion-ion (repulsive), electron-electron (repulsive), and the ion-electron (attractive). The Born-Oppenheimer approximation splits the ionic and electronic contributions and assumes they can be computed separately. Electrons being much lighter than ions, they are usually treated as a different object, simplifying further the quantum mechanical problem. Then the Hohenberg-Kohn theorem establishes that the electron density can be used as sole parameter of the total energy. Another important simplification regards getting rid of the numerically expensive many-body parts of the problems. In order to achieve that, the system is modeled as a system of non interacting single particles, with different wave functions, assuming both real and approximated states have the same ground state energy. This is also known as the Kohn-Sham hypothesis, effectively creating an approximation term that contains all the non-easily computed part. This is the so-called exchange correlation functional. There exists a variety of exchange correlation functional forms that capture certain notions of real systems, with the most complex forms being more computationally expensive, quite naturally.

- *The Local Density Approximation (LDA)*: in this approximation, the exchange-correlation only depends on the electron density. This is the simplest possible approximation, and usually fails to capture the correct behavior of strongly correlated systems.
- *Generalized Gradient Approximation (GGA)*: computationally more expensive than LDA, the GGA exchange-correlation adds a gradient density to the computation, and usually results in better accuracy.
- *Hybrid functional*: in this approximation, the exchange-correlation is split into two parts, one of them being the GGA approximation, and the other being an exact exchange. The exact exchange does present an explicit dependence on the density matrix, which results in a higher computational cost.

- *Fully non local functional*: unlike other exchange correlation functional forms, the fully non local functional also uses unoccupied states in the computations. This also increases the numerical complexity of the system.

There are numerous technical points that are not addressed in details here, such as the notions of *k-points* and *supercell*. In short, using Fourier transforms helps simplifying the problem, but still keeps an infinite number of wave functions that have to be computed. The *k-points* are reciprocal space points at which one chooses to calculate a finite number of these wavefunctions. The wavefunction is assumed to vary slowly in *k*, which implies that computing at a single *k* gives a valid description in the vicinity of the selected point and that indeed, the space can be split into a *k-grid*. The notion of *supercell* is related and consists in a grouping of *N* unit cells. When applying periodic boundary conditions, the system effectively behaves as a system with more atoms and thus computations are more accurate, at the expense of computation time. For larger unit cells, the *k-grid* can be reduced. This still does not solve the problem that there is an infinite number of wavefunctions to be computed. To solve that problem, a cutoff energy is introduced. This energy is the threshold above which a plane wave is considered as not contributing to the band theory. This is of course a strong hypothesis and it should be remembered that once conclusions are drawn, it is reasonable to check that the energy cutoff does not change results significantly. The last often-used approximation is that of the pseudo potential. It simplifies the rapidly oscillating wavefunction close to the ionic cores by a much more monotonic one, effectively reducing the number of plane waves required to calculate the system with reasonable accuracy.

The DFT computational method can be used for various systems. The most interesting systems for magnetic heat capacity applications are silicon and  $\text{MnF}_2$ . Silicon is non-magnetic, cheap, and readily measurable and studied. Predicting its phonon spectrum should be straightforward and verifying the heat capacity fits and unit cell volume should be straightforward.  $\text{MnF}_2$  is one of the simplest antiferromagnetic compounds, and is thus a good toy-compound to verify magnetic properties predictions.

### 11.2.2 Silicon

The convergence of the DFT calculations for silicon was ensured by verifying the total energy convergence with different energy cutoffs, grids and k-point grid. An energy cutoff of 650 eV was selected, and the k-point grid size was a cube of seven units. Fig. 11.5 shows the results of calculated and measured specific heat. The calculations were performed using the phonopy package[246]. Heat capacity was measured using the heat capacity measurement option of a PPMS.

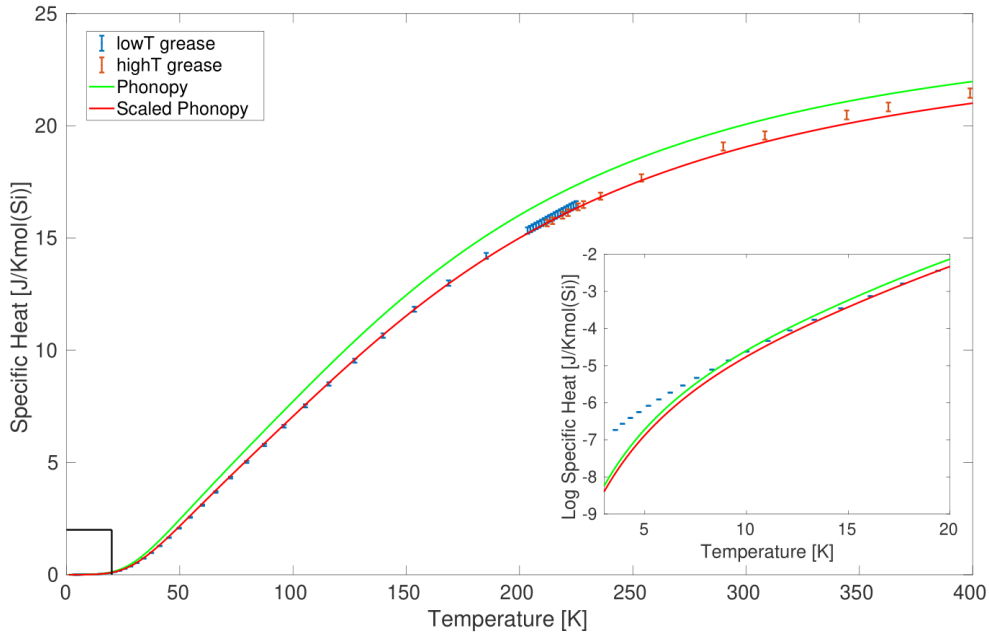


Figure 11.5: Heat capacity measured in blue and red (with errorbars), the green solid line shows the result predicted by DFT, the red solid line corresponds to scaled numerical results. The inset shows a y-axis log-scale of the same figure, zoomed in to highlight low temperature differences.

The green curve shows the result of the calculation, obtained from calculating the phonon dispersion. It has been determined that there is some uncertainty both on the obtained temperature and on the obtained heat capacity. The DFT generated data was thus scaled. In order to determine the best scaling parameters, a parameter space search was carried out, trying to minimize the difference between measured and calculated heat capacities. This introduced a cost function that has to be minimized, stated in equation (11.12). The results of this minimization can be observed in Fig. 11.6.

$$\sum_{i=T} \left( \frac{C_{p, \text{Phonopy}}^T - C_{p, \text{Measured}}^T}{C_{p, \text{Measured}}^T} \right)^2 \quad (11.12)$$

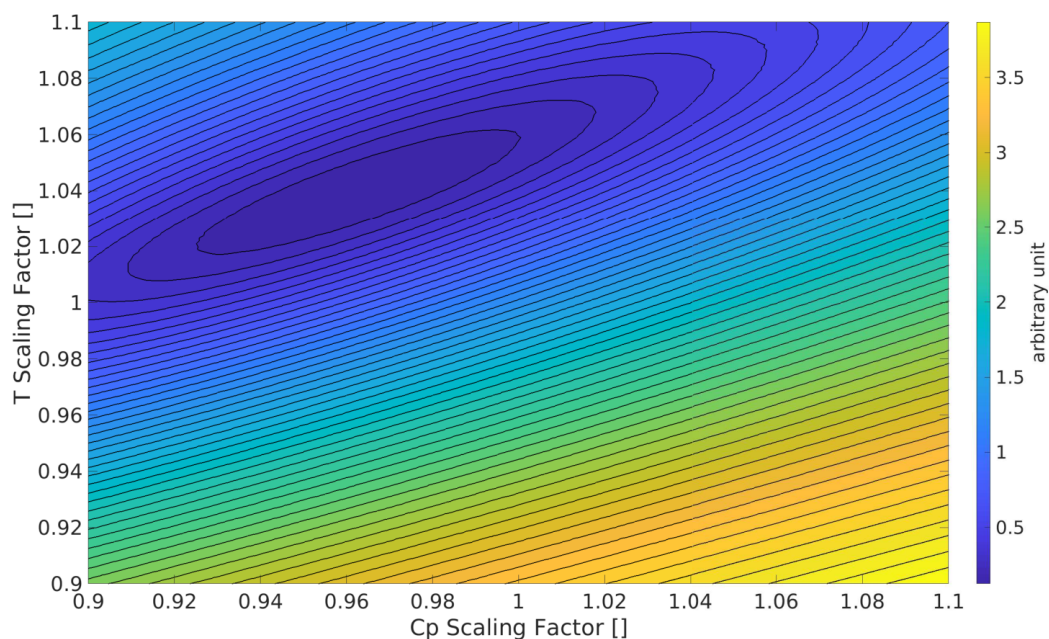


Figure 11.6: Cost function result of scaling parameters to minimize difference between calculated and measured silicon heat capacity.

A clear minimum appears around a scaling parameter of 1.04 for the temperature, and 0.97 for the heat capacity. These corrections lead to the red curve in Fig. 11.5. The deviation at low temperature has been attributed to a doping effect coming from the Boron in the sample. For a non negligible doping indeed, one expects such a low temperature correction to the heat capacity coming from the electronic component. Unfortunately, it turns out that silicon is best modeled by several Debye branches, which the fitting routine does not tolerate, so this did not give opportunity for comparison, but still confirmed that the heat capacity can be computed by DFT in a simple system, in good agreement with measurements.



### 11.2.3 MnF<sub>2</sub>

The heat capacity of MnF<sub>2</sub> has already been reported in the literature[247], and presents the sign of a transition to a magnetically long range ordered state at a transition temperature of 67.3 K. In order to compute the heat capacity using DFT, the GGA of Perdew-Burke-Ernzerhof[248] exchange correlation functional form was used. Initial computations did not meet any success, since the magnetism in Mn atoms involves 3d electrons, typically strongly correlated to local magnetic fields, out of the scope of what can be performed with standard DFT. The spin polarizations have been added to the simulation but simple DFT calculations still fail to reproduce the reported band structure, density of states, and thus heat capacity of the sample. Instead, a DFT+U method was used, correcting the energies. Here again, the heat capacity was measured, on a sample of 1.75 milligram of MnF<sub>2</sub> using the heat capacity option of the PPMS. The results are presented in Fig. 11.7.

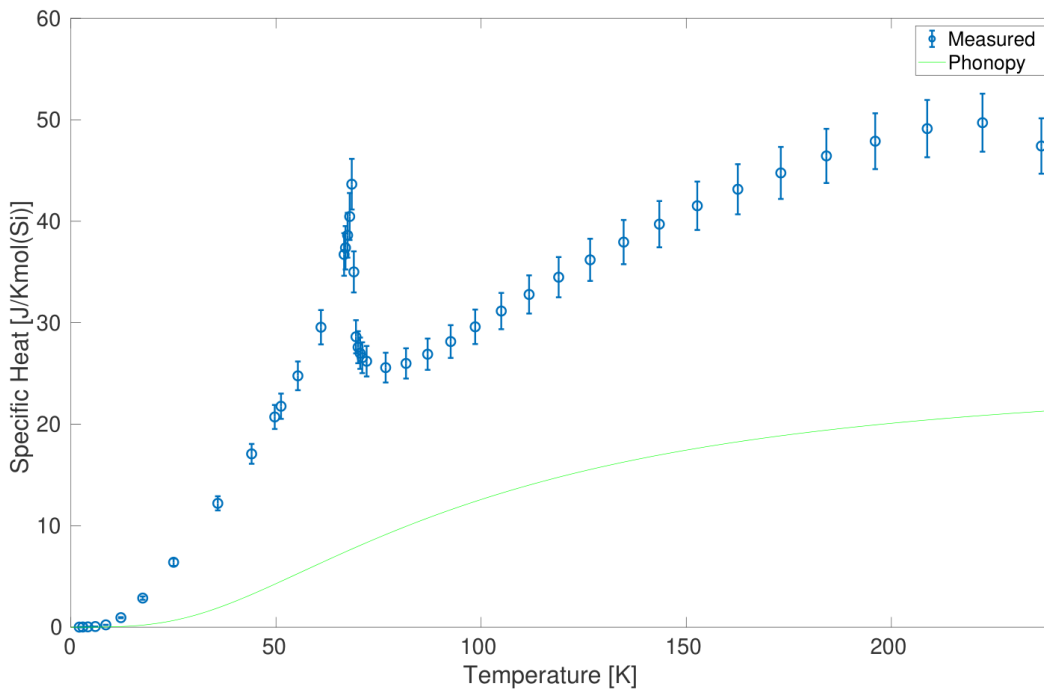


Figure 11.7: Heat capacity measured in blue (with errorbars), the green solid line shows the result predicted by DFT, using the DFT+U method with GGA.

Fig. 11.7. shows in blue the measured data. The magnetic peak is clearly observed below 70 K. The green, solid line is the calculated heat capacity. It is quite straightforward to see that the model completely fails to reproduce the experimental data. Even in the case of a strong contribution of the magnetism to the heat capacity, it seems unrealistic that such a difference could happen, since the difference between the DFT predicted solution and the experimental data does not appears to change significantly up to 250 K. Possible reasons for this failure include, but are not limited to, a problem with the exchange correlation, which should be chosen more carefully, but more importantly, a lack of precision in the computation.

Indeed, the space group of  $\text{MnF}_2$  is tetragonal, which has a much lower symmetry than cubic silicon. This subtle difference directly translates in numerical expenses: one should try to run the calculations with a bigger supercell and more k-points. Far reaching is this approach, more work is needed to investigate and perfect the original idea. One of the principal shortcomings of this modeling of the theory is that it is extremely computationally expensive, particularly so as the system symmetry is low. The main problem from the physics side is that the theory relies on the choice of a proper exchange correlation function, which turns out to be an approximation to the exact quantum theory and that these approximations tend to not describe magnetic systems properly due to the interaction between electrons in such systems. More advanced methods such as DFT+U have been developed in that regard.



## Conclusion

The work presented in this thesis is twofold. On the one hand, the primary goal of the research is quite naturally to progress in the field by deepening the understanding that the general community has of physics, and in particular, of quantum magnetism. On the other hand, and on a more personal level, it can be realized quickly when reading this thesis that a substantial part of it is dedicated to the description of the fundamental theoretical and experimental background that is a prerequisite to understand and carry out the measurements and the reasoning exposed in this thesis. This reflects the fact that this PhD and this thesis work was not limited to the sole understanding and manipulation of physical phenomena. The author, being relatively unfamiliar with experimental physics, also had to dwell on many concepts. In that view, the content of this thesis can be considered as relatively self-contained, and should be understood by any student with reasonable knowledge of the field of physics in general, and not condensed matter physics in particular.

A brief overview of magnetism has thus been portrayed: many of the interesting quantum magnetism compounds are indeed insulators. The origins of the magnetic exchange have also been demonstrated, and the fundamental ground states associated to the very commonly realized Heisenberg Hamiltonian have been shown. It has been stressed that the contemporary field of frustrated physics is an extensive playground to test the knowledge of fundamental physics with many phenomena occurring, ranging from competition between classical and quantum ground states on the triangular lattice, to the fully quantum picture of quantum spin liquids. In a second step, emphasis has been placed on the experimental means of probing systems and verifying their expected properties, including Josephson junction based SQUID magnetometers, Heat Capacity measurement systems, muon spin rotation, and of course, neutron scattering, which, by taking advantage of the magnetic moment of the neutron remains to-date one of the best ways of confirming experimentally magnetic ground states and observing spin dynamics.

All these fundamental tools have been applied to actual systems and many measurements were carried out. In particular, it has been evidenced that  $\text{Cu}_2\text{OSO}_4$  is modeled by a Kagomé-like lattice of spin half copper atoms -a third of which are replaced by dimers- and retains its structure down to one Kelvin, undergoing a second order phase transition to a state featuring

## Conclusion

---

magnetic long range order at 20 K. The ground state can be characterized as a ferromagnetic configuration of spins close to the  $120^\circ$  configuration, which differs significantly from the predicted spin-liquid ground state of the Kagomé lattice, but is still close to the classical ground state of the triangular lattice. Curie-Weiss temperatures, obtained by fits of DC-susceptibility high temperature data confirm that frustration is important in the sample, and reported DM interaction in the sample place it on the verge of a quantum phase transition to a disordered, spin-liquid phase. Inelastic neutron scattering on single crystals has been carried out and unveils the directional dependent character of spin excitations in the system. Despite the best efforts, a fully quantum model to describe these fluctuation processes could not be established but significant information could be extracted. The gaped spectrum and the ground state magnetic structure are both consistent with a magnetic field originating from the dimers canting the other spins, then forming an alternating antiferromagnetic chain, close to half saturation. Kagomé layers are connected by weak couplings, compared to both in plane couplings. In the current scheme, lattices formed by the two crystallographically inequivalent copper atoms are decoupled, and the effect of one onto the other is modeled by this mean-field. In a typical fully quantum model, one should replace this effective mean-field by a genuine magnetic interaction that has yet to be found.

Another system that was studied extensively is the spin liquid candidate  $\text{K}_2\text{Ni}_2(\text{SO}_4)_3$ . In this compound, it has been evidenced that no clear sign of magnetic ordering can be observed down to 20 mK and dilution temperatures: the DC-susceptibility shows a rather isotropic behavior, varying slightly slower than the Curie-Weiss fit at low temperature. While heat capacity measurements do suggest soupçons of transitions, neither the DC susceptibility, nor  $\mu\text{SR}$ , nor the neutron diffraction showed clear signs of magnetic order.  $\mu\text{SR}$  data showed the low temperature ground state is quite dynamical. Polarized and unpolarized neutron diffraction revealed the presence of a broad correlated peak of confirmed magnetic origin at low values of inverse d-spacing. A high-resolution diffraction experiment revealed that magnetic peaks appear on top of this broad contribution coming from short range order. These peaks are of extremely low intensity compared to that of the short range order contribution, confirming that the long range order has to go through hindrances and is not realized in a straightforward way. The magnetic structure has been found to be described by three distinct magnetic propagation vectors:  $(1/3\ 0\ 0)$ ,  $(1/3\ 1/3\ 0)$ , and  $(1/3\ 1/3\ 1/3)$ . The details of the ground state configuration have however not been refined yet, since too many free parameters in the model do not allow to obtain a sensible physical information out of the possible model refinements. The main candidate reasons for the obstacles to long range order are the geometrical frustration and the quantum fluctuations. The details of magnetic couplings in the system are yet-to-be revealed, however, inelastic neutron scattering experiments indicate that the excitations of the magnetic ground states are dispersive and that they show a continuum. This character of the excitation spectrum is lost at higher temperatures, already at 2 K, where it takes the form of broad scattering, diffuse, and roughly energy independent, typical of spin-liquid states.

The last contribution of this thesis to the field of quantum magnetism is of slightly less fundamental relevance, and is more technical. A tentative fit routine has been established, in order to fit the heat capacity of magnetic materials. Indeed, subtracting the lattice contribution from the total heat capacity opens up the possibility of extracting the purely magnetic entropy of a system, which can be linked to its spin state. Heat capacity data is typically hard to fit, since its high temperature part hardly changes when exploring the parameter space in the model. To try and make this fit more robust, a combined fit also utilizing the unit-cell volume has been implemented and applied to many different spin systems, with reasonable success. In order to confirm these results, a theoretical work has been started to predict the fits that are performed and verify the effectiveness of the method. Magnetic systems are computationally expensive to model, and the study has not yet provided clear conclusions.

Overall, as is often the case in science when trying to solve a problem by answering a set of questions, many more deep and fascinating questions arise. This thesis leaves the reader with a significant number of them, and it is hoped that it will trigger the interest of physicists to further study frustrated physics, quantum magnetism, and condensed matter physics in general.



## Bibliography

- [1] Hesameddin Ilatikhameneh, Tarek Ameen, Bozidar Novakovic, Yaohua Tan, Gerhard Klimeck, and Rajib Rahman. Saving moore's law down to 1 nm channels with anisotropic effective mass. *Scientific Reports*, 6(1):31501, Aug 2016. ISSN 2045-2322. doi: 10.1038/srep31501. URL <https://doi.org/10.1038/srep31501>.
- [2] Nguyen Duy Khanh, Taro Nakajima, Xiuzhen Yu, Shang Gao, Kiyu Shibata, Max Hirschberger, Yuichi Yamasaki, Hajime Sagayama, Hironori Nakao, Licong Peng, Kiyomi Nakajima, Rina Takagi, Taka-hisa Arima, Yoshinori Tokura, and Shinichiro Seki. Nanometric square skyrmion lattice in a centrosymmetric tetragonal magnet. *Nature Nanotechnology*, 15(6):444–449, Jun 2020. ISSN 1748-3395. doi: 10.1038/s41565-020-0684-7. URL <https://doi.org/10.1038/s41565-020-0684-7>.
- [3] C. D. Stanciu, F. Hansteen, A. V. Kimel, A. Kirilyuk, A. Tsukamoto, A. Itoh, and Th. Rasing. All-optical magnetic recording with circularly polarized light. *Phys. Rev. Lett.*, 99:047601, Jul 2007. doi: 10.1103/PhysRevLett.99.047601. URL <https://link.aps.org/doi/10.1103/PhysRevLett.99.047601>.
- [4] Andrei Kirilyuk, Alexey V. Kimel, and Theo Rasing. Ultrafast optical manipulation of magnetic order. *Rev. Mod. Phys.*, 82:2731–2784, Sep 2010. doi: 10.1103/RevModPhys.82.2731. URL <https://link.aps.org/doi/10.1103/RevModPhys.82.2731>.
- [5] Fredrik Hansteen, Alexey Kimel, Andrei Kirilyuk, and Theo Rasing. Femtosecond photo-magnetic switching of spins in ferrimagnetic garnet films. *Phys. Rev. Lett.*, 95:047402, Jul 2005. doi: 10.1103/PhysRevLett.95.047402. URL <https://link.aps.org/doi/10.1103/PhysRevLett.95.047402>.
- [6] Cuixiu Zheng, Mykola Dvornik, Chengjie Wang, Dun Xiao, Yaowen Liu, Zongzhi Zhang, Yan Zhou, Hamid Mazraati, Martina Ahlberg, Ahmad A. Awad, and Johan Åkerman. Tuning magnetic droplets in nanocontact spin-torque oscillators using electric fields. *Phys. Rev. Applied*, 14:054001, Nov 2020. doi: 10.1103/PhysRevApplied.14.054001. URL <https://link.aps.org/doi/10.1103/PhysRevApplied.14.054001>.
- [7] Mohammad Zahedinejad, Ahmad A. Awad, Shreyas Muralidhar, Roman Khymyn, Himanshu Fulara, Hamid Mazraati, Mykola Dvornik, and Johan Åkerman. Two-dimensional mutually synchronized spin hall nano-oscillator arrays for neuromor-



- phic computing. *Nature Nanotechnology*, 15(1):47–52, Jan 2020. ISSN 1748-3395. doi: 10.1038/s41565-019-0593-9. URL <https://doi.org/10.1038/s41565-019-0593-9>.
- [8] J.C. Maxwell. On physical lines of force. *Philosophical Magazine*, 90(sup1):11–23, 2010. doi: 10.1080/14786431003659180. URL <https://doi.org/10.1080/14786431003659180>.
- [9] B. Lake, H. M. Rønnow, N. B. Christensen, G. Aeppli, K. Lefmann, D. F. McMorow, P. Vorderwisch, P. Smeibidl, N. Mangkorntong, T. Sasagawa, M. Nohara, H. Takagi, and T. E. Mason. Antiferromagnetic order induced by an applied magnetic field in a high-temperature superconductor. *Nature*, 415(6869):299–302, Jan 2002. ISSN 1476-4687. doi: 10.1038/415299a. URL <https://doi.org/10.1038/415299a>.
- [10] N. B. Christensen, D. F. McMorow, H. M. Rønnow, B. Lake, S. M. Hayden, G. Aeppli, T. G. Perring, M. Mangkorntong, M. Nohara, and H. Takagi. Dispersive excitations in the high-temperature superconductor  $\text{La}_{2-x}\text{Sr}_x\text{CuO}_4$ . *Phys. Rev. Lett.*, 93:147002, Sep 2004. doi: 10.1103/PhysRevLett.93.147002. URL <https://link.aps.org/doi/10.1103/PhysRevLett.93.147002>.
- [11] B. Vignolle, S. M. Hayden, D. F. McMorow, H. M. Rønnow, B. Lake, C. D. Frost, and T. G. Perring. Two energy scales in the spin excitations of the high-temperature superconductor  $\text{La}_{2-x}\text{Sr}_x\text{CuO}_4$ . *Nature Physics*, 3(3):163–167, Mar 2007. ISSN 1745-2481. doi: 10.1038/nphys546. URL <https://doi.org/10.1038/nphys546>.
- [12] J. Chang, Ch. Niedermayer, R. Gilardi, N. B. Christensen, H. M. Rønnow, D. F. McMorow, M. Ay, J. Stahn, O. Sobolev, A. Hiess, S. Pailhes, C. Baines, N. Momono, M. Oda, M. Ido, and J. Mesot. Tuning competing orders in  $\text{La}_{2-x}\text{Sr}_x\text{CuO}_4$  cuprate superconductors by the application of an external magnetic field. *Phys. Rev. B*, 78:104525, Sep 2008. doi: 10.1103/PhysRevB.78.104525. URL <https://link.aps.org/doi/10.1103/PhysRevB.78.104525>.
- [13] Applied Technology Council. Earthquake damage evaluation data for California. Technical report, Seismic Safety Commission, Applied Technology Council (ATC), California, 1985.
- [14] Tobias Kosub, Martin Kopte, Ruben Hühne, Patrick Appel, Brendan Shields, Patrick Maletinsky, René Hübner, Maciej Oskar Liedke, Jürgen Fassbender, Oliver G. Schmidt, and Denys Makarov. Purely antiferromagnetic magnetoelectric random access memory. *Nature Communications*, 8(1):13985, Jan 2017. ISSN 2041-1723. doi: 10.1038/ncomms13985. URL <https://doi.org/10.1038/ncomms13985>.
- [15] Daniel I. Khomskii. *Transition Metal Compounds*. Cambridge University Press, 2014. doi: 10.1017/CBO9781139096782.
- [16] N. Binggeli and M. Altarelli. Orbital ordering, jahn-teller distortion, and resonant x-ray scattering in  $\text{KCuF}_3$ . *Phys. Rev. B*, 70:085117, Aug 2004. doi: 10.1103/PhysRevB.70.085117. URL <https://link.aps.org/doi/10.1103/PhysRevB.70.085117>.

- 
- [17] E. Pavarini, E. Koch, and A. I. Lichtenstein. Mechanism for orbital ordering in  $\text{KCuF}_3$ . *Phys. Rev. Lett.*, 101:266405, Dec 2008. doi: 10.1103/PhysRevLett.101.266405. URL <https://link.aps.org/doi/10.1103/PhysRevLett.101.266405>.
- [18] P. W. Anderson. Antiferromagnetism. theory of superexchange interaction. *Phys. Rev.*, 79:350–356, Jul 1950. doi: 10.1103/PhysRev.79.350. URL <https://link.aps.org/doi/10.1103/PhysRev.79.350>.
- [19] Junjiro Kanamori. Superexchange interaction and symmetry properties of electron orbitals. *Journal of Physics and Chemistry of Solids*, 10(2):87 – 98, 1959. ISSN 0022-3697. doi: [https://doi.org/10.1016/0022-3697\(59\)90061-7](https://doi.org/10.1016/0022-3697(59)90061-7). URL <http://www.sciencedirect.com/science/article/pii/0022369759900617>.
- [20] John B. Goodenough. An interpretation of the magnetic properties of the perovskite-type mixed crystals  $\text{La}_{1-x}\text{Sr}_x\text{CoO}_{3-\lambda}$ . *Journal of Physics and Chemistry of Solids*, 6(2):287 – 297, 1958. ISSN 0022-3697. doi: [https://doi.org/10.1016/0022-3697\(58\)90107-0](https://doi.org/10.1016/0022-3697(58)90107-0). URL <http://www.sciencedirect.com/science/article/pii/0022369758901070>.
- [21] John B. Goodenough. Theory of the role of covalence in the perovskite-type manganites  $[\text{La}, m(\text{II})]\text{MnO}_3$ . *Phys. Rev.*, 100:564–573, Oct 1955. doi: 10.1103/PhysRev.100.564. URL <https://link.aps.org/doi/10.1103/PhysRev.100.564>.
- [22] L. F. Mattheiss. Electronic band properties and superconductivity in  $\text{La}_{2-x}\text{Y}_x\text{CuO}_4$ . *Physical Review Letters*, 58(10):1028–1030, March 1987. ISSN 0031-9007. doi: 10.1103/PhysRevLett.58.1028. URL <https://link.aps.org/doi/10.1103/PhysRevLett.58.1028>.
- [23] P.D. Dernier. The crystal structure of  $\text{V}_2\text{O}_3$  and  $(\text{V}_{0.962}\text{Cr}_{0.038})_2\text{O}_3$  near the metal-insulator transition. *Journal of Physics and Chemistry of Solids*, 31(11):2569–2575, November 1970. ISSN 0022-3697. doi: 10.1016/0022-3697(70)90076-4. URL <http://www.sciencedirect.com/science/article/pii/0022369770900764>.
- [24] John Hubbard. Electron correlations in narrow energy bands. *26 November 1963*, 276 (1365):20, November 1963. doi: <https://doi.org/10.1098/rspa.1963.0204>.
- [25] Martin C. Gutzwiller. Effect of Correlation on the Ferromagnetism of Transition Metals. *Physical Review Letters*, 10(5):159–162, March 1963. ISSN 0031-9007. doi: 10.1103/PhysRevLett.10.159. URL <https://link.aps.org/doi/10.1103/PhysRevLett.10.159>.
- [26] Junjiro Kanamori. Electron Correlation and Ferromagnetism of Transition Metals. *Progress of Theoretical Physics*, 30(3):275–289, September 1963. ISSN 0033-068X. doi: 10.1143/PTP.30.275. URL <https://academic.oup.com/ptp/article-lookup/doi/10.1143/PTP.30.275>.
- [27] N. D. Mermin and H. Wagner. Absence of Ferromagnetism or Antiferromagnetism in One- or Two-Dimensional Isotropic Heisenberg Models. *Physical Review Letters*, 17(22):1133–1136, November 1966. ISSN 0031-9007. doi: 10.1103/PhysRevLett.17.1133. URL <https://link.aps.org/doi/10.1103/PhysRevLett.17.1133>.

- [28] J. Goldstone. Field theories with « superconductor » solutions. *Il Nuovo Cimento (1955-1965)*, 19(1):154–164, Jan 1961. ISSN 1827-6121. doi: 10.1007/BF02812722. URL <https://doi.org/10.1007/BF02812722>.
- [29] Hans Bethe. Zur Theorie der Metalle. *Zeitschrift für Physik*, page 22, 1931.
- [30] T. Holstein and H. Primakoff. Field Dependence of the Intrinsic Domain Magnetization of a Ferromagnet. *Physical Review*, 58(12):1098–1113, December 1940. ISSN 0031-899X. doi: 10.1103/PhysRev.58.1098. URL <https://link.aps.org/doi/10.1103/PhysRev.58.1098>.
- [31] L. Passell, O. W. Dietrich, and J. Als-Nielsen. Neutron scattering from the Heisenberg ferromagnets EuO and EuS. I. The exchange interactions. *Physical Review B*, 14(11):4897–4907, December 1976. ISSN 0556-2805. doi: 10.1103/PhysRevB.14.4897. URL <https://link.aps.org/doi/10.1103/PhysRevB.14.4897>.
- [32] F. Moussa, B. Hennion, J. Moss, and G. Pepy. Measurements of spin waves in K<sub>2</sub>CuF<sub>4</sub> in the low energy range. *Solid State Communications*, 27(2):141–144, July 1978. ISSN 00381098. doi: 10.1016/0038-1098(78)90819-0. URL <https://linkinghub.elsevier.com/retrieve/pii/0038109878908190>.
- [33] C. G. Shull, W. A. Strauser, and E. O. Wollan. Neutron Diffraction by Paramagnetic and Antiferromagnetic Substances. *Physical Review*, 83(2):333–345, July 1951. ISSN 0031-899X. doi: 10.1103/PhysRev.83.333. URL <https://link.aps.org/doi/10.1103/PhysRev.83.333>.
- [34] J. G. Valatin. Comments on the theory of superconductivity. *Il Nuovo Cimento*, 7(6):843–857, March 1958. ISSN 0029-6341, 1827-6121. doi: 10.1007/BF02745589. URL <http://link.springer.com/10.1007/BF02745589>.
- [35] N. N. Bogoljubov. On a new method in the theory of superconductivity. *Il Nuovo Cimento*, 7(6):794–805, March 1958. ISSN 0029-6341, 1827-6121. doi: 10.1007/BF02745585. URL <http://link.springer.com/10.1007/BF02745585>.
- [36] Andreas Läuscher and Andreas M. Läuchli. Exact diagonalization study of the antiferromagnetic spin-1/2 Heisenberg model on the square lattice in a magnetic field. *Physical Review B*, 79(19):195102, May 2009. ISSN 1098-0121, 1550-235X. doi: 10.1103/PhysRevB.79.195102. URL <https://link.aps.org/doi/10.1103/PhysRevB.79.195102>.
- [37] P. Babkevich, Vamshi M. Katukuri, B. Fak, S. Rols, T. Fennell, D. Paji, H. Tanaka, T. Pardini, R. R. P. Singh, A. Mitrushchenkov, O. V. Yazyev, and H. M. Ronnow. Magnetic Excitations and Electronic Interactions in Sr<sub>2</sub>CuTeO<sub>6</sub>: A Spin-1/2 Square Lattice Heisenberg Antiferromagnet. *Physical Review Letters*, 117(23):237203, December 2016. ISSN 0031-9007, 1079-7114. doi: 10.1103/PhysRevLett.117.237203. URL <https://link.aps.org/doi/10.1103/PhysRevLett.117.237203>.
- [38] Brett Leedahl. Origin of Ising magnetism in Ca<sub>3</sub>Co<sub>2</sub>O<sub>6</sub> unveiled by orbital imaging. *Nature Communications*, page 7, 2019.

- [39] Virgile Yves Favre, Gregory S. Tucker, Clemens Ritter, Romain Sibille, Pascal Manuel, Matthias D. Frontzek, Markus Kriener, Lin Yang, Helmuth Berger, Arnaud Magrez, Nicola P. M. Casati, Ivica Živković, and Henrik M. Rønnow. Ferrimagnetic 120° magnetic structure in  $\text{Cu}_2\text{OSeO}_4$ . *Phys. Rev. B*, 102:094422, Sep 2020. doi: 10.1103/PhysRevB.102.094422. URL <https://link.aps.org/doi/10.1103/PhysRevB.102.094422>.
- [40] Shin-ichi Shamoto, Takashi U. Ito, Hiroaki Onishi, Hiroki Yamauchi, Yasuhiro Inamura, Masato Matsuura, Mitsuhiro Akatsu, Katsuaki Kodama, Akiko Nakao, Taketo Moyoshi, Koji Munakata, Takashi Ohhara, Mitsutaka Nakamura, Seiko Ohira-Kawamura, Yuichi Nemoto, and Kaoru Shibata. Neutron scattering study of yttrium iron garnet. *Physical Review B*, 97(5):054429, February 2018. ISSN 2469-9950, 2469-9969. doi: 10.1103/PhysRevB.97.054429. URL <https://link.aps.org/doi/10.1103/PhysRevB.97.054429>.
- [41] Toru Moriya. Anisotropic Superexchange Interaction and Weak Ferromagnetism. *Physical Review Archive*, page 8, 1960.
- [42] I. Dzyaloshinsky. A thermodynamic theory of “weak” ferromagnetism of antiferromagnetics. *Journal of Physics and Chemistry of Solids*, 4(4):241–255, January 1958. ISSN 00223697. doi: 10.1016/0022-3697(58)90076-3. URL <https://linkinghub.elsevier.com/retrieve/pii/0022369758900763>.
- [43] A. S. Sukhanov, Praveen Vir, A. S. Cameron, H. C. Wu, N. Martin, S. Mühlbauer, A. Heinemann, H. D. Yang, C. Felser, and D. S. Inosov. Increasing skyrmion stability in  $\text{Cu}_2\text{OSeO}_3$  by chemical substitution. *Physical Review B*, 100(18):184408, November 2019. ISSN 2469-9950, 2469-9969. doi: 10.1103/PhysRevB.100.184408. URL <https://link.aps.org/doi/10.1103/PhysRevB.100.184408>.
- [44] Judit Romhányi and Karlo Penc. Multiboson spin-wave theory for  $\text{Ba}_2\text{CoGe}_2\text{O}_7$ : A spin-3/2 easy-plane Néel antiferromagnet with strong single-ion anisotropy. *Physical Review B*, 86(17):174428, November 2012. ISSN 1098-0121, 1550-235X. doi: 10.1103/PhysRevB.86.174428. URL <https://link.aps.org/doi/10.1103/PhysRevB.86.174428>.
- [45] B. T. SHIRK and W. R. BUESSEM. Magnetic properties of barium ferrite formed by crystallization of a glass. *Journal of the American Ceramic Society*, 53(4):192–196, 1970. doi: <https://doi.org/10.1111/j.1151-2916.1970.tb12069.x>. URL <https://ceramics.onlinelibrary.wiley.com/doi/abs/10.1111/j.1151-2916.1970.tb12069.x>.
- [46] R. Masrour, E.K. Hlil, M. Hamedoun, A. Benyoussef, O. Mounkachi, and H. El Moussaoui. Electronic and magnetic structures of  $\text{Fe}_3\text{O}_4$  ferrimagnetic investigated by first principle, mean field and series expansions calculations. *Journal of Magnetism and Magnetic Materials*, 378:37 – 40, 2015. ISSN 0304-8853. doi: <https://doi.org/10.1016/j.jmmm.2014.10.135>. URL <http://www.sciencedirect.com/science/article/pii/S0304885314010580>.
- [47] S. Aasland, H. Fjellvåg, and B. Hauback. Magnetic properties of the one-dimensional  $\text{Ca}_3\text{Co}_2\text{O}_6$ . *Solid State Communications*, 101(3):187 – 192, 1997. ISSN 0038-1098. doi:

- [https://doi.org/10.1016/S0038-1098\(96\)00531-5](https://doi.org/10.1016/S0038-1098(96)00531-5). URL <http://www.sciencedirect.com/science/article/pii/S0038109896005315>.
- [48] S. Toth, B. Lake, K. Hradil, T. Guidi, K. C. Rule, M. B. Stone, and A. T. M. N. Islam. Magnetic soft modes in the distorted triangular antiferromagnet  $\alpha$ - $\text{CaCr}_2\text{O}_4$ . *Phys. Rev. Lett.*, 109:127203, Sep 2012. doi: 10.1103/PhysRevLett.109.127203. URL <https://link.aps.org/doi/10.1103/PhysRevLett.109.127203>.
- [49] J Richter, M Härtel, D Ihle, and S-L Drechsler. Thermodynamics of the frustrated ferromagnetic spin-1/2 heisenberg chain. *Journal of Physics: Conference Series*, 145: 012064, jan 2009. doi: 10.1088/1742-6596/145/1/012064. URL <https://doi.org/10.1088%2F1742-6596%2F145%2F1%2F012064>.
- [50] K. Yu. Povarov, V. K. Bhartiya, Z. Yan, and A. Zheludev. Thermodynamics of a frustrated quantum magnet on a square lattice. *Phys. Rev. B*, 99:024413, Jan 2019. doi: 10.1103/PhysRevB.99.024413. URL <https://link.aps.org/doi/10.1103/PhysRevB.99.024413>.
- [51] J. S. Helton, K. Matan, M. P. Shores, E. A. Nytko, B. M. Bartlett, Y. Yoshida, Y. Takano, A. Suslov, Y. Qiu, J.-H. Chung, D. G. Nocera, and Y. S. Lee. Spin dynamics of the spin-1/2 kagome lattice antiferromagnet  $\text{ZnCu}_3(\text{OH})_6\text{Cl}_2$ . *Phys. Rev. Lett.*, 98:107204, Mar 2007. doi: 10.1103/PhysRevLett.98.107204. URL <https://link.aps.org/doi/10.1103/PhysRevLett.98.107204>.
- [52] Johannes Richter, Olesia Krupnitska, Taras Krokhmal'skii, and Oleg Derzhko. Frustrated diamond-chain quantum xxz heisenberg antiferromagnet in a magnetic field. *Journal of Magnetism and Magnetic Materials*, 379:39 – 44, 2015. ISSN 0304-8853. doi: <https://doi.org/10.1016/j.jmmm.2014.11.082>. URL <http://www.sciencedirect.com/science/article/pii/S0304885314012013>.
- [53] L. Heinze, H. Jeschke, A. Metavitsiadis, M. Reehuis, R. Feyerherm, J. U. Hoffmann, A. U. B. Wolter, X. Ding, V. Zapf, C. C. Moya, F. Weickert, M. Jaime, K. C. Rule, D. Menzel, R. Valentí, W. Brenig, and S. Söllow. Atacamite  $\text{Cu}_2\text{Cl}(\text{OH})_3$ : A model compound for the  $s = 1/2$  sawtooth chain?, 2019.
- [54] G. C. Lau, B. G. Ueland, R. S. Freitas, M. L. Dahlberg, P. Schiffer, and R. J. Cava. Magnetic characterization of the sawtooth-lattice olivines  $\text{ZnL}_2\text{S}_4$  ( $l = \text{Er, Tm, Yb}$ ). *Phys. Rev. B*, 73: 012413, Jan 2006. doi: 10.1103/PhysRevB.73.012413. URL <https://link.aps.org/doi/10.1103/PhysRevB.73.012413>.
- [55] Yang Chi, Jing Xu, Huai-Guo Xue, Yueping Zhang, Xiaolong Chen, Myung-Hwan Whangbo, Sheng-Ping Guo, and Shuiquan Deng. Triple-kagomé-layer slabs of mixed-valence rare-earth ions exhibiting quantum spin liquid behaviors: Synthesis and characterization of  $\text{Eu}_9\text{MgS}_2\text{B}_{20}\text{O}_{41}$ . *Journal of the American Chemical Society*, 141(24): 9533–9536, 2019. doi: 10.1021/jacs.9b04627. URL <https://doi.org/10.1021/jacs.9b04627>. PMID: 31184141.

- 
- [56] R. Siddharthan, B. S. Shastry, and A. P. Ramirez. Spin ordering and partial ordering in holmium titanate and related systems. *Phys. Rev. B*, 63:184412, Apr 2001. doi: 10.1103/PhysRevB.63.184412. URL <https://link.aps.org/doi/10.1103/PhysRevB.63.184412>.
  - [57] K Matsuhira, Y Hinatsu, and T Sakakibara. Novel dynamical magnetic properties in the spin ice compound  $\text{dy}_2\text{ti}_2\text{o}_7$ . *Journal of Physics: Condensed Matter*, 13(31):L737–L746, jul 2001. doi: 10.1088/0953-8984/13/31/101. URL <https://doi.org/10.1088%2F0953-8984%2F13%2F31%2F101>.
  - [58] Gang Chen and Leon Balents. Spin-orbit effects in  $\text{na}_4\text{ir}_3\text{o}_8$ : A hyper-kagome lattice antiferromagnet. *Phys. Rev. B*, 78:094403, Sep 2008. doi: 10.1103/PhysRevB.78.094403. URL <https://link.aps.org/doi/10.1103/PhysRevB.78.094403>.
  - [59] K.H.J. Buschow (Ed.). Handbook of magnetic materials, 2014.
  - [60] P. Dalmas de Réotier, A. Yaouanc, L. Keller, A. Cervellino, B. Roessli, C. Baines, A. Forget, C. Vaju, P. C. M. Gubbens, A. Amato, and P. J. C. King. Spin dynamics and magnetic order in magnetically frustrated  $\text{tb}_2\text{sn}_2\text{o}_7$ . *Phys. Rev. Lett.*, 96:127202, Mar 2006. doi: 10.1103/PhysRevLett.96.127202. URL <https://link.aps.org/doi/10.1103/PhysRevLett.96.127202>.
  - [61] Philippe Mendels and Fabrice Bert. Quantum kagome frustrated antiferromagnets: One route to quantum spin liquids. *Comptes Rendus Physique*, 17(3):455 – 470, 2016. ISSN 1631-0705. doi: <https://doi.org/10.1016/j.crhy.2015.12.001>. URL <http://www.sciencedirect.com/science/article/pii/S1631070515002467>. Physique de la matière condensée au XXIe siècle: l’héritage de Jacques Friedel.
  - [62] P. Mendels, F Bert, M. A. de Vries, A. Olariu, A. Harrison, F. Duc, J. C. Trombe, J. S. Lord, A. Amato, and C. Baines. Quantum Magnetism in the Paratacamite Family: Towards an Ideal Kagomé Lattice. *Physical Review Letters*, 98(7):077204, February 2007. ISSN 0031-9007, 1079-7114. doi: 10.1103/PhysRevLett.98.077204. URL <https://link.aps.org/doi/10.1103/PhysRevLett.98.077204>.
  - [63] J. Des Cloizeaux and J.J. Pearson. Spin-wave spectrum of the antiferromagnetic linear chain. *Physical Review*, 128(5):2131–2135, 1962. doi: 10.1103/PhysRev.128.2131. URL <https://www.scopus.com/inward/record.uri?eid=2-s2.0-33645892368&doi=10.1103%2FPhysRev.128.2131&partnerID=40&md5=c894d8f2e6b5370f5ab4c842017bc59c>. cited By 689.
  - [64] Martin Mourigal, Mechthild Enderle, Axel Klöpperpieper, Jean-Sébastien Caux, Anne Stunault, and Henrik M. Rønnow. Fractional spinon excitations in the quantum heisenberg antiferromagnetic chain. *Nature Physics*, 9(7):435–441, Jul 2013. ISSN 1745-2481. doi: 10.1038/nphys2652. URL <https://doi.org/10.1038/nphys2652>.
  - [65] B. Lake, D. A. Tennant, J.-S. Caux, T. Barthel, U. Schollwöck, S. E. Nagler, and C. D. Frost. Multispinon continua at zero and finite temperature in a near-ideal heisenberg chain. *Phys. Rev. Lett.*, 111:137205, Sep 2013. doi: 10.1103/PhysRevLett.111.137205. URL <https://link.aps.org/doi/10.1103/PhysRevLett.111.137205>.

- [66] P.W. Anderson. Resonating valence bonds: A new kind of insulator? *Materials Research Bulletin*, 8(2):153–160, 1973. doi: 10.1016/0025-5408(73)90167-0. URL <https://www.scopus.com/inward/record.uri?eid=2-s2.0-0015586907&doi=10.1016%2f0025-5408%2873%2990167-0&partnerID=40&md5=93792d11cdda455f961fe778f5ac835a>. cited By 1774.
- [67] L. Balents. Spin liquids in frustrated magnets. *Nature*, 464(7286):199–208, 2010. doi: 10.1038/nature08917. URL <https://www.scopus.com/inward/record.uri?eid=2-s2.0-77949366361&doi=10.1038%2fnature08917&partnerID=40&md5=9d868142970f9b473296b125b216365c>. cited By 2055.
- [68] M.P. Shores, E.A. Nytko, B.M. Bartlett, and D.G. Nocera. A structurally perfect  $s = 1/2$  kagomé antiferromagnet. *Journal of the American Chemical Society*, 127(39):13462–13463, 2005. doi: 10.1021/ja053891p. URL <https://www.scopus.com/inward/record.uri?eid=2-s2.0-25844514824&doi=10.1021%2fja053891p&partnerID=40&md5=ea460c2db84db0f3caaaa474fd28ede4>. cited By 484.
- [69] O. Mustonen, S. Vasala, E. Sadrollahi, K. P. Schmidt, C. Baines, H. C. Walker, I. Terasaki, F. J. Litterst, E. Baggio-Saitovitch, and M. Karppinen. Spin-liquid-like state in a spin-1/2 square-lattice antiferromagnet perovskite induced by d10–d0 cation mixing. *Nature Communications*, 9(1):1085, Mar 2018. ISSN 2041-1723. doi: 10.1038/s41467-018-03435-1. URL <https://doi.org/10.1038/s41467-018-03435-1>.
- [70] Vamshi M. Katukuri, P. Babkevich, O. Mustonen, H. C. Walker, B. Fåk, S. Vasala, M. Karppinen, H. M. Rønnow, and O. V. Yazyev. Exchange interactions mediated by non-magnetic cations in double perovskites. *Phys. Rev. Lett.*, 124:077202, Feb 2020. doi: 10.1103/PhysRevLett.124.077202. URL <https://link.aps.org/doi/10.1103/PhysRevLett.124.077202>.
- [71] M. Mambrini and F. Mila. Rvb description of the low-energy singlets of the spin 1/2 kagomé antiferromagnet. *The European Physical Journal B - Condensed Matter and Complex Systems*, 17(4):651–659, Oct 2000. ISSN 1434-6036. doi: 10.1007/PL00011071. URL <https://doi.org/10.1007/PL00011071>.
- [72] Masayoshi Fujihala, Katsuhiko Morita, Richard Mole, Setsuo Mitsuda, Takami Tohyama, Shin-ichiro Yano, Dehong Yu, Shigetoshi Sota, Tomohiko Kuwai, Akihiro Koda, Hirotaka Okabe, Hua Lee, Shinichi Itoh, Takafumi Hawaii, Takatsugu Masuda, Hajime Sagayama, Akira Matsuo, Koichi Kindo, Seiko Ohira-Kawamura, and Kenji Nakajima. Gapless spin liquid in a square-kagome lattice antiferromagnet. *Nature Communications*, 11(1):3429, Jul 2020. ISSN 2041-1723. doi: 10.1038/s41467-020-17235-z. URL <https://doi.org/10.1038/s41467-020-17235-z>.
- [73] J Rodríguez-Carvajal, M. T Fernández-Díaz, J. L Martínez, F Fernández, and R Saez-Puche. Structural Phase Transitions and Three-Dimensional Magnetic Ordering in

- the  $\text{Nd}_2\text{NiO}_4$  Oxide. *Europhysics Letters (EPL)*, 11(3):261–268, February 1990. ISSN 0295-5075, 1286-4854. doi: 10.1209/0295-5075/11/3/013. URL <https://iopscience.iop.org/article/10.1209/0295-5075/11/3/013>.
- [74] A. P. Ramirez, A. Hayashi, R. J. Cava, R. Siddharthan, and B. S. Shastry. Zero-point entropy in ‘spin ice’. *Nature*, 399(6734):333–335, May 1999. ISSN 0028-0836, 1476-4687. doi: 10.1038/20619. URL <http://www.nature.com/articles/20619>.
- [75] W. F. Giauque and J. W. Stout. The Entropy of Water and the Third Law of Thermodynamics. The Heat Capacity of Ice from 15 to 273K. *Journal of the American Chemical Society*, 58(7):1144–1150, July 1936. ISSN 0002-7863, 1520-5126. doi: 10.1021/ja01298a023. URL <https://pubs.acs.org/doi/abs/10.1021/ja01298a023>.
- [76] T. Fennell, P. P. Deen, A. R. Wildes, K. Schmalzl, D. Prabhakaran, A. T. Boothroyd, R. J. Aldus, D. F. McMorrow, and S. T. Bramwell. Magnetic Coulomb Phase in the Spin Ice  $\text{Ho}_2\text{Ti}_2\text{O}_7$ . *Science*, 326(5951):415–417, October 2009. ISSN 0036-8075, 1095-9203. doi: 10.1126/science.1177582. URL <https://www.sciencemag.org/lookup/doi/10.1126/science.1177582>.
- [77] P. ZEEMAN. The Effect of Magnetisation on the Nature of Light Emitted by a Substance. *Nature*, 55(1424):347–347, February 1897. ISSN 1476-4687. doi: 10.1038/055347a0. URL <https://doi.org/10.1038/055347a0>.
- [78] A. Landé. Über den anomalen Zeemaneffekt (Teil I). *Zeitschrift für Physik*, 5(4):231–241, July 1921. ISSN 0044-3328. doi: 10.1007/BF01335014. URL <https://doi.org/10.1007/BF01335014>.
- [79] Z. Barber, C. Hoyt, C. Oates, L. Hollberg, A. Taichenachev, and V. Yudin. Direct Excitation of the Forbidden Clock Transition in Neutral Yb 174 Atoms Confined to an Optical Lattice. *Physical Review Letters*, 96(8):083002, March 2006. ISSN 0031-9007, 1079-7114. doi: 10.1103/PhysRevLett.96.083002. URL <https://link.aps.org/doi/10.1103/PhysRevLett.96.083002>.
- [80] K. Heuzé, M. Fourmigué, P. Batail, C. Coulon, R. Clérac, E. Canadell, P. Auban-Senzier, S. Ravy, and D. Jérôme. A Genuine Quarter-Filled Band Mott Insulator, (EDT-TTF-CONMe<sub>2</sub>)<sub>2</sub>AsF<sub>6</sub>: Where the Chemistry and Physics of Weak Intermolecular Interactions Act in Unison. *Advanced Materials*, 15(15):1251–1254, August 2003. ISSN 0935-9648, 1521-4095. doi: 10.1002/adma.200305247. URL <http://doi.wiley.com/10.1002/adma.200305247>.
- [81] A. Olariu, P. Mendels, F. Bert, F. Duc, J. C. Trombe, M. A. de Vries, and A. Harrison. O 17 NMR Study of the Intrinsic Magnetic Susceptibility and Spin Dynamics of the Quantum Kagome Antiferromagnet  $\text{ZnCu}_3(\text{OH})_6\text{Cl}_2$ . *Physical Review Letters*, 100(8):087202, February 2008. ISSN 0031-9007, 1079-7114. doi: 10.1103/PhysRevLett.100.087202. URL <https://link.aps.org/doi/10.1103/PhysRevLett.100.087202>.



- [82] B. Náfrádi, Á. Antal, T. Fehér, L. F. Kiss, C. Mézière, P. Batail, L. Forró, and A. Jánossy. Frustration-induced one-dimensionality in the isosceles triangular antiferromagnetic lattice of delta  $-(\text{EDT-TTF-CONMe}_2)_2\text{AsF}_6$ . *Physical Review B*, 94(17):174413, November 2016. ISSN 2469-9950, 2469-9969. doi: 10.1103/PhysRevB.94.174413. URL <https://link.aps.org/doi/10.1103/PhysRevB.94.174413>.
- [83] László Mihály, Balázs Dóra, András Ványolos, Helmuth Berger, and László Forró. Spin-Lattice Interaction in the Quasi-One-Dimensional Helimagnet  $\text{LiCu}_2\text{O}_2$ . *Physical Review Letters*, 97(6):067206, August 2006. ISSN 0031-9007, 1079-7114. doi: 10.1103/PhysRevLett.97.067206. URL <https://link.aps.org/doi/10.1103/PhysRevLett.97.067206>.
- [84] SJ Blundell. Spin-polarized muons in condensed matter physics. *Contemporary Physics*, 40(3):175–192, 1999.
- [85] Adriana Bungau, Robert Cywinski, Cristian Bungau, Philip King, and James Lord. Simulations of surface muon production in graphite targets. *Physical Review Special Topics - Accelerators and Beams*, 16(1):014701, January 2013. ISSN 1098-4402. doi: 10.1103/PhysRevSTAB.16.014701. URL <https://link.aps.org/doi/10.1103/PhysRevSTAB.16.014701>.
- [86] Siti Nur Afifi Ahmad, Shukri Sulaiman, Dang Fatihah Hasan Baseri, Lee Sin Ang, Nor Zakiah Yahaya, Hasni Arsad, and Isao Watanabe. Density Functional Theory Studies of Muon Stopping Sites and Hyperfine Interaction in  $[\text{Au}_{25}(\text{SR})_{18}]^0$  Nanocluster. *Journal of the Physical Society of Japan*, 89(1):014301, January 2020. ISSN 0031-9015, 1347-4073. doi: 10.7566/JPSJ.89.014301. URL <https://journals.jps.jp/doi/10.7566/JPSJ.89.014301>.
- [87] F. J. Hartmann, H. Daniel, Chr Maierl, M. Mühlbauer, W. Schott, P. Wojciechowski, P. Hauser, C. Petitjean, D. Taqqu, F. Kottmann, and V. E. Markushin. Experiments with low-energy muons. *Hyperfine Interactions*, 101-102(1):623–632, December 1996. ISSN 0304-3834, 1572-9540. doi: 10.1007/BF02227675. URL <http://link.springer.com/10.1007/BF02227675>.
- [88] E. Morenzoni. Low energy muons as probes of thin films and surfaces. *Applied Magnetic Resonance*, 13(1-2):219–229, July 1997. ISSN 0937-9347, 1613-7507. doi: 10.1007/BF03161982. URL <http://link.springer.com/10.1007/BF03161982>.
- [89] E Morenzoni, T Prokscha, A Suter, H Luetkens, and R Khasanov. Nano-scale thin film investigations with slow polarized muons. *Journal of Physics: Condensed Matter*, 16(40):S4583–S4601, October 2004. ISSN 0953-8984, 1361-648X. doi: 10.1088/0953-8984/16/40/010. URL <https://iopscience.iop.org/article/10.1088/0953-8984/16/40/010>.
- [90] E. Stilp, A. Suter, T. Prokscha, E. Morenzoni, H. Keller, B. M. Wojek, H. Luetkens, A. Gozar, G. Logvenov, and I. Božović. Magnetic phase diagram of low-doped  $\text{La}_{2-x}\text{Sr}_x\text{CuO}_4$  thin films studied by low-energy muon-spin rotation. *Physical Review B*, 88(6):064419, August 2013. ISSN 1098-0121, 1550-235X. doi: 10.1103/PhysRevB.88.064419. URL <https://link.aps.org/doi/10.1103/PhysRevB.88.064419>.

- [91] Ryugo S. Hayano, Yasutomo J. Uemura, Jun Imazato, Nobuhiko Nishida, Kanetada Nagamine, Toshimitsu Yamazaki, Yoshikazu Ishikawa, and Hiroshi Yasuoka. Spin fluctuations of itinerant electrons in mnsi studied by muon spin rotation and relaxation. *Journal of the Physical Society of Japan*, 49(5):1773–1783, 1980. doi: 10.1143/JPSJ.49.1773. URL <https://doi.org/10.1143/JPSJ.49.1773>.
- [92] A Amato, R Feyerherm, F N Gygax, and A Schenck. Muon-spin-relaxation studies on the heavy-fermion system with non-Fermi-liquid behavior  $\text{CeCu}_{5.9}\text{Au}_{0.1}$ . *Physical Review B*, page 3, 1995.
- [93] V. H. Tran, P. Rogl, P. Dalmas de Réotier, and A. Yaouanc. Muon spin rotation and relaxation study of the ferromagnet  $\beta\text{-UB}_2\text{C}$ . *Physical Review B*, 83(14):144417, April 2011. ISSN 1098-0121, 1550-235X. doi: 10.1103/PhysRevB.83.144417. URL <https://link.aps.org/doi/10.1103/PhysRevB.83.144417>.
- [94] P. K. Biswas, H. Luetkens, T. Neupert, T. Stürzer, C. Baines, G. Pascua, A. P. Schnyder, M. H. Fischer, J. Goryo, M. R. Lees, H. Maeter, F. Brückner, H.-H. Klauss, M. Nicklas, P. J. Baker, A. D. Hillier, M. Sigrist, A. Amato, and D. Johrendt. Evidence for superconductivity with broken time-reversal symmetry in locally noncentrosymmetric  $\text{SrPtAs}$ . *Physical Review B*, 87(18):180503, May 2013. ISSN 1098-0121, 1550-235X. doi: 10.1103/PhysRevB.87.180503. URL <https://link.aps.org/doi/10.1103/PhysRevB.87.180503>.
- [95] F. Xiao, F. M. Woodward, C. P. Landee, M. M. Turnbull, C. Mielke, N. Harrison, T. Lancaster, S. J. Blundell, P. J. Baker, P. Babkevich, and F. L. Pratt. Two-dimensional X Y behavior observed in quasi-two-dimensional quantum Heisenberg antiferromagnets. *Physical Review B*, 79(13):134412, April 2009. ISSN 1098-0121, 1550-235X. doi: 10.1103/PhysRevB.79.134412. URL <https://link.aps.org/doi/10.1103/PhysRevB.79.134412>.
- [96] H Bragg. The reflection of X-rays by crystals. *Proceedings of the Royal Society A*, page 11, 1913.
- [97] G.D. Gu, K. Takamuku, N. Koshizuka, and S. Tanaka. Large single crystal  $\text{Bi-2212}$  along the c-axis prepared by floating zone method. *Journal of Crystal Growth*, 130(1-2): 325–329, May 1993. ISSN 00220248. doi: 10.1016/0022-0248(93)90872-T. URL <https://linkinghub.elsevier.com/retrieve/pii/002202489390872T>.
- [98] Juan Rodriguez-Carvajal. Recent advances in magnetic structure determination by neutron powder diffraction. *Physica B*, page 15, 1993.
- [99] Armel Le Bail. Whole powder pattern decomposition methods and applications: A retrospection. *Powder Diffraction*, 20(4):316–326, December 2005. ISSN 0885-7156, 1945-7413. doi: 10.1154/1.2135315. URL [https://www.cambridge.org/core/product/identifier/S0885715600002980/type/journal\\_article](https://www.cambridge.org/core/product/identifier/S0885715600002980/type/journal_article).
- [100] H. M. Rietveld. A profile refinement method for nuclear and magnetic structures. *Journal of Applied Crystallography*, 2(2):65–71, 1969. doi: 10.1107/S0021889869006558. URL <https://onlinelibrary.wiley.com/doi/abs/10.1107/S0021889869006558>.

## Bibliography

---

- [101] Iliya Radulov, Vassil Lovchinov, and Dimitar Dimitrov. Magnetostriction in orthorhombic manganites. *Journal of Physics*, page 8, 2009.
- [102] G. L. Greene, N. F. Ramsey, W. Mampe, J. M. Pendlebury, K. Smith, W. B. Dress, P. D. Miller, and Paul Perrin. Measurement of the neutron magnetic moment. *Phys. Rev. D*, 20:2139–2153, Nov 1979. doi: 10.1103/PhysRevD.20.2139. URL <https://link.aps.org/doi/10.1103/PhysRevD.20.2139>.
- [103] Varley F. Sears. Neutron scattering lengths and cross sections. *Neutron News*, 3 (3):26–37, 1992. doi: 10.1080/10448639208218770. URL <https://doi.org/10.1080/10448639208218770>.
- [104] Paul Adrien Maurice Dirac and Niels Henrik David Bohr. The quantum theory of the emission and absorption of radiation. *Proceedings of the Royal Society of London. Series A, Containing Papers of a Mathematical and Physical Character*, 114(767):243–265, 1927. doi: 10.1098/rspa.1927.0039. URL <https://royalsocietypublishing.org/doi/abs/10.1098/rspa.1927.0039>.
- [105] Enrico Fermi. Sopra lo spostamento per pressione delle righe elevate delle serie spettrali. *Il Nuovo Cimento (1924-1942)*, 11(3):157, Sep 2008. ISSN 1827-6121. doi: 10.1007/BF02959829. URL <https://doi.org/10.1007/BF02959829>.
- [106] P. Babkevich, L. Testa, K. Kimura, T. Kimura, G. S. Tucker, B. Roessli, and H. M. Rønnow. Magnetic structure of Ba(TiO)Cu<sub>4</sub>(PO<sub>4</sub>)<sub>4</sub> probed using spherical neutron polarimetry. *Phys. Rev. B*, 96:214436, Dec 2017. doi: 10.1103/PhysRevB.96.214436. URL <https://link.aps.org/doi/10.1103/PhysRevB.96.214436>.
- [107] T. Weber, J. Waizner, P. Steffens, A. Bauer, C. Pfleiderer, M. Garst, and P. Böni. Polarized inelastic neutron scattering of nonreciprocal spin waves in mnsi. *Phys. Rev. B*, 100:060404, Aug 2019. doi: 10.1103/PhysRevB.100.060404. URL <https://link.aps.org/doi/10.1103/PhysRevB.100.060404>.
- [108] G. L. Squires. *Introduction to the Theory of Thermal Neutron Scattering*. Cambridge University Press, 3 edition, 2012. doi: 10.1017/CBO9781139107808.
- [109] L. Clark, Goran Nilsen, E. Kermarrec, G. Ehlers, K. Knight, Andrew Harrison, J. Attfield, and B. Gaulin. From spin glass to quantum spin liquid ground states in molybdate pyrochlores. *Physical review letters*, 113, 05 2014. doi: 10.1103/PhysRevLett.113.117201.
- [110] P.W. Anderson. Resonating valence bonds: A new kind of insulator? *Materials Research Bulletin*, 8(2):153 – 160, 1973. ISSN 0025-5408. doi: [https://doi.org/10.1016/0025-5408\(73\)90167-0](https://doi.org/10.1016/0025-5408(73)90167-0). URL <http://www.sciencedirect.com/science/article/pii/0025540873901670>.
- [111] P. Fazekas and P. W. Anderson. On the ground state properties of the anisotropic triangular antiferromagnet. *Philosophical Magazine*, 30(2):423–440, August 1974. ISSN

- 0031-8086. doi: 10.1080/14786439808206568. URL <http://www.tandfonline.com/doi/abs/10.1080/14786439808206568>.
- [112] M. Collins and O. Petrenko. Triangular antiferromagnets. *Can J Phys* 75:605. *Canadian Journal of Physics*, 75:605–, 09 1997. doi: 10.1139/p97-007.
- [113] Francesco Ferrari, Alberto Parola, Sandro Sorella, and Federico Becca. Dynamical structure factor of the  $J_1 - J_2$  Heisenberg model in one dimension: The variational Monte Carlo approach. *Physical Review B*, 97(23), June 2018. ISSN 2469-9950, 2469-9969. doi: 10.1103/PhysRevB.97.235103. URL <https://link.aps.org/doi/10.1103/PhysRevB.97.235103>.
- [114] O Mustonen, S Vasala, E Sadrollahi, KP Schmidt, C Baines, HC Walker, I Terasaki, FJ Litterst, E Baggio-Saitovitch, and M Karppinen. Spin-liquid-like state in a spin-1/2 square-lattice antiferromagnet perovskite induced by d 10–d 0 cation mixing. *Nature communications*, 9(1):1085, 2018. URL <https://www.nature.com/articles/s41467-018-03435-1>.
- [115] Matthew P. Shores, Emily A. Nytko, Bart M. Bartlett, and Daniel G. Nocera. A Structurally Perfect  $S = 1/2$  Kagomé Antiferromagnet. *Journal of the American Chemical Society*, 127(39):13462–13463, October 2005. ISSN 0002-7863, 1520-5126. doi: 10.1021/ja053891p. URL <http://pubs.acs.org/doi/abs/10.1021/ja053891p>.
- [116] Philippe Mendels and Fabrice Bert. Quantum kagome frustrated antiferromagnets: One route to quantum spin liquids. *Comptes Rendus Physique*, 17(3-4):455–470, March 2016. ISSN 16310705. doi: 10.1016/j.crhy.2015.12.001. URL <http://linkinghub.elsevier.com/retrieve/pii/S1631070515002467>.
- [117] J. S. Helton, K. Matan, M. P. Shores, E. A. Nytko, B. M. Bartlett, Y. Yoshida, Y. Takano, A. Suslov, Y. Qiu, J.-H. Chung, D. G. Nocera, and Y. S. Lee. Spin Dynamics of the Spin-1/2 Kagome Lattice Antiferromagnet  $\text{ZnCu}_3(\text{OH})_6\text{Cl}_2$ . *Physical Review Letters*, 98(10), March 2007. ISSN 0031-9007, 1079-7114. doi: 10.1103/PhysRevLett.98.107204. URL <https://link.aps.org/doi/10.1103/PhysRevLett.98.107204>.
- [118] A. Zorko, S. Nellutla, J. van Tol, L. C. Brunel, F. Bert, F. Duc, J.-C. Trombe, M. A. de Vries, A. Harrison, and P. Mendels. Dzyaloshinsky-Moriya Anisotropy in the Spin-1/2 Kagome Compound  $\text{ZnCu}_3(\text{OH})_6\text{Cl}_2$ . *Physical Review Letters*, 101(2), July 2008. ISSN 0031-9007, 1079-7114. doi: 10.1103/PhysRevLett.101.026405. URL <https://link.aps.org/doi/10.1103/PhysRevLett.101.026405>.
- [119] Stefan Depenbrock, Ian P. McCulloch, and Ulrich Schollwöck. Nature of the Spin-Liquid Ground State of the  $S = 1/2$  Heisenberg Model on the Kagome Lattice. *Physical Review Letters*, 109(6), August 2012. ISSN 0031-9007, 1079-7114. doi: 10.1103/PhysRevLett.109.067201. URL <https://link.aps.org/doi/10.1103/PhysRevLett.109.067201>.
- [120] F. Mila. Low-Energy Sector of the  $S = 1/2$  Kagome Antiferromagnet. *Physical Review Letters*, 81(11):2356–2359, September 1998. ISSN 0031-9007, 1079-7114. doi: 10.1103/PhysRevLett.81.2356. URL <https://link.aps.org/doi/10.1103/PhysRevLett.81.2356>.

## Bibliography

---

- [121] Rajiv R. P. Singh and David A. Huse. Ground state of the spin-1/2 kagome-lattice Heisenberg antiferromagnet. *Physical Review B*, 76(18), November 2007. ISSN 1098-0121, 1550-235X. doi: 10.1103/PhysRevB.76.180407. URL <https://link.aps.org/doi/10.1103/PhysRevB.76.180407>.
- [122] Simeng Yan, David A. Huse, and Steven R. White. Spin-Liquid Ground State of the  $S = 1/2$  Kagome Heisenberg Antiferromagnet. *Science*, 332(6034):1173–1176, 2011. ISSN 0036-8075. doi: 10.1126/science.1201080. URL <https://science.sciencemag.org/content/332/6034/1173>.
- [123] Stefan Depenbrock, Ian P. McCulloch, and Ulrich Schollwöck. Nature of the Spin-Liquid Ground State of the  $S = 1/2$  Heisenberg Model on the Kagome Lattice. *Physical Review Letters*, 109(6), August 2012. ISSN 0031-9007, 1079-7114. doi: 10.1103/PhysRevLett.109.067201. URL <https://link.aps.org/doi/10.1103/PhysRevLett.109.067201>.
- [124] Michael Hermele, Ying Ran, Patrick A. Lee, and Xiao-Gang Wen. Properties of an algebraic spin liquid on the kagome lattice. *Physical Review B*, 77(22), June 2008. ISSN 1098-0121, 1550-235X. doi: 10.1103/PhysRevB.77.224413. URL <https://link.aps.org/doi/10.1103/PhysRevB.77.224413>.
- [125] L. Clark, J. C. Orain, F. Bert, M. A. De Vries, F. H. Aidoudi, R. E. Morris, P. Lightfoot, J. S. Lord, M. T. F. Telling, P. Bonville, J. P. Attfield, P. Mendels, and A. Harrison. Gapless Spin Liquid Ground State in the  $S = 1/2$  Vanadium Oxyfluoride Kagome Antiferromagnet [  $\text{NH}_4$  ]  $_2$  [  $\text{C}_7\text{H}_{14}\text{N}$  ] [  $\text{V}_7\text{O}_6\text{F}_{18}$  ]. *Physical Review Letters*, 110(20), May 2013. ISSN 0031-9007, 1079-7114. doi: 10.1103/PhysRevLett.110.207208. URL <https://link.aps.org/doi/10.1103/PhysRevLett.110.207208>.
- [126] Yasir Iqbal, Federico Becca, Sandro Sorella, and Didier Poilblanc. Gapless spin-liquid phase in the kagome spin-  $1/2$  Heisenberg antiferromagnet. *Physical Review B*, 87(6), February 2013. ISSN 1098-0121, 1550-235X. doi: 10.1103/PhysRevB.87.060405. URL <https://link.aps.org/doi/10.1103/PhysRevB.87.060405>.
- [127] Mingxuan Fu, Takashi Imai, Tian-Heng Han, and Young S. Lee. Evidence for a gapped spin-liquid ground state in a kagome Heisenberg antiferromagnet. *Science*, 350(6261): 655–658, 2015. ISSN 0036-8075. doi: 10.1126/science.aab2120. URL <https://science.sciencemag.org/content/350/6261/655>.
- [128] Mikio Takano, Teruya Shinjo, and Toshio Takada. On the spin arrangement in kagome lattice of antiferromagnetic  $\text{kFe}_3(\text{OH})_6(\text{SO}_4)_2$ . *Journal of the Physical Society of Japan*, 30(4):1049–1053, 1971. doi: 10.1143/JPSJ.30.1049.
- [129] Yoshihiko Okamoto, Hiroyuki Yoshida, and Zenji Hiroi. Vesignieite  $\text{BaCu}_3\text{V}_2\text{O}_8(\text{OH})_2$  as a Candidate Spin-1/2 Kagome Antiferromagnet. *Journal of the Physical Society of Japan*, 78(3):033701, March 2009. ISSN 0031-9015, 1347-4073. doi: 10.1143/JPSJ.78.033701. URL <http://journals.jps.jp/doi/10.1143/JPSJ.78.033701>.

- 
- [130] T. H. Han, J. S. Helton, S. Chu, A. Prodi, D. K. Singh, C. Mazzoli, P. Müller, D. G. Nocera, and Y. S. Lee. Synthesis and characterization of single crystals of the spin-1/2 kagome-lattice antiferromagnets  $\text{Zn}_x\text{Cu}_{4-x}(\text{OH})_6\text{Cl}_2$ . *Physical Review B*, 83(10), March 2011. ISSN 1098-0121, 1550-235X. doi: 10.1103/PhysRevB.83.100402. URL <https://link.aps.org/doi/10.1103/PhysRevB.83.100402>.
  - [131] B. Martínez, F. Sandiumenge, A. Rouco, A. Labarta, J. Rodríguez-Carvajal, M. Tovar, M.T. Causa, S. Galí, and X. Obradors. Magnetic dilution in the strongly frustrated kagome antiferromagnet  $\text{SrGa}_{12-x}\text{Cr}_x\text{O}_{19}$ . *Physical Review B*, 46(17):10786–10792, November 1992. ISSN 0163-1829, 1095-3795. doi: 10.1103/PhysRevB.46.10786. URL <https://link.aps.org/doi/10.1103/PhysRevB.46.10786>.
  - [132] Zenji Hiroi, Masafumi Hanawa, Naoya Kobayashi, Minoru Nohara, Hidenori Takagi, Yoshitomo Kato, and Masashi Takigawa. Spin-1/2 kagome-like lattice in volborthite  $\text{Cu}_3\text{V}_2\text{O}_7(\text{OH})_2\cdot 2\text{H}_2\text{O}$ . *Journal of the Physical Society of Japan*, 70(11):3377–3384, 2001. doi: 10.1143/jpsj.70.3377.
  - [133] Philippe Mendels and Fabrice Bert. Quantum Kagome Antiferromagnet  $\text{ZnCu}_3(\text{OH})_6\text{Cl}_2$ . *Journal of the Physical Society of Japan*, 79(1):011001, January 2010. ISSN 0031-9015, 1347-4073. doi: 10.1143/JPSJ.79.011001. URL <http://journals.jps.jp/doi/10.1143/JPSJ.79.011001>.
  - [134] M. G. Townsend, G. Longworth, and E. Roudaut. Triangular-spin, kagome plane in jarosites. *Phys. Rev. B*, 33:4919–4926, Apr 1986. doi: 10.1103/PhysRevB.33.4919. URL <https://link.aps.org/doi/10.1103/PhysRevB.33.4919>.
  - [135] M Wolf and K D Schotte. Ising model with competing next-nearest-neighbour interactions on the Kagome lattice. *Journal of Physics A: Mathematical and General*, 21(9): 2195–2209, may 1988. doi: 10.1088/0305-4470/21/9/032. URL <https://doi.org/10.1088/0305-4470/21/9/032>.
  - [136] O. Cépas, C. M. Fong, P. W. Leung, and C. Lhuillier. Quantum phase transition induced by Dzyaloshinskii-Moriya interactions in the kagome antiferromagnet. *Physical Review B*, 78(14), October 2008. ISSN 1098-0121, 1550-235X. doi: 10.1103/PhysRevB.78.140405. URL <https://link.aps.org/doi/10.1103/PhysRevB.78.140405>.
  - [137] Yejin Huh, Lars Fritz, and Subir Sachdev. Quantum criticality of the kagome antiferromagnet with Dzyaloshinskii-Moriya interactions. *Physical Review B*, 81(14), April 2010. ISSN 1098-0121, 1550-235X. doi: 10.1103/PhysRevB.81.144432. URL <https://link.aps.org/doi/10.1103/PhysRevB.81.144432>.
  - [138] B. Dalla Piazza, M. Mourigal, N. B. Christensen, G. J. Nilsen, P. Tregenna-Piggott, T. G. Perring, M. Enderle, D. F. McMorrow, D. A. Ivanov, and H. M. Rønnow. Fractional excitations in the square-lattice quantum antiferromagnet. *Nature Physics*, 11(1):62–68, Jan 2015. ISSN 1745-2481. doi: 10.1038/nphys3172. URL <https://doi.org/10.1038/nphys3172>.

- [139] E. Flügel-Kahler. Die Kristallstruktur von Dolerophanit,  $\text{Cu}_2\text{O}(\text{SO}_4)$ . *Acta Crystallographica*, 16(10):1009–1014, Oct 1963. doi: 10.1107/S0365110X6300267X. URL <https://doi.org/10.1107/S0365110X6300267X>.
- [140] M Belaiche, M Drillon, J Aride, A Boukharis, T Biaz, and P Legoll. Application du modele Heisenberg a la chaine ferrimagnetique d ions Cu(II) dans  $\text{Cu}_2\text{OSO}_4$ . *J Chim Phys*, pages 1713–1719, 1991. URL <https://jcp.edpsciences.org/articles/jcp/abs/1991/01/jcp199188p1713/jcp199188p1713.html>.
- [141] M Drillon, M Belaiche, and JM Heintz. G. vileneuve”, a. boukhari” and j. aride’. *Organic and Inorganic Low-Dimensional Crystalline Materials*, 168:421, 2013.
- [142] Naoki Takahashi, Susumu Okubo, Hitoshi Ohta, Takahiro Sakurai, Masashi Fujisawa, and Hikomitu Kikuchi. Dzyaloshinsky-Moriya Interaction Estimated by AFMR of Kagome Like Substance  $\text{Cu}_2\text{O}(\text{SO}_4)$  Observed at 1.8K. *Journal of Physics: Conference Series*, 400(3):032097, December 2012. ISSN 1742-6588, 1742-6596. doi: 10.1088/1742-6596/400/3/032097. URL <http://stacks.iop.org/1742-6596/400/i=3/a=032097?key=crossref.b694501d96695745f7dc1dc8f1adf7d4>.
- [143] Takeshi Asai, Hiroshi Saheki, and Ryôiti Kiriyama. Magnetic Studies on Basic Salts of Copper, Dicopper Arsenate Hydroxide, Dicopper Hydroxide Phosphate, and Dicopper Oxide Sulfate. *Bulletin of the Chemical Society of Japan*, 52(2):310–314, February 1979. ISSN 0009-2673, 1348-0634. doi: 10.1246/bcsj.52.310. URL <http://www.journal.csj.jp/doi/10.1246/bcsj.52.310>.
- [144] Kirrily C. Rule, Richard A. Mole, and Dehong Yu. Which glue to choose? A neutron scattering study of various adhesive materials and their effect on background scattering. *Journal of Applied Crystallography*, 51(6):1766–1772, Dec 2018. doi: 10.1107/S1600576718014930. URL <https://doi.org/10.1107/S1600576718014930>.
- [145] Yu Song, John Van Dyke, I. K. Lum, B. D. White, Sooyoung Jang, Duygu Yazici, L. Shu, A. Schneidewind, Petr Čermák, Y. Qiu, M. B. Maple, Dirk K. Morr, and Pengcheng Dai. Robust upward dispersion of the neutron spin resonance in the heavy fermion superconductor  $\text{Ce}_1\text{-x}\text{Yb}_x\text{CoIn}_5$ . *Nature Communications*, 7(1):12774, Sep 2016. ISSN 2041-1723. doi: 10.1038/ncomms12774. URL <https://doi.org/10.1038/ncomms12774>.
- [146] D. Lançon, H. C. Walker, E. Ressouche, B. Ouladdiaf, K. C. Rule, G. J. McIntyre, T. J. Hicks, H. M. Rønnow, and A. R. Wildes. Magnetic structure and magnon dynamics of the quasi-two-dimensional antiferromagnet  $\text{FePS}_3$ . *Phys. Rev. B*, 94:214407, Dec 2016. doi: 10.1103/PhysRevB.94.214407. URL <https://link.aps.org/doi/10.1103/PhysRevB.94.214407>.
- [147] C. dela Cruz, F. Yen, B. Lorenz, Y. Q. Wang, Y. Y. Sun, M. M. Gospodinov, and C. W. Chu. Strong spin-lattice coupling in multiferroic  $\text{HoMnO}_3$ : Thermal expansion anomalies and pressure effect. *Phys. Rev. B*, 71:060407, Feb 2005. doi: 10.1103/PhysRevB.71.060407. URL <https://link.aps.org/doi/10.1103/PhysRevB.71.060407>.

- [148] Koichi Momma and Fujio Izumi. VESTA3 for three-dimensional visualization of crystal, volumetric and morphology data. *Journal of Applied Crystallography*, 44(6):1272–1276, Dec 2011. doi: 10.1107/S0021889811038970. URL <https://doi.org/10.1107/S0021889811038970>.
- [149] M. Yoshida, M. Takigawa, H. Yoshida, Y. Okamoto, and Z. Hiroi. Phase diagram and spin dynamics in volborthite with a distorted kagome lattice. *Phys. Rev. Lett.*, 103:077207, Aug 2009. doi: 10.1103/PhysRevLett.103.077207. URL <https://link.aps.org/doi/10.1103/PhysRevLett.103.077207>.
- [150] Tural Mehmetoglu. Use of einstein-debye method in the analytical and semi empirical analysis of isobaric heat capacity and thermal conductivity of nuclear materials. *Journal of Nuclear Materials*, 527:151827, 2019. ISSN 0022-3115. doi: <https://doi.org/10.1016/j.jnucmat.2019.151827>. URL <http://www.sciencedirect.com/science/article/pii/S0022311519307226>.
- [151] T. Quinn, A. R. Colclough, and T. Chandler. A new determination of the gas constant by an acoustical method. *Philosophical Transactions of the Royal Society of London. Series A, Mathematical and Physical Sciences*, 283:367 – 420, 1976.
- [152] Pallab Bag, P. R. Baral, and R. Nath. Cluster spin-glass behavior and memory effect in Cr 0.5 Fe 0.5 Ga. *Physical Review B*, 98(14), October 2018. ISSN 2469-9950, 2469-9969. doi: 10.1103/PhysRevB.98.144436. URL <https://link.aps.org/doi/10.1103/PhysRevB.98.144436>.
- [153] Santanu Pakhira, Chandan Mazumdar, R. Ranganathan, S. Giri, and Maxim Avdeev. Large magnetic cooling power involving frustrated antiferromagnetic spin-glass state in R<sub>2</sub>NiSi<sub>3</sub> (R = Gd, Er). *Physical Review B*, 94(10), September 2016. ISSN 2469-9950, 2469-9969. doi: 10.1103/PhysRevB.94.104414. URL <https://link.aps.org/doi/10.1103/PhysRevB.94.104414>.
- [154] Donald W. Rogers. *Einstein's "Other" Theory: The Planck-Bose-Einstein Theory of Heat Capacity*. Princeton University Press, 2005. URL <https://link.aps.org/doi/10.1103/PhysRevB.94.104414>.
- [155] Xin-Yi Wang, Lu Wang, Zhe-Ming Wang, Gang Su, and Song Gao. Coexistence of spin-canting, metamagnetism, and spin-flop in a (4,4) layered manganese azide polymer. *Chemistry of Materials*, 17(25):6369–6380, Dec 2005. ISSN 0897-4756. doi: 10.1021/cm0521830. URL <https://doi.org/10.1021/cm0521830>.
- [156] Bao-Qing Ma, Hao-Ling Sun, Song Gao, and Gang Su. A novel azido and pyrazine-dioxide bridged three-dimensional manganese(ii) network with antiferromagnetic ordering (tn = 62 k) and a spin flop state. *Chemistry of Materials*, 13(6):1946–1948, Jun 2001. ISSN 0897-4756. doi: 10.1021/cm000941a. URL <https://doi.org/10.1021/cm000941a>.



- [157] Juan Rodríguez-Carvajal. Recent advances in magnetic structure determination by neutron powder diffraction. *Physica B: Condensed Matter*, 192(1):55 – 69, 1993. ISSN 0921-4526. doi: [https://doi.org/10.1016/0921-4526\(93\)90108-I](https://doi.org/10.1016/0921-4526(93)90108-I). URL <http://www.sciencedirect.com/science/article/pii/092145269390108I>.
- [158] Clemens Ritter. Neutrons Not Entitled to Retire at the Age of 60: More than Ever Needed to Reveal Magnetic Structures. In *Solid Compounds of Transition Elements*, volume 170 of *Solid State Phenomena*, pages 263–269. Trans Tech Publications Ltd, 3 2011. doi: 10.4028/www.scientific.net/SSP.170.263.
- [159] J. Rodríguez-Carvajal. BASIREPS: a program for calculating irreducible representations of space groups and basis functions for axial and polar vector properties, Part of the FullProf Suite of programs available at: [www.ill.eu/sites/fullprof/](http://www.ill.eu/sites/fullprof/)., 2012.
- [160] Toru Moriya and Kei Yosida. On the Origin of the Anisotropy Energy of CuCl<sub>2</sub>-2H<sub>2</sub>O. *Progress of Theoretical Physics*, 9(6):663–675, 06 1953. ISSN 0033-068X. doi: 10.1143/ptp/9.6.663. URL <https://doi.org/10.1143/ptp/9.6.663>.
- [161] M H L Pryce. A modified perturbation procedure for a problem in paramagnetism. *Proceedings of the Physical Society. Section A*, 63(1):25–29, jan 1950. doi: 10.1088/0370-1298/63/1/304. URL <https://doi.org/10.1088/0370-1298/63/1/304>.
- [162] Dadi Dai, Hongjun Xiang, and Myung-Hwan Whangbo. Effects of spin-orbit coupling on magnetic properties of discrete and extended magnetic systems. *Journal of Computational Chemistry*, 29(13):2187–2209, 2008. doi: <https://doi.org/10.1002/jcc.21011>. URL <https://onlinelibrary.wiley.com/doi/abs/10.1002/jcc.21011>.
- [163] Jia Liu, Hyun-Joo Koo, Hongjun Xiang, Reinhard K. Kremer, and Myung-Hwan Whangbo. Most spin-1/2 transition-metal ions do have single ion anisotropy. *The Journal of Chemical Physics*, 141(12):124113, 2014. doi: 10.1063/1.4896148. URL <https://doi.org/10.1063/1.4896148>.
- [164] Naoki Takahashi, Susumu Okubo, Hitoshi Ohta, Takahiro Sakurai, Masashi Fujisawa, and Hikomitu Kikuchi. Dzyaloshinsky-Moriya Interaction Estimated by AFMR of Kagome Like Substance Cu<sub>2</sub>O(SO<sub>4</sub>) Observed at 1.8K. *Journal of Physics Conference Series*, 400: 2097–, 12 2012. doi: 10.1088/1742-6596/400/3/032097.
- [165] Ioannis Rousochatzakis, Salvatore R. Manmana, Andreas M. Läuchli, Bruce Normand, and Frédéric Mila. Dzyaloshinskii-Moriya anisotropy and nonmagnetic impurities in the  $s = \frac{1}{2}$  kagome system ZnCu<sub>3</sub>(OH)<sub>6</sub>Cl<sub>2</sub>. *Phys. Rev. B*, 79:214415, Jun 2009. doi: 10.1103/PhysRevB.79.214415. URL <https://link.aps.org/doi/10.1103/PhysRevB.79.214415>.
- [166] O. Cépas, C. M. Fong, P. W. Leung, and C. Lhuillier. Quantum phase transition induced by Dzyaloshinskii-Moriya interactions in the kagome antiferromagnet. *Phys. Rev. B*, 78: 140405, Oct 2008. doi: 10.1103/PhysRevB.78.140405. URL <https://link.aps.org/doi/10.1103/PhysRevB.78.140405>.

- [167] Robert M. White. *The Magnetic Hamiltonian*, pages 29–68. Springer Berlin Heidelberg, Berlin, Heidelberg, 1983. ISBN 978-3-662-02360-0. doi: 10.1007/978-3-662-02360-0\_2. URL [https://doi.org/10.1007/978-3-662-02360-0\\_2](https://doi.org/10.1007/978-3-662-02360-0_2).
- [168] Hélène Feldner, Zi Yang Meng, Thomas C. Lang, Fakhre F. Assaad, Stefan Wessel, and Andreas Honecker. Dynamical signatures of edge-state magnetism on graphene nanoribbons. *Phys. Rev. Lett.*, 106:226401, May 2011. doi: 10.1103/PhysRevLett.106.226401. URL <https://link.aps.org/doi/10.1103/PhysRevLett.106.226401>.
- [169] C. Kawabata, M. Takeuchi, and A.R. Bishop. Simulation of the dynamic structure factor for two-dimensional classical heisenberg ferromagnets. *Journal of Magnetism and Magnetic Materials*, 54-57:871 – 872, 1986. ISSN 0304-8853. doi: [https://doi.org/10.1016/0304-8853\(86\)90292-1](https://doi.org/10.1016/0304-8853(86)90292-1). URL <http://www.sciencedirect.com/science/article/pii/0304885386902921>.
- [170] Harikrishnan S Nair, Michael O Ogunbunmi, C M N Kumar, D T Adroja, P Manuel, D Fortes, J Taylor, and A M Strydom. Pr-magnetism in the quasi-skutterudite compound PrFe<sub>2</sub>As<sub>8</sub>. *Journal of Physics: Condensed Matter*, 29(34):345801, jul 2017. doi: 10.1088/1361-648x/aa7b98. URL <https://doi.org/10.1088/1361-648x/aa7b98>.
- [171] Alexandru Petrescu, Marie Piraud, Guillaume Roux, I. P. McCulloch, and Karyn Le Hur. Precursor of the laughlin state of hard-core bosons on a two-leg ladder. *Phys. Rev. B*, 96: 014524, Jul 2017. doi: 10.1103/PhysRevB.96.014524. URL <https://link.aps.org/doi/10.1103/PhysRevB.96.014524>.
- [172] Jiří Chaloupka and Giniyat Khaliullin. Highly frustrated magnetism in relativistic  $d^4$  mott insulators: Bosonic analog of the kitaev honeycomb model. *Phys. Rev. B*, 100: 224413, Dec 2019. doi: 10.1103/PhysRevB.100.224413. URL <https://link.aps.org/doi/10.1103/PhysRevB.100.224413>.
- [173] A. Rubio-García, J. Dukelsky, D. R. Alcoba, P. Capuzzi, O. B. Oña, E. Ríos, A. Torre, and L. Lain. Variational reduced density matrix method in the doubly-occupied configuration interaction space using four-particle  $n$ -representability conditions: Application to the xxz model of quantum magnetism. *The Journal of Chemical Physics*, 151(15):154104, 2019. doi: 10.1063/1.5118899. URL <https://doi.org/10.1063/1.5118899>.
- [174] S Toth and B Lake. Linear spin wave theory for single-q incommensurate magnetic structures. *Journal of Physics: Condensed Matter*, 27(16):166002, mar 2015. doi: 10.1088/0953-8984/27/16/166002. URL <https://doi.org/10.1088/0953-8984/27/16/166002>.
- [175] J Merino, Ross H McKenzie, J B Marston, and C H Chung. The heisenberg antiferromagnet on an anisotropic triangular lattice: linear spin-wave theory. *Journal of Physics: Condensed Matter*, 11(14):2965–2975, jan 1999. doi: 10.1088/0953-8984/11/14/012. URL <https://doi.org/10.1088/0953-8984/11/14/012>.

## Bibliography

---

- [176] Ryogo Kubo. The spin-wave theory of antiferromagnetics. *Phys. Rev.*, 87:568–580, Aug 1952. doi: 10.1103/PhysRev.87.568. URL <https://link.aps.org/doi/10.1103/PhysRev.87.568>.
- [177] R. Pauthenet. Experimental verification of spin-wave theory in high fields (invited). *Journal of Applied Physics*, 53(11):8187–8192, 1982. doi: 10.1063/1.330287. URL <https://doi.org/10.1063/1.330287>.
- [178] Tôru Sakai and Minoru Takahashi.  $S = 1$  antiferromagnetic heisenberg chain in a magnetic field. *Physical review. B, Condensed matter*, 43:13383–13393, 07 1991. doi: 10.1103/PhysRevB.43.13383.
- [179] Mahboobeh Shahri Naseri, George Japaridze, Saeed Mahdavifar, and Saber Farjami Shayesteh. Magnetic properties of the spin  $s = 1/2$  heisenberg chain with hexamer modulation of exchange. *Journal of physics. Condensed matter : an Institute of Physics journal*, 24:116002, 03 2012. doi: 10.1088/0953-8984/24/11/116002.
- [180] A. Zheludev, S. M. Shapiro, Z. Honda, K. Katsumata, B. Grenier, E. Ressouche, L.-P. Regnault, Y. Chen, P. Vorderwisch, H.-J. Mikeska, and A. K. Kolezhuk. Dynamics of an anisotropic haldane antiferromagnet in a strong magnetic field. *Phys. Rev. B*, 69:054414, Feb 2004. doi: 10.1103/PhysRevB.69.054414. URL <https://link.aps.org/doi/10.1103/PhysRevB.69.054414>.
- [181] Gerhard Müller, Harry Thomas, Hans Beck, and Jill C. Bonner. Quantum spin dynamics of the antiferromagnetic linear chain in zero and nonzero magnetic field. *Phys. Rev. B*, 24:1429–1467, Aug 1981. doi: 10.1103/PhysRevB.24.1429. URL <https://link.aps.org/doi/10.1103/PhysRevB.24.1429>.
- [182] Z. Tun, W. J. L. Buyers, R. L. Armstrong, K. Hirakawa, and B. Briat. Haldane-gap modes in the  $s=1$  antiferromagnetic chain compound  $\text{csncl}_3$ . *Phys. Rev. B*, 42:4677–4681, Sep 1990. doi: 10.1103/PhysRevB.42.4677. URL <https://link.aps.org/doi/10.1103/PhysRevB.42.4677>.
- [183] C. Broholm, R. J. Cava, S. A. Kivelson, D. G. Nocera, M. R. Norman, and T. Senthil. Quantum spin liquids. *Science*, 367(6475), 2020. ISSN 0036-8075. doi: 10.1126/science.aay0668. URL <https://science.sciencemag.org/content/367/6475/eaay0668>.
- [184] Yi Zhou, Kazushi Kanoda, and Tai-Kai Ng. Quantum spin liquid states. *Rev. Mod. Phys.*, 89:025003, Apr 2017. doi: 10.1103/RevModPhys.89.025003. URL <https://link.aps.org/doi/10.1103/RevModPhys.89.025003>.
- [185] Lucile Savary and Leon Balents. Quantum spin liquids: a review. *Reports on Progress in Physics*, 80(1):016502, nov 2016. doi: 10.1088/0034-4885/80/1/016502. URL <https://doi.org/10.1088/0034-4885/80/1/016502>.
- [186] B. Lake, D. A. Tennant, J.-S. Caux, T. Barthel, U. Schollwöck, S. E. Nagler, and C. D. Frost. Multispinon continua at zero and finite temperature in a near-ideal heisenberg

- chain. *Phys. Rev. Lett.*, 111:137205, Sep 2013. doi: 10.1103/PhysRevLett.111.137205. URL <https://link.aps.org/doi/10.1103/PhysRevLett.111.137205>.
- [187] Y. Shimizu, K. Miyagawa, K. Kanoda, M. Maesato, and G. Saito. Spin liquid state in an organic mott insulator with a triangular lattice. *Phys. Rev. Lett.*, 91:107001, Sep 2003. doi: 10.1103/PhysRevLett.91.107001. URL <https://link.aps.org/doi/10.1103/PhysRevLett.91.107001>.
- [188] Matthew P. Shores, Emily A. Nytko, Bart M. Bartlett, and Daniel G. Nocera. A structurally perfect  $s = 1/2$  kagomé antiferromagnet. *Journal of the American Chemical Society*, 127(39):13462–13463, Oct 2005. ISSN 0002-7863. doi: 10.1021/ja053891p. URL <https://doi.org/10.1021/ja053891p>.
- [189] Yuesheng Li, Devashibhai Adroja, Pabitra K. Biswas, Peter J. Baker, Qian Zhang, Juanjuan Liu, Alexander A. Tsirlin, Philipp Gegenwart, and Qingming Zhang. Muon spin relaxation evidence for the  $u(1)$  quantum spin-liquid ground state in the triangular antiferromagnet  $\text{YbMgGaO}_4$ . *Phys. Rev. Lett.*, 117:097201, Aug 2016. doi: 10.1103/PhysRevLett.117.097201. URL <https://link.aps.org/doi/10.1103/PhysRevLett.117.097201>.
- [190] Tian-Heng Han, Joel S. Helton, Shaoyan Chu, Daniel G. Nocera, Jose A. Rodriguez-Rivera, Collin Broholm, and Young S. Lee. Fractionalized excitations in the spin-liquid state of a kagome-lattice antiferromagnet. *Nature*, 492(7429):406–410, Dec 2012. ISSN 1476-4687. doi: 10.1038/nature11659. URL <https://doi.org/10.1038/nature11659>.
- [191] M. A. de Vries, J. R. Stewart, P. P. Deen, J. O. Piatek, G. J. Nilsen, H. M. Rønnow, and A. Harrison. Scale-free antiferromagnetic fluctuations in the  $s = 1/2$  kagome antiferromagnet herbertsmithite. *Phys. Rev. Lett.*, 103:237201, Dec 2009. doi: 10.1103/PhysRevLett.103.237201. URL <https://link.aps.org/doi/10.1103/PhysRevLett.103.237201>.
- [192] Rebecca Dally, Tom Hogan, Alex Amato, Hubertus Luetkens, Chris Baines, Jose Rodriguez-Rivera, Michael J. Graf, and Stephen D. Wilson. Short-range correlations in the magnetic ground state of  $\text{Na}_4\text{Ir}_3\text{O}_8$ . *Phys. Rev. Lett.*, 113:247601, Dec 2014. doi: 10.1103/PhysRevLett.113.247601. URL <https://link.aps.org/doi/10.1103/PhysRevLett.113.247601>.
- [193] Shravani Chillal, Yasir Iqbal, Harald O. Jeschke, Jose A. Rodriguez-Rivera, Robert Bewley, Pascal Manuel, Dmitry Khalyavin, Paul Steffens, Ronny Thomale, A. T. M. Nazmul Islam, Johannes Reuther, and Bella Lake. Evidence for a three-dimensional quantum spin liquid in  $\text{PbCuTe}_2\text{O}_6$ . *Nature Communications*, 11(1):2348, May 2020. ISSN 2041-1723. doi: 10.1038/s41467-020-15594-1. URL <https://doi.org/10.1038/s41467-020-15594-1>.
- [194] Satoru Nakatsuji, Yusuke Nambu, Hiroshi Tonomura, Osamu Sakai, Seth Jonas, Collin Broholm, Hirokazu Tsunetsugu, Yiming Qiu, and Yoshiteru Maeno. Spin disorder on a triangular lattice. *Science*, 309(5741):1697–1700, 2005. ISSN 0036-8075. doi: 10.1126/science.1114727. URL <https://science.sciencemag.org/content/309/5741/1697>.

## Bibliography

---

- [195] Alexei Kitaev. Anyons in an exactly solved model and beyond. *Annals of Physics*, 321(1):2 – 111, 2006. ISSN 0003-4916. doi: <https://doi.org/10.1016/j.aop.2005.10.005>. URL <http://www.sciencedirect.com/science/article/pii/S0003491605002381>. January Special Issue.
- [196] A. Banerjee, C. A. Bridges, J.-Q. Yan, A. A. Aczel, L. Li, M. B. Stone, G. E. Granroth, M. D. Lumsden, Y. Yiu, J. Knolle, S. Bhattacharjee, D. L. Kovrizhin, R. Moessner, D. A. Tennant, D. G. Mandrus, and S. E. Nagler. Proximate kitaev quantum spin liquid behaviour in a honeycomb magnet. *Nature Materials*, 15(7):733–740, Jul 2016. ISSN 1476-4660. doi: 10.1038/nmat4604. URL <https://doi.org/10.1038/nmat4604>.
- [197] C. Pfleiderer, S. R. Julian, and G. G. Lonzarich. Non-fermi-liquid nature of the normal state of itinerant-electron ferromagnets. *Nature*, 414(6862):427–430, Nov 2001. ISSN 1476-4687. doi: 10.1038/35106527. URL <https://doi.org/10.1038/35106527>.
- [198] C. Pfleiderer, G. J. McMullan, S. R. Julian, and G. G. Lonzarich. Magnetic quantum phase transition in mnsi under hydrostatic pressure. *Phys. Rev. B*, 55:8330–8338, Apr 1997. doi: 10.1103/PhysRevB.55.8330. URL <https://link.aps.org/doi/10.1103/PhysRevB.55.8330>.
- [199] Sergei V. Isakov, John M. Hopkinson, and Hae-Young Kee. Fate of partial order on trillium and distorted windmill lattices. *Phys. Rev. B*, 78:014404, Jul 2008. doi: 10.1103/PhysRevB.78.014404. URL <https://link.aps.org/doi/10.1103/PhysRevB.78.014404>.
- [200] John M. Hopkinson and Hae-Young Kee. Geometric frustration inherent to the trillium lattice, a sublattice of the b20 structure. *Phys. Rev. B*, 74:224441, Dec 2006. doi: 10.1103/PhysRevB.74.224441. URL <https://link.aps.org/doi/10.1103/PhysRevB.74.224441>.
- [201] D. Speer and E. Salje. Phase transitions in langbeinites i: Crystal chemistry and structures of k-double sulfates of the langbeinite type  $m_2 + k_2(\text{so}_4)_3$ ,  $m + \text{mg}$ ,  $\text{ni}$ ,  $\text{co}$ ,  $\text{zn}$ ,  $\text{ca}$ . *Physics and Chemistry of Minerals*, 13(1):17–24, Jan 1986. ISSN 1432-2021. doi: 10.1007/BF00307309. URL <https://doi.org/10.1007/BF00307309>.
- [202] Krzysztof Kubiak, Dariusz Szeliga, Jan Sieniawski, and Arkadiusz Onysko. 11 - the unidirectional crystallization of metals and alloys (turbine blades). In Peter Rudolph, editor, *Handbook of Crystal Growth (Second Edition)*, Handbook of Crystal Growth, pages 413 – 457. Elsevier, Boston, second edition edition, 2015. ISBN 978-0-444-63303-3. doi: <https://doi.org/10.1016/B978-0-444-63303-3.00011-0>. URL <http://www.sciencedirect.com/science/article/pii/B9780444633033000110>.
- [203] Taro Nakajima, Hiroshi Oike, Akiko Kikkawa, Elliot P. Gilbert, Norman Booth, Kazuhisa Kakurai, Yasujiro Taguchi, Yoshinori Tokura, Fumitaka Kagawa, and Taka-hisa Arima. Skyrmion lattice structural transition in mnsi. *Science Advances*, 3(6), 2017. doi: 10.1126/sciadv.1602562. URL <https://advances.sciencemag.org/content/3/6/e1602562>.
- [204] S. L. Zhang, A. Bauer, D. M. Burn, P. Milde, E. Neuber, L. M. Eng, H. Berger, C. Pfleiderer, G. van der Laan, and T. Hesjedal. Multidomain skyrmion lattice state in  $\text{Cu}_2\text{OSeO}_3$ . *Nano*

- Letters*, 16(5):3285–3291, May 2016. ISSN 1530-6984. doi: 10.1021/acs.nanolett.6b00845. URL <https://doi.org/10.1021/acs.nanolett.6b00845>.
- [205] D. Alan Tennant, Roger A. Cowley, Stephen E. Nagler, and Alexei M. Tsvelik. Measurement of the spin-excitation continuum in one-dimensional  $\text{KCuF}_3$  using neutron scattering. *Phys. Rev. B*, 52:13368–13380, Nov 1995. doi: 10.1103/PhysRevB.52.13368. URL <https://link.aps.org/doi/10.1103/PhysRevB.52.13368>.
- [206] John M. Hopkinson and Hae-Young Kee. Geometric frustration inherent to the trillium lattice, a sublattice of the b20 structure. *Phys. Rev. B*, 74:224441, Dec 2006. doi: 10.1103/PhysRevB.74.224441. URL <https://link.aps.org/doi/10.1103/PhysRevB.74.224441>.
- [207] Sergei V. Isakov, John M. Hopkinson, and Hae-Young Kee. Fate of partial order on trillium and distorted windmill lattices. *Phys. Rev. B*, 78:014404, Jul 2008. doi: 10.1103/PhysRevB.78.014404. URL <https://link.aps.org/doi/10.1103/PhysRevB.78.014404>.
- [208] Tusharkanti Dey, A. V. Mahajan, P. Khuntia, M. Baenitz, B. Koteswararao, and F. C. Chou. Spin-liquid behavior in  $J_{\text{eff}} = \frac{1}{2}$  triangular lattice compound  $\text{Ba}_3\text{IrTi}_2\text{O}_9$ . *Phys. Rev. B*, 86:140405, Oct 2012. doi: 10.1103/PhysRevB.86.140405. URL <https://link.aps.org/doi/10.1103/PhysRevB.86.140405>.
- [209] Kavita Mehlawat, A. Thamizhavel, and Yogesh Singh. Heat capacity evidence for proximity to the kitaev quantum spin liquid in  $A_2\text{IrO}_3$  ( $a = \text{Na, Li}$ ). *Phys. Rev. B*, 95:144406, Apr 2017. doi: 10.1103/PhysRevB.95.144406. URL <https://link.aps.org/doi/10.1103/PhysRevB.95.144406>.
- [210] Satoshi Yamashita, Takashi Yamamoto, Yasuhiro Nakazawa, Masafumi Tamura, and Reizo Kato. Gapless spin liquid of an organic triangular compound evidenced by thermodynamic measurements. *Nature Communications*, 2(1):275, Apr 2011. ISSN 2041-1723. doi: 10.1038/ncomms1274. URL <https://doi.org/10.1038/ncomms1274>.
- [211] Jie Xing, Liurukara D. Sanjeeva, Jungsoo Kim, G. R. Stewart, Andrey Podlesnyak, and Athena S. Sefat. Field-induced magnetic transition and spin fluctuations in the quantum spin-liquid candidate  $\text{CsYbSe}_2$ . *Phys. Rev. B*, 100:220407, Dec 2019. doi: 10.1103/PhysRevB.100.220407. URL <https://link.aps.org/doi/10.1103/PhysRevB.100.220407>.
- [212] H. J. Silverstein, K. Fritsch, F. Flicker, A. M. Hallas, J. S. Gardner, Y. Qiu, G. Ehlers, A. T. Savici, Z. Yamani, K. A. Ross, B. D. Gaulin, M. J. P. Gingras, J. A. M. Paddison, K. Foyevtsova, R. Valenti, F. Hawthorne, C. R. Wiebe, and H. D. Zhou. Liquidlike correlations in single-crystalline  $\text{Y}_2\text{Mo}_2\text{O}_7$ : An unconventional spin glass. *Phys. Rev. B*, 89:054433, Feb 2014. doi: 10.1103/PhysRevB.89.054433. URL <https://link.aps.org/doi/10.1103/PhysRevB.89.054433>.
- [213] A. P. Ramirez, B. Hessen, and M. Winklemann. Entropy balance and evidence for local spin singlets in a kagomé-like magnet. *Phys. Rev. Lett.*, 84:2957–2960, Mar 2000. doi: 10.1103/PhysRevLett.84.2957. URL <https://link.aps.org/doi/10.1103/PhysRevLett.84.2957>.

## Bibliography

---

- [214] Y. Xu, J. Zhang, Y. S. Li, Y. J. Yu, X. C. Hong, Q. M. Zhang, and S. Y. Li. Absence of magnetic thermal conductivity in the quantum spin-liquid candidate  $\text{YbMgGaO}_4$ . *Phys. Rev. Lett.*, 117:267202, Dec 2016. doi: 10.1103/PhysRevLett.117.267202. URL <https://link.aps.org/doi/10.1103/PhysRevLett.117.267202>.
- [215] M J P Gingras and P A McClarty. Quantum spin ice: a search for gapless quantum spin liquids in pyrochlore magnets. *Reports on Progress in Physics*, 77(5):056501, may 2014. doi: 10.1088/0034-4885/77/5/056501. URL <https://doi.org/10.1088%2F0034-4885%2F77%2F5%2F056501>.
- [216] L. Clark, J. C. Orain, F. Bert, M. A. De Vries, F. H. Aidoudi, R. E. Morris, P. Lightfoot, J. S. Lord, M. T. F. Telling, P. Bonville, J. P. Attfield, P. Mendels, and A. Harrison. Gapless spin liquid ground state in the  $s=1/2$  vanadium oxyfluoride kagome antiferromagnet  $[\text{nh}_4]_2[\text{c}_7\text{h}_{14}\text{N}][\text{v}_7\text{o}_6\text{f}_{18}]$ . *Phys. Rev. Lett.*, 110:207208, May 2013. doi: 10.1103/PhysRevLett.110.207208. URL <https://link.aps.org/doi/10.1103/PhysRevLett.110.207208>.
- [217] Yogesh Singh, Y. Tokiwa, J. Dong, and P. Gegenwart. Spin liquid close to a quantum critical point in  $\text{Na}_4\text{Ir}_3\text{O}_8$ . *Phys. Rev. B*, 88:220413, Dec 2013. doi: 10.1103/PhysRevB.88.220413. URL <https://link.aps.org/doi/10.1103/PhysRevB.88.220413>.
- [218] Lei Ding, Pascal Manuel, Sebastian Bachus, Franziska Grueßler, Philipp Gegenwart, John Singleton, Roger D. Johnson, Helen C. Walker, Devashibhai T. Adroja, Adrian D. Hillier, and Alexander A. Tsirlin. Gapless spin-liquid state in the structurally disorder-free triangular antiferromagnet  $\text{NaYbO}_2$ . *Phys. Rev. B*, 100:144432, Oct 2019. doi: 10.1103/PhysRevB.100.144432. URL <https://link.aps.org/doi/10.1103/PhysRevB.100.144432>.
- [219] Weiwei Liu, Zheng Zhang, Jianting Ji, Yixuan Liu, Jianshu Li, Xiaoqun Wang, Hechang Lei, Gang Chen, and Qingming Zhang. Rare-earth chalcogenides: A large family of triangular lattice spin liquid candidates. *Chinese Physics Letters*, 35(11):117501, oct 2018. doi: 10.1088/0256-307x/35/11/117501. URL <https://doi.org/10.1088%2F0256-307x%2F35%2F11%2F117501>.
- [220] Lucy Clark, Gabriele Sala, Dalini D. Maharaj, Matthew B. Stone, Kevin S. Knight, Mark T. F. Telling, Xueyun Wang, Xianghan Xu, Jaewook Kim, Yanbin Li, Sang-Wook Cheong, and Bruce D. Gaulin. Two-dimensional spin liquid behaviour in the triangular-honeycomb antiferromagnet  $\text{LiNbO}_3$ . *Nature Physics*, 15(3):262–268, Mar 2019. ISSN 1745-2481. doi: 10.1038/s41567-018-0407-2. URL <https://doi.org/10.1038/s41567-018-0407-2>.
- [221] P. W. Anderson. Knight shift in superconductors. *Phys. Rev. Lett.*, 3:325–326, Oct 1959. doi: 10.1103/PhysRevLett.3.325. URL <https://link.aps.org/doi/10.1103/PhysRevLett.3.325>.
- [222] I. J. Lee, S. E. Brown, W. G. Clark, M. J. Strouse, M. J. Naughton, W. Kang, and P. M. Chaikin. Triplet superconductivity in an organic superconductor probed by nmr knight shift. *Phys. Rev. Lett.*, 88:017004, Dec 2001. doi: 10.1103/PhysRevLett.88.017004. URL <https://link.aps.org/doi/10.1103/PhysRevLett.88.017004>.

- [223] Y. Shimizu, K. Miyagawa, K. Kanoda, M. Maesato, and G. Saito. Emergence of inhomogeneous moments from spin liquid in the triangular-lattice mott insulator  $\kappa-(\text{ET})_2\text{Cu}_2(\text{CN})_3$ . *Phys. Rev. B*, 73:140407, Apr 2006. doi: 10.1103/PhysRevB.73.140407. URL <https://link.aps.org/doi/10.1103/PhysRevB.73.140407>.
- [224] Xiang-Long Yu, Da-Yong Liu, Peng Li, and Liang-Jian Zou. Ground-state and finite-temperature properties of spin liquid phase in the j1–j2 honeycomb model. *Physica E: Low-dimensional Systems and Nanostructures*, 59:41 – 49, 2014. ISSN 1386-9477. doi: <https://doi.org/10.1016/j.physe.2013.12.017>. URL <http://www.sciencedirect.com/science/article/pii/S1386947713004542>.
- [225] Y. J. Uemura, A. Keren, K. Kojima, L. P. Le, G. M. Luke, W. D. Wu, Y. Ajiro, T. Asano, Y. Kuriyama, M. Mekata, H. Kikuchi, and K. Kakurai. Spin fluctuations in frustrated kagomé lattice system  $\text{SrCr}_8\text{Ga}_4\text{O}_{19}$  studied by muon spin relaxation. *Phys. Rev. Lett.*, 73: 3306–3309, Dec 1994. doi: 10.1103/PhysRevLett.73.3306. URL <https://link.aps.org/doi/10.1103/PhysRevLett.73.3306>.
- [226] Joseph A M Paddison, J Ross Stewart, and Andrew L Goodwin. spinvert: a program for refinement of paramagnetic diffuse scattering data. *Journal of Physics: Condensed Matter*, 25(45):454220, oct 2013. doi: 10.1088/0953-8984/25/45/454220. URL <https://doi.org/10.1088/0953-8984/25/45/454220>.
- [227] Seung-Hwan Do, Sang-Youn Park, Junki Yoshitake, Joji Nasu, Yukitoshi Motome, Yong Seung Kwon, D. T. Adroja, D. J. Voneshen, Kyoo Kim, T.-H. Jang, J.-H. Park, Kwang-Yong Choi, and Sungdae Ji. Majorana fermions in the kitaev quantum spin system  $\alpha\text{-ruCl}_3$ . *Nature Physics*, 13(11):1079–1084, Nov 2017. ISSN 1745-2481. doi: 10.1038/nphys4264. URL <https://doi.org/10.1038/nphys4264>.
- [228] Pranab Kumar Das, Neeraj Kumar, R. Kulkarni, and A. Thamizhavel. Magnetic properties of the heavy-fermion antiferromagnet  $\text{CeMg}_3$ . *Phys. Rev. B*, 83:134416, Apr 2011. doi: 10.1103/PhysRevB.83.134416. URL <https://link.aps.org/doi/10.1103/PhysRevB.83.134416>.
- [229] G. C. Lau, R. S. Freitas, B. G. Ueland, B. D. Muegge, E. L. Duncan, P. Schiffer, and R. J. Cava. Zero-point entropy in stuffed spin-ice. *Nature Physics*, 2(4):249–253, Apr 2006. ISSN 1745-2481. doi: 10.1038/nphys270. URL <https://doi.org/10.1038/nphys270>.
- [230] Scott C. Riggs, O. Vafek, J. B. Kemper, J. B. Betts, A. Migliori, F. F. Balakirev, W. N. Hardy, Ruixing Liang, D. A. Bonn, and G. S. Boebinger. Heat capacity through the magnetic-field-induced resistive transition in an underdoped high-temperature superconductor. *Nature Physics*, 7(4):332–335, Apr 2011. ISSN 1745-2481. doi: 10.1038/nphys1921. URL <https://doi.org/10.1038/nphys1921>.
- [231] G. Grissonnanche, O. Cyr-Choinière, F. Laliberté, S. René de Cotret, A. Juneau-Fecteau, S. Dufour-Beauséjour, M.-È. Delage, D. LeBoeuf, J. Chang, B. J. Ramshaw, D. A. Bonn, W. N. Hardy, R. Liang, S. Adachi, N. E. Hussey, B. Vignolle, C. Proust, M. Sutherland,



- S. Krämer, J.-H. Park, D. Graf, N. Doiron-Leyraud, and Louis Taillefer. Direct measurement of the upper critical field in cuprate superconductors. *Nature Communications*, 5(1):3280, Feb 2014. ISSN 2041-1723. doi: 10.1038/ncomms4280. URL <https://doi.org/10.1038/ncomms4280>.
- [232] Tristin Metz, Seokjin Bae, Sheng Ran, I-Lin Liu, Yun Suk Eo, Wesley T. Fuhrman, Daniel F. Agterberg, Steven M. Anlage, Nicholas P. Butch, and Johnpierre Paglione. Point-node gap structure of the spin-triplet superconductor  $\text{Ute}_2$ . *Phys. Rev. B*, 100:220504, Dec 2019. doi: 10.1103/PhysRevB.100.220504. URL <https://link.aps.org/doi/10.1103/PhysRevB.100.220504>.
- [233] C. Q. Xu, B. Li, J. J. Feng, W. H. Jiao, Y. K. Li, S. W. Liu, Y. X. Zhou, R. Sankar, Nikolai D. Zhigadlo, H. B. Wang, Z. D. Han, B. Qian, W. Ye, W. Zhou, T. Shiroka, Pabitra K. Biswas, Xiaofeng Xu, and Z. X. Shi. Two-gap superconductivity and topological surface states in  $\text{TaOSe}_2$ . *Phys. Rev. B*, 100:134503, Oct 2019. doi: 10.1103/PhysRevB.100.134503. URL <https://link.aps.org/doi/10.1103/PhysRevB.100.134503>.
- [234] Toshiro Sakakibara, Shunichiro Kittaka, and Kazushige Machida. Angle-resolved heat capacity of heavy fermion superconductors. *Reports on Progress in Physics*, 79(9):094002, aug 2016. doi: 10.1088/0034-4885/79/9/094002. URL <https://doi.org/10.1088/0034-4885/79/9/094002>.
- [235] M. X. Gu, Chang Q. Sun, Z. Chen, T. C. Au Yeung, S. Li, C. M. Tan, and V. Nosik. Size, temperature, and bond nature dependence of elasticity and its derivatives on extensibility, debye temperature, and heat capacity of nanostructures. *Phys. Rev. B*, 75:125403, Mar 2007. doi: 10.1103/PhysRevB.75.125403. URL <https://link.aps.org/doi/10.1103/PhysRevB.75.125403>.
- [236] E. Lara-Curzio, A. F. May, O. Delaire, M. A. McGuire, X. Lu, Cheng-Yun Liu, E. D. Case, and D. T. Morelli. Low-temperature heat capacity and localized vibrational modes in natural and synthetic tetrahedrites. *Journal of Applied Physics*, 115(19):193515, 2014. doi: 10.1063/1.4878676. URL <https://doi.org/10.1063/1.4878676>.
- [237] L. Yang, M. Jeong, P. Babkevich, V. M. Katukuri, B. Náfrádi, N. E. Shaik, A. Magrez, H. Berger, J. Schefer, E. Ressouche, M. Kriener, I. Živković, O. V. Yazyev, L. Forró, and H. M. Rønnow.  $\text{J}_1 - \text{J}_2$  square lattice antiferromagnetism in the orbitally quenched insulator  $\text{MoOPO}_4$ . *Physical Review B*, 96(2), July 2017. ISSN 2469-9950, 2469-9969. doi: 10.1103/PhysRevB.96.024445. URL <http://link.aps.org/doi/10.1103/PhysRevB.96.024445>.
- [238] Hadi Papi, Virgile Yves Favre, Hossein Ahmadvand, Mojtaba Alaei, Mohammad Khondabi, Denis Sheptyakov, Lukas Keller, Parviz Kameli, Ivica Živković, and Henrik M. Rønnow. Magnetic and structural properties of Ni-substituted magnetoelectric  $\text{Co}_4\text{Nb}_2\text{O}_9$ . *Phys. Rev. B*, 100:134408, Oct 2019. doi: 10.1103/PhysRevB.100.134408. URL <https://link.aps.org/doi/10.1103/PhysRevB.100.134408>.

- [239] Z. W. Ouyang, F. W. Wang, Q. Huang, W. F. Liu, Y. G. Xiao, J. W. Lynn, J. K. Liang, and G. H. Rao. Magnetic structure, magnetostriction, and magnetic transitions of the laves-phase compound  $\text{NdCo}_2$ . *Phys. Rev. B*, 71:064405, Feb 2005. doi: 10.1103/PhysRevB.71.064405. URL <https://link.aps.org/doi/10.1103/PhysRevB.71.064405>.
- [240] Z. W. Ouyang, F. W. Wang, Q. Huang, W. F. Liu, Y. G. Xiao, J. W. Lynn, J. K. Liang, and G. H. Rao. Magnetic structure, magnetostriction, and magnetic transitions of the laves-phase compound  $\text{NdCo}_2$ . *Phys. Rev. B*, 71:064405, Feb 2005. doi: 10.1103/PhysRevB.71.064405. URL <https://link.aps.org/doi/10.1103/PhysRevB.71.064405>.
- [241] Jorge I. Facio, D. Betancourth, N.R. Cejas Bolecek, G.A. Jorge, Pablo Pedrzzini, V.F. Correa, Pablo S. Cornaglia, V. Vildosola, and D.J. García. Lattice specific heat for the  $\text{rmin5}$  ( $\text{r}=\text{gd, la, y}$ ;  $\text{m}=\text{co, rh}$ ) compounds: Non-magnetic contribution subtraction. *Journal of Magnetism and Magnetic Materials*, 407:406 – 411, 2016. ISSN 0304-8853. doi: <https://doi.org/10.1016/j.jmmm.2016.01.053>. URL <http://www.sciencedirect.com/science/article/pii/S0304885316300531>.
- [242] Jan Zubáč, Kristina Vlášková, Jan Prokleška, Petr Proschek, and Pavel Javorský. Magnetic properties and phase diagram of  $\text{ndpd5a2}$ . *Journal of Alloys and Compounds*, 675:94 – 98, 2016. ISSN 0925-8388. doi: <https://doi.org/10.1016/j.jallcom.2016.02.256>. URL <http://www.sciencedirect.com/science/article/pii/S0925838816305345>.
- [243] J.W. Kim, Y.S. Oh, K.S. Suh, Y.D. Park, and Kee Hoon Kim. Specific heat of a  $\text{ycro3}$  single crystal as investigated by a  $\text{si-n}$  membrane based microcalorimeter. *Thermochimica Acta*, 455(1):2 – 6, 2007. ISSN 0040-6031. doi: <https://doi.org/10.1016/j.tca.2006.12.007>. URL <http://www.sciencedirect.com/science/article/pii/S0040603106006125>. 6th KSTP Symposium.
- [244] Itamar Kimchi, John P. Sheckelton, Tyrel M. McQueen, and Patrick A. Lee. Scaling and data collapse from local moments in frustrated disordered quantum spin systems. *Nature Communications*, 9(1):4367, Oct 2018. ISSN 2041-1723. doi: 10.1038/s41467-018-06800-2. URL <https://doi.org/10.1038/s41467-018-06800-2>.
- [245] Guochu Deng, Yiming Cao, Wei Ren, Shixun Cao, Andrew J. Studer, Nicolas Gauthier, Michel Kenzelmann, Gene Davidson, Kirrily C. Rule, Jason S. Gardner, Paolo Imperia, Clemens Ulrich, and Garry J. McIntyre. Spin dynamics and magnetoelectric coupling mechanism of  $\text{Co}_4\text{Nb}_2\text{O}_9$ . *Phys. Rev. B*, 97:085154, Feb 2018. doi: 10.1103/PhysRevB.97.085154. URL <https://link.aps.org/doi/10.1103/PhysRevB.97.085154>.
- [246] A Togo and I Tanaka. First principles phonon calculations in materials science. *Scr. Mater.*, 108:1–5, Nov 2015.
- [247] W. O. J. Boo and J. W. Stout. Heat capacity and entropy of  $\text{mnf2}$  from 10 to 300 k. evaluation of the contributions associated with magnetic ordering. *The Journal of Chemical Physics*, 65(10):3929–3934, 1976. doi: 10.1063/1.432885. URL <https://doi.org/10.1063/1.432885>.

## Bibliography

---

- [248] S. López-Moreno, A. H. Romero, J. Mejía-López, and A. Muñoz. First-principles study of pressure-induced structural phase transitions in mnf<sub>2</sub>. *Phys. Chem. Chem. Phys.*, 18:33250–33263, 2016. doi: 10.1039/C6CP05467F. URL <http://dx.doi.org/10.1039/C6CP05467F>.



# Virgile Favre

## Expert data analyst

in [linkedin.com/in/virgilefavre/](https://www.linkedin.com/in/virgilefavre/)

✉ [virgile.favre@alumni.epfl.ch](mailto:virgile.favre@alumni.epfl.ch)

☎ +41 78 888 25 49

📍 Chemin Benjamin-Dumur 8  
1004 Lausanne

🕒 26 y.o. (28.03.94) Swiss single

## Technical skills

Data analysis  
X-ray and neutron scattering  
Machine learning  
Deep learning  
Physical systems modelling  
Numerical Physics  
Plasma physics  
Thin film deposition  
Evaporation, magnetron sputtering  
Magnetic measurements,  
Kinetics of chemical processes

## Computer science skills

C++, Python, MATLAB, LABVIEW  
Git, Bash, TCL  
Modelling : SolidWorks, Autocad  
Inventor, Orcad, OpenGL.  
LaTeX, Microsoft tools: Word, Excel,  
Power Point.  
Internet: html, css.  
Adobe CS: Indesign, Illustrator

## Language skills

English	C2-C1
Portuguese	B2
German	B1
Japanese	Notions
French	Native

## Interests

- Judo
- Rugby
- Jogging & trail running
- Climbing and bouldering
- Cooking
- Japan and Japanese culture

## About me

Passionate, hard working, I am a versatile engineer in applied physics. I am fueled by my passion for understanding the nuances of real-world phenomena. I consider myself a lifelong learner, eager to both build on my academic foundations in theoretical and applied physics, and stay in tune with the latest digital world developments through continued coursework and professional development.

## Experience

**Research assistant, [LQM - EPFL](#), Lausanne**.....Dec. 2016 - ongoing  
Leading projects from scratch, and analysing large data sets with self-developed numerical tools. Investigating the quantum properties of novel compounds using a wide variety of methods :

- X-ray and neutron scattering
- Magnetometry, specific heat
- Data Analysis, Big Data, Physical Modelling

**Tutoring, [EPFL](#), Lausanne** .....Sep. 2012 - ongoing  
Teaching and helping students in analysis, general physics, analytical mechanics and electromagnetism. Helping teachers creating innovative problem sets & solutions, detailed presentation of a subject in front of an undergraduate audience.

**Judo Instructor, [Reighikhan Dojo](#), Lausanne**.....Dec. 2009 - ongoing  
Train, coach and accompany students for competitions.

**R&D intern, [senseFly](#), Cheseaux-sur-Lausanne**.....Sep. 2015 - Feb. 2016  
Conceiving and realizing testbenches for drones using Matlab, C++, SCPI. Main tasks: deployment in production site, production management, traceability system creation, camera calibration, automation, computation time reduction and conception of automatic flight test for drones.

**Coach, [Physics section](#), EPFL, Lausanne**.....Sep. 2015 - Sep. 2016  
Introducing freshers to the scolar and cultural environment in Lausanne.

## Education

**PhD in Physics - EPFL, Lausanne**.....Dec. 2016 - Mar. 2021  
Physical properties of novel quantum magnets

**Masters in Physics Engineering - EPFL, Lausanne**.....Sep. 2014 - Sep. 2016  
Specialized in numerical and condensed matter physics, first class honours

**Bachelor in Physics - EPFL, Lausanne**.....Sep. 2011 - Sep. 2014  
Specialized in computational physics and optics, first class honours

**Scientific baccalaureate - Lycée Jean Moulin**.....Sep. 2009 - Sep. 2011  
Specialized in engineering sciences

## Projects

Thesis: Stuctural and magnetic properties of novel quantum magnets  
Synchrotron charaterization of chemical reaction kinetics  
Exotic ground state of  $3D, S=1$ , quantum spin liquid realized in  $K_2Ni_2(SO_4)_3$   
[Ferrimagnetic  \$120^\circ\$  magnetic structure in  \$Cu\_2OSO\_4\$](#)   
[Magnetic and structural properties of Ni-substituted magnetoelectric  \$Co\_4Nb\_2O\_9\$](#)   
[Commissioning of multi-million dollars spectrometer CAMEA at PSI](#)  
Applet creation for x-ray detection of motors in UCI-approved bicycles  
Statistical physics: Black and Scholes formula derivation